Characterisation of cryogenically assisted drilling of titanium alloy

Ellis Taylor

August 2021
Thesis submitted to the University of Sheffield
in partial fulfilment of the requirements for the degree of Doctor of Engineering

Department of Mechanical Engineering
The University of Sheffield

Abstract

Cryogenic machining uses cold fluids in the form of carbon dioxide or nitrogen to replace traditional water-based emulsions/solution or straight oils in material removal processes. It is emerging as a potential technology to further add value to the manufacturing industry through increased productivity, improved sustainability and improved working conditions. Drilling remains the most effective way to produce a hole in manufacturing and makes up 30% of all machining operations, however, there has been little published literature exploring the effectiveness of cryogenic drilling. Further information is therefore needed for industry to benefit from this technology. The aim of this work was to understand the behaviour and performance of cryogenic drilling with liquid carbon dioxide (LCO_2) in titanium alloy.

Initial trials were conducted at conventional cutting data (cutting speed and feed) to test the feasibility of employing a LCO_2 cooling strategy in drilling titanium alloys. The tests highlighted the need to modify the cutting data and enable adequate chip formation. These trials successfully identified cutting data that provided a stable chip formation.

Testing methodologies were developed to capture force and temperature of the LCO_2 drilling process. These were then deployed using a design of experiments approach to explore the influence of pertinent parameters on cutting performance. This process highlighted the importance of LCO_2 mass flow rate, cutting feed and workpiece thickness on the tool performance, and empirical models of the independent variables were obtained. Cutting feeds of 0.2mm/rev and the maximum achievable LCO_2 mass flow rates of 10kg/hr were identified as the optimal process parameters. Trials exploring peck drilling (drilling with intermittent feed) found lower temperatures and hole exit burr height with a peck cycle of 0.5mm cut with a 0.05mm retract.

Eight prototype tools with different coolant hole sizes and positions, and cutting edge rounding were designed, manufactured and tested to explore the effect of tool design on the process. Coolant hole size was shown to impact the cutting performance with increased normal forces and lower burr height, whereas coolant hole position had no impact. Reducing the cutting edge rounding counteracted the normal force increase with LCO_2.

Adherence of workpiece material to the cutting edges and margin were observed. Therefore trials with wet, dry and MQL strategies, to explore this adherence of material were conducted. Results from these trials highlighted the role of lubrication to minimise the adherence of workpiece material to the cutting tool. The wet strategy proved most adept at preventing adhered material on the margin as MQL was not able to access the drill margin as readily as the wet strategy.

Finally, tool wear trials were conducted. The tool wear mechanism on the LCO_2 assisted drills was identified as diffusion wear on the drill margin, where material was shown to diffuse from the tool into

the workpiece resulting in the formation of craters on the drill margin. This was in contrast to flank wear (as a result of an abrasive wear mechanism) for wet drilling, highlighting the importance of the LCO_2 cooling fluid to access the drill margin. Suggestions for achieving this are proposed and include using higher pressure LCO_2 flow to act as a carrier for lubricant to the drill margin.

The work presented in this thesis improves the understanding of LCO_2 assisted drilling of titanium alloys to inform Sandvik Coromant of future tool design for LCO_2 drilling to enable improved future sustainability of the manufacturing industry.

Acknowledgments

I would like to extend my utmost thanks to my supervisors. To Tom Slatter for introducing me to the world of cryogenic machining, and without whose guidance I would not have completed this degree. I thank you for the endless conversations and meetings, always offering a word of encouragement during the tougher times, and reading and mentoring me through the process. To Raphael Royer for the continued support and expert guidance throughout. I thank you for your enthusiam and support, for reading the thesis and providing feedback, and also producing the brilliant tool wear SEM images. And to Chris Taylor for helping me navigate the AMRC procedures, supporting me with the practical experiments, and always providing good machining discussions.

I would like to thank the machine operators at the AMRC, in particular Gary Barnsley, Matt Young and Jon Avill for their practical support and insight on machine during the numerous trials I conducted.

I'd like to extend my gratitude to Justin Davies and Steve Weston at Sandvik Coromant for both financial and technical support throughout the project as well as John Limb and the team at Sandvik Coromant Sheffield for providing machine and measurement equipment support at their site. I'd also like to thank Krystian Wika at the NAMRC for the discussions we had and the support that you provided.

I also thank my IDC friends and colleagues for providing a good sound board to discuss ideas and theories, as well as keeping things humourous and enjoyable in the office.

I also thank Clare Clarke and Francesca Breeden for their tireless work and support behind the scenes at the IDC.

I'd also like to thank my family and friends for their unwavering patience and support that they have given me throughout. And finally Emily, for standing by me through the ups and downs of putting the research together and for letting me know when I needed a break and a walk outside to get away from my desk. Thank you.

Contents

1 Introduction **12**

1.1 Cutting tools, machining and cryogenic machining . . . 12
1.2 Project aim and objectives . . . 14
1.3 Industrial context . . . 15
1.4 Thesis structure . . . 16

2 Machining background **18**

2.1 Introduction . . . 18
2.2 Machining . . . 18
2.3 Drills . . . 19
2.3.1 Drill manufacture . . . 20
2.3.2 Drill geometry . . . 21
2.3.2.1 Chisel . . . 22
2.3.2.2 Helix . . . 22
2.3.2.3 Cutting edge . . . 23
2.3.2.4 Cutting edge preparation . . . 24
2.4 Chip formation and evacuation in drilling . . . 26
2.5 Machinability and the metrics of tool performance . . . 27
2.5.1 Tool wear mechanisms and observable wear types . . . 28
2.5.1.1 Abrasive wear and mechanical damage . . . 29
2.5.1.2 Thermal damage . . . 30
2.5.1.3 Adhesive wear . . . 31
2.6 Titanium . . . 34
2.6.1 Titanium alloy applications . . . 34
2.6.2 Machinability of titanium alloys . . . 35
2.6.2.1 High local cutting temperature . . . 35
2.6.2.2 Difficult cutting conditions . . . 36
2.6.2.3 Chemical reactivity . . . 36
2.7 Design of experiments . . . 37
2.7.1 Full Factorial . . . 37
2.7.2 D-Optimal . . . 37
2.7.2.1 Candidate set and design matrix . . . 39

2.7.2.2 Information matrix and dispersion matrix . . . 40
2.7.3 Comparison with full factorial for increasing number of factors. . . . 40
2.8 Health and safety hazards with Metal Working Fluids . . . 41
2.8.1 Carbon dioxide hazards . . . 41
2.8.2 Traditional metalworking fluid hazards . . . 42
2.9 Thermodynamic considerations of LCO_2 as a cryogenic cutting fluid . . . 43

3 Literature Review **47**
3.1 Introduction . . . 47
3.2 The role of Metalworking Fluids (MWFs) in machining . . . 47
3.3 Metalworking fluids in drilling . . . 48
3.4 Cryogenic coolant . . . 50
3.5 Influence of cryogenics on machining processes . . . 51
3.5.1 Friction . . . 51
3.5.2 Heat generation/ thermal aspects . . . 52
3.5.3 Effect of cryogenic MWFs on chip form . . . 54
3.6 Turning with cryogenic media . . . 54
3.7 Milling with cryogenic media . . . 55
3.8 Drilling with cryogenic media . . . 57
3.8.1 Tool wear in drilling . . . 58
3.8.2 Drill exit burr height . . . 60
3.8.3 Edge rounding . . . 60
3.9 Sustainability and life cycle analysis of cryogenic machining . . . 61
3.10 Application of cryogenic coolants . . . 63
3.11 Summary . . . 64

4 Methodology **65**
4.1 Introduction . . . 65
4.2 Variables discovery . . . 65
4.3 Machine Tool . . . 66
4.4 Cutting tools used . . . 68
4.4.1 Prototype tools . . . 70
4.5 Initial trials to assess LCO_2 drilling functionality . . . 70
4.6 Process variable understanding . . . 72
4.7 Drilling cycle study . . . 73
4.8 Prototype tooling experiments . . . 74
4.9 Observations with alternative MWF (wet, dry and MQL) . . . 74
4.10 Observations with alternative cutting tool geometries . . . 74
4.11 Tool wear life tests . . . 75

4.12 Material . . . 76
4.12.1 Workpiece preparation . . . 76
4.13 Inspection of tools . . . 79
4.14 Force measurement . . . 81
4.14.1 Force measurement experimental set-up . . . 83
4.14.2 Force calculations . . . 84
4.14.3 Correcting the cutting force signal and extracting force data . . . 85
4.14.4 Stages of the cutting cycle . . . 89
4.14.4.1 Initial contact to fully engaged (z_0 to z_1) . . . 89
4.14.4.2 Fully engaged to beginning of exit (z_1 to z_2) . . . 90
4.14.4.3 Drill tip at exit to whole of drill tip exited (z_2 to z_3) . . . 90
4.14.4.4 Drill through the hole exit, prior to reversing through the hole (z_3 to z_4) 91
4.14.5 Process for extracting the pecking data from the force data . . . 91
4.14.5.1 Using the torque wrench to ensure that the calculations are correct. . . 92
4.15 Temperature measurement . . . 97
4.16 Hole quality measurement . . . 98
4.16.1 Geometry . . . 98
4.16.1.1 Diameter and Cylindricity . . . 99
4.16.1.2 Circularity . . . 100
4.16.2 Hole exit burr height measurement . . . 100
4.16.3 Hole surface roughness measurement . . . 101

5 Initial trials to assess cryogenic drilling functionality 103
5.1 Testing the LCO_2 cryogenic mass flow rate through the machine tool . . . 103
5.2 First drilling trials with the CoroDrill R846 heat resistant super alloy (HRSA) optimised drill . . . 104
5.2.1 Chip formation . . . 105
5.2.2 Surface roughness . . . 108
5.2.3 Burr height . . . 109
5.2.4 Summary . . . 109
5.3 Testing the hypothesis of expanded cutting data to improve chip formation. . . . 110
5.3.1 Chip formation . . . 110
5.3.2 Summary of increasing the cutting feed . . . 115
5.4 Conclusions of chapter . . . 116

6 Process variables, with forces as primary response. 117
6.1 Outline and experimental design of the process variables experiment- forces based. . . . 117
6.1.1 Responses/ dependent variables . . . 119

6.2 Data overview of the effects of the process variables captured during the forces rig experimental set-up . . . 119
6.3 Influence of factors in the force experiment . . . 123
6.3.1 Liquid CO_2 mass flow rate . . . 124
6.3.2 Feed rate . . . 125
6.3.3 Workpiece thickness . . . 126
6.3.4 Summary . . . 128
6.4 Significance of the factors on the responses and mathematical modelling of the responses from variables . . . 129
6.4.1 Normal Forces . . . 131
6.4.2 Torsional forces . . . 133
6.4.3 Chip form . . . 134
6.4.4 Hole quality . . . 135
6.4.4.1 Cylinder (max inscribed) . . . 135
6.4.4.2 Diameter (least squares) . . . 137
6.4.4.3 Circularity . . . 138
6.4.4.4 Burr height . . . 139
6.4.4.5 Surface roughness (R_a) . . . 141
6.5 Conclusions of chapter . . . 142

7 The effect of process variables on the temperatures generated 143
7.1 Overview of the experiment design . . . 143
7.2 Mathematical model for temperature . . . 144
7.2.1 The relationship between drill exit temperature, hole quality and drill parameters 146
7.2.2 Cutting feed . . . 148
7.2.3 LCO_2 mass flow rate . . . 149
7.2.4 Workpiece thickness . . . 150
7.3 Drill cycle study (peck drilling) . . . 152
7.3.1 Burr height and hole quality when peck drilling . . . 154
7.4 Influence of hole number . . . 155
7.5 Conclusions of chapter . . . 157

8 Observations with alternative tool features, coolant type, and tool geometry 158
8.1 Forces generated with different coolant hole size and position, and cooling strategies . . . 158
8.1.1 Tool wear with alternative cooling media . . . 166
8.1.2 Hole Quality . . . 172
8.2 Alternative tool geometries . . . 176
8.2.1 Chip form . . . 178
8.3 Conclusions of chapter . . . 181

9 Tool life **182**
9.1 Introduction . . . 182
9.2 Tool life tests of prototype tools with LCO_2 . . . 182
9.3 Hole quality with increased number of holes during the tool life tests . . . 187
9.4 SEM images of tools . . . 191
9.5 Conclusions of chapter . . . 195

10 Discussion **196**
10.1 Introduction . . . 196
10.2 Chip formation . . . 196
10.3 Cutting forces . . . 197
10.4 Temperature . . . 199
10.5 Hole geometry . . . 200
10.5.1 Hole diameter . . . 200
10.5.2 Circularity . . . 200
10.6 Exit burr height . . . 201
10.7 Tool life . . . 201

11 Conclusions **203**
11.1 Introduction . . . 203
11.2 Objective 1: Determine a suitable operating window for LCO_2 assisted drilling . . . 203
11.3 Objective 2: Observe the influence of LCO_2 process parameters on forces, temperature and workpiece quality . . . 203
11.4 Objective 3: Determine the impact of altering key design features on the drill with a view to positively improve the LCO_2 drilling process . . . 204
11.5 Objective 4: Compare observations to alternative cooling media . . . 204
11.6 Objective 5: Apply the changes to the LCO_2 process and determine tool life and tool wear mechanism in comparison to wet drilling with emulsion . . . 205
11.7 Concluding remarks and recommendations . . . 205
11.8 Future work . . . 206
11.9 Papers in preparation . . . 207

Nomenclature

t	time	[s]
α	Flank angle	[degrees]
$\bar{S}$	Cutting edge profile average cutting edge rounding	[μm]
Δr	Cutting edge profile flattening	[μm]
γ	Rake angle	[degrees]
ϕ	Apex angle of the cutting edge profile	[degrees]
ϕ	Shear angle	[degrees]
θ	Helix angle	[degrees]
θ_i	Helix angle at point i	[degrees]
c_{ct}	Difference between cutting edges	[mm]
r_{dr}	Drill radius	[mm]
r_i	Radial distance of point P on cutting edge from central axis of drill	[mm]
r_n	Cutting edge profile radius	[μm]
S_α	Cutting edge segment on flank face	[μm]
S_γ	Cutting edge segment on rake face	[μm]
t_0	Uncut chip thickness	[mm]
t_c	Chip thickness	[mm]
BHD	Between hole dwell	[seconds]
FL	Flow rate	[kg/hr]
FR	Feed	[mm/rev]
i	Arbitrary point along cutting edge	[-]

Nomenclature

K	Cutting edge profile form factor	[-]
L	Lead length	[mm]
RD	Retract distance	[mm]
WT	Workpiece thickness	[mm]

1 Introduction

1.1 Cutting tools, machining and cryogenic machining

Tools allow humans to achieve feats that would otherwise be difficult or impossible to achieve. Human tool making has origins stretching over 2.6 million years ago, with the first known evidence in Africa at the Oldowan archaeological sites. At this site, evidence shows that Homo Habilis (Handy Man) took one stone and repeatedly struck it against another stone to chip away some of the stone, creating the first known cutting edge [1]. Continued human innovation and development of the tools resulted in a diverse range of raw materials being used as tools such as bone and ivory, which were later replaced with bronze and iron tools.

From the late 19th century and the early 20th century, during the industrial revolution, technology and tool development accelerated rapidly, kick started by the need for improved productivity during the world wars. Steam power and then later electricity provided the power driven machinery to enable the increase in productivity. While the advent of high speed steel, tungsten carbide and ceramic tools ensured the cutting tools could withstand the increased stresses on the tool as a result of the increased productivity. The key events in manufacturing during this period are summarised in Figure 1.1.

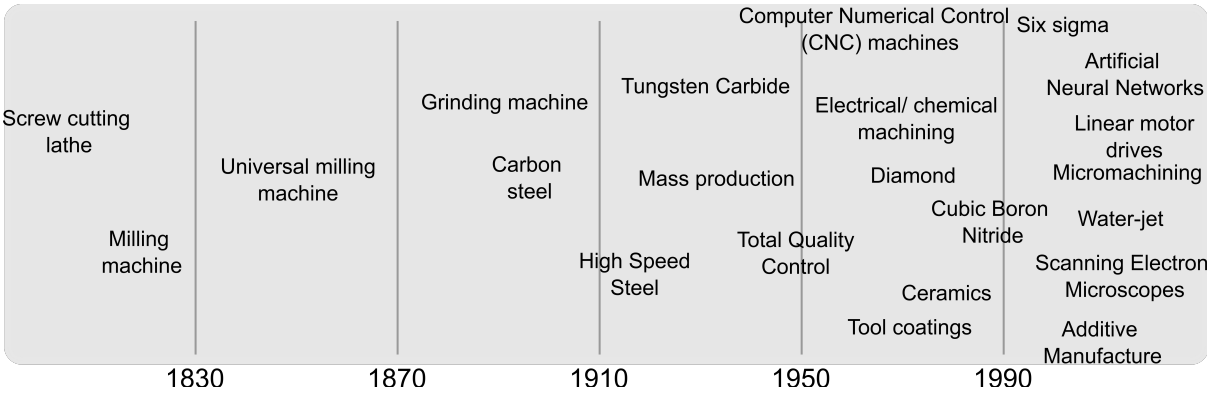

Figure 1.1: Timeline of key events in machining.

Machining is a subtractive manufacturing process and involves the removal of unwanted material from a component or workpiece with a cutting tool. The volume of material removed in machining varies. In extreme roughing, cut depths of millimetres are often taken when machining freshly cast components. In contrast during precision grinding processes it is common for submicrometre cut depths to be used, removing small material volumes. Each process during manufacture and machining adds value to the component irrespective of the amount of material removed and the process used. The type of the added

value can attributed to the function of the part and the reason for conducting the machining process. For example, a grinding process may be used to provide a closer dimensional control with an improved ability to achieve tighter tolerances. The process may also be used to improved surface quality and control of the surface topology and surface residual stresses, such as a burnishing process. The process may need to create a geometrical feature that cannot be created using an alternative method, or it may provide an economical benefit compared to another techniques.

The advances of machining methods in the manufacturing industry are driven by the pull of industry for solutions to machining problems, and by technological developments that push the new machining and manufacturing techniques to industry who have to adopt them to remain competitive. Among the current trends that are driving the need for the manufacturing industry to continue to develop and innovate are:

1. Lighter, harder and stronger part materials being preferred on components.
2. More capable and adaptable multi-axis machines, that run with improved accuracy and precision due to sturdier drives and improved design.
3. A greater adoption of automation, through robots and Industry 4.0 (the ongoing automation and computerisation of manufacturing), due to the ability to collect and record greater amounts of on-machine data.
4. The interconnected global economy, facilitated by improved communication and data transmission technology.
5. The need for process sustainability, due to the impact on the environment of increased raw material and energy consumption cause by large population growth. It is expected that sustainable processes will act as a barrier to entry to certain industries in the future, as evidenced by the publication of the United Nations 2030 goals in the agenda for sustainable development [2].

Cryogenic machining is where traditional metalworking fluids (MWFs) (also termed coolants, and as such are used interchangeably throughout the thesis), are replaced with an alternative medium in the form of typically carbon dioxide (CO_2) or nitrogen (N_2) either in the compressed liquid state or as a vapour. Cryogenic machining has the potential to add value to the machining industry in the context of the current and future trends of the manufacturing industry, both directly and indirectly. This thesis focuses on using compressed liquid CO_2 as a MWF, using an industrially available retrofitted through spindle device.

Cryogenic machining has been shown to improve tool life, part quality and finished part residual stresses, including in difficult to machine materials, and as such may provide productivity improvements in these cases [3]. A full understanding of the mechanisms underpinning these improvements are yet to be established [4], however the influence to lower the cutting temperature at the cutting zone and subsequently tribological conditions at the tool workpiece interfaces are understood to contribute to the improvements [3]. Additionally, potential for sustainability improvements can be realised through

the removal of harmful chemicals and contaminants contained within the fluid. This improves the environment cost and lowers process cost to industry, no longer requiring further costly processing prior to disposal of the contaminated fluids. Cryogenic machining lowers the consumption of raw materials contained within the fluids, including fresh water [5] (a scarce resource in certain parts of the world) and non-renewable products such as oils.

By replacing these fluids with CO_2 and N_2, the machining process system becomes cleaner; improving the health of the operators as they are no longer exposed to the harmful bacteria and contaminants typically found within the cutting fluids, providing a cleaner finished component that have better characteristics for future coatings [6] with fewer additional processing steps.

Despite these beneficial claims of the advantages of the cryogenic machining process, full adoption of the technology is yet to be realised across the machining industry. The technology is only proven for a limited number of processes and materials and is not able to be used, without risk, for the whole of the processes that are required in the production of a component. One such process is drilling which is the most effective means of producing a hole in manufacturing and makes up 30% of all machining operations [7].There is limited understanding around cryogenic drilling and how changing to a different fluid this impacts the current system. This includes unknowns around process settings to use, possible design changes to the drill and how the part quality is affected by the drill.

This thesis provides an improved understanding of cryogenic drilling and how drilling can be adopted in the cryogenic machining process to allow the manufacturing industry to realise the benefits of cryogenic machining.

1.2 Project aim and objectives

The aim of this project was to understand the behaviour and performance of the solid carbide drill in LCO_2 assisted drilling processes.

To do this the following objectives were defined:

1. Determine a suitable operating window for LCO_2 assisted drilling for further experimentation, primarily through chip formation.
2. Observe the effects of the LCO_2 drilling process parameters on cutting force, cutting temperature and workpiece quality.
3. Determine the impact of altering key design features on the drill with a view to positively improve the drilling process.
4. Compare observations to alternative cooling media.
5. Apply the changes to the LCO_2 process and determine tool life and tool wear mechanism and compare to wet drilling with emulsion.

1.3 Industrial context

Sandvik Coromant, a key stakeholder and a sponsor of the project that led to this thesis, is one of the world's largest cutting tool manufacturers who produce all manner of cutting tools. Solid carbide drills are sold within the solid round tools division around three offerings; versatile, optimised and customised. Versatile tools are designed to machine a variety of materials. Optimised tools are used when machining specific materials to achieve improved performance over versatile tools. Customised tools are unique products. They are made specific to customer needs, where versatile and optimised solutions cannot meet that need.

The tool designers use their knowledge to produce tools capable of operating in these avenues. This piece of work is intended to contribute to the tool designer's body of knowledge to enable them to provide tools and operating parameters to customers looking to drill with CO_2 cooling capability. Future demand for this is anticipated to increase in future with improved sustainability in the manufacturing sector.

Drilling performance (the ability to form a hole in material with a tool) is evaluated by observing the effects of parameters that are most relevant to industry and their application, these include (Figure 1.2):

1. Proper chip formation to allow adequate chip evacuation from the machined hole. Preventing chip and tool jamming in the hole, breaking the drill.
2. Diametrical accuracy of the hole.
3. Cost per hole, feed rate and productivity.
4. The total energy consumed within the process.
5. Burrs formed on the hole as a result of the drilling operation, in particular the exit burr.
6. Good subsurface and surface quality of the hole (including surface roughness), within the confined process of drilling.
7. Shape tolerance including the cylindricity and circularity of the hole.
8. Forces of the drill (torsional and axial forces).
9. Cleanliness of the component/workpiece after machining, and the impact of residues on the component on further processes in the production line.

The weighting and importance of each of these parameters will vary depending on application and the part being machined. For example, drilling a deep hole at high production rates is likely to place a greater emphasis on chip formation and cost per hole, as opposed to a hole drilled through thin plate into an exotic material at an aerospace company, where greater emphasis is likely to be placed on hole forces, hole quality and exit burr formation. The top four of the identified parameters that are mentioned here are the most common parameters across most applications.

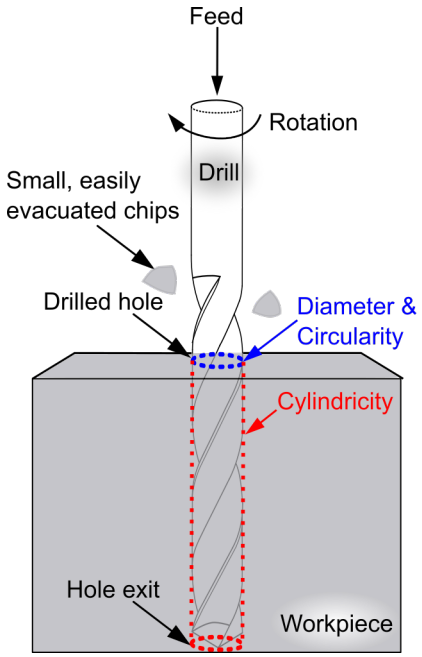

Figure 1.2: Some important parameters illustrated in drilling.

1.4 Thesis structure

- Chapter 2 provides background for the common themes considered with machining and drilling. It provides context to why titanium alloys have been chosen and background to the design of experimental techniques employed in the thesis.
- Chapter 3 explores the purpose of metalworking fluids (coolants) and the work conducted with cryogenic coolants to influence the cutting process. It identifies gaps in literature that remain as avenues for successfully implementing LCO_2 assisted drilling.
- Chapter 4 provides an outline of the methodology employed for the experimental trials conducted in subsequent chapters. It details the machine, material and tools used in the trials as well as the development of force measurement rig set-up and analysis, along with the temperature test set-up.
- Chapter 5 details the initial trial conducted with LCO_2 assisted drilling, and the need to alter the cutting parameters to achieve a stable secure process for future exploration of the process.
- Chapter 6 makes use of the findings from Chapter 5 to explore in detail, with design of experiments methodologies, the influence of several factors on key performance variables associated with drilling using the force-measurement set-up. Empirical relationships are determined from the multi-variate analysis conducted.
- Chapter 7 complements Chapter 6 and further builds upon the findings to explore how the temperature is influenced by the key factors identified from Chapter 6.
- Chapter 8 explores the influence of alternative cutting fluids and drill design on the process.

- Chapter 9 details a tool life test with the determined parameters from the work conducted in Chapters 5, 6, 7. The tool wear mechanism of LCO_2 assisted drilling in titanium alloy is identified and the results are compared to an equivalent process using a wet cooling strategy.
- Chapter 10 discusses the work conducted, and acts to tie the experimental chapters together. It also introduces opportunities for future work.
- Chapter 11 concludes the thesis with recommendations for Sandvik Coromant.

2 Machining background

2.1 Introduction

This purpose of this chapter is to provide background for the thesis. It begins by outlining machining and the orthogonal cutting model, before introducing drills and the nomenclature for a typical solid round drill. It then goes on to cover machinability and the metrics of tool performance, including the importance of chip evacuation in drilling. Titanium, and the the machinability of it's alloys is then explored. A section outlining the design of experiment techniques in this thesis is provided, before finally the hazards and thermodynamics of LCO_2 cutting fluids is covered.

2.2 Machining

Subtractive material removal (or machining) can be a stage in the manufacturing process of a component or part. It utilises a hard and sharp cutting tool to add value to the workpiece by removing material to produce the desired shape, size and surface finish. The cutting tool industry adds value to the machining stages of the manufacturing process through technological advances. These include improving productivity as increased material removal rate (MRR), streamlining manufacturing by reducing the number of tool changes and pre and post processes, as well as reducing costs through improved tool life.

The most basic representation of machining is in the form of the the two dimensional orthogonal cutting model, Figure 2.1, first proposed by Merchant in 1945 [8]. In this model, a straight edge cutting tool moves relative to the workpiece in the cutting direction removing a layer of material from the workpiece denoted the uncut chip thickness or chip load, t_0. This layer of material is removed at a shear angle, ϕ to form a chip of thickness, t_c.

The formed chip slides up the tool's rake face at rake angle, γ (measured from the normal to the work surface plane). The flank face meets the rake face at the cutting point, to form the cutting wedge. The angle between the flank face and the workpiece is the flank angle, α and is used to minimise the frictional contact of this face with the workpiece. Due to plastic deformation of the workpiece, part of the flank face rubs along the work surface during machining, and forms the surface finish in turning and milling processes. In the drilling process, the margin rubs against the hole wall and contributes to the final hole surface finish.

The chip formation process involves a severe high shear action in the vicinity of the cutting edge of the cutting tool. Heat is generated in machining as a result of plastic deformation and overcoming friction

between tool and workpiece at the interfaces. In the primary shear zone, heat is generated as a result of elasto-plastic deformation and in the secondary and tertiary deformation zone, heat accumulates as a result of elastic deformation and friction [9]. Heat is dissipated away from these shear zones in the cutting tool, chip, workpiece and cutting fluid.

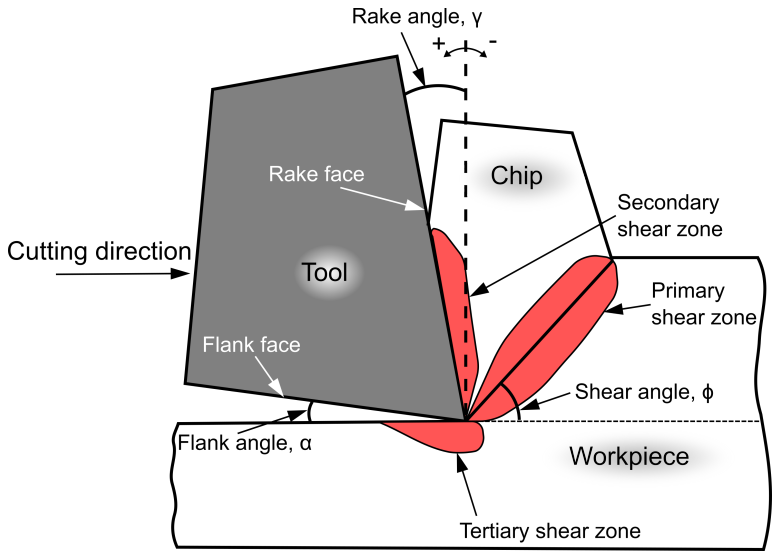

Figure 2.1: A schematic drawing of the 2D orthogonal cutting model.

2.3 Drills

Drilling comprises approximately 30% [10] of the number of operations when compared to other machine operations and is generally carried out towards the end of manufacturing when there is a lot of value in the manufactured part from other operations already completed on the component. A drilling tool (drill), a schematic example of which is shown in Figure 2.2, is used to produce a hole of the same nominal diameter as itself. Drills are characterised by their fairly large length to diameter ratios (regular drills have ratios typically between three and ten [7], above this ratio deep hole drilling techniques must be considered).

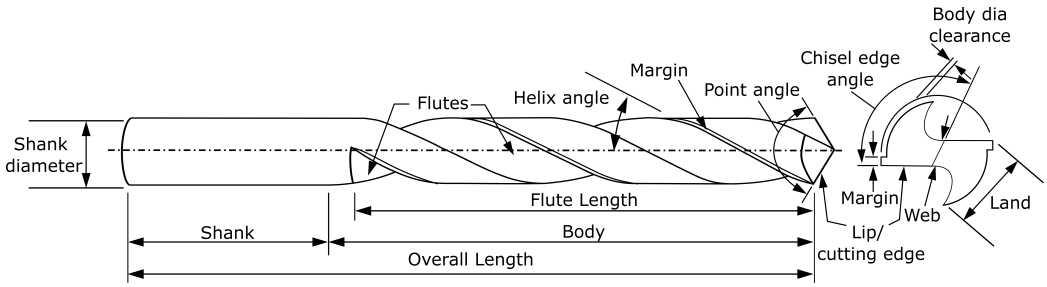

Figure 2.2: Schematic of a chisel edge drill, showing the key features, and detailing the drill nomenclature.

2.3.1 Drill manufacture

Drills are made from different materials to suit their application and purpose. The three broad categories that drills are made from include; high speed steels (HSS), cemented carbide, and polycrystalline diamond (PCD). Each of these materials has unique properties suiting them to different applications. Common high speed steel tools utilise high alloyed steels (containing W-Mo-V-Co) and have the greatest bending strength of all the tool materials. This characteristic means that they are particularly suited to non-rigid machining system set-ups, and find applications in using older machinery or non-rigid part holding strategies where vibration of the machined part means the increased ductility of the HSS tool prevents tool chipping and premature tool failure. HSS tools have better resistance to edge chipping and improved mechanical strength over other cutting tool materials, therefore a sharper cutting edge can be created on HSS cutting tools compared to the other two materials. The sharper cutting edge results in lower the cutting forces and temperatures, improving surface finish and part tolerances. HSS tools are a low cost solution that provides the best resistant to thermal shocks.

Cemented carbides are the most widely used tool material, and consist of hard grains (W and/or Ti, V, Cr, Zr, Mo) bound together by a softer metallic binder (Co, Ni and/ Fe). WC (tungsten carbide) with a Co (cobalt) binder is the most common cemented carbide material.

Cemented carbides have lower toughness than HSS but are harder, and are able to machine at higher cutting speeds owing to their higher hot hardness (Figure 2.3). Yet, to maximise the performance of cemented carbide tools, other components of the drilling system need to be high quality with rigid machinery, sufficient toolholding and well maintained metal working fluid (MWF). Otherwise, the lower toughness of cemented carbide tool makes them susceptible to chipping with unpredictable and premature tool failure due to excessive tool vibration and chatter [11]. Cemented carbides are particularly suited to cryogenic machining applications as they have been found to retain their strength and toughness at cryogenic temperatures [12].

Diamond coated tools are typically used to machine highly abrasive materials such as lightweight metal matrix composite materials containing hard abrasive particles (such as silica and alumina) and CFRP. Diamond has high hardness and does not experience high abrasive wear rates when machining these materials like the alternative materials do but they are more expensive that the other two materials.

The tools used in this thesis are solid carbide and hence made from cemented carbide, because it is the optimal tool material for machining the difficult to machine Ti6Al4V [11].

In general solid carbide drills are made using three broad processes; the preparation and creation of the tool substrate material, grinding the substrate to the required shape, and then coating the substrate with a hard layer of material. The tool substrate material is typically a sintered tungsten carbide-cobalt (WC-Co or WC) due to the high melting point (˜2800°C) and combination of hardness and toughness. The substrate is made using a carefully controlled powder metallurgy process and consists of the following main steps:

1. Processing ore materials and extracting the carbide materials.

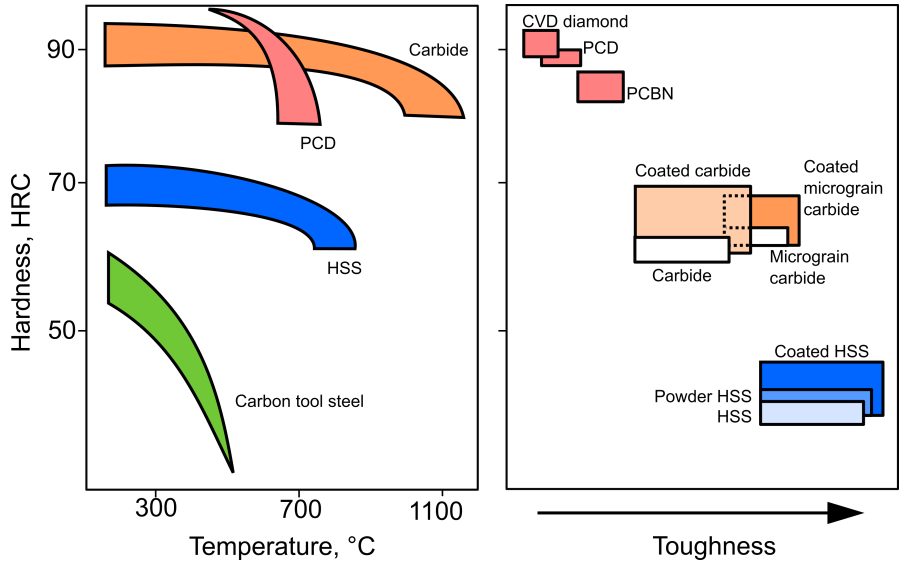

Figure 2.3: Hardness vs. temperature for the various tool substrate materials. (Modified from Astakov[7])

2. Milling the carbide powders in to small enough grain sizes (100µm).

3. Selecting grain sizes and mixing of various carbides.

4. Extrusion to form the shape. The powder is mixed with a blend of acids and glycols and extruded as a paste to form the overall shape of the substrate [13]. This includes the internal coolant holes in the shape of a helix to a specified pitch.

5. Sintering. The heating up and cooling down of the substrate is carefully controlled to remove impurities, control grain size and product densification [14].

6. Hot isostatic pressing to form the nominal shape of the tool. Is done to reduce the porosity that could be left after the sintering process.

7. Grinding the finished substrate to final geometry sizes.

8. An optional coating of the tool with a hard wear resistant coating.

2.3.2 Drill geometry

Figure 2.2 shows a schematic of one of the simplest drill types, the chisel-edge drill, highlighting the key features of a drill. Each drill has three main components: the shank, body and point. Drills can be manufactured with either a straight or tapered shank depending on the hole diameter. Typically tapered shanks are used when drilling medium or large diameter holes [15]. The drill is held and driven by the toolholder at the shank, which may or may not be the same diameter as the drill.

While each drill will have the basic features shown here, different drill manufacturers will modify these features so that they are better suited to machine different workpiece materials.

The body of the drill is made up of two or more helical grooves (flutes), which form the cutting edges or lips at the drill point, which is ground to the required drill point angle (ϕ_p). The geometry of the drill point impacts drilling characteristics. Various point angles and lip clearances can be used, and they have an impact on all of the characteristics of drilling. The geometry of the point affects the hole quality (size, straightness and burr), size and shape of chip formation, strength of the cutting edge, heat produced, rate of wear, drilling pressure and the capacity to run at various speeds and feeds [16].

At the centre of the drill point is the chisel. The chisel acts as an indenting punch with velocity in the drill feed direction. Chips form at both the cutting edges and at the chisel, the shape and extent of these chips depend on the chisel geometry adopted. Split point chisels, commonly adopted by cutting tool manufacturers, facilitate increased rigidity with a thicker web. Thicker web drills have a higher thrust limit and a higher effective rake angle, improving the chip formation at the chisel and self-centering ability of the drill [7]. The chips that are formed at the primary and secondary cutting edge are evacuated through the flute, opposite to the cutting feed direction, out of the drilled hole.

2.3.2.1 Chisel

Work conducted by Hoshi and Zhao [9] in 1989 studied the common tool tip shape that is used today and found on some Sandvik Coromant CoroDrills (the s-shaped centre edge). This geometry positively influences performance through reducing thrust forces exerted on the drill. In their work they compared an s-shaped centre edge drill against conically ground, three-rake, and spiral point drills. These alternative tools were designed with the purpose of reducing the thrust force exerted on the drill by minimising the chisel edge. Results in this work show that the s-shaped centre edge geometries are favourable in terms of improved tool life, lower thrust forces, lower torque and favourable chip formation. Further design and optimisation of a drill geometry is possible. This was shown by Paul et al. [17], where they optimised drill cutting lips and chisel edge to minimise for thrust, torque, and both together using genetic algorithm techniques.

2.3.2.2 Helix

The two helices facilitate the evacuation of chips and cutting fluid out of the produced hole. These helices are ground on to the drill at the helix angle, θ (Figure 2.4). The helix angle of the drill is modified depending on the material being manufactured. Low helix angles are preferred when drilling soft materials (e.g. brass) and/or shallow holes, where chip evacuation is not a problem and drill penetration is prioritised for maximum production. High helix angled flutes are preferred when drilling deeper holes in materials such as aluminium or copper where the chips experience evacuation difficulties and thus require more screwing action from the drill. The screw action of the drill in the higher helix angled drills acts to mechanically remove the chips from the hole. Coupled with a wider flute, chip evacuation from the hole is enabled.

Equation 2.1 demonstrates how the helix angle is computed, where L is the lead length and r_{dr} is the outer radius of the drill.

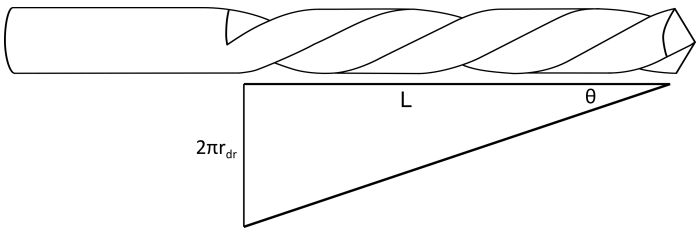

Figure 2.4: Schematic to show the definition of the helix angle in the drill.

$$\tan\theta_{dr} = \frac{2\pi r_{dr}}{L} \tag{2.1}$$

The helix angle variation can be shown by using the definition of the helix angle described in Equation 2.1. Consider Figure 2.4, showing a schematic of a drill. If the helix of the drill is unwrapped a full 360 degrees at the drills outer edge then using the distance this covers over the length of the drill, lead length L, the helix angle θ can be found. In this instance $2\pi r$ is the circumference of the drill and r_{dr} the outer drill radius.

Now consider a point i, on the cutting edge that is a distance r_i from the drill centre. Using the known helix angle, it is possible to calculate the helix angle at that point θ_i using the ratio or radius at point i to radius of drill using Equation 2.2.

$$\theta_i = \arctan\left(\frac{r_i}{r_{dr}}\tan\theta_{dr}\right) \tag{2.2}$$

Therefore, as point i moves closer to the centre of the drill, resulting in a smaller ratio of r_i/r_{dr}, and thus helix angle. The helix angle directly determines the rake angle of the drill [18], and with the decreasing helix angle towards the centre of the drill the rake angle of the cutting edge will decrease.

2.3.2.3 Cutting edge

The cutting edge or cutting lips are the primary source of cutting. The geometry of the cutting edge is highly complex and three dimensional in nature. Unlike orthogonal cutting where the rake and flank angles are assumed constant, the rake angle and flank angle and helix angle vary along the cutting edge. These angles and geometries are covered and derived in detail by Astakov [19]. A variety of cutting edge shapes are used for varying applications as the shape modifies the cutting process. Illustrated is the variation of the rake angle of the simplest drill with a straight edged cutting edge. The rake angle is dependent on the point angle and the web thickness of the drill. Equation 2.3 shows the rake angle as a function of the drill radius at point i, where c_{ct} is the distance between the cutting edges when the drill is viewed point on, and $r_{pr} = \frac{r_i}{cos(\mu_r)}$ where μ_r is the angle at point i from the centre of drill (see Figure 2.5).

$$\gamma(r_i) = -arctan\left(\frac{c_{ct}}{2r_{pr}}cos(\frac{\rho}{2})\right) \tag{2.3}$$

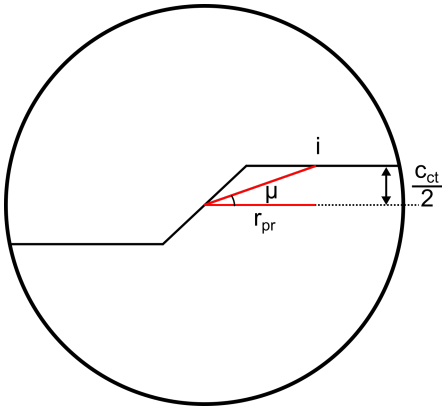

Figure 2.5: Schematic showing the drill, point on, with the relevant parameters shown that are used to calculate the rake angle at point *i*.

2.3.2.4 Cutting edge preparation

During the drill manufacture both the helix and drill point facets are ground. These form the rake and flank faces of the drill, meeting at a sharp edge on the cutting lips. A sharp edge has low strength, caused by cutting edge and surface defects such as burrs, micro cracks and poor surface roughness. A sharp tool edge chips and experiences cutting edge fracture, leading to tool failure [20, 21, 22]. The sharp cutting edge can be honed, micro-blasted or abrasive brushed to produce an engineered edge geometry free from burrs, micro-cracks and other defects. Figure 2.6 shows a schematic of the cutting edge before and after edge preparation.

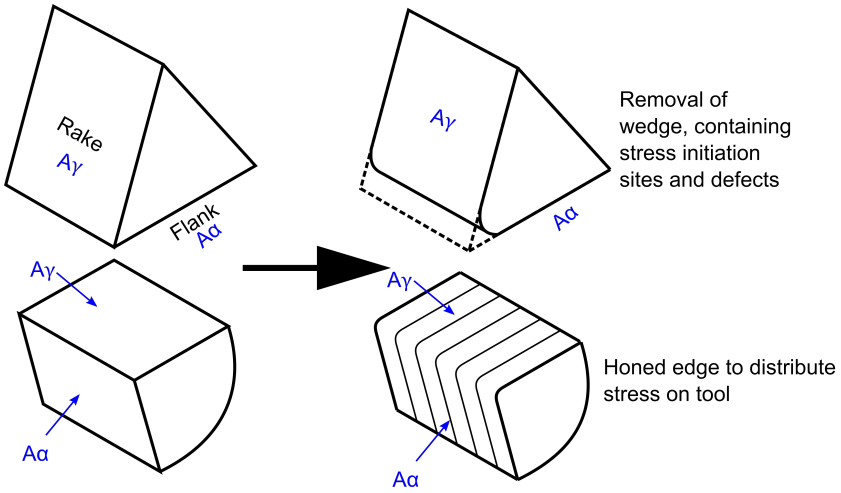

Figure 2.6: Before and after edge preparation (modified from [23]).

The size shape and type of cutting edge preparation applied to the cutting edge can be altered for different applications. These can be honed (or rounded) edges, or a flat chamfered edge (Figure 2.7).

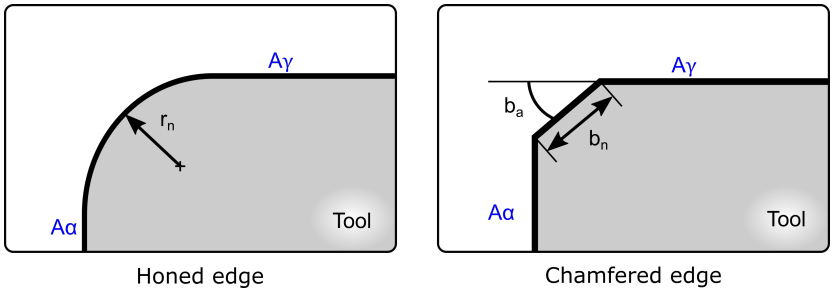

Figure 2.7: Honed and chamfered cutting edge shapes commonly used to strengthen the cutting edge of tools (modified from [23]).

The choice and size of edge preparation size is determined primarily by tool macrogeometry, for example, larger edge rounding or a chamfer would be needed for higher rake angles because of the increased stress concentrations experienced by the cutting edge during cutting.

When edge preparation is used, the effective rake angle is changed in the local region around the edge preparation area (Figure 2.8a). This results in a localised decrease in rake angle. The result is the pushing of material and formation of a stagnation zone (stationary material) in front of the cutting edge. This is depicted by an area of low strain rate, i.e. stagnation because of no material flow at this point [24]. This forms as built-up edge (BUE) on the cutting edge. This stagnation zone is larger in chamfered cutting edges and as such a larger BUE will form.

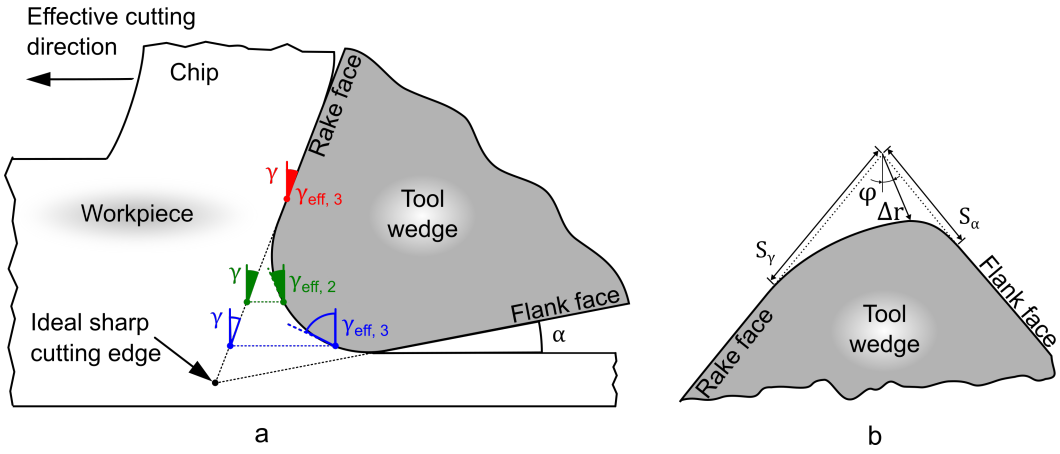

Figure 2.8: a) Edge preparation changing the effective rake angle at the position of cutting. b) Nomenclature used to describe the edge rounding when it is noticeably unsymmetrical (modified from [25]).

Measurement of the edge rounding is typically done using a white light chromatic sensor to obtain a cloud of data points to represent the edge. A contour is then fitted to the obtained data to represent the cutting edge where the edge rounding is then obtained using a circle fitting method to capture the edge radius, r_n [26].

Circle fitting cannot be used to describe the edge rounding when the edge profile is not a symmetrical circle with tangents at the rake and flank faces, instead has a degree of skewness. The edge rounding can be skewed either to the flank face or the rake face and described by the cutting edge segment on flank

face, S_α and cutting edge segment on rake face, S_γ to denote the extent of the edge rounding on either face. This is described by Denkena et al. [22] and presented in Figure 2.8b. In this method, a sharp edge profile is imposed over the cutting edge profile. S_α and S_γ are defined as the distance along the flank and rake face respectively, between the superimposed sharp tool point and the tool surface. Profile flattening, Δr defines the shortest distance between the sharp tool point and the tool. The location of this relative to the intersection line of the flank and rake faces is defined by the Apex angle ϕ. This notation is then used to define the cutting edge profile in terms of the average cutting edge rounding, as $\bar{S} = \frac{S_\alpha + S_\gamma}{2}$ and the form factor as $K = \frac{S_\gamma}{S_\alpha}$.

Denkena et al. [22] showed microgeometry can be tailored depending on the material being machined, and that the values of S_α and S_γ can be altered to protect the cutting edge from wear when it is expected on each cutting face. For example, to protect the rake face from crater wear- S_γ is reduced moving Δr towards the rake face.

2.4 Chip formation and evacuation in drilling

The basic single shear model of chip formation was introduced in Section 2.2. This single shear model is somewhat limited when modelling the chip formation in a realistic manner. Astakov [27] points out the following limitations of the single shear model:

- It models a 3D phenomenon in 2 dimensions.
- Assumes shear takes place across a single plane.
- The assumed infinite deceleration at the shear plane assumes infinite strain rate.
- Unrealistically high shear strain rates implies that the strain exceeds that achieved at fracture during mechanical testing, when calculated.
- Improper resistance of the work material to be cut.
- Unrealistic of the tool-workpiece contact.
- Inapplicable to brittle materials.

Komanduri [26] compared realistic machining to this single shear model and suggested that these models, and those parameters derived from them, such as the chip thickness ratio and shear angle, should not be used to describe the machining characteristics of titanium alloys due to the segmented chip formation found when machining titanium alloys. Instead they provide a framework to analyse the cutting system.

In drilling, the primary chip flows towards to the periphery of the drill, as the velocity of the cutting edge varies from zero at the centre to maximum at the periphery, the chip interacts with the formed wall of the drilled hole to form the chip. Generally a cone like chip is formed as the chip is longer at the periphery than the centre and thus is travelling faster, this causes the chip to curl inwards. If the chip rotation cannot keep up with the formation of the drill then the chip will either break or move along

the flute without spinning. Ke et al. [28] investigated chip form at different cutting speed and feed for different drill diameters, and found that the spiral chips were related to the maximum area of the flute.

The chisel edge of the drill also forms a chip, which is known as the secondary chip. This is formed by either a punch web or the high negative rake of a split point geometry, depending on the design of the centre of the drill. Chips that are individual and discontinuous in nature are favourable, as they are more easily evacuated from the flute of the drill out of the drilled hole, and as such entanglement and trapping of the chip is prevented. It can be drawn from literature that the key consideration in the formation of the chip is the combination of tool geometry and the coolant to impart mechanical work on the chip to induce chip curl and chip breakage as it interacts with the hole wall of the drilled hole [19]. Chip breakers (which are shaped surfaces on the cutting tool) and careful positioning of the location of the coolant exit holes can be used to induce mechanical work on to the chip so that it aids the formation of the chip.

Another consideration is the temperature during the machining of the material, it is known that the shear strength of material is effected by the temperature [29]. Temperature changes may affect the point at which shearing occurs and thus how the chip forms during machining. Cutting parameters, cutting speed and feed influence the formation of the chips. With increasing speed, friction is reduced so that the chip has less curl, and the chip is thicker with increased feed rate, as essentially equivalent uncut chip thickness is thicker. This holds with cryogenic machining of Ti6Al4V, where Bermingham et al. [30] found that chips are thicker when the feed and cut depth are increased. The point angle and drill flute angle influence the formation of the chip through its interaction with the wall of the hole and the drill flute during formation. This interaction is increased at deeper hole depths. Ke et al. [31] produced models to show that the average chip lengths of continuous chips are related to drill point angle and flute helix angle. This was done with AISI 1038 steel, which is a continuous chip formation, unlike the segmented chip formation of titanium, so is unlikely to be applicable to the work presented in this thesis.

2.5 Machinability and the metrics of tool performance

The machinability of a material is loosely defined in the machining industry as the ease or difficulty with which a material can be machined using a cutting tool. Depending on the application of the user it can contain a definition of tool life (or tool wear), quality of the component generated and the component forces that are required to machine the material (the efficiency of energy consumption in the process) [32].

No one specific definition exists as the requirements for different operations varies in the goal of the process, Mills et al. [33] suggest that machinability should be restricted to how the material wears the cutting tool when it is machined and that cutting energy and forces should be considered separately. The machinability of the material should therefore be arrived at empirically, taking in to account the specific conditions of the process under consideration.

The productivity of a machining operation directly expands upon the machinability of a material in that maximum productivity is achieved from creating a balance between maximising cutting process parameters whilst simultaneously minimising tool wear. Tool performance, or the life of a tool is the

productive lifetime of a tool, where the tool has not experienced excess wear and produces products or parts which are "acceptable" in terms of their quality. The acceptability criterion for part quality can be a multitude of factors, such as surface finish, geometry and subsurface condition. Therefore, depending on the requirements of the operation, different acceptability criteria are defined.

One example where this acceptability criterion may vary is the process type (for example roughing or finishing cuts). In finishing cuts, the surface finish and final geometrical form are examples of the acceptance criteria and are generally defined to lower and tighter tolerances that roughing cuts. A small change to the cutting edge due to wear may result in the tool being unable to produce acceptable components, indicating that tool life in finishing tools may be shorter, all be it with less aggressive process parameters (mainly cut depth).

In roughing operations a larger amount of wear could be admissible because there are different acceptance criteria which allow for an increased amount of wear, such as; adequate chip form, workpiece quality (chipping and form) or simply avoiding catastrophic tool failure.

Tools are designed for these acceptance criteria in mind. Finishing tools generally have a sharper edge radius than roughing tools, and different geometrical shapes based on their use in application. The machining process is a particularly harsh environment for cutting tools due to the high temperatures, local and high pressures, leading to wear, as cutting parameters are increased for improved performance, so to is the wear on the tool.

2.5.1 Tool wear mechanisms and observable wear types

During machining, the relative motion of the tool with the workpiece material, as the formed chip slides over the tool rake face and the workpiece past the flank, causing a loss of material from the cutting tool causing the tool to wear away. Under steady conditions the extent of this tool wear is proportional to the speed of the relative motion and the load between the contact, according to Archard's wear law [34]. Archard made the distinction between abrasive and adhesive wear. In these distinctions he stated that abrasive wear is caused by harder particles scratching a softer material removing a smaller volume of material as wear debris. Whilst adhesive wear is the removal of material is torn form a surface where two asperities on each mating surface having locally welded to each other. According to Childs [35], in machining applications the classification of these wear mechanisms can be made with reference to cutting temperature. Figure 2.9 provides a generalised illustration of tool wear rate to cutting temperature. The abrasive wear mechanism is shown to be independent of cutting temperature, whilst thermal damage increases drastically with increasing cutting temperature. Adhesive damage on a cutting tool is found to have a localised maximum at a particular cutting temperature.

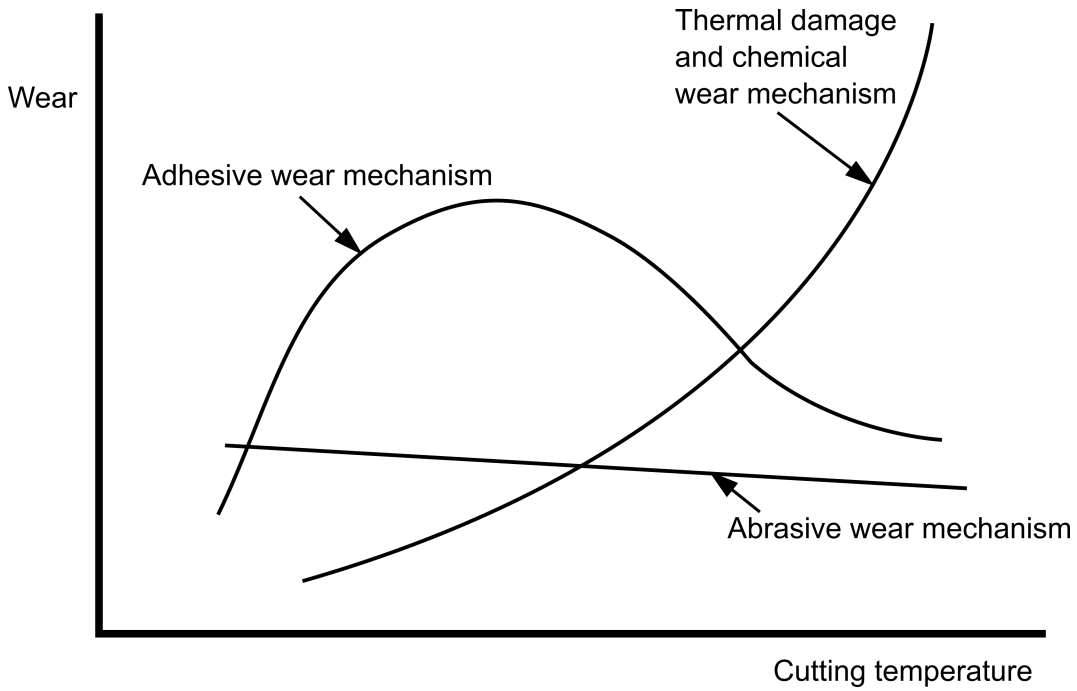

Figure 2.9: The relationship between the wear mechanism and the temperature (modified from Childs [35]).

2.5.1.1 Abrasive wear and mechanical damage

Abrasive wear on tools is caused by hard particles in the workpiece material (e.g. cementite (Fe_3C) in ferrous materials), possible sand inclusions in the workpiece from the casting process, or small abrasive hard particles of the tool coating that have broken off the cutting tool. These particles slide along surface of the tool causing a progressive loss of material due to the relative motion between the tool and the workpiece. If the chip adheres to the cutting edge (high adhesive load) then sliding will occur in the chip and not over the cutting edge of the tool, and abrasive wear will be substituted by adhesive wear (see Section 2.5.1.3). Ideally the abrasive wear is proportional to the sliding distance of the contact, and independent of cutting velocity and temperature.

The origin of abrasive wear in Ti6Al4V was explored by Nguyen and colleagues [36]. In their study they found that by using orientation image microscopy, with electron backscatter diffraction (EBSD), the source of flank wear originated from the alpha grains and alpha clusters in the Ti6Al4V. In machining this is usually observed as flank wear (shown in Figure 2.10). Flank wear is viewed as the most desirable type of wear as it can be predicted and controlled.

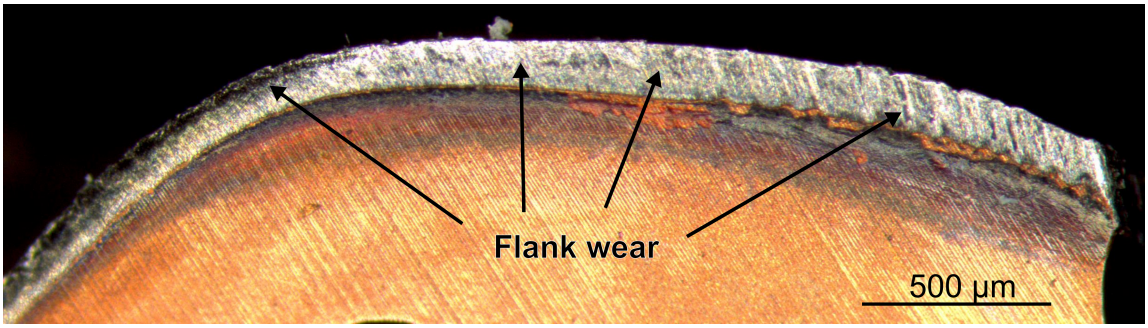

Figure 2.10: Flank wear shown across the entire cutting edge on the flank face of a solid carbide drill (image supplied by Sandvik Coromant).

2.5.1.2 Thermal damage

This wear mechanism occurs when the tool is subjected to excessive temperatures. How these excessive temperatures are achieved vary from process to process. With continuous cutting processes, such as drilling, turning and grooving, the tool is heated continuously. The resulting high temperatures in combination with the high compressive forces experienced by the tool can result in macroscopic plastic deformation changes to the tool. Plastic deformation of a cutting edge results in a loss of geometrical form and surface damage to the workpiece. An example of a tool plastically deformed is shown in Figure 2.11.

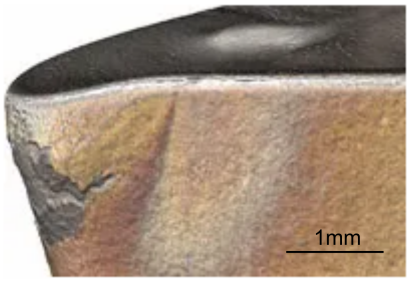

Figure 2.11: Plastic formation shown on a turning insert. Note the deformation of the cutting edge downwards (image supplied by Sandvik Coromant).

Alternatively in processes with intermittent cutting, such as milling, the cutting edges are exposed to rapid increases and decreases in extreme temperature. This can be exacerbated with coolants that remove the heat more rapidly. This results in large thermal gradients with high tensile stress on the outside of the tool. When these tensile stresses exceed the strength of the material, cracks are formed. They are often called comb cracks as they have the appearance of a comb, and are commonly perpendicular to the cutting edge. An example of comb cracks is shown in Figure 2.12.

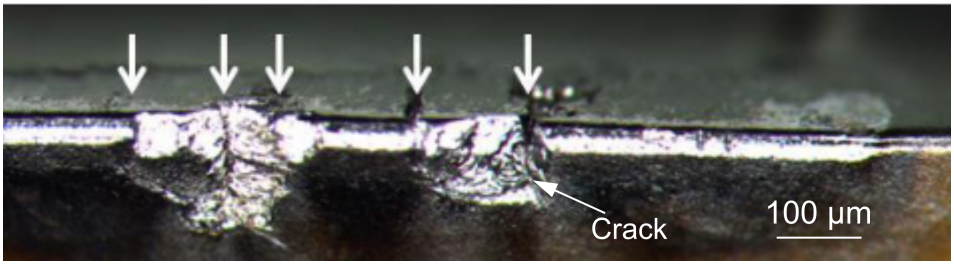

Figure 2.12: Comb cracks (arrows) present in inserts when face milling grey cast iron, image from Garcia 2017 [37].

Wear can also occur as a result of thermal diffusion of material where, at elevated temperatures elements from the cutting tool diffuse in to the structure of the workpiece. The opposite is also true where elements from the workpiece diffuse into the tool. The removal of this material from the tool results in the weakening of the tool, subsequently causing the cutting tool to break. In titanium alloys this is particularly problematic. It has been shown that material from the tool readily diffuses to the workpiece [38] when machining titanium alloys. When machining Ti6Al4V with uncoated carbide tools Zhang et al. [39] showed that the cobalt binder in the tool diffused into the titanium alloy during machining, weakening the structure supporting the hard tungsten grains in the cutting tool. These hard grains are then removed from the surface of the tool resulting in the formation of crater on the tool, crater wear.

Crater wear is observed where the chip and tool are in continuous contact and under high thermo-mechanical load, particularly the rake face of the tool. High thermal conductivity and low solubility of the tool material in the workpiece material therefore result in conditions for reduced crater wear. Figure 2.13 shows an example of crater wear on the rake face of a drill.

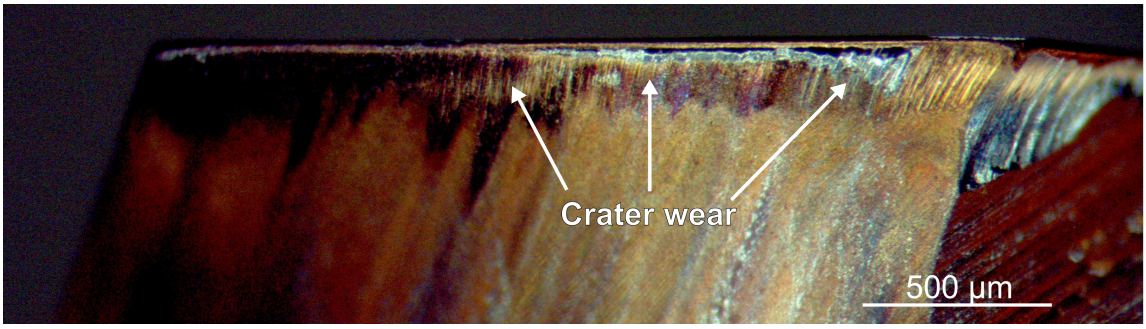

Figure 2.13: Crater wear on the rake face of a solid carbide drill (image supplied by Sandvik Coromant).

2.5.1.3 Adhesive wear

Strong adhesion can occur between the chip and the cutting tool or workpiece and cutting tool. The effect of this strong adhesion generally requires high temperature. If the adhesive shear strength between the tool and the workpiece is stronger than the failure strength at the interface, then adhesive transfer of material will occur. Transfer of material will be from the chip or workpiece to the tool if this weakest point at the interface is in the chip or workpiece. This results in built-up edge formation of material on

the tool. When the weakest point of the contact occurs within the tool, transfer of material from the tool to the workpiece occurs. The repeated adhesion of material to the tool and failure of the tool results in adhesion wear. The maximum rate of adhesive wear occurs at different temperatures depending on the cutting tool and workpiece combination. At low cutting temperatures, it is reduced because of low adhesion tendency, and at high cutting temperatures it is also reduced because of thermal softening of the workpiece material.

An example of built-up edge forming on the cutting edge is shown in Figure 2.14. The image shows that, as a result of a build up of workpiece material on the cutting edge, chipping on the tool has occurred. This chip in the tool has formed due to the tool being weaker than the adhesion strength between the tool and the adhered material.

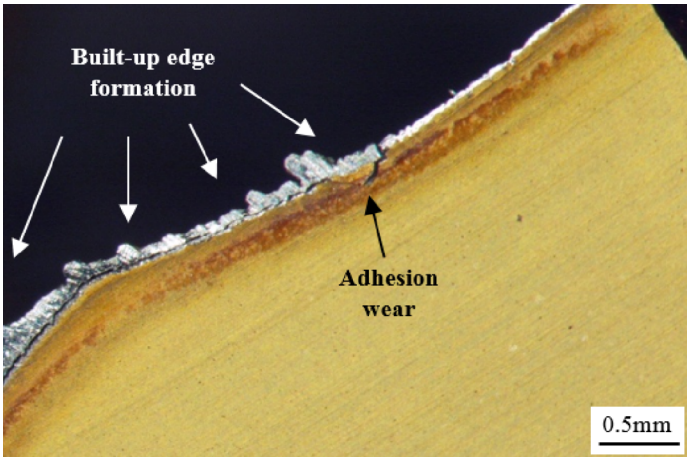

Figure 2.14: Example of built-up edge formation on the cutting edge of a drill (from [40]).

An extreme example of chipping is shown in Figure 2.15, here three chips have formed on the tool. The formal definition of chipping on a tool is defined by a breakdown of the cutting edge line. As can be seen there has been a clear breakdown of the cutting edge line.

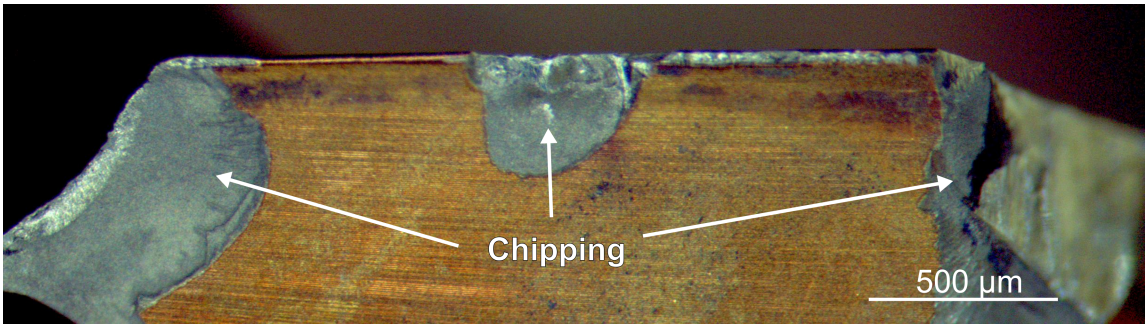

Figure 2.15: Example of chipping observed on a solid carbide drill (image supplied by Sandvik Coromant).

It should be noted that although the adhesion mechanism is the main cause of chipping [41], it can also occur due to an intermittent thermal load on the tool. For example, as shown in Figure 2.12 chips have formed where the tool is in weakened state, where two of the comb cracks has joined up removing

a chip from the tool, resulting in a breakdown of the tools cutting edge line.

2.6 Titanium

Titanium alloy has a comparatively high specific strength [42] and good corrosion resistance due to its resilient oxide layer and density 60% that of steel and nickel-based super alloys [42, 43]. These properties make titanium alloy the ideal material for use in aircraft structures or gas turbine engines.

Titanium is an allotropic element and exists in more than one crystallographic structure. Commercially pure (CP) titanium is arranged in hexagonal close packed (HCP) arrays, also known as “alpha” titanium. Alternatively, “beta” titanium is arranged in the body centred cubic (BCC) structure. Alloying elements and temperature can alter the crystal structure of the metal. The temperature at which this transition occurs is called the beta transus temperature. The percentage volume of beta phase increases as the temperature increases over this temperature, approximately 800°C [44].

Certain elements are alloyed with titanium to maintain a BCC atomic structure at a lower temperatures through lowering the transus temperature of the alloy. These elements are termed ‘beta’ stabilisers and include molybdenum, vanadium, iron and chromium. Conversely other elements, ‘alpha’ stabilisers, are alloyed with the titanium to increase the beta transus temperature (at which the alpha phase is stable) and include aluminium, oxygen and nitrogen [43]. The addition of alloying elements change the material microstructure material properties, expanding the possible uses and applications of the alloy.

2.6.1 Titanium alloy applications

Figure 2.16 shows how different levels of aplha and beta stabilisers within the titanium alloy alters the properties of the titanium alloy. Commercially Pure (CP) titanium has lower strength than titanium containing alloying elements, and is used in the aircraft industry for jet engine shrouds due to low density and cheaper production costs compared to titanium alloys. Ti6Al4V is an alpha-beta alloy that is one of the most widely used titanium alloys (50% of all titanium tonnage worldwide, 80% of which is used in the aerospace industry) as it combines attractive properties with good workability and formability, in addition to commercial and economical reliability making it the standard alloy to which others are compared [43].

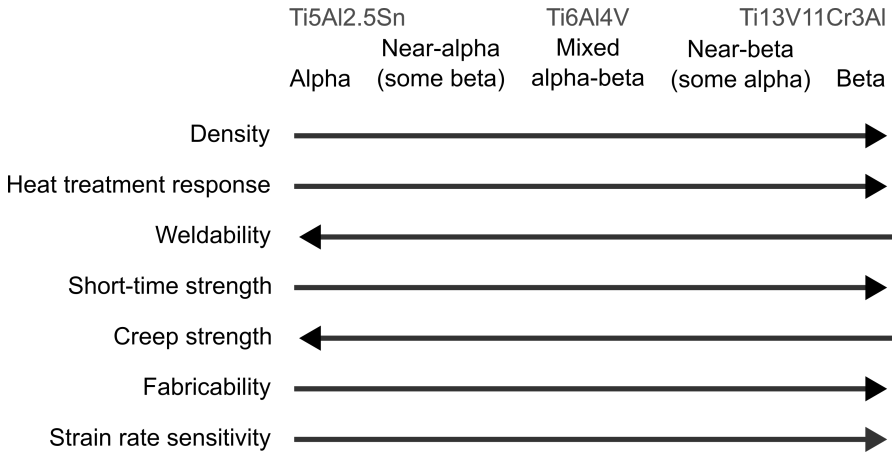

Figure 2.16: The properties of different titanium alloys (modified from [43])

Beta titanium alloys are commonly used in landing gear because they have the highest strength the titanium alloys and have uniform tensile properties at the surface and central locations [43]. They also have higher hardenability and improved forgeability. However, unlike alpha-beta alloys they do not maintain their strength at elevated temperatures. Beta alloys such as Ti5Al5Mo5V3Cr are more difficult to machine than alpha-beta alloys such as Ti6Al4V because of higher mechanical properties (hardness and tensile strength at temperatures experienced in cutting $\approx$ 400°C). This is due to the differences in the microstructure with a variable quantity of alpha phase and the morphology of the transformed beta phase [45].

2.6.2 Machinability of titanium alloys

Titanium machining is difficult due to excessively high cutting temperatures, difficult cutting conditions in that the material has high strength but low modulus, and the chemical reactivity of titanium alloys [46, 47, 48, 49, 50]. To carry out machining requires relatively slow cutting speeds compared to other commonly machined materials [43]. These required changes to the cutting parameters result in comparatively low material removal rates lowering process productivity rates. Any increase in the cutting parameters to improve productivity, results in rapid tool wear.

2.6.2.1 High local cutting temperature

In machining, a common assumption is that all of the mechanical energy input by the cutting tool is converted to heat [51]. This heat is generated in the primary and secondary shear zones, (see Figure 2.1) and the interface between the flank and machined surface. In the primary shear zone, heat is generated as a result of elasto-plastic deformation and in the secondary and tertiary deformation zone, heat accumulates from elastic deformation and friction. Heat is dissipated in the cutting tool, chip, workpiece and cutting fluid.

When machining Ti6Al4V, the strain in the primary shear zone is confined to narrow bands, as the chip forms under catastrophic thermoplastic (adiabatic) shear, creating a region of high localised temperature, unlike the bulk plastic deformation observed in steel chip formation [26].

The local temperature generated at the cutting interface depends upon the rate of heat generation, the rate of heat removal by the chip and the cutting fluid, and the heat conducted through the tool itself. The thermal conductivity of Ti6Al4V (7.3W/mK) is much lower than in AISI1045 steel (50.7W/mK) [52], therefore this heat is not dissipated away from the cutting interface as readily as when machining steel. The combination of poor thermal conductivity in Ti6Al4V coupled with a small primary deformation zone, results in a thin chip and high localised temperature across a small area at the tool tip [53]. Figure 2.17 illustrates how, because of the poor thermal properties of titanium, more heat is dissipated in to the tool, 80% as opposed to 60%, when machining steel [52, 54], because of this increased thermal stresses are placed upon the tool.

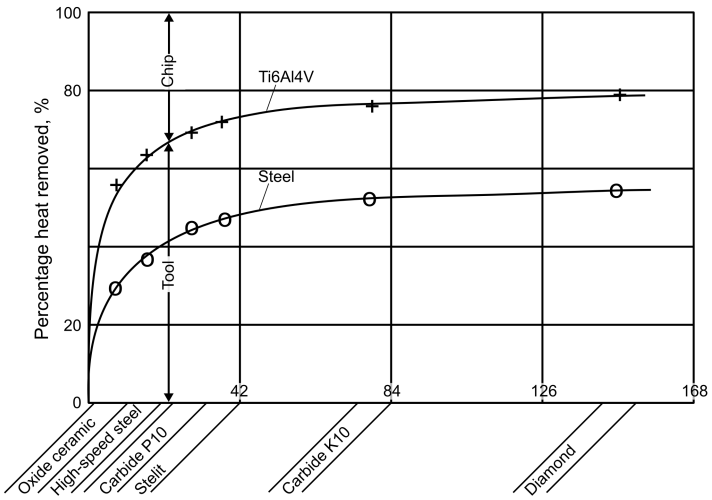

Figure 2.17: Heat dissipated into chip and tool for various tool materials, comparison with machining titanium (modified from [52]).

2.6.2.2 Difficult cutting conditions

The high strength at elevated temperatures [53] and low modulus of Ti6Al4V mean that higher cutting force is required to form a chip. Additionally, due to the ductility of Ti6Al4V, the material will deflect elastically more than other materials during machining. This distortion causes additional heat generation through friction between the tool material and the part workpiece in the tertiary shear zone. The low chip compression ratio and consequently small contact area at the interface between the work and the chip (three to four times smaller than that found when machining steel alloys [49, 46] increase the local stress and temperature on the rake face of the tool. Titanium also has a tendency to work harden [49].

2.6.2.3 Chemical reactivity

Chemical reactivity of titanium occurs at machining temperatures exceeding 500ºC, resulting in chemical tool wear. This can be particularly problematic with carbide tools whereby the cobalt contained within the carbide tool reacts with the titanium in close intimate contact with the tool and diffuses in to the workpiece material. If these tribological conditions are sustained, the cobalt matrix structure within the tool which acts as a structural binding matrix for the hard tungsten carbide particles, is removed from the tool resulting in loss of strength and breakdown of the tool, with the hard WC particles removed in the mechanical motion of the chip over the cutting tool [55].

Zhang [56] suggests this will impact the hardness and wear resistance of the tool, and is the dominant cause of crater wear. Despite these drawbacks, carbide tooling is still the preferred choice for machining titanium as it allows for higher speeds than High speed steel tools, and the chemical reactivity is even higher for diamond and cubic born nitride tooling [57]. Negating chemical wear is generally done through the application of coolant to remove as much heat as possible from the cutting cutting area and control the heat that is generated in the cutting zone, and plays a key role in ensuring effective

machining of titanium alloys.

2.7 Design of experiments

This section details the different types of design of experiment techniques that are used in this thesis. Of the many experimental designs available two experiment designs were used in this study of cryogenic drilling: the full factorial and D-optimal method.

2.7.1 Full Factorial

The full factorial method observes the effects of all the factors at all the levels as chosen by the experimenter. The experiment order is also completely randomised to minimise the effect of systematic errors biasing the results of the experiments. The effect of random variables are also taken in to consideration through the use of repeated experimental trials. Figure 2.18 shows the experimental design space for a 2 level 3 factor experiment.

Chapter 7 utilised the full factorial method. In this the number of factors to be studied were low enough that adequate resource were available to produce a linear model of these factors.

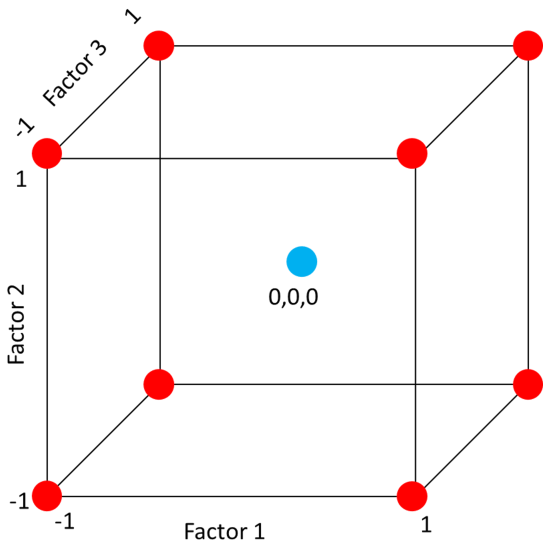

Figure 2.18: Experimental design space for 3 factors at 2 levels, using expanded notation for the levels.

2.7.2 D-Optimal

The D-optimal method of selecting an experimental design was used in the thesis primarily where there were a large number of experimental variables to be studied, and the levels of the factors were not symmetrical. D-optimal corresponds to the determinant optimal, which is an experimental design that aims to capture the maximum amount of information from the experiment, for a given number of experimental runs imposed upon the experimenter.

To highlight how the experimental designs are formed, take a linear model, where y denotes a response from the system affected by the factors $x_1, x_2 ... x_g$, with $\beta_0, \beta_2 ... \beta_p$ the regression coefficients in the model, and ε the random part of the model with zero mean and a normally distributed variance σ^2, independent of x.

$$y = \beta_0 + \beta_1 x_1 + ... + \beta_p x_g + \varepsilon \tag{2.4}$$

Extending this to N number of responses, results in N number of equations,

$$y_i = \beta_0 + \beta_1 x_{i1} + ... + \beta_p x_{ig} + \varepsilon_i \; i = 1...N \tag{2.5}$$

which can be re-written in matrix notation

$$Y = XB + E \tag{2.6}$$

where

$$Y = \begin{bmatrix} y_1 \\ \vdots \\ y_N \end{bmatrix}, \quad X = \begin{bmatrix} 1 & x_1 & \dots & x_{1g} \\ \vdots & \vdots & \ddots & \vdots \\ 1 & x_{N1} & \dots & x_{Ng} \end{bmatrix}, \quad \beta = \begin{bmatrix} \beta_1 \\ \vdots \\ \beta_N \end{bmatrix}, \quad \varepsilon = \begin{bmatrix} \varepsilon_1 \\ \vdots \\ \varepsilon_N \end{bmatrix}$$

Here the matrix X is denoted the design matrix, and represents the factors (independent variables) and levels (size of the independent variable) that are assigned during the experiment. To describe these levels of the factors, three types of notation can be used; namely unscaled factors in the units of the factor, standard notation, where the upper and lower are denoted by plus and minus sign and extended notation with -1 and 1 denoting upper and lower setting. An example of this notation for 2^2 full factorial design is shown in Table 2.1. Here two factors are being studied, $x_1$and $x_2$for any number of responses. Centre points are also shown here, because they are also used at the beginning, middle and end of the experiment to determine any drift or trends over time.

Extended notation is generally the preferred notation system as it allows values other than upper and lower to be assigned to the levels of the factors studied in the experiment.

	Unscaled factors		Standard notation		Extended notation	
No.	x_1	x_2	x_1	x_2	x_1	x_2
1	20	0.5	+	+	1	1
2	20	0.3	+	-	1	-1
3	10	0.5	-	+	-1	1
4	10	0.3	-	-	-1	-1
5	15	0.4	0	0	0	0
6	15	0.4	0	0	0	0
7	15	0.4	0	0	0	0

Table 2.1: Illustration of standard notation and extended notation for a 2^2 full factorial design.

2.7.2.1 Candidate set and design matrix

The candidate set contains all of the theoretically possible (including those that are not physically possible) experimental runs for the number of factors and levels selected. For example, for two factors (x_1 and x_2) at two levels (-1 and 1) there are four runs, shown by Figure 2.19.

$$\varepsilon_4 = \overbrace{\begin{matrix} x_1 & x_2 \end{matrix}}^{\text{factors}} \begin{bmatrix} -1 & -1 \\ -1 & 1 \\ 1 & -1 \\ 1 & 1 \end{bmatrix} \begin{matrix} \text{run 1} \\ \text{run 2} \\ \text{run 3} \\ \text{run 4} \end{matrix}$$

Figure 2.19: Candidate set of two factors at 2 levels.

With a given model and candidate set, a design matrix X, can be contructed with n number of experiments (chosen by experimenter) and p coefficients. The number of experiments in the design matrix is less than or equal to the number in the candidate set.

For an interaction model, Equation 2.7

$$y = \beta_0 + \beta_1 x_1 + \beta_2 x_2 + \beta_{12} x_1 x_2 + \varepsilon \tag{2.7}$$

And using the candidate set, the design matrix X can be produced. The first column denotes the constant term in the model equation, the middle two columns define the candidate set, and the interaction term, which is the product $x_1.x_2$ is shown in the last column.

$$X = \begin{bmatrix} 1 & -1 & -1 & 1 \\ 1 & -1 & 1 & -1 \\ 1 & 1 & -1 & -1 \\ 1 & 1 & 1 & 1 \end{bmatrix} \tag{2.8}$$

2.7.2.2 Information matrix and dispersion matrix

Taking the model with matrix notation,

$$y = X\beta + E \tag{2.9}$$

The estimated values of the coefficients $\hat{\beta}$, using the least squares estimation is given by

$$\hat{\beta} = (X'X)^{-1}X'Y$$

See Box et al. [58] and de Aguiar et al. [59] for mathematical proof of this estimation.

The information matrix is defined as $X'X$ and dispersion matrix defined as $(X'X)^{-1}$. The criteria for the best D-optimal design is one that maximises the determinant of the information matrix, so that the optimal design matrix X^*contain n experiments that maximise $\left|X^{*'} \quad X^*\right|$, and therefore spans the largest possible volume of the experimental design space.

$$\left|X^{*'} \quad X^*\right| = max(\left|X' \quad X\right|) \tag{2.10}$$

2.7.3 Comparison with full factorial for increasing number of factors.

As the number of experiments increases, so does the number of experimental runs required. Table 2.2 shows the number of runs required for the full factorial, and the equivalent number of runs achieved with D-optimal. As can be seen with increasing number of factors the number of experiments for full factorial drastically increases. However with D-optimal this number remains much lower, because the experiment is optimised for maximum information and minimum runs.

	Number of experiments	
Number of factors	Full Factorial	D Optimal
3	8	8
4	16	16
5	32	18
6	64	28
7	128	35
10	1024	62

Table 2.2: A comparison of the number of runs required for differing numbers of factors.

2.8 Health and safety hazards with Metal Working Fluids

This section considers the health and safety aspects of using carbon dioxide enabled machines on the shop floor of a factory and conducting research on these machines. Also considered is how this relates to the health and safety of traditional MWFs currently used.

2.8.1 Carbon dioxide hazards

Carbon dioxide is a chemically stable and inert gas at atmospheric conditions. It is denser than air, and falls and collects in pits, therefore higher concentration of CO_2 gas is concentrated at lower levels and care must be taken if working at low levels of a CO_2 machine. CO_2 occurs in the atmosphere at 0.03%. When concentrated at 3%, it can cause headaches and respiratory disturbances. At higher concentrations in air of 10% it can lead to cramps, unconsciousness and death. Therefore care must be taken to avoid inhalation of CO_2. It is impossible to detect with the human sense as it is odourless and colourless. Detection is done using a CO_2 sensor, not an O_2 sensor because O_2 levels can remain at normal levels (19%) even with 10% CO_2 concentrations. It is the high CO_2 concentrations that are hazardous, not lack of O_2. A safe limit of CO_2 is set at 0.5% volume [60].

Precautions need to be taken to prevent inhalation of CO_2. These include, using CO_2 sensors near to pressurised cylinders, and turning off cylinders after use. It is stored in liquid form at 57bar at 20°C, any leaks need to be sealed immediately. The room in which it is contained needs to be well ventilated to allow the CO_2 to disperse to the atmosphere. In the event of undetected leaks, low lying levels of factory's need to be evacuated first, and people entering the rooms with high concentrations of CO_2 need to use respiratory equipment when fixing and investigating a possible leak.

During operation, the liquid is abruptly depressurised to atmospheric pressure, which results in a drop in temperature due to the isenthalpic expansion and production of solid CO_2 (see Section 2.9 for details). This lowers the temperature to approximately -75°C. Handling of tools and toolholders must be done using thermal insulating gloves after operation, to prevent cryogenic burns on hands.

After operation, time must be allowed for the gas to disperse prior to opening the door to prevent the inhalation of high concentrations of CO_2 gas. For example, 1kg of liquid CO_2 yields approximately 300 to 400 litres of gas. Typically, there is a delay on the machine to prevent the doors being immediately opened after operation.

2.8.2 Traditional metalworking fluid hazards

Directions around the Health and Safety standards for metalworking fluids are provided, in the US, by the ASTM sub committee E34.50. Within this sub-committee there are published standards around the various hazards of traditional metalworking fluids. These include:

1. Standard practice for selecting water-miscible and straight oils and their safe use.
2. Testing for toxicity and for carcinogenic potential.
3. Standards for checking bacteria, endotoxin and ATP.
4. Controlling for respiratory hazards.
5. Evaluating foaming tendency.
6. Standards for safe removal.

2.9 Thermodynamic considerations of LCO_2 as a cryogenic cutting fluid

One of the roles of the metalworking fluid is to remove the unwanted heat developed within the cutting zone. Of consideration when using cryogenic cooling fluid is the rate of cooling on the material being machined and to what extent does it change the properties of the material, see Figure 3.4 showing how the material properties of Ti6Al4V change with cryogenic temperatures. This occurs when the cryogenic cutting fluid is not directly positioned at the cutting interface, and is excessively positioned on to the work material resulting increases in material hardness and strength lead to increased cutting forces.

The extent to which metal working fluids (MWFs) are able to enter the interfaces between the tool, workpiece and chip is dependent on the MWF type [61]. Improvements are also found when the cutting fluid flow is directed into the interface, using the fluid density and body force to penetrate further into the cutting interfaces. Additionally MWF manufacturers of water based coolants use additives to modify the surface tension of cutting fluids to further penetrate this cutting interface. The motivation behind this is to remove some of the heat generated in cutting closer to the local region of heat.

MWFs also reduce the temperature by affecting the power spent in plastic deformation of the workpiece material [7], typically 60-80% of the total power. Astakov [7] estimates the power per volume is proportional to the ultimate tensile strength (σ_{UTS}) and fracture toughness (ε_f) of the material, Equation 2.11.

$$power\,per\,unit\,volume \approx \frac{1}{2}\sigma_{UTS}\varepsilon_f \tag{2.11}$$

Subsequently, machining materials with higher values of these properties is more difficult as more power is required for plastic deformation to transform the uncut chip layer of material in to chips. Machining has been shown to be thermally enhanced by softening the workpiece [62].

Carbon dioxide is stored under pressure at 58bar (gauge) at 20°C in a manifold of cylinders in liquid phase. Dip sticks contained within the cylinders extract the liquid from the bottom of the cylinders, and supply it under pressure prior to being used. When used as a refrigerant, carbon dioxide is referred to as R744. CO_2 is present in three phases, with a triple point at T= 216.591K, P=0.518MPa [63, 64], shown in Figure 2.20. The dotted line illustrates the pressure that the fluid is stored, which is just above the saturation line at 20°C. As the storage volume is constant, increases in the fluid temperature will result in increased pressure, using the ideal gas law.

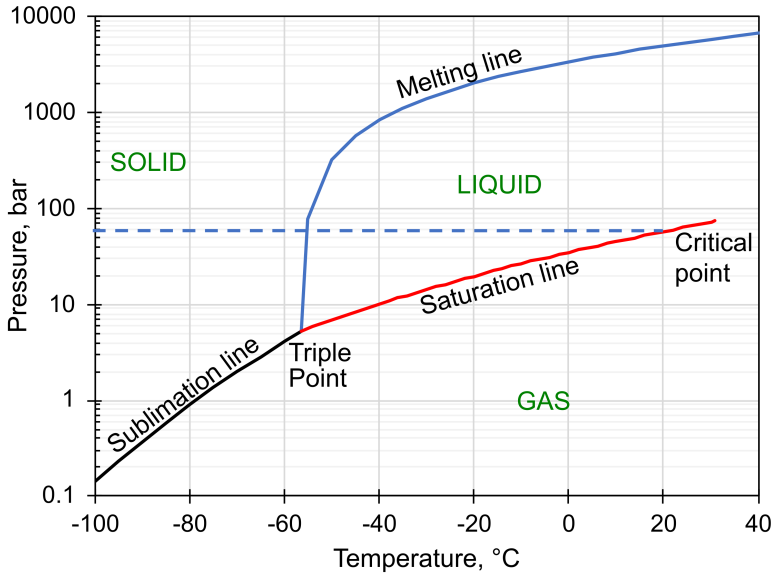

Figure 2.20: Pressure temperature curve for CO_2, illustrating the three phases of CO_2. The dotted line shows the pressure of the fluid in its stored form.

During operation, the flow travels along pressure resistant supply lines to the rear of the cutting tool via the toolholder. The LCO_2 is expelled at the tool exit to atmospheric pressure resulting in a sudden pressure drop. This causes the flow to expand suddenly, throttling the flow in an isenthalpic expansion. The effect on the temperature of the flow can be described by the pressure-enthalpy graph and the Joule-Thomson coefficient. The pressure-enthalpy diagram of carbon dioxide, shown in Figure 2.21, created using data from from Span and Wagner [63] equation of state, and CoolProp software [65], illustrates this process and heat removal.

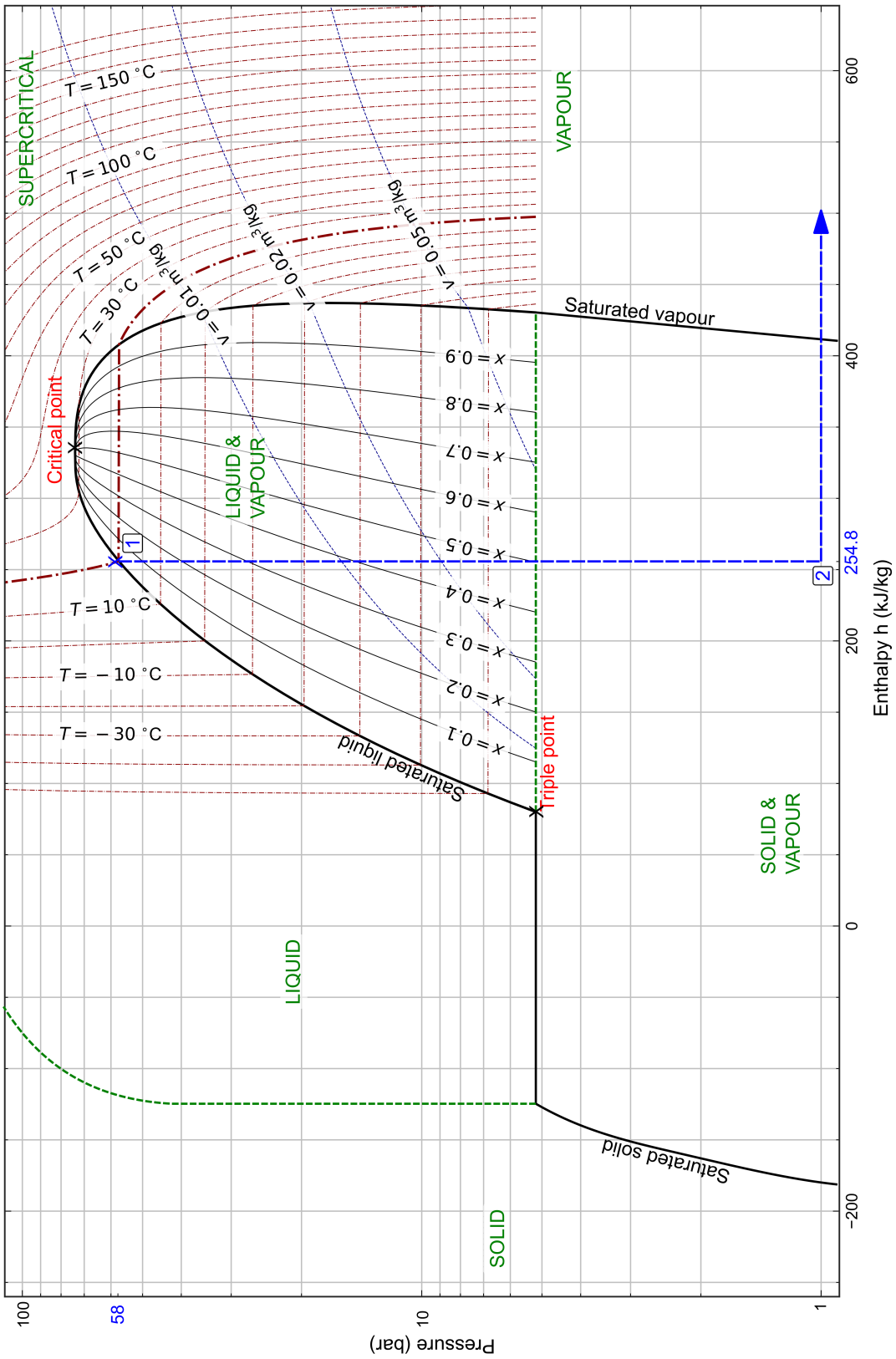

Figure 2.21: Pressure enthalpy curve of carbon dioxide, data increasing from the triple point is plotted using data from Span and Wagner[63] and CoolProp software[65].

The assumed storage and supply state of the carbon dioxide is plotted at position 1. During the isenthalpic expansion of the liquid to atmospheric pressure of 1 bar, properties move to position 2 on the plot. This results in a drop of temperature to -96°C (177K) and phase change to a solid and vapour mixture. The solid particles then sublimate, without a change in the temperature. To do this, the latent heat of sublimation must be absorbed before the temperature starts to change. The change in enthalpy here is $410 - 254.8 = 155.2 KJ/kg$

As the pressure decreases in the isenthalpic expansion, the change in temperature that occurs is described by the Joule-Thomson coefficient (Equation 2.12). For CO_2 the Joule-Thomson coefficient is 10.05 at atmospheric pressure and 35°C, five times that of N_2 [66].

$$\mu_{JT} = \frac{\partial T}{\partial P}_H \tag{2.12}$$

3 Literature Review

3.1 Introduction

This chapter explores metalworking fluids and their role in machining. It introduces and analyses the literature surrounding the use of cryogenic cutting fluids in machining. The chapter then reviews the literature on cryogenic drilling before outlining how it is applied in machinery. The chapter concludes with a summary of the literature and outline of the project aim and objectives.

3.2 The role of Metalworking Fluids (MWFs) in machining

Machining is commonly aided by metalworking fluids (MWFs), commonly referenced as coolants, to improve the performance of cutting by removing unwanted heat and providing some lubrication [67]. ASTM D2881-19 [68] classifies the various MWFs that are used in the varying applications of machining. For processes that require a greater heat removal capacity, such as grinding, water based MWFs have traditionally been used. This includes both petroleum and non-petroleum based fluids that are mixed with water to a concentration between 5 and 15%. Additives to improve the wetability and anti-corrosive properties of the fluid are also added. For applications requiring a greater degree of lubricity, such as gear hobbing, straight oils are preferred. These fluids do not have the same heat capacity as water and thus are not used where heat removal is essential.

The primary functions of MWFs are to provide cooling and lubrication to the cutting tool and the workpiece where the aim is to favourably alter, through lubrication and cooling, the tribological conditions at the tool-workpiece interfaces in order to improve the cutting process performance through prevention of thermal damage to the workpiece and lead to a reduction in tool wear [67]. Consequently, MWFs impact all of the critical aspects of machining. The cutting forces [69], the heat dissipation and cutting temperature [70], workpiece accuracy and surface finish [71], tool life [72, 73] and the surface integrity[74].

In their 2015 paper, Brinksmeier et al. [67] highlight the detailed complexity of MWFs, and how they are substances with transient properties with variations in age, composition, concentration, supply pressure and flow rate. Each of these parameters are significant in manufacturing processes, and as such the paper provides a template for providing this information in future publications. Cryogenic machining goes some way towards reducing the number of these variables; such as age, composition and concentration, however the supply pressure and mass flow rate of the media, in addition to type of media and how it behaves, must also be taken into consideration. As conventional MWFs have been shown to have such a large impact on the process, the parameters surrounding the delivery of the CO_2 to the

cutting zone, are yet to be explored, and thus offer a great avenue of improving the cryogenic drilling process.

3.3 Metalworking fluids in drilling

Various studies have observed the effect of MWFs in drilling. Haan et al. [71] externally applied a water-soluble oil MWF in drilling of aluminium alloys and cast iron. In that work the MWF influenced the surface roughness of the hole, and impacted the hole cylindricity and perpendicularity. They concluded from their findings that the MWF mainly lubricated the drill margin to improve the hole surface finish. However the efficacy of the MWF to lubricate the cutting zone has been observed to reduce with increasing cutting speeds. Cassin et al. [75], in their experiments machining copper, found that at increasing cutting speeds the cutting fluid failed to penetrate the cutting interface. Additionally, where penetration did occur, this was due to diffusion through the metal, and a solid lubricant boundary layer was formed between the due to the chemical reaction with the copper. The extent of this boundary layer was dependent on the MWF and the cutting speed.

A vapour blanket is formed in the viscinity of the high local cutting temperatures when MWF is directed on to the cutting interfaces during machining, preventing the MWF from accessing the cutting zone. This problem is magnified in machining materials with low thermal conductivity, such as titanium alloys, where the local temperature at the cutting interface is higher. Mohd-hadley et al. [76] demonstrate that high pressure, high velocity flows are used to counteract this, where the momentum of the fluid breaks through this vapour blanket to penetrate the cutting interfaces. Under these conditions they found a reduction in the cutting temperature and cutting forces, through the use of increased MWF pressure with cutting of Ti6Al4V, which they attributed to the reduction of friction at the cutting zone.

The MWF has been found to influence the formation and the evacuation of chips that are formed in drilling. The degree of the curl on the chip is dependent on the amount of heat that is removed by the MWF [71].

Oezkaya et al. [77] used CFD to model and analyse the effects of coolant hole diameter and flow pressure on the direction of the water-based MWF as it exits the coolant holes of the drill. The streamlines presented in this study show the flow moving in the direction away from the cutting edge on exiting the coolant hole, towards a path of least resistance. Dead zones, with no flow, occur at the cutting edge centre and outer corner of the drill cutting edge. One suggestion of this by the authors is due to the rotation of the drill, however Johns et al. [78] have shown that, with the use of the Rossby number (the ratio of fluid inertia to coriolis force due to rotation) the rotation of the drill does not cause the flow of the fluid to move away from the cutting zone. It is suggested by Oezkaya et al. that this flow is caused by incorrect tool geometry, and suggest alterations to the flank face geometry. Oezkaya et al. also suggest that a smaller hole for the same back pressure results in lower mass flow of coolant when the medium is a water based MWF, however, only minimal reductions in the flow velocity are observed, and the larger mass flow rate of the larger coolant holes will have little impact on the tool life and hole quality, as the flow is not being used in the useful area of the drill. To improve the access of the MWF to the critical

cutting areas of the drill recesses were removed from the drill on the flank face and margin of the drill (Figure 3.1). This is presented by Oezkaya's team in Bucker et al. [79], where their findings resulted in improved flank wear, however the machined slots on the flank face and margin weakened the drill resulting in drill failure, albeit in nickel alloy.

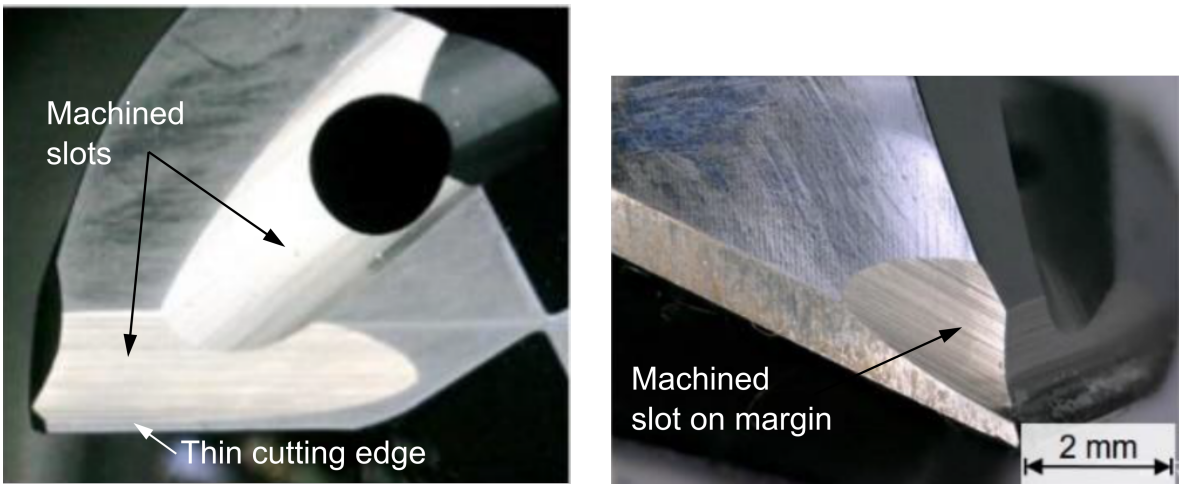

Figure 3.1: The machined slots on the flank face and margin edge of drills to encourage increased fluid flow to these areas by Bucker et al. [79].

Studies have yet to be completed studying the effect of coolant hole diameter and mass flow rate with alternative MWFs such as cryogenic media, including CO_2 and LN_2.

MWF mass flow rate and coolant hole position have been shown to influence the performance of MWFs by Fallenstein et al. [80]. They found that by moving the coolant holes closer to the cutting edge, the heat flux, closer to the cutting zone on the flank face, increased (Figure 3.2). The increase seen through doing this, improved the heat flux effect an order of magnitude similar to that of increasing the flow rate four times - coolant positions, EP1 vs EP5.

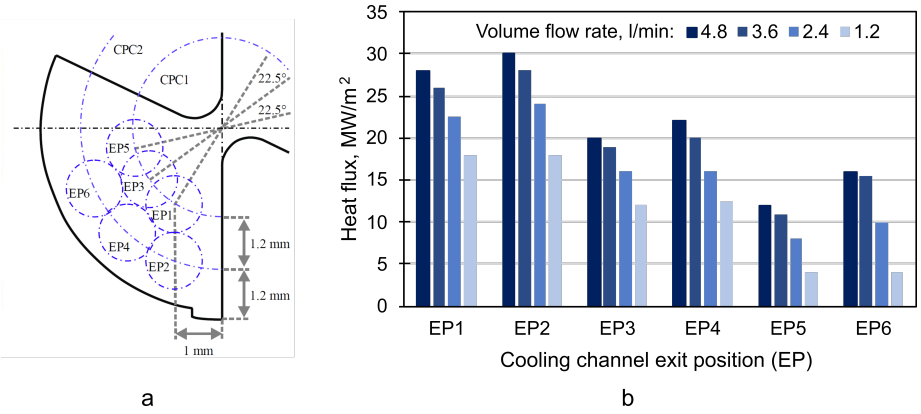

Figure 3.2: a) The coolant channel exit positions adopted. b) The effect of the coolant hole positioning and mass flow rate on the heat flux of the drill (modified from [80]).

3.4 Cryogenic coolant

The earliest published use of liquefied gases as a coolant in machining processes is by Reitz in 1919 [81], and it was not until 1968 that the term cryogenic machining was used by Uehara and Kumagai [82]. The motivation for replacing conventional coolants with cryogenic alternatives, is to enable a more sustainable manufacturing process by eliminating/or reducing the consumption of cutting fluids (and water) which require costly post processing, safe disposal and regular maintenance. Additionally, studies have indicated that people exposed to conventional cutting fluids are at higher risk of developing certain cancers, dermatitis and respiratory diseases [83].

Cryogenic machining involves replacing traditionally used emulsion coolants with a fluid that has a low temperature, such as liquid nitrogen (LN_2) or carbon dioxide (CO_2). Here the gas simply disperses in to the atmosphere, leaving the part with a residue free surface, eliminating clean down time. However, it must be noted that because of the extremely cold temperatures of the cryogenic coolant and the displacement of oxygen by the dispersion of the gas, frostbite (when handling gas and cold tools) and asphyxiation are two health and safety concerns that need to be taken into consideration. Yasa [84] points out that the cold temperatures affecting tolerances of in-process measuring systems are possibly the reason why the technology is yet to be fully taken up by industry. Temperatures typically defined, in literature, for the cryogenic region are below -150°C, while the boiling point of most permanent gases (nitrogen, oxygen, hydrogen) is -180°C. Most research in cryomachining involves the use of liquid nitrogen (LN_2) [3], but the use of CO_2 as a coolant [85, 86] has also been termed cryomachining, despite a boiling point of -78.5°C. CO_2 as a coolant is easier to implement from a practical perspective, as opposed to liquid nitrogen, due to its physical chemistry and ability to be stored as a liquid at room temperature. Additionally, LN_2 is produced by the fractional distillation of air, which requires a substantial amount of energy for production [87, 88], whilst LCO_2 is utilised as a by product of other industrial processes such ammonia and hydrogen production.

The storage and supply of nitrogen to the cutting zone requires insulated storage tanks, supply lines [89] and specially insulated tooling to ensure safe operation of the process increasing the expense and difficulty of implementing the process. CO_2 as a liquid coolant is somewhat easier to apply as a MWF, as it is stored at medium pressure (˜55bar) and ambient temperature. It remains in its liquid state prior to expansion to atmosphere by utilising pressure resistant supply pipes from the coolant store pipes to the toolholder.

As the liquid CO_2 (LCO_2) exits the tool (or nozzle) and expands, the liquid CO_2 undergoes a phase change from liquid to a mixture of solid and gaseous CO_2 (60% gas 40% solid). The energy associated with the phase change (energy of sublimation) and the sudden expansion of the liquid (Joule-Thomson effect) enables temperatures to reach as low as -78.5°C. LN_2 offers improved cooling because boiling occurs at -196ºC, and thus a greater temperature difference between cutting and the coolant allows improved dissipation of heat. The rapid vapourisation of the LN_2 with a hot surface can lead to the formation of an insulating gaseous film layer, reducing the cooling effect [90]. An alternative is to use supercritical ($scCO_2$) coolant, the higher pressures of the supply amplify the Joule-Thomson effect and

provide improved cooling over LN_2, which has a five times higher Joule-Thomson coefficient than LN_2 [91]. Supercritical CO_2, however, consumes large volumes of CO_2 leading to environmental concerns.

Cryomachining also modifies the cutting tool properties during machining. Most studies of cryomachining have been completed using carbide tooling because of the low price of tooling and the ability to retain transverse rupture and impact strength and increases in hardness at cryogenic temperatures [92, 12]. These properties reduce tool wear and allow higher productivity with lower energy consumption. Furthermore improved penetration of cryogenic gas into the cutting edge, with the flow directed directly at the wedge formed by tool and workpiece/chip at the flank and rake faces, has been shown by Wang et al [61] (Figure 3.3). They found that there was a 100% penetration of the coolant leading edge into the wedge for the cryogenic coolant as opposed to 30% and 21% for flood and MQL respectively. Indicating that the placement of the cryogenic jet nozzle influences the penetration of the coolant to the heat generation zones at the cutting edge of the tool.

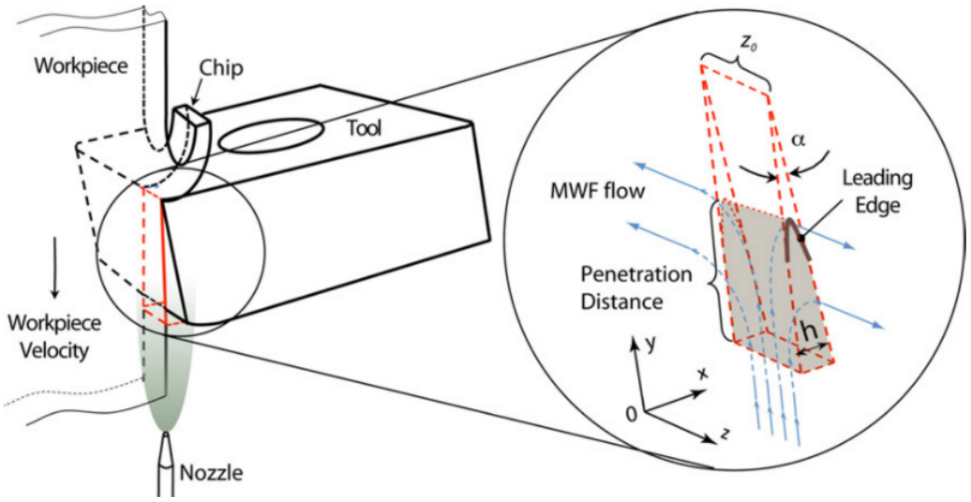

Figure 3.3: Schematic showing the penetration of MWF into the wedge between the flank face of the tool and the workpiece (from Wang [61]).

3.5 Influence of cryogenics on machining processes

3.5.1 Friction

Heat generation at the tool interface occurs by plastic deformation of the workpiece as the tool forms a chip in the primary shear zone, and at the secondary and tertiary shear zones as the workpiece flows over the secondary shear zone (rake face) and tertiary shear zone (flank face). Hong and Ding [93] found LN_2 (compared to dry) to reduce the coefficient of friction on the rake face by measuring the forces exerted on the tool. This method takes an average of the friction coefficient on a macroscale and does not account for changes in the deformation physics caused by the cold temperatures of the gas, such as work hardening. Furthermore, the positioning of the nozzles was found to have a large influence on the friction coefficient, and as such may have provided a hydraulic lubricating cushion of gas [94]. In more

traditional methods of measuring the coefficient of friction, such as pin on ring method, Hong [95] and El-Tayeb et al. [96] both studied Ti6Al4V with a carbide tool material for dry and LN_2 coolant. Hong et al. found a decrease in the friction, while El-Tayeb et al. found the friction to increase when LN_2 coolant was used. However, El-Tayeb found that the interaction between the contact load and speeds had the most influence on the friction effect rather than the application of the LN_2 coolant. An open tribometer was used by Courbon et al. [97] to test the friction between a TiN coated pin and Ti6Al4V lubricated with LCO_2 and LCO_2+MQL. They found similar coefficients of friction for both regimes, suggesting that the high chemical affinity between the coating and Ti6Al4V prevented the benefit of the addition of MQL to aid friction and suggest further work to be completed. A possible way of achieving this may be through the use of supercritical CO_2 ($scCO_2$). Supekar et al. [91] have demonstrated that, when mixed with soybean oil, a reduction in friction is observed as the $scCO_2$ can carry the lubricant in to the cutting zone due to the greater penetration and solubility characteristics of $scCO_2$. Surprisingly the lubricity of straight $scCO_2$ (not containing any oils) was shown to be statistically indistinguishable from oil based micro emulsion in water in tapping torque tests [98], which was further enhanced with the addition of soybean oil. By mixing $scCO_2$ with MQL oils, improvements in lubricity over straight MQL oils were found. It has been suggested that the reduction of friction with the $scCO_2$+MQL is due to improved penetration of the $scCO_2$ into the cutting zone due to the increased pressure and velocity of delivery with $scCO_2$ over MQL systems [61, 91].

3.5.2 Heat generation/ thermal aspects

All materials respond differently to machining and temperature. The strategy adopted for improving machining varies on the material being machined. For example, low carbon steel experiences difficulties in chip breaking while HRSA materials cause excessive tool wear. For machining Ti6Al4V with cryogenic media, the cold temperature of the material needs to be considered. The effect of cold temperatures, down to -196°C, on Ti6Al4V has been tested by Zhao et al. [29] (Figure 3.4). In their studies, they found the properties of the Ti6Al4V to evolve as the temperature at which the material was tested was reduced. There was no evidence of cryogenic embrittlement, with ductility maintained at the cryogenic temperatures whilst concurrently, increases in tensile and yield strength were found in addition to increased hardness. These findings indicate the potential of an increase in the mechanical load on the cutting tool during machining, increasing forces exerted on the tool. It is therefore essential to ensure that the cryogenic MWF is directed at the correct location during machining. If applied correctly to titanium, Hong et al. [89] has suggested that the difficult cutting characteristics associated with titanium (Section 2.6.2) make it an ideal candidate to benefit from the use of cryomachining, resulting in lower cutting temperatures and enhancing chemical stability during cutting.

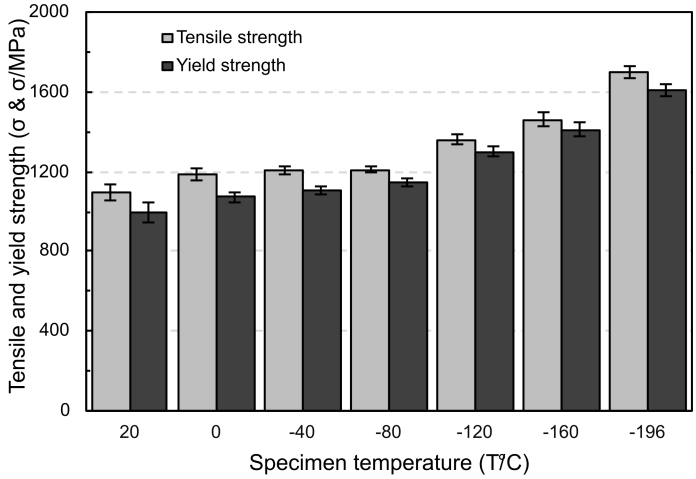

Figure 3.4: Effect of cryogenic temperatures on titanium properties (modified from Zhao [29]).

The temperature at the cutting zone is lowered by the coolant accessing the cutting zone through interfacial capillaries and reducing the cutting energy required and enhancing the capacity of heat extraction [3]. This extraction of heat from the cutting zone has been illustrated by Dhar et al. [99] in an FE model of turning plain carbon steel, as a proof of concept in comparison with dry machining whilst Sun et al. [100] observed a lower chip temperature when they compared cryogenic compressed air to dry machining.

For internally supplied CO_2 coolant, tool geometry and the conditions of the coolant flow on the cutting zone have been shown to influence the cutting temperature. Jawahir et al. [3] reviewed two German papers that illustrated improved cooling, in turning, with smaller diameter coolant nozzles (0.75mm to 1mm), which gave better cooling when located as close as possible to the surface to be cooled. Work completed by Pusavec et al. [101] is in agreement that effective location of the cryogenic coolant flow is essential to effective cryogenic machining. This is due to the need for perpendicular positioning of coolant flow to the heat source and the mechanism by which heat is removed. For emulsion coolants, heat removal is primarily through heat conduction due to the temperature gradient between local cutting zone. In contrast to LN_2 and LCO_2 where heat removal is via the latent heats of vaporisation and sublimation as well as the cooling due to the Joule-Thomson effect.

In drilling, improved location of the coolant holes and tool geometry in reducing temperature has been demonstrated by Dix et. al. [102]. However, repetition of these results are difficult as no tool geometry or process data is given. Effective cryogenic machining of titanium can be achieved by directing a focused jet of cryogenic fluid at the cutting zone. This ensures the strength and hardness of the titanium is not increased, whilst at the same time lowering the cutting temperature and improving the chemical stability of the tool and workpiece [89].

Penetration of the coolant into the cutting zone is important in removing heat from the machining process. Supekar et al. [91] demonstrated an improved cooling effect in the supercritical CO_2 ($scCO_2$) cooling in turning of Ti6Al4V and milling compacted graphite iron (CGI), utilising a heat removal efficacy (HRE) parameter. In this paper flank wear was measured, and favourable results using $scCO_2$

The authors attributed the higher HRE over MQL to the ability of the gas to penetrate the cutting interface, and over nitrogen gas to the Joule-Thomson effect and sublimation of the dry-ice crystals, removing a greater amount of heat. With a higher gas pressure the change in enthalpy during the adiabatic expansion results in a larger cooling effect.

3.5.3 Effect of cryogenic MWFs on chip form

To this author's knowledge there is little published research on the influence of cryogenic MWFs on chip form. Bermingham et al. [103] found changes in the chip form and tool-chip contact length when applying cryogenic coolant to a turning application. They suggest that, while cryogenic coolant may offer an increased amount of heat extraction from the cutting zone, the delivery of the coolant from the rake face on to the chip acts to mechanically lift the chip away from the rake face and reduce the tool-chip contact length. Further studies by Bermingham and his colleagues [30], comparing LN_2 cryogenic cooling with high pressure emulsion, also found that cutting speed, coolant type and delivery method all influenced the tool-chip contact length. Shah et al. [104] have observed the chip formation in drilling applications of Ti6Al4V and found that the chips do not shear with LN_2 nor LCO_2 and form long chips that concertina and get trapped in the hole. This offers an opportunity to explore this phenomena, and provide solutions so that the chips can be safely evacuated out of the hole preventing tool failure.

3.6 Turning with cryogenic media

The majority of the work studying cryogenic media has been conducted in turning operations. Therefore, even though this work primarily focuses on a drilling operation, it would be remiss to omit some of the key work conducted in turning operations.

Cryogenic media application in turning has shown to favourably improve cutting performance in terms of tool life and workpiece surface finish. Venugopal et al. [105, 106] compared the tool wear in LN_2 turning of Ti6Al4V to both dry and wet machining conditions using uncoated microcrystalline grade carbide inserts. They found, despite the type of MWF strategy, that the Ti6Al4V adhered strongly to the rake face of the tool as the chip flowed over the rake face of the tool. This resulted in adhesion and thus diffusion wear, forming a crater on the rake face of the tool. This was attributed to the high temperatures and small tool chip contact length typical of titanium machining. This wear was reduced at moderate cutting velocities (70m/min) by using LN_2 due to the improved cooling ability of the LN_2. However, at increased cutting speeds (117m/min), due to improper penetration of the fluid and the Leidenfrost effect [107], the ability of the LN_2 to remove heat from the cutting zone was negated. Further, Bordin et al. [108] also observed a reduction in adhesion wear using LN_2 over dry machining additively manufactured Ti6Al4V, again attributed to the improved heat removal capacity of the LN_2 to minimise the diffusion wear on the rake face.

The location of the cryogenic media applied to the cutting zone has also been shown to improve cutting performance. Mia et al. [109] used a dual-jet system of LN_2 applied to both the rake and the flank face

which resulted in a reduction in specific energy and lower cutting temperature over the single-jet applied to the rake face alone and dry machining. Similarly, in the turning of Ti6Al4V with TiAlN coated inserts, Dhananchezian et al. [110] used special tools, with holes on the rake face, and tool flank faces to better direct the LN_2 to the tool workpiece interfaces. In doing so, the cutting temperature reduced by 60% over flood cooling and reductions in the cutting force were observed. The reduction in cutting force was attributed to improved lubrication of the nitrogen at the chip-tool interface and work surface -tool interface due to the formation of a fluid cushion between the interfaces preventing the adhesion of the interacting surfaces [95]. This resulted in improved tool life and reduced workpiece surface roughness. The findings of LN_2 to act as a lubricant, with correct application, are also corroborated by Bermingham et al. [103], where they found cutting forces decreased in the turning of Ti6Al4V with LN_2 over dry, when the LN_2 was directed on the flank face. When turning the LN_2 off the flank face, and just applying it to the rake face they found the forces to increase over dry machining, and state that "competing factors determine the friction and cutting forces during machining. On one hand higher cutting speed and thermal softening reduce friction between the chip and tool whereas cryogenic coolant strengthens the workpiece, reduces thermal softening and can increase friction. If the liquid nitrogen is delivered between the sliding surfaces, the lubricating effect of the coolant can reduce friction." These findings are corroborated in other papers [93, 95]. Similar friction reduction effects can be realised with the use of LCO_2 when it is directed into the cutting zone. The work conducted by Jerold et al. [111] found that reductions in force of 12% were seen with LCO_2 over flood in machining AISI1045 steel and by 20 to 40% over flood in their other work [112] in turning Ti6Al4V. In fact LCO_2 was shown to improve lubricity over LN_2 due to the increased hardness imparted on the workpiece with the colder LN_2. The improved penetration of the cryogenic media and subsequent improvement in lubrication correlated with improvements in surface finish as found in the previous studies and is also supported by others [113]. Furthermore, adding lubricating oils into the cryogenic media have been shown drastically improve the performance of machining in terms of reduced forces and improved surface roughness due to reductions in friction at the tool workpiece interfaces [91, 114]. In these cases, the cryogenic media, due to improved penetration effects, acts as a carrier of the lubricating fluid into the cutting zone to provide a lubricating boundary layer between a greater area of the contact between the tool and the workpiece. This effect is particularly pronounced when supercritical CO_2 is used because, unlike when using LCO_2 and LN_2 , the MQL is dissolved in to the $scCO_2$ and smaller particles of MQL are formed which can penetrate further into the cutting zone which are under higher pressures [91].

3.7 Milling with cryogenic media

This section focuses on work involving cryogenic milling. Unlike turning and drilling, where there is constant contact of the tool with the workpiece during the cut, in milling the tool moves out of cut with varying degrees depending on the radial engagement of the tool. Due to this it is possible that different tool behaviour may be observed during machining, and thus an outline of work conducted in cryogenic milling is included.

Improvements in the tool life have been shown in cryogenic milling applications. In the face milling of Ti6Al4V Sadik et al. [115] with LCO_2 cooling, they showed that improved tool life could be achieved over emulsion coolants. In their work, they also showed that with increasing mass flow rate of the CO_2 further improvements in the tool life could be achieved. The authors identified that cracking of the tooling insert was the dominant wear failure mode for both emulsion and LCO_2, due to the thermal cycling of the tool. In their work they found a 40 minute tool life increase with a CO_2 mass flow rate increase from 9 kg/hr to 39 kg/hr, while little change was observed for different emulsion flow rates. This improvement when using LCO_2 was hypothesised to be due to the ability of the LCO_2 to maintain a more stable thermal gradient on the tool, however measurements of the temperature were not taken.

This improved tool life with cryogenic media over flood has also been demonstrated by Shokrani et al. [116] in end milling of Ti6Al4V with LN_2, with comparisons to MQL. Interestingly, they found that straight MQL out performed straight LN_2 in terms of flank wear measurement across a range of cutting speeds. A hybrid approach consisting of LN_2 + MQL performed above MQL at lower cutting speeds and worse than MQL at higher cutting speeds. They attributed this to the improved lubricity of the MQL to prevent the adhesion of the titanium to the tool, and ability of the LN_2 to maintain the cutting temperature below that which causes the cobalt binder in the tool to soften (800°C). At the higher cutting speed however, they attributed the worse performance to the increased temperature observed with higher cutting speeds, causing the boiling of the LN_2 [117], which then acts as a thermal barrier preventing heat removal. They identified the wear mechanism as diffusion wear leading to rapid flank wear on the tool. The use of a lubricant in milling to provide improvements in the tool life have also been shown by others [118, 119]. Alternatively cutting edge geometry can be altered to modify the friction on the contact during machining to further improve the process. The flank and rake faces of the a milling tool were increased to further extend tool life [120], however it should be noted that further increases in these tool angles may lead to weakening of the tool.

The proximity of the coolant nozzles have been shown to influence tool life by Gross et al. [121]. In their work they looked at different nozzle diameter sizes and flow rates. They found that with higher mass flow rates of LCO_2 and a nozzle with closer proximity to the cut, that tool wear was improved. Additionally, they found that for the small diameter nozzle (0.2 mm) a cooler temperature was maintained further downstream from the orifice that a larger nozzle for equal flow rate (the pressure is increased for the smaller orifice). However, their results around whether this improved in tool wear were inconclusive.

When cryogenic media is applied in the milling process, it has been shown that the cutting forces increase over dry machining [122] and conventional cutting [123] for both steels and difficult to cut materials. The reason for the higher forces has been attributed to the higher strength of the material at a lower temperature. When machining with conventional coolant or dry, more heat is built up in the primary shear zone of the material when compared to cryogenic machining. This lack of heat build up with the application of cryogenic media results in less thermal softening in the primary shear zone of the material and is observed as increased cutting forces [123, 124, 125]. Increased forces were also observed in the cryogenic milling of titanium by Zhao et al. [126]. These findings are in contrast to turning where a lubricating cushion can be set up, due to the improved penetration effects of the cryogenic media, to

improve lubricity and thus lower forces. Attempts have been made to make use of this phenomena. In their 2019 paper, Kummamkandath and colleagues [127] investigated the use of directing LCO_2 to the flank face and rake face in the face milling of Ti6Al4V. They found that cutting forces do not decrease for the LCO_2 application over MQL and flood strategies, and attribute this to the increased shear resistance of the workpiece material at the colder temperatures. However, they observed lower deformation in the secondary shear zone through observation of the chip microstructure, and less adhered material, indicating lower friction. Pittala [128] also showed the direction of the coolant supply to the cutting zone to have an impact on the flank wear of the tool with solid end mills in milling of Ti6Al4V. This was shown as an improvement in the reduction in flank wear with optimised LCO_2 flow to the cutting edge.

Further work has looked at the effect of cryogenic media on the finished surface roughness of a part. Improved surface quality has been demonstrated by Wang et al. [129] in their work in the milling of Ti6Al4V. This is inline with Kummankandath and colleagues [127] who also found similar results and both attribute the improved surface finish due to the lower amount of adhered material on the flank face of the tools.

3.8 Drilling with cryogenic media

Since 2013 when Shokrani et al. [94] quoted only three papers that had looked at cryogenic drilling: Bhattacharyya and Horrigan [130] studied the use of cryogenics in the drilling of Kevlar, Ke et al. [31] used cryogenics for the end milling of holes in Ti6Al4V and Dhokia et al. [131] drilled carbon fibre utilising cryogenic fluids.

Since then, Dix [102] has modelled cryogenic drilling, Govindarayu, Ahmed and Kumar [132, 133, 134], have studied cryogenic drilling for inserted drills on a variety of materials. Sadik et al. [135] has also studied the indexable insert drilling of Al-SiC metal matrix composite. After a lull in cryogenic drilling research 2020 and 2021 saw an influx of new papers. Kanagaraju et al. [136] compared LN_2 with wet in drilling of super duplex stainless steel. Merzouki et al. [137] explored the effect of hole shrinkage in drilling with LN_2 and in dry conditions, Khanna et al. [138, 139] compared LN_2 and dry drilling of solid carbide tools in composites and Inconel 718. Most recently, Sterle et al. [140] has investigated the effects of LCO_2 cooling on drilling with solid carbide drills in 42CrMo4 Steel.

Zeilmann et al. [141] presented a method for measuring the temperature of drilling in Ti6Al4V by using thermocouples embedded at various depths in the adjacent material perpendicular to the drilled hole. This method of temperature measurement was used by Govindaraju, Ahmed and Kumar [132, 133, 134], in drilling of AISI 1045 steel, unalloyed titanium and Ti6Al4V with the thermocouple measuring temperature at the bottom of the hole (maximum temperature). Each of these papers have observed a reduction in temperature somewhat lower than those reported elsewhere. Cutting temperatures of approximately 450ºC were suggested by Dix [102], which is much higher than those observed here. The expected increase of the cutting temperature with the speed is also not observed here. An alternative way of measuring the temperature was illustrated by Sterle [140], where they measured the temperature at the drill exit using an infrared pyrometer. Temperature measurements were taken using a similar method in

this thesis.

Kanagaraju et al. [136] observed increased normal forces when drilling with LN_2 and higher cutting feed when compared to a wet strategy, this was also in line with findings by Tran et al. [142] where they also found cryogenic machining to increase normal cutting forces in drilling.

Bagci [143] showed that when dry drilling steel and aluminium the cutting temperature reduced when the feed was increased, at a constant cutting speed. This temperature rose to a maximum and then plateaued for the remainder of the cut. The quality of the drilled hole is important in drilling as this reduces work needed for further finishing of the hole. In the drilling of aluminium alloys and gray cast iron, Haan et al. [71] presented results that consistently showed an improvement in the hole surface finish (R_a) with the application of oil emulsion cutting fluid as opposed to machining dry. When machining dry, they found that the troughs in the surface roughness trace coincided with the extraction revolutions of the drill.

Here the effect of LN_2 shows that LN_2 can both increase and reduce the surface roughness of the holes. Unfortunately in these papers, little information is given to the other parameters that have been used. However, the ability to produce holes of lower surface roughness is certainly encouraging for cryogenic cooling technology.

Ahmed et al. [134, 133], also studied the effect of using cryogenic coolant on the cylindricity and circularity of drilled holes in unalloyed titanium and Ti6Al4V alloys. When drilling Ti6Al4V, they found an improvement in the circularity and cylindricity of the hole, which they attribute the reduction in thermal expansion due to colder temperatures. The thermal expansion of the drill or workpiece could also play a role in producing these favourable results. In studying unalloyed titanium, they found the opposite to be true, higher circularity (from 12% to 206%) and cylindricity values, in this they attributed the degradation of the hole surface, shown as rougher surface.

Biermann and Hartman [144] also found that by applying CO_2 at the exit of the hole, burr formation at the exit of the hole was reduced compared to results for dry machining and those found with conventional coolant. The quality of the drilled hole is not only influenced by the coolant type, but also by the coolant strategy that is adopted. Sadik et al. [135] found that using externally supplied CO_2 does not provide an improvement on hole surface roughness or hole precision. However, when coolant is supplied internally both surface roughness (R_z) and hole precision improvements are found due to the protection of the peripheral insert and the prevention of the built up edge on the insert resulting in the best precision and surface finish. These improvements correlated with an increase in the tool life of the drill when adopting the internal supply of CO_2.

3.8.1 Tool wear in drilling

Adopting cryogenic coolant in machining has shown a reduction in the tool wear in turning, milling and metal matrix composite drilling [106, 145, 146, 108, 135, 115].

Astakov [7] states; “with proper design and manufacture, selection of the correct cutting parameters, and a suitable MWF, flank wear should be the dominant wear mechanism in drilling.” In the drilling

studies utilising cryogenic cooling fluid (Table 3.1) various modes of tool wear were identified, of the three utilising solid carbide tools, flank wear and edge chipping has been identified on the tools.

Paper	Year	Cryogenic fluid	Material machined	Drill type	Tool wear mechanism
Govindaraju et al.[132]	2014	LN_2	AISI1045	Indexable	Cutting edge chipping
Ahmed et al. [133]	2015	LN_2	Ti6Al4V	Indexable	Cutting edge deformation
Ahmed et al. [134]	2015	LN_2	Titanium (commercially pure)	Indexable	None
Ahmed et al. [147]	2016	LN_2	Ti6Al4V	Indexable	Cutting edge chipping
Sadik et al. [135]	2016	CO_2	AlSiC (metal matrix composite)	Indexable	Flaking of tool coating
Merzouki et al. [137]	2020	LN_2	Ti6Al4V	Indexable	Margin adhesion
Koklu et al.[148]	2020	LN_2	AZ31	Solid carbide	Flank
Khanna et al. [149]	2020	LN_2	In718	Solid carbide	Cutting edge chipping
Shah et al.[104]	2021	LN_2 and LCO_2	Ti6Al4V	Solid carbide	Flank

Table 3.1: Comparison of tool wear mechanism identified for the different studies of cryogenic assisted drilling.

In plain steel drilling with inserts, chipping was found to be the predominant tool wear mechanism. This was characterised by high thermal shock loading, with insufficient coolant and is characteristic of those results found in the dry drilling of titanium [150]. When LN_2 was applied the cutting edge chipping was reduced. In unalloyed titanium drilling, flank wear was identified as the dominant wear mechanism, and for wet coolant chipping was the dominant wear mechanism. When machining Ti6Al4V, it is claimed that the LN_2 has better penetration to the cutting zone, maintaining lower cutting temperatures, however as stated previously LN_2 forms a vapour cloud on the surface due to evaporation. Overall the results showed a large amount rake and nose wear.

Sadik and Grenmyr [135] studied the tool wear for both internally and externally applied CO_2 and emulsion in the drilling of MMC Al-SiC (20% SiC). Findings from their work showed that when coolant is supplied internally, the wear is transferred from the peripheral insert to the central insert. The effect of this was to improve hole surface finish and precision in the form of the diameter. While the wear mechanisms of the externally supplied coolant (both emulsion and CO_2) showed similar wear mechanisms on the corner of the peripheral insert, there was a marked difference for the internally supplied coolants. Flaking of the diamond coating occurred on the insert for CO_2 coolant, and flank wear dominated in conventional coolant supply likely caused by 3rd body abrasive wear from the diamond flakes. For this CO_2 operation, tool life improvements were seen and substantially more holes were drilled for all speed and feed combinations in comparison to emulsion coolant. The results for the tool life for CO_2 indicated that the coolant was more speed dependent (higher speed producing more holes), while emulsion was feed dependent (higher feed producing more holes, at lower cutting speeds). Based on their results they recommended only through tool (internal) coolant supply should be used as it gives much longer tool life. The longer tool life could be attributed to a reduction in the temperature, as observed by Zeilmann [141], who found lower cutting temperatures with through tool MQL coolant.

The presence of a built up edge on the cutting tool edge can increase the rate of tool wear [30], resulting poor workpiece surface finish in turning operations, less so in drilling. It is often desirable to have a built up edge present on the cutting edge as it acts as a layer of protection of the relative motion of the tool and workpiece.

Cutting speeds and feeds influence the amount of wear experienced on a tool, and an operating window exists where optimal tool wear can be achieved. In milling trials of Ti6Al4V with both CO_2 and emulsion, Sadik et al. [151] demonstrated a 6 times increase in tool life with increased the cutting data, however when the data was reduced the tool life equalled that of emulsion coolant. In contrast, Bermingham et al. [30] looked at identical process parameters (speeds, feeds, tool, material) for the high pressure (100bar) emulsion coolant and LN_2 at 8 bar. In this study he found that both LN_2 supplied coolant and high pressure coolant both improved tool life. The LN_2 coolant results were sensitive to the coolant nozzle position and 80% improvements in tool life were achieved when the coolant nozzle was directed precisely into the cutting zone interface. While, these results have shown improved tool life for high pressure coolant, there is a clear distinction of pressures of the flow which also may be influencing the wear rates. Sadik [115] and Supekar [91] have shown that the pressure and flow rate of the coolant influence the tool life, possibly through improved penetration of the coolant in to the cutting zone. [MOVE]

3.8.2 Drill exit burr height

Abdelhafeez et al. [152] and Patil et al. [153] found the cutting speed and feed have an impact on exit burr height. A relationship between the cutting speed, cutting feed, cutting temperature and resultant cutting forces was established by Joy et al. [154]. Herein, the forces exerted on the drill therefore influence the exit burr height, which has by Rimault et al. [155]. Drilling cooling conditions have been shown to impact burr height by two authors, Mathew [156] and Biermann [144] where cooling cutting produced a smaller burr height. The effect of cryogenic machining on the exit burr height with through tool cooling has yet to be established in a test representative of an industrial process.

3.8.3 Edge rounding

Denkena and Biermann [25] in their review of cutting geometries, show that the cutting edge rounding has a large influence on the thermal loads in cutting and that an optimal cutting edge geometry exists for each workpiece material, tool substrate/coating and machining parameters (including coolant). Larger edge radius and flank face segment S_α increase the thermal load on the cutting wedge due to increased friction on flank segment and increase secondary shear zone deformation. The surface area over which the generated heat dissipates increases however, therefore optimal solutions exist within this range.

Experimental results have shown that with small changes in the edge radii minimal increases in the temperature ($\approx$10%) on the rake face of the tool is experienced [24, 157]. However, when radii are increased, a shift of the location of the maximum temperature occurs towards the flank face [22, 158]. This shift is also related to the uncut chip thickness described by the ratio $\frac{t_0}{\bar{S}}$ (where $\bar{S}$ is the average edge rounding). With decreasing ratio, the maximum temperature moves towards the flank face.

The mechanical loads within the cutting edge are widely determined by the edge rounding, see Figure 3.5. While the cutting forces are increased with increasing edge rounding the stress concentrations within the tool are reduced. With increasing rounding the stresses increase on the flank face due to greater contact area with the workpiece. This is shown by the greater increase in the feed force. At low feed rates, and thus uncut thickness, the relationship becomes non-linear owing to the change to the ploughing force dominating.

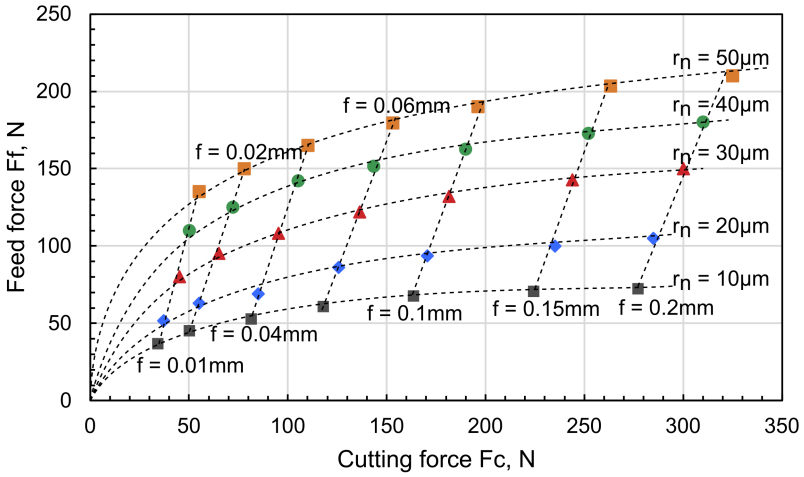

Figure 3.5: The effect of edge rounding on the cutting force and feed for in turning Ti6Al4V (modified from [24]).

In machining titanium, high cutting forces and temperatures are experienced [46]. Denkena et al. [22] suggest that the edge rounding is kept low to minimise the thermo-mechanical load on the tool to maximise tool wear resistance. Through introducing cooling, the thermal load reduces, enabling a larger radius to be used with increased mechanical stability and less edge chipping.

3.9 Sustainability and life cycle analysis of cryogenic machining

This section looks at the work that has been conducted around the sustainability of the cryogenic machining process. Sustainability takes into considerations three pillars of impact; society, economic and environmental.

There are large social benefits of moving towards cryogenic machining solutions and away from traditional conventional coolants. These are primarily around the health and safety of operators. The health and safety considerations of using CO_2 have been covered in Section 2.8 outlining the risks associated with CO_2 toxicity and frostbite, and it has been identified that these can be mitigated against. In contrast conventional water based MWFs present greater occupational risks, through dermal contact manifesting as dermatitis [159, 4], and respiratory diseases such as asthma and bronchitis [160].

The widespread adoption of cryogenic MWFs, without the use of incentivisation schemes, will depend on their financial viability. If companies are to convert to CO_2 MWFs, then the cost of doing so needs to be taken into consideration. Current systems require the purchasing and retrofitting of CO_2 standalone machines to existing machines which has a high initial cost. It is anticipated that the future costs of

the technology are likely to go down. This is anticipated in two ways. The first being the reduction in machine upfront costs as machine tool operators begin to include CO_2 supply systems on machines as standard. Secondly, as knowledge of the CO_2 machining process is increased, production improvements and tooling solutions will provide economically viable production to offset the initial capital investment [4]. This has already been suggested through reduced machining cost, tooling usage and energy [161].

As CO_2 is a greenhouse gas, any release of this into the environment, as occurs in a CO_2 machining process is a concern. This therefore requires further analysis, particularly considering the UN target of reduced global CO_2 emissions of 45% by 2030 [2]. It should be noted that CO_2 is not being produced in the cryogenic machining process it is being used as a byproduct from the industrial processes of fertiliser and alcohol production. This is contrast to the production of N_2, which is produced from the distillation of air, which is an energy intensive process [87, 88]. Work to quantify this impact and compare it conventional approaches has been conducted using life cycle analysis (LCA). This is a tool that is used to assess the sustainability of a product or process in the environment. This tool looks at the process or from the beginning to the end, and works on the principle that everything must become a waste [162]. LCA has been conducted by several authors in the cryogenic machining field, where both the impact of nitrogen and carbon dioxide has been studied in comparison to other machining strategies.

Pusavec et al. [88] completed a study comparing conventional, high pressure jet and N_2 machining. In their work they looked at the process for a turning operation. For the conventional and high pressure jet processes, they identified both CO_2 and sulphur dioxide wastes, contributing to global warming and acidification of the atmosphere. Additionally, they identified solid wastes and water usage as other wastes. The energy consumption of all the processes was considered, and they showed that in order to produce N_2 for usage in the process, an energy intensive process is required. They referenced that approximately 140 000MJ of energy usage [87], compared to 700MJ for an equivalent operation in conventional and high pressure jet, is required to produce N_2. The emissions arising from this energy production are dependent on the source for this energy. In this paper, they assumed that this energy came from renewable resources, and did not account for the emissions from this electricity production. This skewed their results in favour of N_2, as it is unrealistic to omit this, due to only 25% uptake of renewable energy worldwide as of 2019 [163]. Agrawal et al. [164] identified the high carbon emissions of using N_2. However, they showed that by increasing production in a turning operation through increased surface speed when using N_2 over conventional, the high carbon emissions of N_2 could be offset.

Further detailed work looking at emissions have been conducted in other LCA's. Clarens et al. [165] have shown gas-based systems such as those using CO_2 and N_2 rather than water-based systems to reduce solid waste by 60%, water usage by 90% and aquatic toxicity by 80%, while virtually eliminating all occupational health concerns. However, they found an increase in the global warming potential of gas-based solutions. These findings are in agreement with a more recent study by Supekar et al. [166] whereby gas-based and water-based MWFs were compared using part throughput as a measure of productivity. They found both CO_2 and N_2 to have increased energy consumption over water-based. That is because when oils are used in the process as lubrication, the water-burden is pushed upstream in the farming and production of the oils (e.g. soybean oil production). In their work they took data from

multiple sources of cryogenic machining articles to quantify the improvements obtained by the gas-based MWF, and then considered that data in their analyses. By focussing on throughput as a measure of productivity to meaningfully reduce energy usage per unit of material removed, they found tool life improvements to increase the productivity when the baseline improvement was 3 to 7 minutes over the water based equivalent. However, above this tool life gains were stated to have a negligible effect on productivity because the throughput gain depended on the reduction in downtime from fewer tool changes and this gain diminishes with increasing tool life. In their work they suggested that to reduce the water and energy usage of gas-based systems, improvements to productivity needed to be achieved by increasing material removal rate for equal tool life by exploiting the more effective lubricating and cooling properties of gas-based plus oil systems. To do this they suggested further work looking at process machining parameters and tool geometry modifications, as well as optimised delivery of the MWF to where it is needed.

These works suggest that gas-based MWFs are emitted to atmosphere, resulting in the increase global warming potential. In the case of CO_2 if the gas can be captured and utilised, the emissions to atmosphere will be removed, lowering the global warming potential of the process. This has been shown to be a feasible solution, however work around this is in its infancy and remains ongoing [167].

3.10 Application of cryogenic coolants

Applying the different types of cryogenic cooling fluids, LN_2 and CO_2, require different approaches for successful application. The initial stabilisation period for LN_2 applications is longer than that of CO_2 applications. 60 seconds is all that is needed for the tool to reach a stable temperature for CO_2, while 600 seconds are required to allow stabilisation of the LN_2 tool shown in Figure 26. The temperature at the exit of the LN_2 outlet fluctuates in temperature because of the gaseous nitrogen which is generated in the supply system.

Both coolant technologies have been applied in industry. Two cooling systems that utilise liquid CO_2 are the Rother system and the CoolClean system. The Rother system uses an array of medium pressure vessels that house the CO_2. These vessels supply directly the CO_2 to the Rother system (which regulates the flow rate) through pressure resistant pipes through the rotary union and machine spindle and into the tool and then in to the cut. This system has been adopted by Starrag on a machine that manufactures small turbine blades. The CoolClean system, has an intermediate stage prior to delivering the coolant to the cutting tool, where the coolant travels through a refrigeration unit to control the exit temperature of the liquid. The CoolClean system requires a little more set-up onto machines in industry. Adopting this technology on to machinery requires few modifications unlike LN_2 systems. These systems require insulated tanks, supply pipes and tooling. Despite these difficulties LN2 coolant is used in an industrial set-up by 5ME. Their system uses vacuum jacketed supply lines and a sub-cooler to maintain 100% liquid phase of the nitrogen. The coolant flows through the tool to just below the cutting edge, and removes heat through thermal conduction through the tool, with no LN_2 expended to atmosphere in the system. Therefore to summarise tool wear improves with move to internal cooling supply in drilling, the

cryogenic mass flow rate and the direction of the coolant impacts cutting performance.

3.11 Summary

With increasing scrutiny and expectation from the public for manufacturing to be cleaner and more sustainable, which is reflected in the Engineering Councils codes of conduct and learning outcomes for registration for professional engineers. It is important for Sandvik Coromant, not only to be sustainable in their own production of products, but also to provide products that allow the customer to be sustainable in their manufacturing.

The most environmentally sustainable way of machining is to use no cutting fluid at all and machine dry. It is possible to do this with certain materials such as cast iron and certain steels, however it is not possible to machine dry titanium materials, due to the likelihood of the machined titanium to catch fire as a consequence of the extreme build up of heat in titanium machining due to the low thermal conductivity and relatively high contact pressures in titanium machining [150].

Cryogenic machining provides one method to overcome these difficulties, where the fluid evaporates in to the atmosphere leaving the workpiece free of residue. However, there still are challenges associated with the release to atmosphere and contribution to greenhouse gases. The carbon dioxide that is used is sourced from recycled sources and commonly used in soda drinks. The comparatively low Young's Modulus and adhesive tendencies of titanium alloys make them difficult to machine. Improved solutions atypical to the methods used in conventional machining have been found in turning and milling applications, with precision directed cryogenic coolant application , offering improvements to the process. However, these have yet to be explored in the drilling process.

The research surrounding cryogenic machining is in the main positive, with wide and consistently quoted improvements in tool life, control of workpiece dimension and surface finish. Most recently, Zhao et al. [126] have shown that the cryogenic machining process has a positive effect on the surface integrity of components, which had previously been perceived as an unknown barrier to entry for the technology. The process still remains a largely non-conventional one, with little perceived uptake in the market and demand for tooling from customers, reflected in the absence of cutting tools optimised for the cryogenic process, likely due to little pull from customers. On the contrary, for demand to exist for a product, customers need to be shown that the process works and it can be adopted. Systems are available on the market to adopt cryogenic machining, with liquid CO_2 systems such as the CoolClean, Rother Technologies, supercritical systems such as the Fusion cooling system, and the 5ME product providing cooling with a closed system of liquid nitrogen. To purchase these tools and thus develop the cutting tools is an expensive exercise. To start this process a starting point is required for the drilling process.

4 Methodology

4.1 Introduction

The methodology to study and explore the thesis objectives is described in this chapter. It starts by providing an outline of the methodology used, and how the process variables were modified throughout each stage of the thesis. The chapter then describes the machine tool, material and cutting tools used in in the thesis, before explaining how forces, temperature and hole quality metrics were measured.

4.2 Variables discovery

An initial discovery of the variables present in the LCO_2 cryogenic drilling system was conducted using the fishbone diagram methodology, the results from this are shown in Figure 4.1. The procedure involved understanding how each of the branches of the structure (such as machine) could influence or be influenced by the LCO_2 cryogenic drilling process. Once a variable was identified, it was assigned to each of the branches.

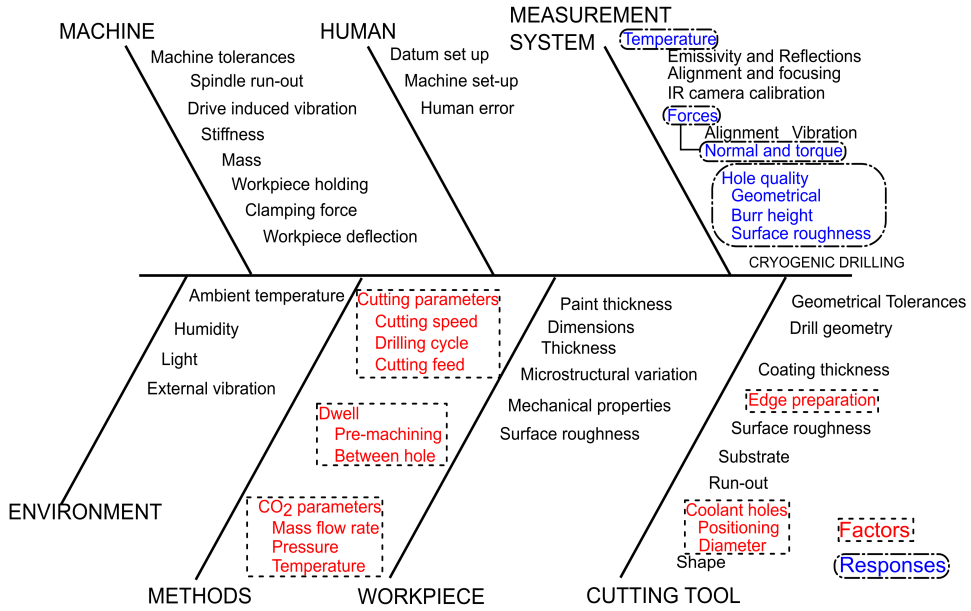

Figure 4.1: Fish diagram, showing the variables present in the cutting process when drilling titanium alloy with cryogenic cutting fluid (CO_2). Highlighted are the variables that have been studied in this thesis.

From these variables, those to be studied within the experiments (factors), and the dependent variables

to be measured (responses) were highlighted. The other variables were monitored, and controlled where necessary.

The study of the effect of these factors on the responses were organised into a structured series of experiments, outlined in Figure 4.2.

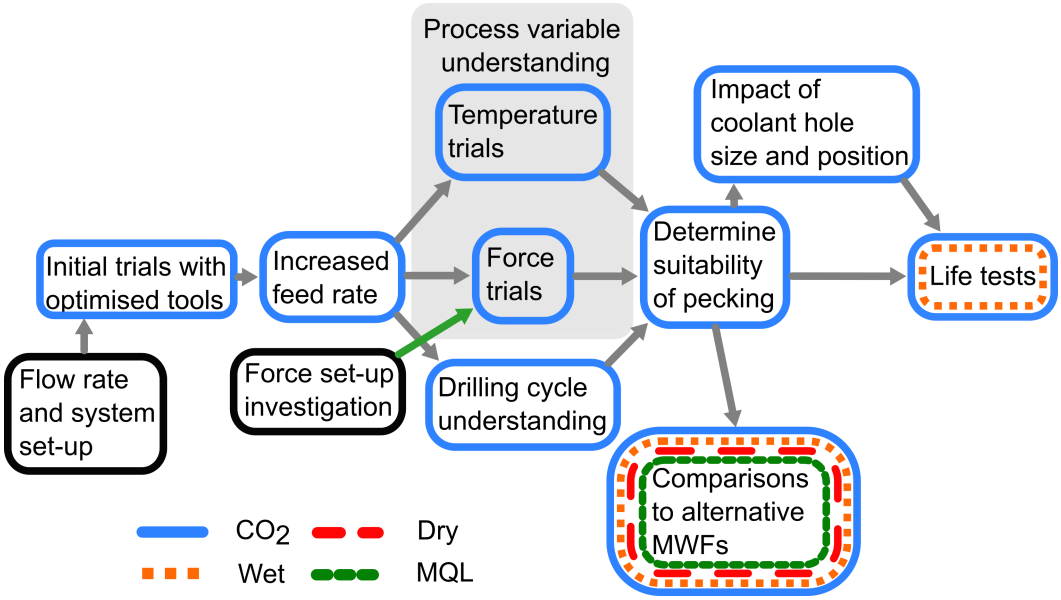

Figure 4.2: Flow diagram of the experiments conducted, showing the direction and flow of the experiments carried out.

4.3 Machine Tool

The experiments were completed on a Starrag LX051, five-axis horizontal milling machine with the spindle oriented horizontally, with CO_2 through tool cooling retrofitted to the machine. While the primary purpose of the machine was designed for multi-axis milling, the spindle rotation and z direction in and outfeed of the machine meant that it was capable of producing drilled holes. The machine set-up is shown in Figure and the capabilities of the machine are summarised in Table 4.1.

Spindle power	28 kW
Spindle torque	181 Nm
Maximum spindle speed	18000 rpm
Maximum workpiece length	400 mm
Maximum workpiece mass	50 kg
CNC- controller	Siemens 840D

Table 4.1: Machine tool parameters.

The machine is retrofitted with LCO_2 supply, which provides a unique rotary union to prevent gas leakage as it travels through the spindle and then through the tool. It is stored at a pressure of 58bar absolute at 20°C. The CO_2 is supplied in liquid phase through 1mm diameter piping, to a specially

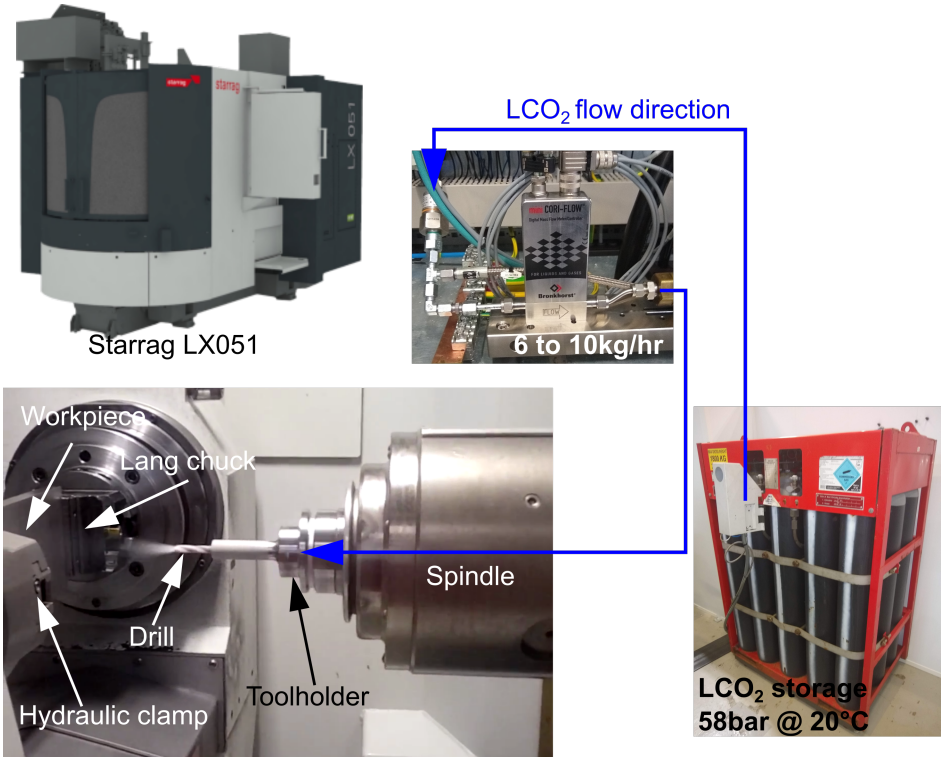

Figure 4.3: Starrag LX machine with the through tool supply of LCO_2 to the back of the tool shown.

designed toolholder where an internal lance is installed. This maintains the same cross-sectional area of the flow pipe preventing liquid expansion and phase changes, directly to the back of the tool, where the fluid splits into the two coolant channels of the drill. This toolholder is shown in Figure 4.4. The flow is driven by the pressure difference between the supply and atmosphere, and the mass flow rate of the liquid is controlled using an inline installed Coriolis flow meter to maintain a mass flow rate at defined levels in the range of 6 and 10 kg/hr. This is specified using a percentage, for example 60% of flow corresponds to 6kg/hr.

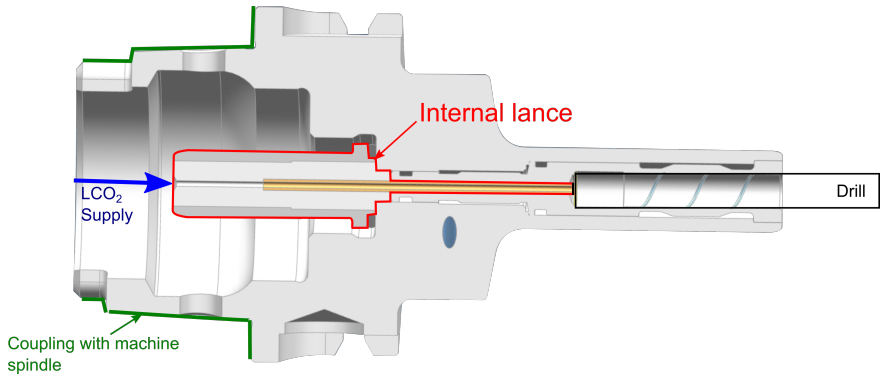

Figure 4.4: CAD image of the modified Sandvik CoroChuck 930 toolholder, highlighting the internal lance. Enabling the transport and supply of liquid CO_2 to the rear of the drill.

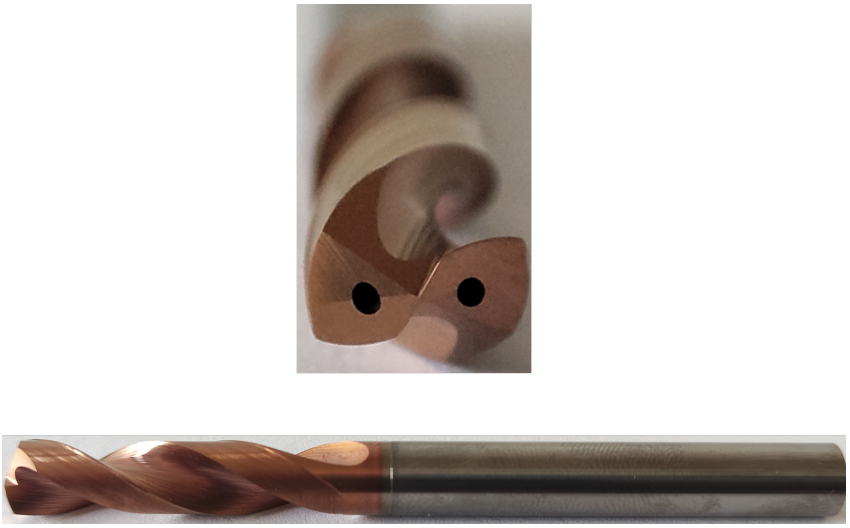

Figure 4.5: CoroDrill R846

4.4 Cutting tools used

Two types of tools were used in the thesis, the CoroDrill R840 and the CoroDrill R846, Table 4.2 and Figure 4.6. The drill used after the initial experiments, observing the effects of the CO_2 parameters, was a drill specifically optimised for machining materials that are categorised as ISO S, typically HRSA (heat resistant super alloys). These materials are difficult to cut and reduce tool life, they create a built up edge, work harden and large amounts of heat are built up at the cutting edge during machining. Within this category are high-alloyed iron and nickel alloys, such as Inconel 718, as well as titanium alloys. The tool is designed to machine all of these materials despite the wide ranging material properties within this category.

Initial experiments	CoroDrill R846
Main experiments	CoroDrill R846
Alternative tooling experiments	CoroDrill R840
Prototype tooling experiments	Prototypes (described in Section 4.4.1)

Table 4.2: Drill types used for each experiment.

This tool is denoted by Sandvik Coromant as CoroDrill R846-0600-30-A1A 1220 (shortened to R846 throughout the thesis from this moment on). This drill has a 6mm diameter with through coolant holes, the drill length is three times the diameter and is made up of grade 1220, and is shown in Figure 4.6. The geometry of the drill cutting edge is curved (or bow shaped), to lengthen the cutting edge and distribute the load across a greater area during cutting.

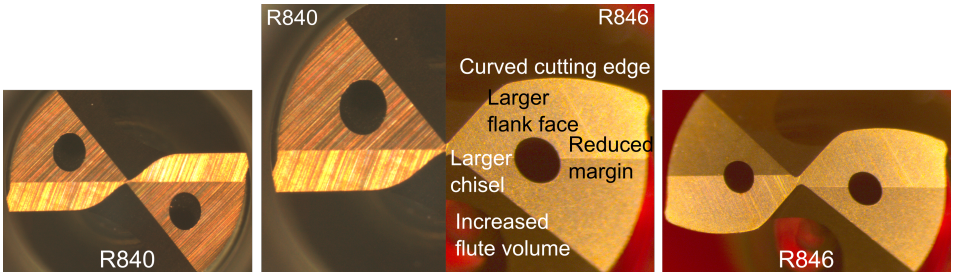

Figure 4.6: Comparison of CoroDrill R846 drill and CoroDrill R840 drill geometry, manufactured by Sandvik Coromant, showing the drill features modified for the R846 where it is optimised for HRSA materials.

The difference can be seen when comparing against the straight cutting edge of the R840 drill, Figure 4.6 and other manufacturers titanium alloy drills, Figure 4.8 where they also lengthen the cutting edge, but achieve this through curving the cutting edge in the opposing direction, in a "hook" shape. This has the effect of increasing the rake angle at the outer periphery of the drill, potentially weakening the drill at this point, however it does reduce the cutting forces, due to the sharper cutting wedge. Additionally, it also changes the inclination angle, to curl the chip further. Cutting tools are complex with a wide range of properties, hence the difference between the solutions of each of the tool manufacturer in achieving a tool for machining titanium alloys.

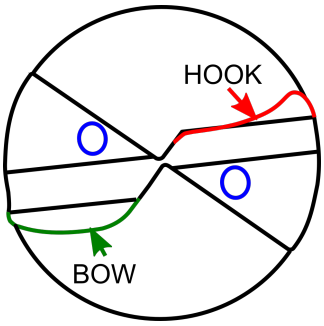

Figure 4.7: A hook and a bow cutting edge to distribute the cutting load across a greater length compared to a straight edged cutting edge.

The diameter of the drills used throughout was 6mm as this provided a compromise between small enough for efficient use of material and large enough that the holes can be analysed easily enough (i.e. enough room to allow the CMM and surface roughness probes in to the holes). The drills produce holes to tolerance of h9 (for a 6mm drill this is a tolerance of +30µm). They are coated with TiAlN in layers to a total thickness of 3µm, using physical vapour deposition (PVD). The drill substrate is made from a cemented carbide grade H10F, consisting of 10% cobalt with 89.5% tungsten carbide and 0.5% other carbide. The grain size of the substrate WC is submicron, approximately 0.8µm in size. This combination of WC size and cobalt content provides hardness of 1600 Vickers, which is balanced between hardness and toughness (see Garcia et al. [14] for an in depth overview of cemented carbide microstructure and how this influences hardness and toughness).

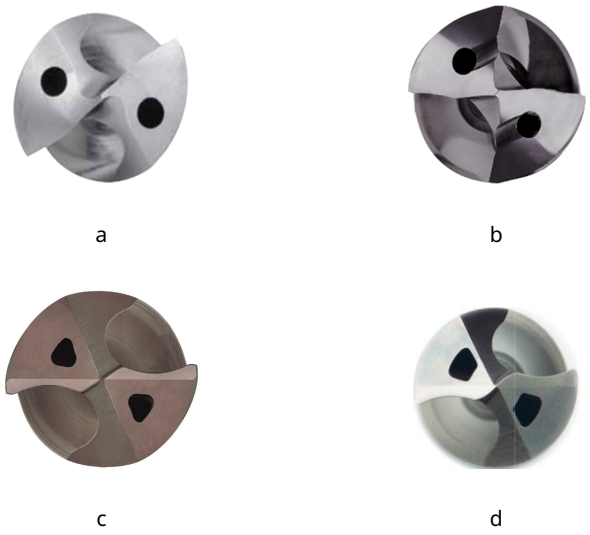

Figure 4.8: Other ISO S or HRSA (heat resistant super alloy) drills manufactured by competitors. a) Kennemetal b) Guhring c) Mitsubishi d) OSG

The edge preparation used on the cutting edge of the drill is honed symmetically round, with $\kappa \approx 1$, and diameter $\approx$ 35µm. Additionally, a thinner margin and increased back taper when compared to the non-optimised drill (R840) attempts to minimise friction with the hole wall during the drilling operation.

4.4.1 Prototype tools

Eight prototype tool variations were designed using the same geometry and grade used on the R846 drill. Of the eight, six of the tools were modified by varying the coolant hole positioning and size, shown in Figure 4.9. The three positions of the coolant holes were equally spaced, 1.5mm radially from the central axis of the drill. Three positions were used. The original, as produced on the R846 drill. Using the original position as the reference datum and with the clockwise rotation positive when looking at the point, 12 degree rotation and a -12 degree rotation.

The two coolant hole diameters used were, 0.35mm and 0.7mm corresponding to an area 0.25x and 1x respectively of the supply pipe of 1mm in diameter. These design modifications were made by Sandvik Coromant. To achieve the smaller coolant hole diameters development at Sandvik Coromant was undertaken so that their extrusion was able to produce the smaller holes.

The remaining two prototypes were made by modifying the edge preparation of the drills with the original coolant hole positioning. The edge preparation for these holes was half that currently used. Therefore the sharper edge rounding was 17.5µm and the larger edge rounding used was 35µm.

4.5 Initial trials to assess LCO_2 drilling functionality

Prior to cutting, the LCO_2 supply system was tested and validated because literature had shown the LCO_2 mass flow rate to have an important influence on cutting performance [115], therefore correct supply and knowledge of the LCO_2 supply ensured accurate findings from experiments that were altering

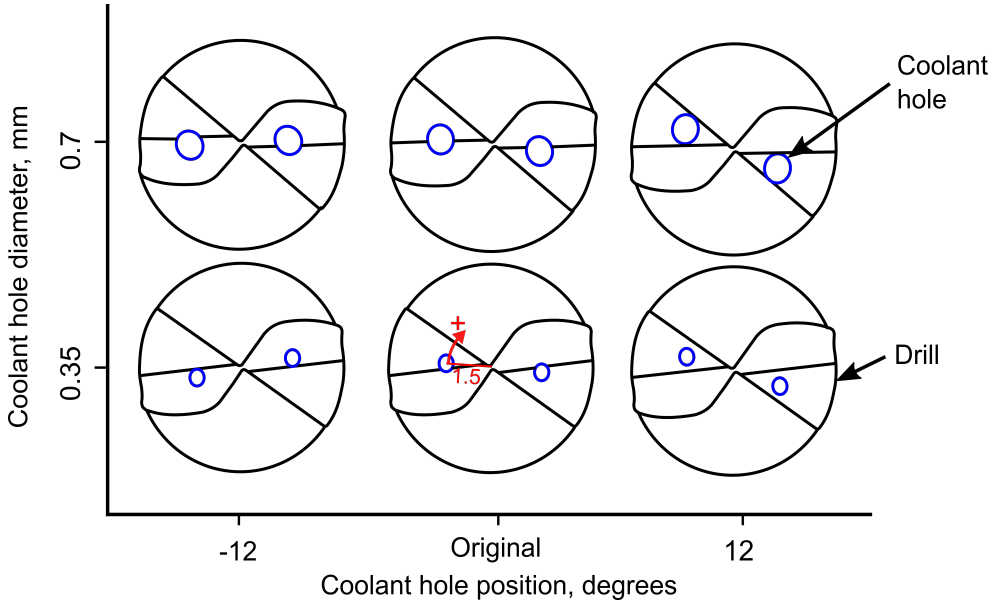

Figure 4.9: Prototype tooling schematic, showing the various positions and diameters of coolant holes produced.

this parameter. To do this, the supply LO_2 mass flow rate was measured and compared against the manufacturers quoted values for the flow rate. Initial observations of the CO_2 flow through the cutting tool showed a useful testing range of 60% to 100% maximum LCO_2 supply, as values lower than this did not provide observable cooling to the cutting tool. This was carried out by measuring the mass change of the CO_2 supply bottles over a period of time. Specifically, the time taken for 1kg to drop from the mass scales was timed for 6kg/hr, 8kg/hr and 10kg/hr, corresponding to 60, 80 and 100% machine setting. Further details and results are presented in 5.1.

As there was no historical data available from Sandvik Coromant using their tools with LCO_2, as Sandvik Coromant were yet to complete trials using the LCO_2 method, the first drilling trial was conducted using a drill and cutting parameters suited for drilling titanium with traditional coolant. An optimised tool geometry for heat resistant super alloys (CoroDrill R846) was therefore used to observe qualitatively, the functionality of the process in terms of the chip shape and form. Additionally, further quantification of the produced chips was done through mass measurement to further understand the chip formation. Further details and results of this trial are presented in Section 5.2.

The first drilling trial with LCO_2 showed that the cutting parameters normally used for traditional coolant were not suitable for LCO_2 resulting in long, concertina chips. These chips can potentially nest around the drill and subsequently cause drill failure. However, increased cutting feed was identified as improving the chip form, therefore further trials with increased cutting feed were conducted (explained and presented in Section 5.3). Further increasing the cutting feed did result in improved chip form and a cutting speed of 40m/min and feed of 0.2mm/rev were selected.

Once cutting parameters, providing a chip formation that was not in danger of nesting and breaking drills, were determined, work focused on establishing testing techniques for force and temperature measurement of the cutting process. This enabled force and temperature measurement of the LCO_2

drilling process. The development of these measurement systems are outlined in Sections 4.14 and 4.15.

4.6 Process variable understanding

Upon establishing measurement techniques for capturing forces and temperature, the effects of the process factors on the identified responses from the variables in the fish diagram (Figure 4.1), were analysed. These effects were conducted using two experiments; one using the forces set-up with the flat plate dynamometer (Kistler type 9129AA) in-situ and the other using the infrared camera (Micro-Epsilon TIM 160) set-up for measuring temperature. The factors studied are labelled as CO_2 parameters and dwell parameters in Figure 4.1. The dwell factors were included with the CO_2 factors as they are intrinsically linked through pre-cooling of the tool before drilling and act to pre-cool the workpiece prior to drilling, and increase the tensile and yield strength of the Ti6Al4V [29]. Additionally, the workpiece thickness was included as this influences time in cut, and the period of each cooling cycle of the tool between each hole and in turn the temperature of the tool. The factors and levels studied in this experiment are therefore outlined in Table 4.3.

	Levels			
Factor	Lower	Centre	Upper	Unit
Between hole dwell (BHD)	1	3	5	s
Flow rate (FL)	6	8	10	kg/hr
Feed (FR)	0.12	0.16	0.2	mm/rev
Retract distance (RD)	2	8.5	15	mm
Workpiece thickness (WT)	6	10	14	mm

Table 4.3: Levels and factors of experiment

The forces experiment organised the independent variables (factors) in to a D-optimal design (see Appendix for the theory of a D-optimal design) as this enabled the maximum number of variables to be studied in as few experiments as possible, minimising experimental cost by maximising the information obtained from the design set-up.

The cutting forces and workpiece quality were identified as the responses in the experiment. The measurement systems used for obtaining the workpiece quality are shown in Section 4.16. The experiments were conducted with a constant cutting speed of 40m/min, using four tools and two workpieces. Findings from this experiment showed the between hole dwell and retract distance to have little influence on the responses therefore were set to 0s and 2mm respectively for future experiments. Mathematical expressions for each of the responses were also obtained and the details and results from these experiments are presented in Chapter 6.

The LCO_2 mass flow rate, workpiece thickness and feed, identified as key performance factors, were further studied using a full factorial design, using the temperature test set-up to measure the hole exit temperature. The full factorial design was chosen due to the reduced number of factors being studied, and it allowed for a non-linear model of the relationship between the factors and responses if necessary.

The factors and levels used for this experiment are shown in Table 4.4, and the details of the experiment and model are presented in Chapter 7.

	Levels			
Factor	Lower	Centre	Upper	Unit
Flow rate (FL)	6	8	10	kg/hr
Feed (FR)	0.12	0.16	0.2	mm/rev
Workpiece thickness (WT)	6	10	14	mm

Table 4.4: Levels and factors of experiment

4.7 Drilling cycle study

Further improvements to the process were explored by studying the drilling cycle. This involved adopting a pecking cycle, which involves drilling the hole intermittently, as it has been shown to improve chip formation and aid chip evacuation whilst improve heat removal [168, 169]. However, this improvement comes at the expense of productivity due to the retract action increasing the time taken over drilling a hole of equal depth with constant feed. The cutting parameters, determined from previous experiments, were controlled at constant values (Table 4.5), and the experiments were conducted using the temperature experimental set-up, Section 4.15.

Cutting conditions	
Cutting feed	0.2 mm/rev
Cutting speed	40 m/min
CO_2 flow rate	10 kg/hr
Feed	424.4 mm/min
Workpiece thickness	10mm

Table 4.5: Cutting conditions used during the pecking and drilling stability analysis.

Two drilling cycles, observing the effects of the pecking cycle on the exit burr temperature of the drilling process, were used, and are shown in Table 4.6. A partial retract where the drill is retracted by 0.05mm between pecking depths of 0.5mm, and a full retract to 2mm above the surface (z_0) of the cutting surface between drilling depths of 1mm were used. It was found that a partial retract produced favourable results, as detailed in Section 4.6. For the partial retract of 0.05mm the distance travelled by the drill would be 20% further, as for each 0.5mm travelled a further 0.1mm would be travelled to account for the retract. This would result in a process taking 20% longer.

Drilling cycle parameter	Retract distance in z, mm	Drill peck distance,mm
Partial retract	-0.1 (gauge)	1
Full retract	-2 (absolute)	1

Table 4.6: Details of the partial and full retract drilling cycle parameters.

4.8 Prototype tooling experiments

The prototype tools, described in Section 4.4.1 were studied at the previously determined cutting parameters shown in Table 4.7. Eight prototypes were studied with each prototype drilling 49 holes through 10mm thick workpieces. The prototypes were manufactured with varying coolant hole position, size, and cutting edge rounding to determine whether these parameters could be used to influence the cutting process. The tests were conducted using the forces test rig (Section 4.14) and the results from this work are presented in Section 8.1.

Parameter	Determined value
Cutting speed	40 m/min
Cutting feed	0.2mm/rev
Coolant flow rate	10kg/hr
Workpiece thickness	10mm
Pecking cycle	Partial retract

Table 4.7: Cutting data used for the prototype tooling, larger diameter drills and the tool wear tests.

4.9 Observations with alternative MWF (wet, dry and MQL)

Further experiments were carried out to determine how the LCO_2 drilling performed in comparison to other cooling media strategies using the cutting parameters that have been developed for the LCO_2 cooling strategy. Wet (flood) coolant, MQL and dry strategies were tested for the parameters in Table 4.7, for three repeats of 49 drilled holes at each of the strategies. The experiments were conducted using the force measurement test set-up. The flood coolant used was Houghton's Hocut 4260 water soluble metal working fluid, which was regularly inspected and maintained by the Advanced Manufacturing Research Centre (who housed the machine) to minimise contamination and maintain concentration levels of 8 to 10% with water. The flood coolant was supplied through tool at 60bar pressure. The MQL solution used was Houghton's Cindolube V30ML, set at an machine setting of high which corresponded to a tank pressure of 5.4bar and nozzle pressure of 6.1bar. These experiments were conducted with the Sandvik Coromant heat resistant super alloy drill, the CoroDrill R846 drills (Section 4.4).

4.10 Observations with alternative cutting tool geometries

A multi purpose drill geometry CoroDrill R840, was used to conduct an experiment across the recommended parameter window supplied by Sandvik Coromant for the R840 drill. These parameters are shown in Table 4.8 and all combinations of the parameters were tested. Chip formation, the internal hole surface roughness and exit burr height were measured, using the methods described and presented in Sections 4.16.2 and 4.16.3.

Cutting Speed (m/min)	Cutting feed rate (mm/rev)
20	0.06
35	0.08
50	0.10

Table 4.8: Cutting parameters for the R840 drill when using emulsion coolant.

4.11 Tool wear life tests

Tool wear trials were then carried out using the best performing tool in the prototype tooling tests. Tools were run until the wear exceeded that of acceptable wear of the tool set at 0.4mm for the flank and margin wear. This was measured using a calibrated microscope during the trials. Again these trials were carried out at cutting data in Table 4.7, and through 10mm thick workpiece.

4.12 Material

Throughout the thesis, workpiece refers to the material that is being machined. In these instances the material is forged Ti6Al4V (grade 5) for all preliminary work prior to the tool wear trials, where the ELI variant is then used. Both variants of Ti6Al4V are in the mill annealed condition (the typical gradual cooling of the material adopted by material producers in order to control the microstructure of the finished material to within the specification for grade 5 Ti6Al4V) with no additional heat treatments. If other workpiece materials are used in any experiments, then they are explicitly stated in their respective sections.

Ti6Al4V accounts for 50% of all titanium components worldwide, 80% of which is used for aerospace components due to the high strength to density ratio [170]. Ti6Al4V is designated as R56400 under the unified numbering system (UNS) [171], with a nominal composition of 6% (5.5 to 6.75%) Aluminium and 4% (3.5 to 4.5%) Vanadium. Other elements are alloyed in small amounts (carbon, nitrogen, iron, oxygen and hydrogen) and are present as interstitial additions altering the properties of the titanium alloy. For example, a change in the oxygen content of titanium from 1000 to 3000 ppm raises the ultimate tensile strength from 600 to 750MPa and reduces elongation before fracture to 6% from 9% [172], therefore the limits of impurities contained within Ti6Al4V are tightly controlled and mandated [170], shown in Table 4.9.

	Impurities limits, wt% max				
	N	C	H	Fe	O
Ti6Al4V	0.05	0.1	0.0125	0.3	0.2
Ti6Al4V ELI	0.05	0.08	0.0125	0.25	0.13

Table 4.9: Limits of impurities and Aluminium and Vanadium tolerances of Ti6Al4V and Ti6Al4V ELI.

Ti6Al4V ELI (extra low interstitial) or grade 23 (UNS R56401), is a higher purity form than Ti6Al4V. The tolerance of Aluminium is 5.5 to 6.5% and Vanadium is 3.5 to 4.5. The ELI variant is used for fracture critical components such as those in medical applications, due to the lower levels of oxygen in the material which lower the ductility of Ti6Al4V.

For experiments carried out in Section 8.1, the chemical composition of the material is presented in Table 4.10.

Element	Ti	Al	V	N	C	H	Fe	O
wt %	89.2275	6.46	3.94	0.005	0.005	0.0025	0.17	0.19

Table 4.10: Composition of Ti6Al4V ELI used in Section 8.1.

4.12.1 Workpiece preparation

The LX051, 5 axis milling machine, detailed in Section 4.3, was used for all the experiments. The machine supports material of thickness 10mm to 50mm with a unique fixturing system: a Lang chuck on

one side and a hydraulic clamp on the other. The Lang chuck requires indents be made in the material (Figure 4.11), to provide secure fixturing with the male teeth on the Lang jaws. The width capacity of the machine is 300mm (between the two fixturing systems), which was minimised to ensure deflections on the workpiece during drilling remained as low as possible.

During force capture experiments the workpieces were cut to facilitate bolting on the the force dynamometer plate (Figure 4.12). For trials requiring multiple workpiece thicknesses, a stepped workpiece was used, where the workpiece had been milled at specific heights to provide different thicknesses for drilling through in the experimental design. This ensured economical use of experimental time, thus preventing removal and replacement of workpieces during the trial. Additionally, this allowed the experiment to be randomised according to workpiece thickness, e.g.the sequence through the different experiments with different workpiece thicknesses.

Black, matt, heat resistant paint (up to 800°C) was applied to the back of the workpieces for the temperature trials (shown in Figure 4.13), where the thermal camera was focused on to the workpiece prior to the drill exiting the workpiece. The black, matt coverage of the paint on the workpiece was used to provide a consistent emissivity value and reduce reflectivity of the workpiece surface that the camera was focused on during drilling. This was to minimise the uncertainty of the temperature measurement, further temperature measurement details are explained in Section 4.15.

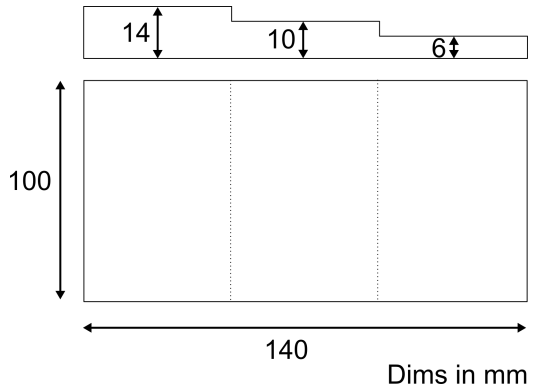

Figure 4.10: Stepped workpiece used in process parameter experiments.

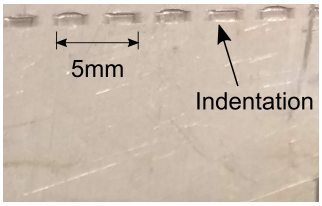

Figure 4.11: Indentations pressed into workpiece for mounting to Lang chuck.

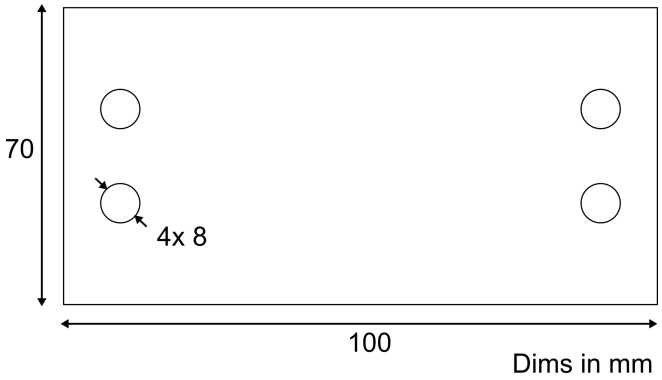

Figure 4.12: Holes drilled in to workpiece for bolting to dynamometer.

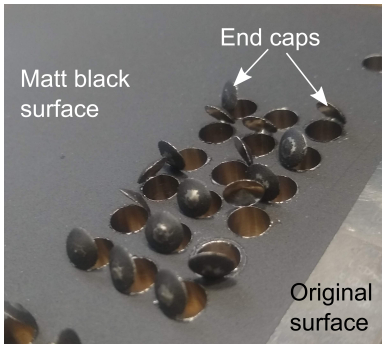

Figure 4.13: Matt black surface of back of plate used for consistent emmisivity surface of material.

4.13 Inspection of tools

Each tool, prior to use, was inspected visually under a microscope to check for any chips to the cutting edge which may act as crack initiation sites during drilling, or areas of poor coating, examples of these are shown in Figure 4.14. Additionally, the cutting edge rounding was measured using either a Helicheck Pro or Alicona optical 3D measurement system. The autonomous Helicheck Pro method for capturing the tool edge rounding was completed by Sandvik Coromant using their standard processes. This Helicheck Pro method involves using a CNC controlled Helicheck Pro machine which houses optical non-contact measurement equipment to provide measurements of the various features of the drill. The required measurements of the tool are pre-programmed in to the machine which allows autonomous measurement of multiple tools, providing a productive way to measure cutting tools in industry. The Alicona method however, involved manually setting up the Alicona 3D measurement system to capture the 3D image of the tool prior to taking an edge rounding measurements. The method for capturing the edge rounding using the Alicona is outlined below.

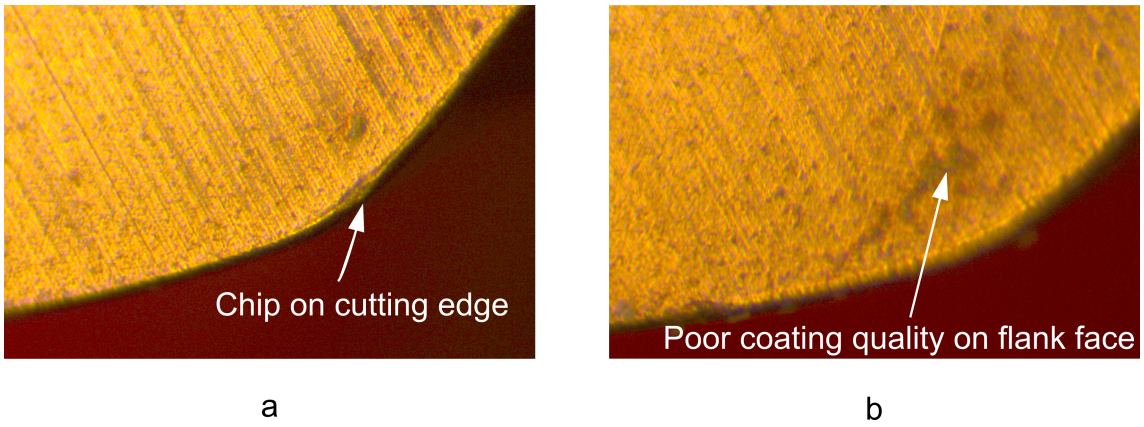

Figure 4.14: Visual inspection of the drills to look for defects such as: a) chips on the cutting edge b) poor coating quality.

To capture the edge rounding of the tool using the Alicona, the tool was set up at 60° to the horizontal plane, and placed under the Alicona optical scope so that the flank and the rake face of the cutting edge were evenly distributed about the vertical plane. An image of the tool was then captured, and a profile of the cutting edge was then captured. To capture the tool edge rounding profile, a 0.1mm wide band was selected 0.6mm from the margin edge of the tool, Figure 4.15a, consisting of 100 profile measurements between each cross shown. A mean value of these profiles was calculated and used to measure the dimensions of the edge rounding. Two edges were fitted to the profile; a circle fit, and an elliptical fit. The circle fit provided the radial rounding of the tool, while the elliptical fit provided the values for the form factor K (see Section 2.3.2.4), Figure 4.15b.

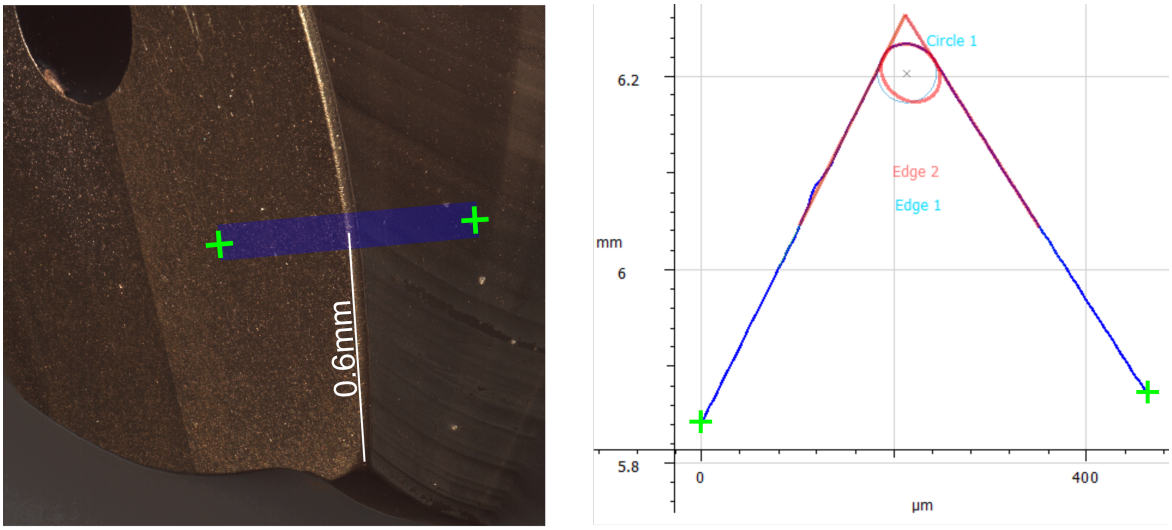

Figure 4.15: a) The image captured by the Alicona 3D measurement system, with the 0.1mm wide sample section. b) The resulting cutting edge rounding profile, showing the circle and elliptical fits used to capture the edge rounding data for the tool.

4.14 Force measurement

As the drill cuts the material, the mechanical strength of the material acts to resist the motion of the drill, and in doing so exerts a force on to the drill. The schematic shown in Figure 4.16 shows the location and direction of these forces acting on a solid twist drill in operation.

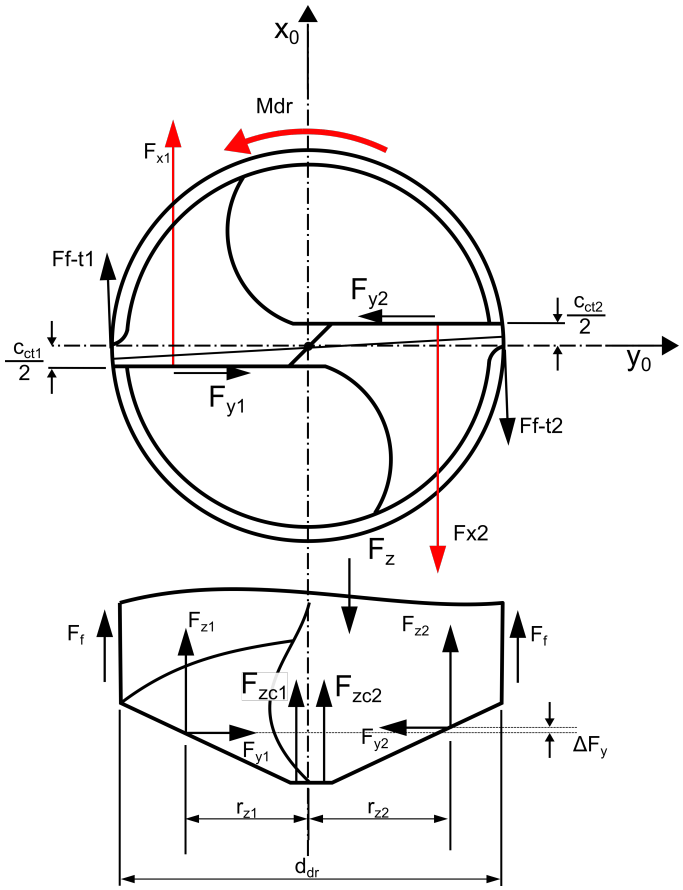

Figure 4.16: The numerous forces acting of the drill during a drilling operation.

Concentrating on the main cutting force acting on the cutting edges (or lips) and taking the 2D case of orthogonal cutting with a realistic edge rounding, Figure 4.17. The cutting force F_a is the result of the feed direction and the cutting direction. These forces also manifest themselves in to a useful cutting force, F_{ch} and wasteful ploughing force F_{pl} due to the edge rounding on the tool. One aims to minimise the ploughing force and minimise the waste when designing tools, so as to have an efficient process. This is done in several ways, such as using a sharper cutting wedge, with a smaller radius minimising the area in contact with the workpiece. However this lowers the strength of the cutting edge, in particular in machining difficult to machine materials with high material strengths, resulting in premature wear. There is therefore a balance to be done with minimising the forces and also preventing the tool from chipping and failing on the cutting edge due to a weak cutting edge. Figure 4.17 represents a schematic showing the classical orthogonal cutting model with a realistic edge radius.

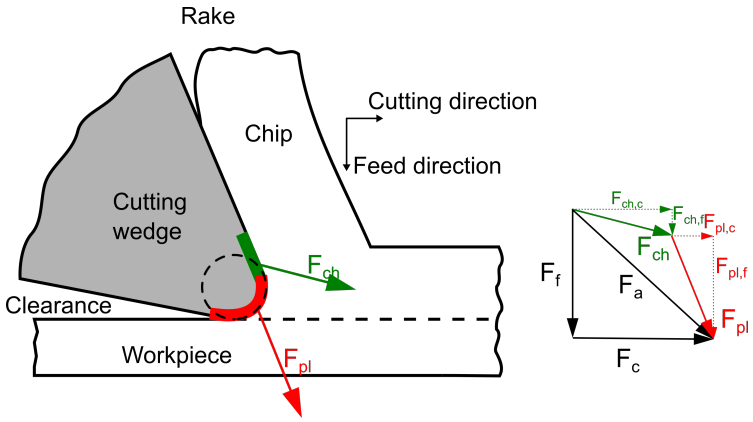

Figure 4.17: The force components acting on the drill, showing the useful cutting force and the wasteful ploughing force.

In drilling these forces manifest as normal forces (thrust) and torque. The normal forces torque exerted on the drill are typically measured directly at the spindle using a dynamometer integrated into the toolholder. The sensing equipment moves with the drill as the machine moves on its axes, providing a consistent point of reference for the measurements for each hole that is drilled.

The requirement of through tool CO_2 coolant flow, meant that this type of direct measurement of the forces at the tool spindle was not viable because it would require a specially manufactured spindle dynamometer with CO_2 through coolant capability. These are not currently available on the market. Additionally, the calibration of spindle dynamometers is conducted at the manufacturer and is not available at temperatures experienced in CO_2 machining (-96°C). These dynamometers utilise sensors made from piezoelectric materials. These materials are pyroelectric, so will respond to temperature changes and provide an electric charge [173]. If housed in the spindle, during cryogenic machining, the large temperature changes of the sensors may provide unreliable readings.

A Kistler flat plate dynamometer type 9129AA was selected to capture cutting forces (thrust and torque) of the cutting tool during machining. The dynamometer uses piezoelectric sensors to capture the force at the workpiece as opposed to the tool itself, and thus further calculations and post processing was required. Each force sensor contains three flat cylinders (washer-like) of quartz material, pre-loaded in the dynamometer by the cover plate. Of these crystals one is sensitive to compressive loads in the z-direction (normal to the cover plate) and the other two are sensitive to shear loads in the x and y directions respectively. Four of these sensors are used in the dynamometer and are placed parallel to each other within the dynamometer, between the cover plate and base plate so that forces exerted on the dynamometer are transferred directly to the forces sensors, located (a,b) from the centre, Figure 4.19.

Depending on the direction of the force exerted, a positive or negative charge and opposite voltage is generated at the charge amplifier. The dynamometer is connected with an eight-channel cable to capture the eight signals supplied to it (Fx_{12}, Fx_{34}, Fy_{14}, Fy_{23}, Fz_1, Fz_2, $Fz_{3,}$, Fz_4), these are then passed through a charge amplifier prior to data capture. The piezocrystals are suited to machining applications as they are capable of capturing high frequency (upto 100kHz) dynamic forces, however due to the natural frequency and associated resonances the flat plate dynamometer used in these trials is limited to 3.5kHz, below the

natural frequency of the dynamometer [174].

A securing plate was manufactured, and clamped in the machine between the two chucks. The flat surface (flatness of 0.1mm) was machined with eight M6 drilled and tapped locating holes for securing the dynamometer. An offset was input into the A-axis of the machine of 90° to locate the flate surface into the vertical plane. The surface of the dynamometer contains tapped holes (see drawing in appendix), for attaching the workpiece and any offsetting plates behind the workpiece. Once the workpiece was attached to the dynamometer using the locating tapped holes, the force dynamometer was zeroed to negate the force applied to the sensors by the addition of the mass on the plate.

4.14.1 Force measurement experimental set-up

The dynamometer was bolted on to a securing plate in the vertical position as shown in Figure 4.18. The dynamometer was mounted to a securing plate clamped between two chucks in a vertial orientation in the machine. The workpiece was subsequently mounted to the face of the dynamometer.

The securing plate thickness was selected based on calculations minimising the deflections of the securing plate. This was to ensure that the dynamometer plate had a secure foundation during the drilling operation. This allowed energy from the drill to directly pass to the dynamometer, and not be absorbed in the deflections of the plate, so that an accurate measurement of the force could be measured.

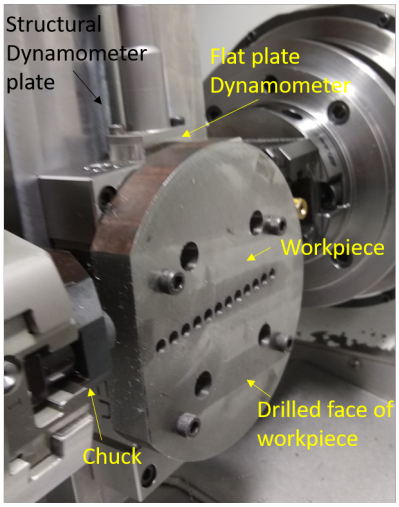

Figure 4.18: Force measurement set-up, showing the vertical orientation of force plate dynamometer, with the securing plate between two chucks with the workpiece bolted on to the face of the dynamometer.

A securing plate thickness of 25mm was chosen and the subsequent deflections of the plate were calculated. A point load was assumed for the calculation where in reality the load would be distributed across the area in contact between the ends of the dynamometer and the workpiece), between two fixed ends (the plate is fixed in the chucks on either side of the plate). This allowed for an over estimation of the deflection for the plate, to allow a safety factor in to the design.

$$\delta_{max} = \frac{FL^3}{192EI} \tag{4.1}$$

Equation 4.1, the maximum deflection of a plate (at the centre) subject to point load, with fixed ends, was used assuming that a point load of the drill acting on the centre of the plate equal to 1kN (value assumed from spindle normal force).The Young's modulus of 180GPa for stainless steel was used, and the length of the plate between the fixed ends was measured as 130mm. To calculate the second moment of area, Equation 4.2 was used.

$$I_x = \frac{bh^3}{12} \tag{4.2}$$

where b is the width and h the thickness of the beam perpendicular to the axis of bending. For these calculations b=200mm and h=25mm. With $I_x = 2.604 \times 10^{-7} m^4$, δ_{max} =244nm.

With such low securing plate deflections, with single point force, it is possible to assume that any movement of the securing plate will have negligible effects on cutting.

4.14.2 Force calculations

The four sensors on the plate, numbered one to four in Figure 4.19 capture four signal outputs in the x and y directions (Fx_{12}, Fx_{34}, Fy_{23}, Fy_{14}). These signals are the sum of the signal from two of the four sensors in either an x or y direction. For example, for signal Fx_{12} the reaction force on sensors one and two in the x direction are summed.

The resultant moment, imparted on the drill when drilling, was calculated using these four signal outputs from the force dynamometer, the location of the drilled hole, and the distances between the four sensors and the centre of the plate. The distances between the centre of the dynamometer and each of the sensors was, in the coordinates of the dynamometer, a = 33mm in the x direction and b=50.5mm in the y direction, Figure 4.19.

The location of each of the drilled holes, with respect to these sensors, was known. The on-machine touch probe was used to set the datum offset for machining at the bottom left hand corner of the dynamometer by probing the left hand edge and bottom edge of the dynamometer. The position of each hole from the centre of the dynamometer is denoted (p_x,p_y).

The moment at the drill can therefore be found by taking anti-clockwise moments at the drill location. With the sum of clockwise moments about the drill equal to zero, Equation 4.3, an expression for the torque containing the force signals and known hole position from the centre can be formed, Equation 4.4.

$$\sum M_{drill\,location} = 0 \tag{4.3}$$

$$-Tz + (b - p_y)Fx_{12} - (b + p_y)Fx_{34} + (a - p_x)Fy_{23} - (a + p_x)Fy_{14} = 0$$

$$-Tz + b(Fx_{12} - Fx_{34}) - p_y(Fx_{12} + Fx_{34}) + a(Fy_{23} - Fy_{14}) - p_x(Fy_{23} + Fy_{14}) = 0$$

$$Tz = b(Fx_{12} - Fx_{34}) - p_y(Fx_{12} + Fx_{34}) + a(Fy_{23} - Fy_{14}) - p_x(Fy_{23} + Fy_{14}) \tag{4.4}$$

The normal force exerted by the drill is the summation of each of the four normal Fz outputs.

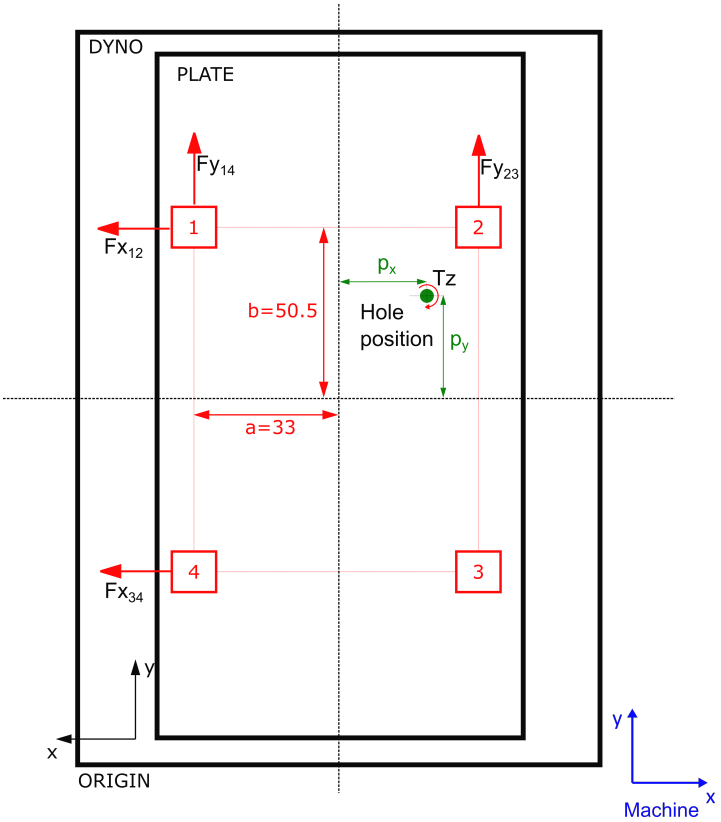

Figure 4.19: Set-up of the work on the force dynamometer, and schematic showing the location of the sensors with respect to the coordinate axes of the dynamometer. The distances from the centre of the dynamometer; a=33mm and b =50.5mm and the positioning of the hole are also shown.

4.14.3 Correcting the cutting force signal and extracting force data

By way of example, Figure 4.20 shows the data captured from the dynamometer for run number six. It shows the eight channels that are collected from, and labelled according to Figure 4.19, where Fz denotes the forces normal to the plate and as a result the components of the thrust force. Fx and Fy components are those associated in the same plane as the workpiece and represent the components captured from the torsional forces exerted by the tool on the workpiece.

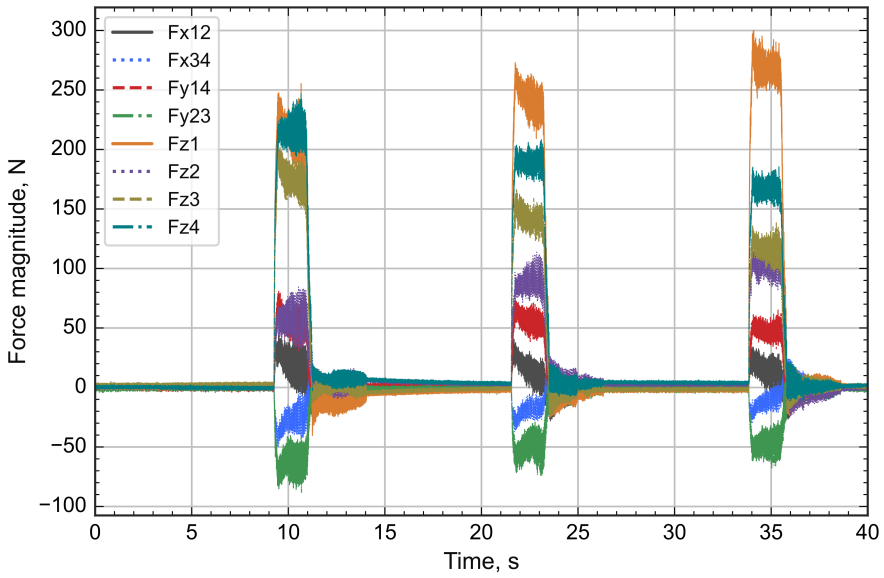

Figure 4.20: Raw data captured from the dynamometer, all six components of the data, for run number 6.

It is noted that during the drilling the sensor measurements exhibit a degree of drift, seen by a lower reading at the end of the hole. This drift is shown in Figure 4.21 for the Fy14 signal captured for the second hole in run six. Illustrated is the reduction in the signal, highlighted in red. This drift was assumed to be linear and due to the thermal instability of the sensors and the knowledge that they typically drift in a linear fashion over a short period of time. It is such a well known phenomena that they exist, inside the packaged software with the dynamometer (Dynoware) and ability to to compensate for this thermal drift. Within this software the drift compensation is linear in nature. This is likely to be caused by the cold nature of the CO_2 causing slight interference with the signal. Additionally, upon exiting the hole, there is a drift rebound region, where the signal experiences a rebound.

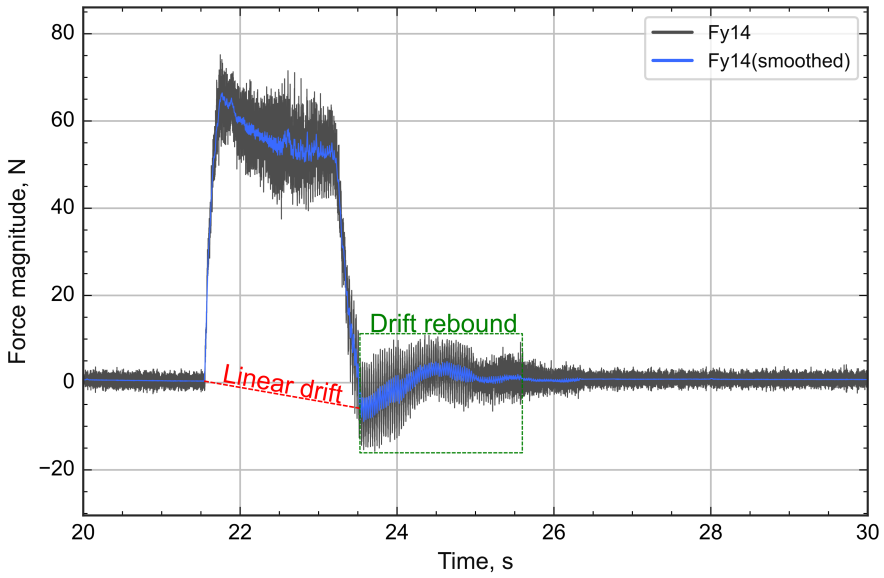

Figure 4.21: Smoothing the signal output

Smoothing of the signals was completed using a Savitzky-Golay filter, with a window size of 201 and polynomial of 2. This filter was used to retain the tendency of the data, whilst at the same time minimising the high frequency vibration caused by the segmentation of the chip. It simply smooths the data using least squares approximations of the data. After smoothing and correcting for linear drift, the signal as shown in Figure 4.22, can be used for further processing of the data where the sum of the Fz data provides the total normal force (thrust) on the drill, and force signals in the x and y directions (Fx12, Fx34, Fy14, Fy23) are further processed to calculate the moment (torque) on the drill (see Section 4.14.2). This process was completed for each of the 8 signals from the dynamometer, for each of the three holes completed for each of the 44 runs.

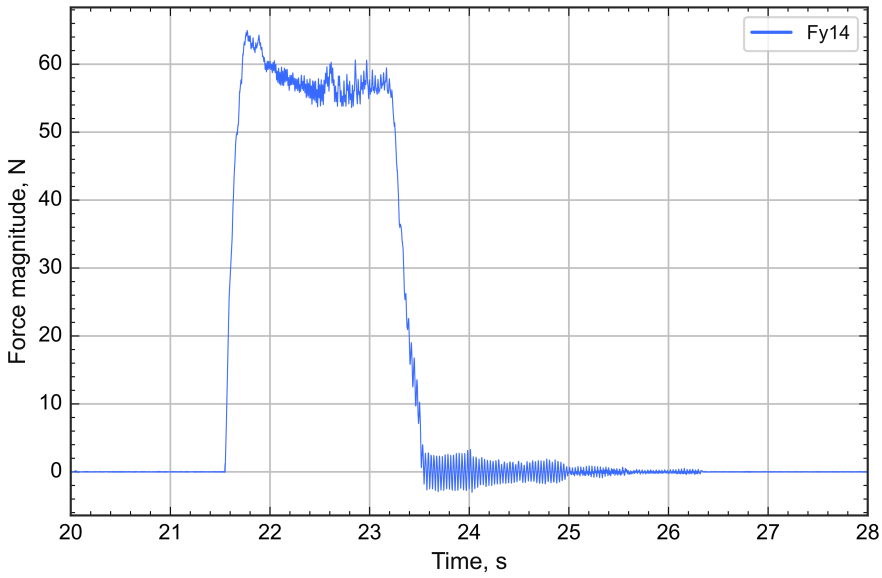

Figure 4.22: Zeroing the signal output from the force dynamometer

4.14.4 Stages of the cutting cycle

The force signals captured for each of the holes show the various stages of the drilling cycle. Figure 4.23. The example show is for hole 2 and run 6, where the hole drilled through 10mm plate at 0.16mm/rev and 40m/min. This corresponds to a feed rate of 5.66mm/s The hole is drilled through the workpiece to z=13mm, 3mm past the back of the workpiece.

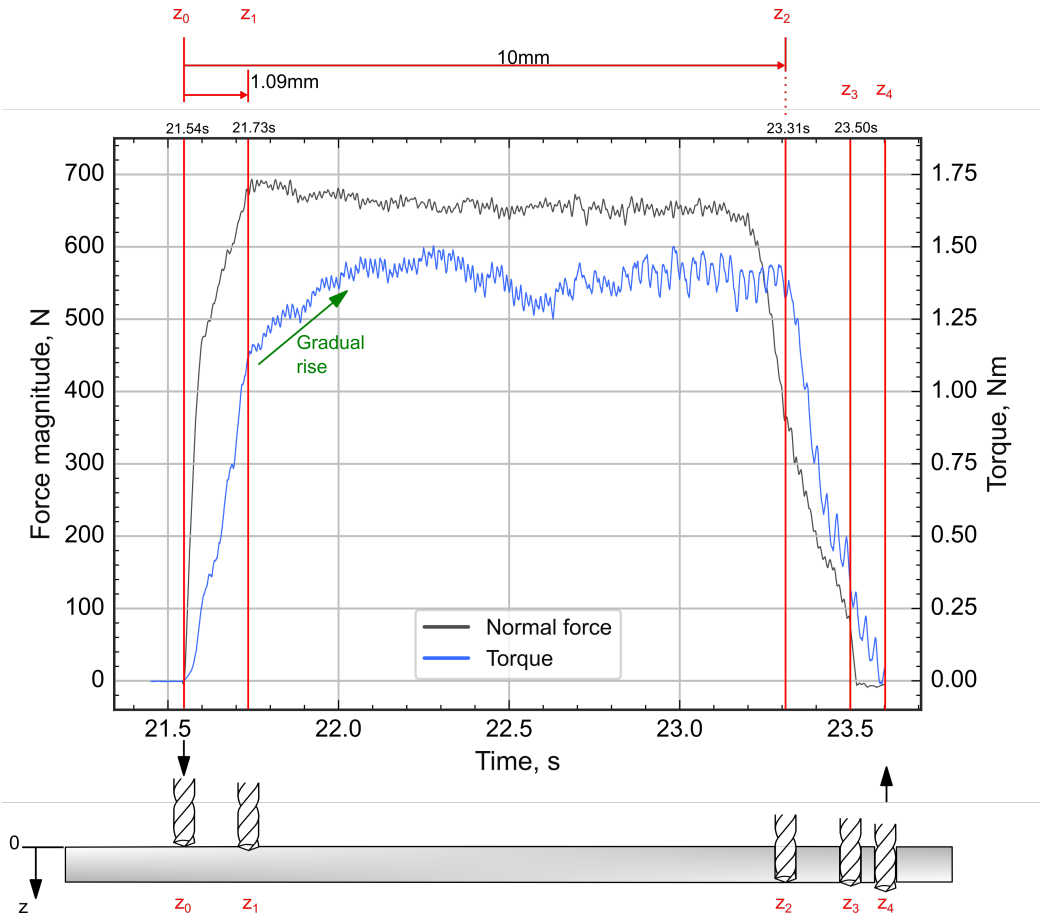

Figure 4.23: The normal force and torque, captured for run 6, hole 2, showing the stages of the force signal that represent each of the stages of the drilled hole (inspired by work conducted by Merzouki et al. [137]).

4.14.4.1 Initial contact to fully engaged (z_0 to z_1)

The force signal begins at z_0 where the drill point and chisel make initial contact with the surface of the workpiece. The force signal increases, as the cutting edges further engage with the workpiece and a larger area of the cutting edges come in to contact with the workpiece. For the drills used, the distance that the drill has to travel in z, before the cutting lips are fully engaged with the workpiece, is found using the drill radius, r_{dr} and the half point angle, $\frac{\phi_p}{2}$, Figure 4.24.

$$z_{tip} = r_{dr} \tan\left(90 - \frac{\phi_p}{2}\right) \tag{4.5}$$
$$z_{tip} = 3\tan(20) = 1.09mm$$

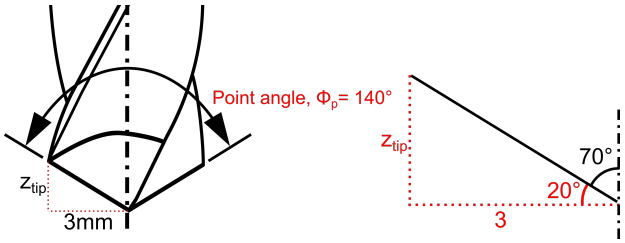

Figure 4.24: Calculating the height of the drill point, x for a drill point angle, 140° and drill diameter 6mm.

Therefore with a feed rate of 5.66mm/s the time taken,for the drill to travel the 1.09mm to fully engage the workpiece is $t = \frac{1.09}{5.66} = 0.193s$, 21.73s at z_1 from 21.54s at z_0.

4.14.4.2 Fully engaged to beginning of exit (z_1 to z_2)

The drill continues to move in the z direction, from $z_1$to z_2. During this stage the majority of the work in producing the hole occurs. The normal force, the force opposing the axial direction of the drill, remains relatively stable during this stage, as the cutting lips are fully engaged with the workpiece. A slight reduction in the normal force may be seen, as a result of thermal softening of the workpiece during the cut. The torque sees a gradual rise initially as a greater area of the margin comes in to contact with the wall of the drilled hole, increasing the overall contact area of the drill with the hole. This does not continue rising due to the back taper of the drill. The variations of the force readings during this stage can be ascribed to a the formation and packing of the chips in the drill flute, the cyclical nature of the chip formation process in titanium machining, and the material variations in drilling the hole.

For no peck drilling, this section of the curve was extracted and the mode value of this data was used as the force measurement for that particular hole.

4.14.4.3 Drill tip at exit to whole of drill tip exited (z_2 to z_3)

At z=10mm, z_2 the drill tip has met the rear surface of the material being drilled. The normal force shows a gradual reduction prior to reaching this stage due to the plastic deformation of the thinning material at the hole exit, forming the exit cap and the exit burr of the drilled hole. The torque on the drill remains at stable levels, showing only the oscillations caused by the chips evacuating, prior to this as the drill is still engaged with material. From z_2 to z_3 the cutting edges gradually disengage with the material completely, evidenced by further reductions in the normal force to zero at z_3. The torque does not reach zero because the margin is still in contact with the walls of the hole and a frictional force is acting on the drill margin.

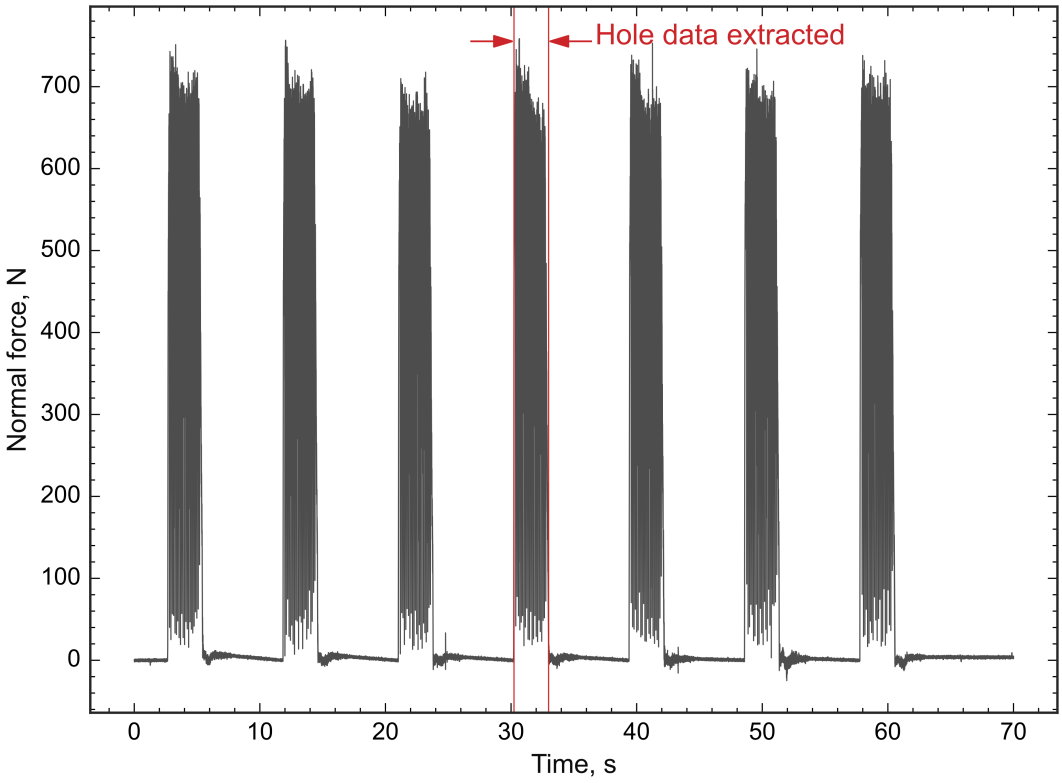

Figure 4.25: a) Detection of the start and finish of hole 32 from the normal force data for hole 29 to 35 for MQL test 3.

4.14.4.4 Drill through the hole exit, prior to reversing through the hole (z_3 to z_4)

From $z_3$to z_4 the drill continues to drill through the hole, and the contact with the margin and the wall reduces. The drill then returns back through the hole to drill the next hole.

4.14.5 Process for extracting the pecking data from the force data

Due to the intermittent engagement and disengagement of the drill with the workpiece the force signal was found to oscillate. Including this disengagement in the force measurement would result in an underestimate of the force. Therefore the data containing the force signal when the drill is engaged needed to be extracted. This section explains the process that was used to capture the force data that utilised pecking during the trials conducted in Chapters 8 and 9. Representative data to show this process is taken from MQL test 3 for the seven holes between 29 and 35.

After the data was zeroed using the process described in Section 4.14.3 each hole was identified using the change point detection algorithm from the ruptures package in Python. Figure 4.25 shows the time points selected by the algorithm to extract data for hole 32.

The data extracted for each hole is then further subdivided. This was done by detecting the minimum values of the force signal, Figure 4.26 and then extracting the data from these positions to obtain data for

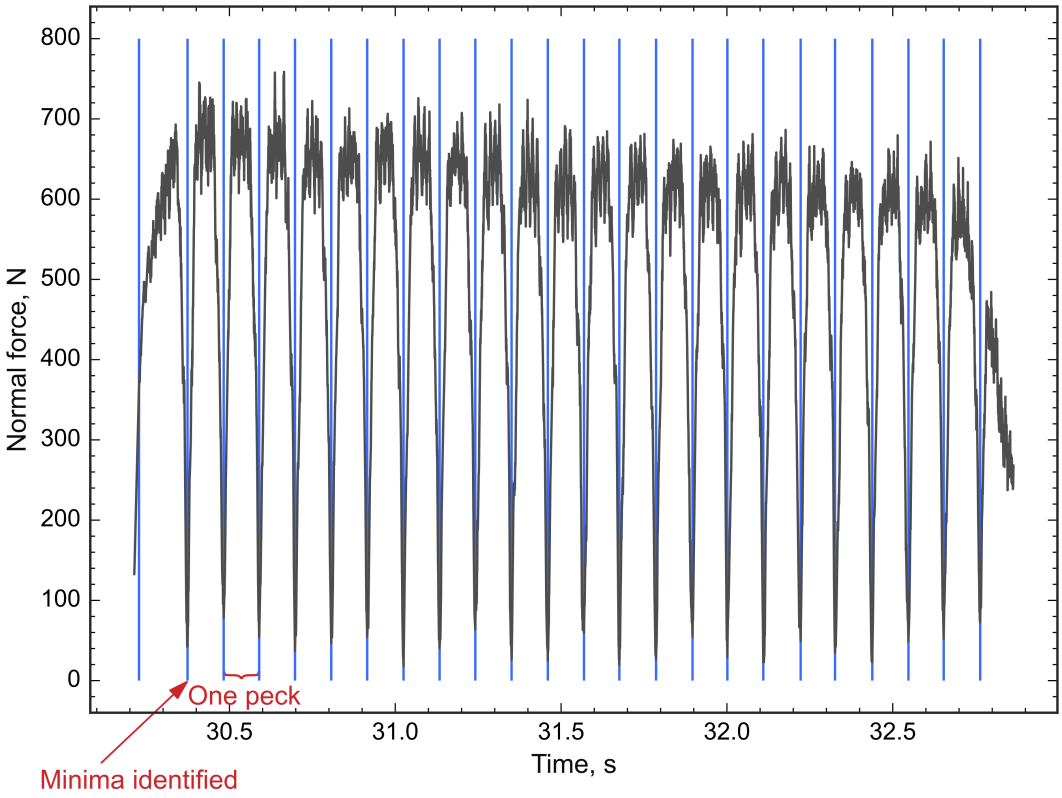

Figure 4.26: Further sub-division of the force signal to obtain data for each individual peck.

each individual peck that the drill completed.

Data obtained from the first peck was discarded as the tool was not fully engaged for this peck, and the central 50% of the data for each subsequent peck was then extracted and the mean value obtained, Figure 4.27. From these force values for each peck, an overall mean was then calculated to obtain a data-point for that hole.

4.14.5.1 Using the torque wrench to ensure that the calculations are correct.

To test the calculations in capturing and calculating the resultant torque 4.14.2, the dynamometer was bolted to the backing plate, which was secured in a vice and bolts loosely screwed in to the tapped holes of the surface of the dynamometer. A torque wrench was then used to tighten the bolts to 3Nm. Figure 4.28 shows the set up used.

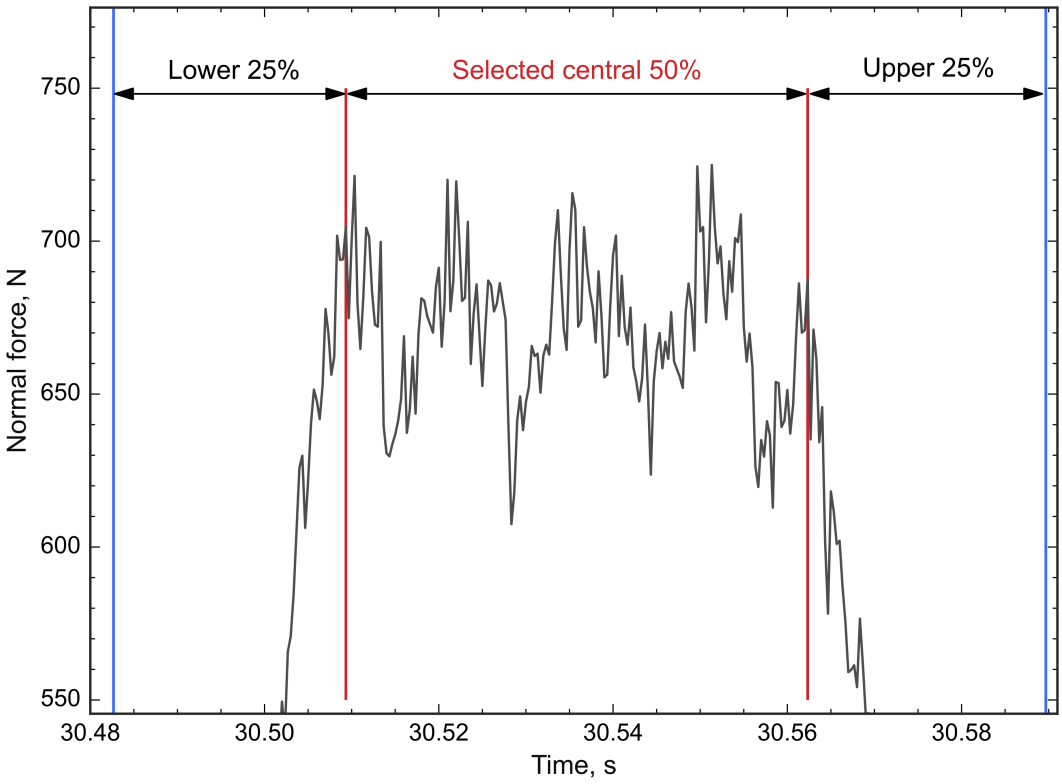

Figure 4.27: Data obtained for peck 3 for hole 32 in MQL test three, showing the central 50% of data that was selected.

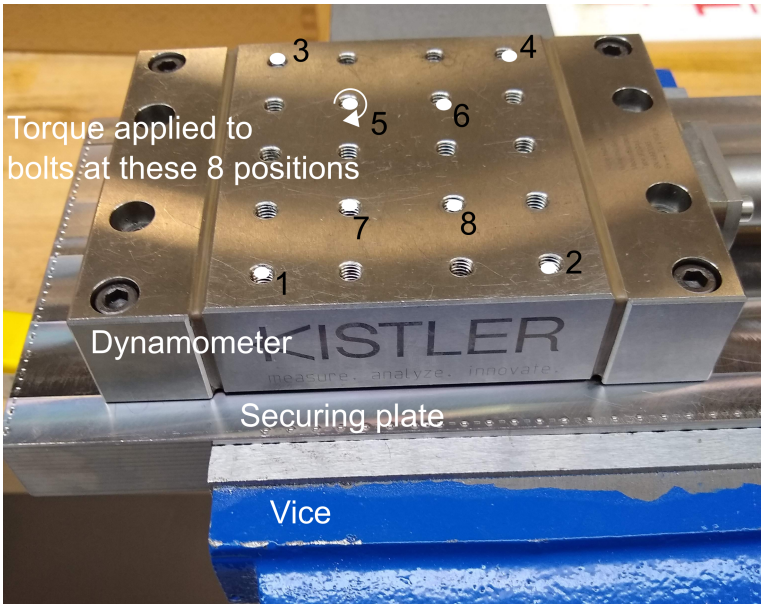

Figure 4.28: Dynamometer bolted to securing plate held in vice, bolts were screwed in to plate at the eight positions shown to test the calculation of torque and repeatability of dynamometer.

Several repeats of imparting the prescribed torque on to the dynamometer at several locations around the dynamometer were carried out. Figure 4.29 shows the captured output from the dynamometer, with 6 repeated measurements at position six on the dynamometer (Figure 4.28). Shown are the four signals used in calculating the torque exerted on the dynamometer from the torque wrench.

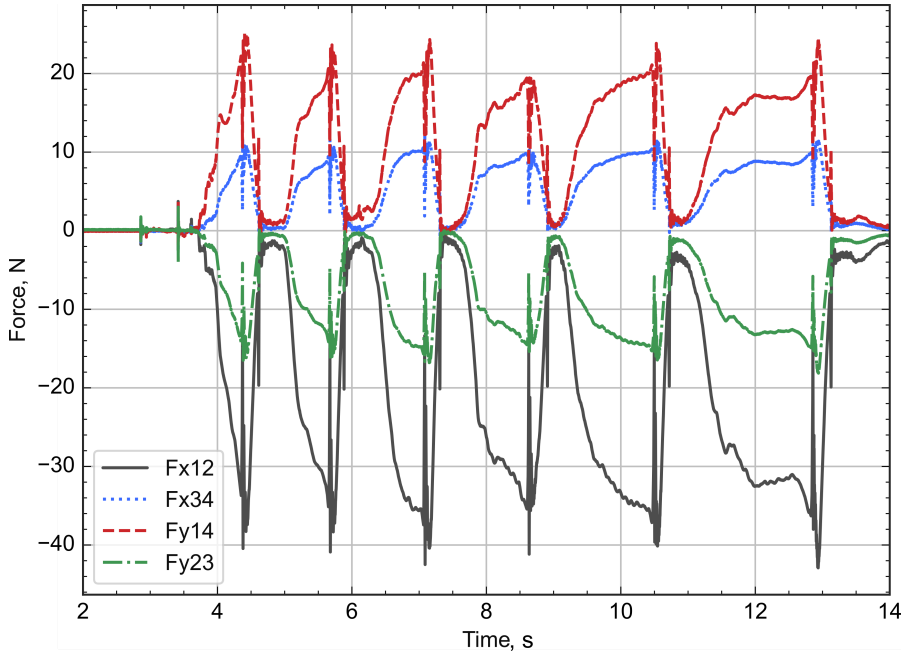

Figure 4.29: Output from each signal.

The signals were then processed using the method described in Section 4.14.2 to produce the measured

torque readings Figure 4.30.

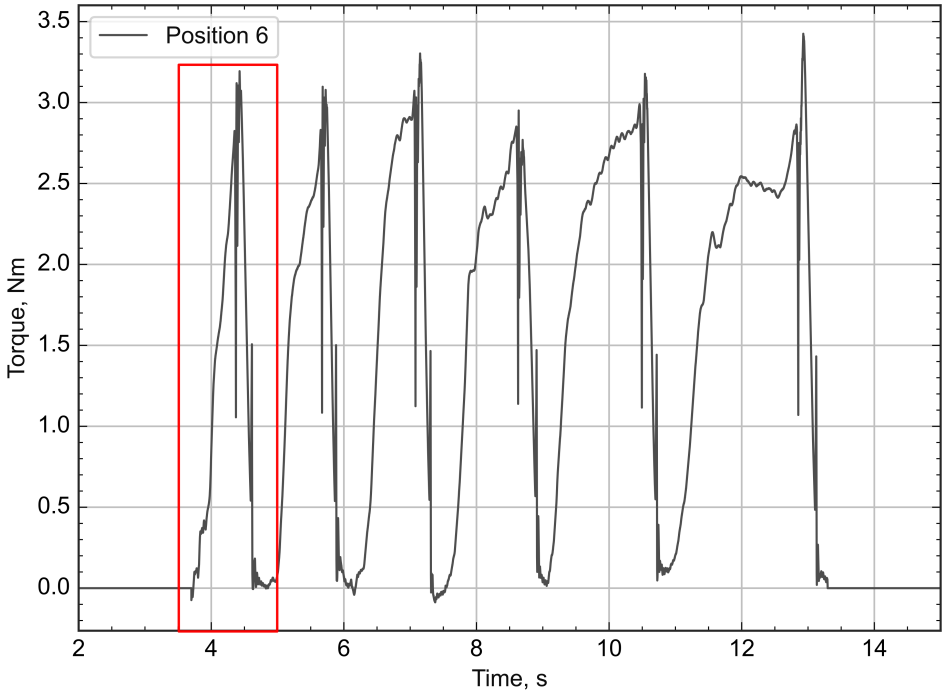

Figure 4.30: Overall output once the moment arms are accounted for.

Focusing on the first measurement (Figure 4.31) it is possible to see how the torque exerted on the dynamometer increases as the torque wrench is rotated in bolt head. Once the torque reaches the level set on the torque wrench, in this case 3Nm, it is possible to see a quick drop in the torque applied to the bolt. The subsequent increase in torque is due to the follow through of the torque wrench as it reengages with the side of the bar. The point at which the torque wrench disengages is a consistent point for each of the measurements, and therefore was used as the value (2.82Nm) of torque for each measurement. This value is lower than the 3Nm set because it was manually set using an analogue scale. Additionally, it is noted that the accuracy of the torque wrench is low, however it acts to verify the calculation and repeatability of the torque measurement across the range of the dynamometer.

Capturing these points across all measurements and locations around the dynamometer (Figure 4.32) it is shown that the dynamometer and method of calculating the torque from the flat plate dynamometer is a valid method. The spread of the data, it is likely due to manual and inherently inconsistent application of torque to the dynamometer with the torque wrench.

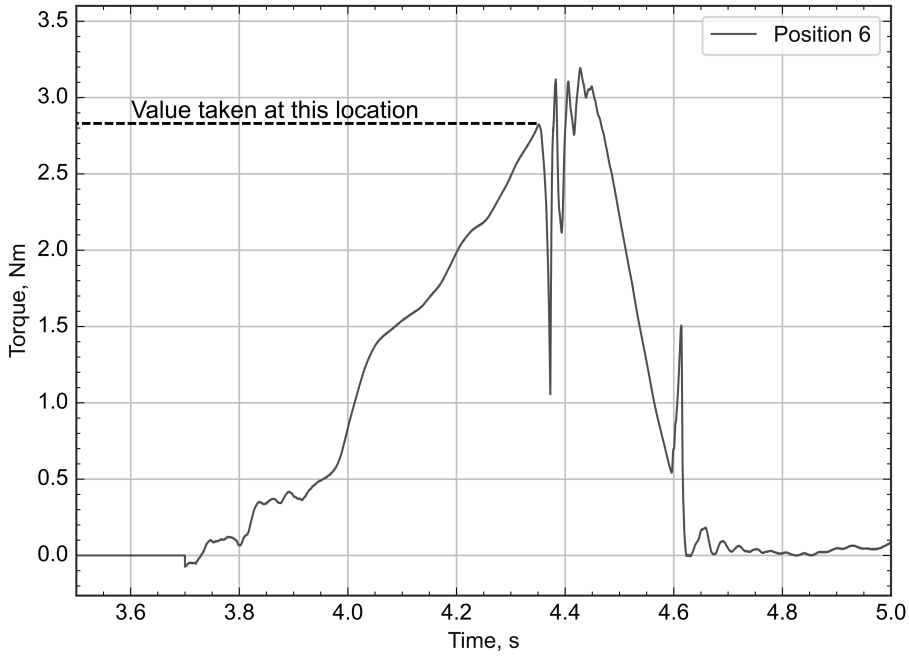

Figure 4.31: Location of where the torque measurement is taken from, just as the torque wrench snaps resulting in a drop in torque.

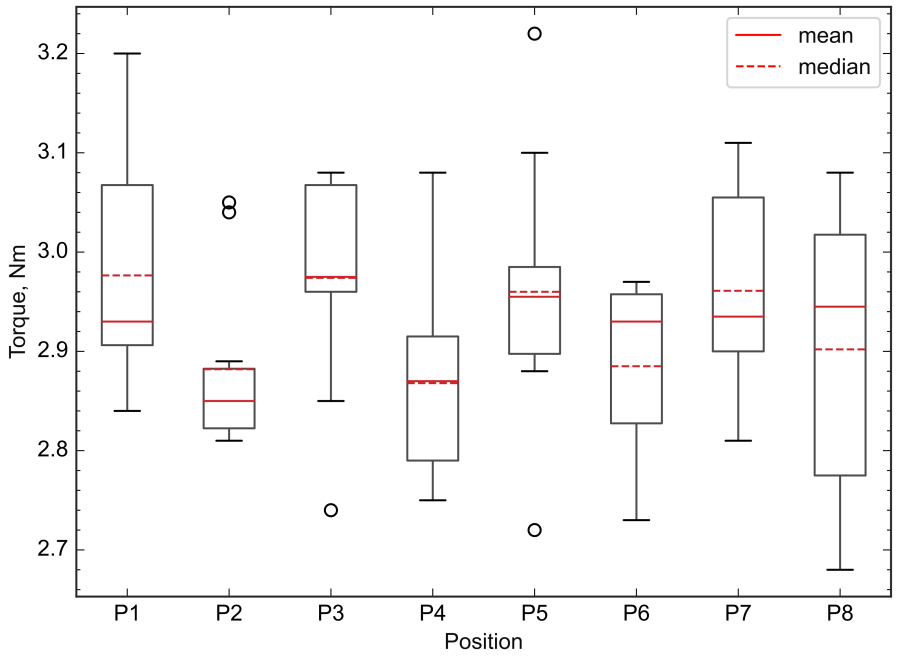

Figure 4.32: Values captured for each of the eight positions in the torque calculation used to check the data calculation methodology.

4.15 Temperature measurement

This section outlines the set-up used for conducting experiments where temperature was primarily captured. Temperature measurements were taken with a Micro-Epsilon TIM 160 thermal imaging camera (see Appendix 2 for full datasheet). The camera was placed, using a magnetic stand, perpendicularly behind the workpiece to measure the cutting temperature as the drill exited the hole, Figure 4.33. The lens within the camera focused the infrared radiation emitted by the plate on to a detector element to generate an electrical signal (voltage) proportional to the radiation emitted from the plate. This was then amplified, processed and interpreted with software provided with the thermal camera, TIM connect.

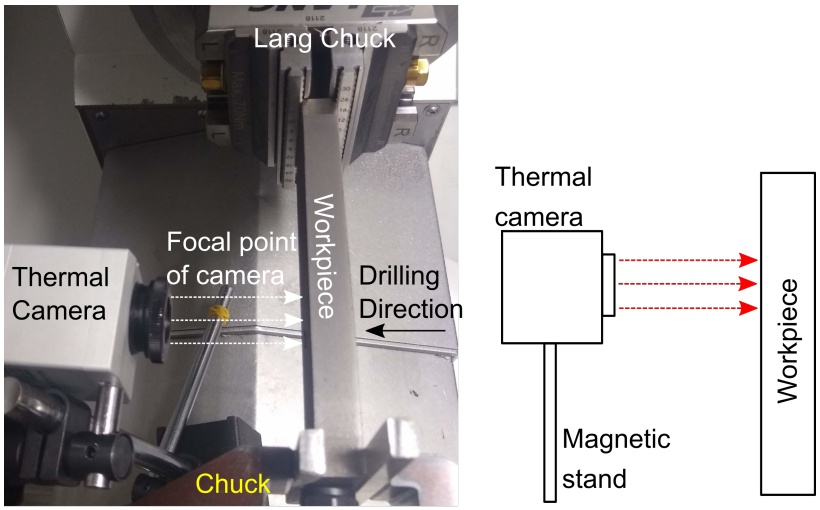

Figure 4.33: a) Birds-eye view of temperature measurement set-up with infra-red camera placed perpendicular to workpiece and focused on the exit of the hole. b) side-view schematic of the infra-red camera placed behind the workpiece.

Calibration of the camera was carried out using a small sample of the workpiece material. The same black, matt paint, as described in Section 4.12.1, was applied to a small sample of the workpiece material. This was to minimise reflections and transmissivity, and maximise emmisivity from the workpiece. Therefore, the surface being measured is as close to a blackbody as possible so that as much of the radiation coming from the surface is due to emission alone, as a black body does not reflect any radiation.

A thermocouple was cemented on to the sample which was then heated up to a temperature of 500°C in a furnace. The emmisivity value of the camera was adjusted so that the temperature indicated by the thermal camera matched that of the thermocouple reading. With the camera set at the temperature measuring range of -25 to 100°C, 0 to 250°C or 150-900°C depending on the temperature being measured. The latest calibration file for the camera, as supplied from the manufacturer, was loaded in to the software prior to measurements.

Thermal images were captured as the drill exited the hole, and example images are shown in Figure 4.34. The temperature reported was the maximum within the area specified by the drawn area within the square.

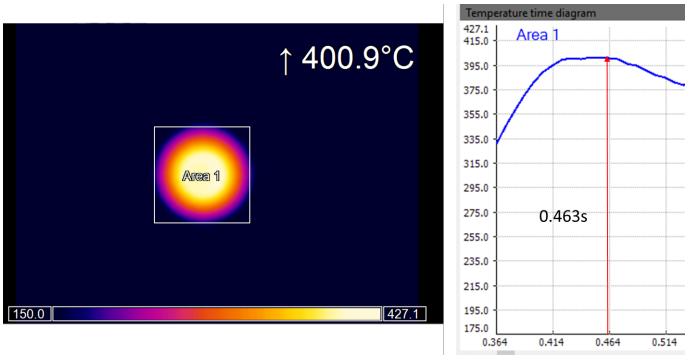

Figure 4.34: Image of thermal camera data, with corresponding graphical output of the maximum temperature generated.

4.16 Hole quality measurement

4.16.1 Geometry

Hole geometry in drilling is a key parameter of drilling performance and is made up of two parameters the hole diameter and hole shape, typically in terms of circularity and cylindricity. A coordinate measurement machine (CMM) was used to measure these features. Prior to putting the workpiece on to the CMM the workpiece was prepared by removing exit caps (examples of these are shown in that remained attached to the exit side of the hole and then, using a soft pipe cleaner so as not to scratch the holes, each hole was brushed internally to remove any debris remaining inside the drilled holes. This ensured the CMM probe made contact with the inside of the hole unobstructed from the presence of any removed material.

The plates were placed on the flat granite surface of the CMM, exit burr facing upwards, to maintain perpendicularity of the holes with the bed and prevent the burrs causing the plate to be misaligned. Entry burrs were checked for and these were deemed uniform and small enough (<0.1mm) to misalign the workpiece. The plates were placed against a horizontal datum on the bed of the CMM and then clamped to the bed as shown in Figure 4.35. The top surface of the plate is then probed at the four corners of the plate to provide the machine with a reference plate.

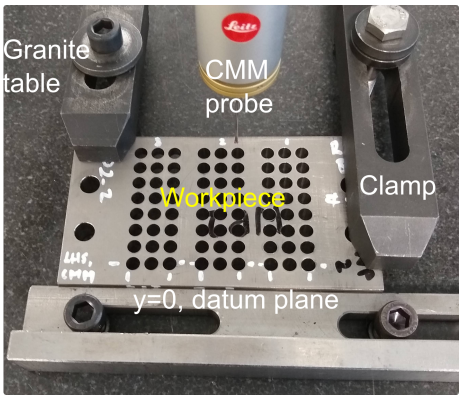

Figure 4.35: Clamping of the workpiece on to the CMM.

The probe used during measurements was 2mm in diameter and a hard ruby tip to prevent deflection during probing operations. For each of the drilled holes three measurements were taken (as shown in Figure 4.36) at the following z positions according to the reference plane datum acquired by the initial probing of the machine:

1. 2mm from the top plane (equivalent to 2mm from the burr)
2. 2mm from the bottom of the plate (equivalent to 2mm from the top surface)
3. In the centre of the plate (using the nominal value of the workpiece thickness).

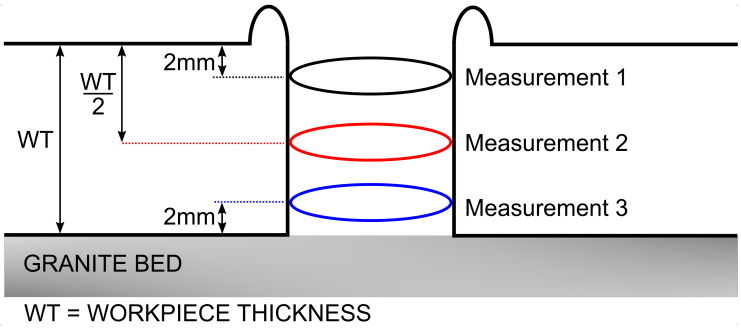

Figure 4.36: The three measurements made by CMM for each drilled hole

For each of the three measurements the ruby tipped CMM scanning probe circumscribes the internal diameter of the hole and collects 1000 datapoints. The data collected provides XYZ coordinate data for the points gathered (in this instance Z is constant). Using this cloud of XY data points the dimensions of the hole are measured. In particular:

1. The diameter at each of the three z positions as least squared and max inscribed circle
2. The cylindricity of the hole least squared and max inscribed circle
3. The circularity at each of the three z positions was also captured.

4.16.1.1 Diameter and Cylindricity

Both diameter and cylindricity are quoted in least squares fitment and maximum inscribed circle. The maximum inscribed measurement represents the largest circle that can be fitted inside the data, and is quoted as the diameter of this circle. For cylindricity a cylinder is constructed out of the three measurements that are made, and again the max inscribed cylinder is found, representing the largest stud that can be inserted into the hole. For the least squares calculation, a circle is fitted to the gathered data to minimise the sum of the squares of the residuals (difference between fitted line and data) and again is applied to the circle and then to the cylinder of the three circles. These are illustrated in Figure 4.37.

4.16.1.2 Circularity

Circularity provides an indication of the form of the cross sections perpendicular to the hole, and was calculated from the datapoints collected by the CMM. The circularity measurement provides the distance between the two circles that are fitted to the inner and outer most datapoints of the capture data from the CMM probe (Figure 4.37).

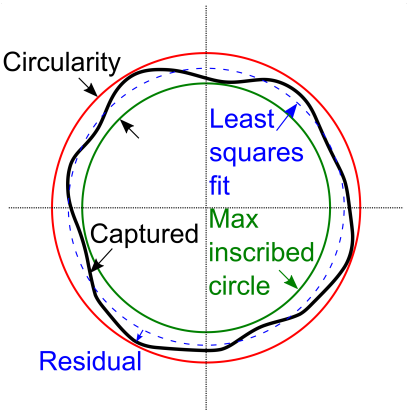

Figure 4.37: Schematic showing circularity, max inscribed and least squares calculated from the measured data.

4.16.2 Hole exit burr height measurement

The exit burr, formed as a result of material plastically deforming as the drill exits the hole, can cause assembly issues due to poor fitment. Figure 4.38 shows an schematic of this burr. Measurement of this burr was done using a specially manufactured height gauge which measured the relative distance from the datum back surface of the plate and the maximum height of the burr itself. The height gauge consists of four flat anvils placed around the hole providing a stable datum, whilst a central anvil is placed on the burr and a measurement is taken, this set up is shown in Figure 4.39. Prior to the measurements being taken the height burr is pressed on to a flat granite surface to zero the gauge. Burr height measurements were taken for each of the holes drilled, with three measurements taken and then an arithmetic mean calculated for the burr height.

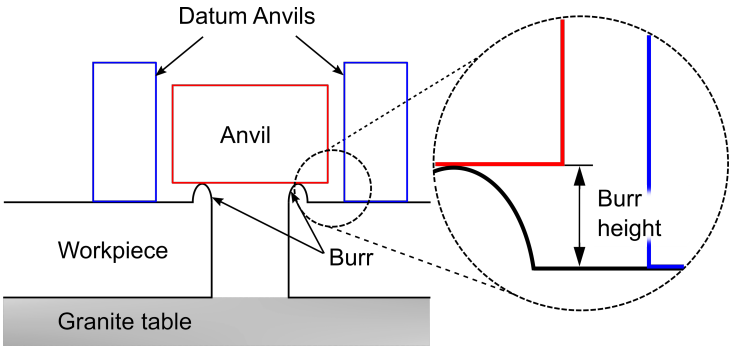

Figure 4.38: Schematic of the burr height measurements

As black paint was painted onto the surface of the plate during the temperature measurement trials, this effectively lifted the height of the datum surface, a dial test indicator was used to measure the thickness of the paint. The dial test indicator was traversed across an unpainted surface on the plate and then over the painted surface, and then the difference between the two provided an estimated thickness of the paint of 0.02±0.0025 mm (95% confidence interval).

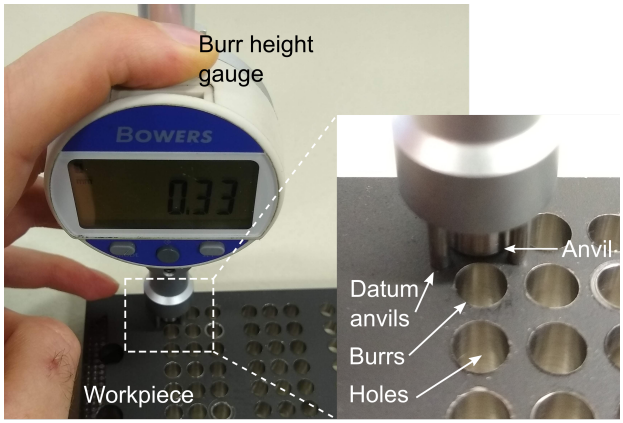

Figure 4.39: Burr height measurement

4.16.3 Hole surface roughness measurement

Linear surface roughness measurements were made on the internal surface of the cleaned drilled holes. This was done using a two dimensional contact linear profilometer. A fine tipped diamond stylus As the stylus traverses the evaluation length over the measured surface, the stylus is deflected by the rough surface in the z direction. The magnitude of the displacement of the stylus is captured by sensors within the housing of the linear profilometer, to plot the captured surface roughness (Figure 4.40).

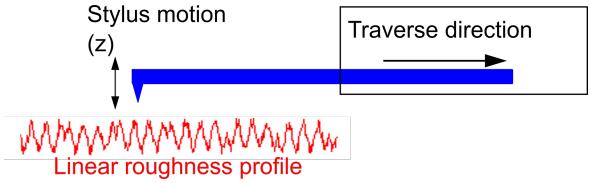

Figure 4.40: Illustration of the motion of the stylus as it captures the roughness of the measured surface.

From this gathered profile, the profilometer calculated the roughness parameters of the surface: the R_a, R_z, and R_{max}. Figure 4.41 illustrates these parameters. R_a is the arithmetic mean deviation of the roughness profile from the centre line of the captured data. $R_z$is the mean of each of the R_{zn} values where n is the number of samples taken across the evaluation length, typically five. Each of the R_{zn} values is the difference between the highest peak and the lowest trough. R_{max} is the distance from the highest peak to the lowest trough in the evaluation length.

Five roughness measurements were made for each hole and then averaged using an arithmetic mean. A reference standard of roughness R_a = 3µm was used to calibrate the profilometer prior to taking measurements.

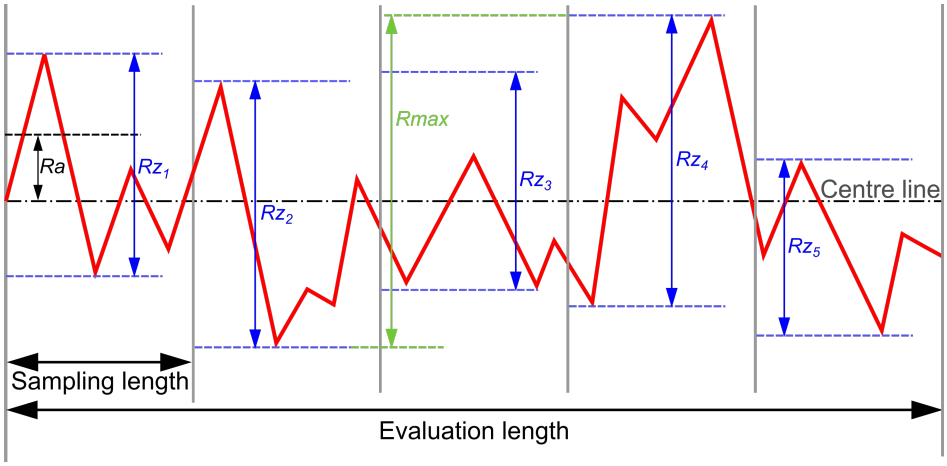

Figure 4.41: Illustration of the surface roughness parameters that were captured of the internal surface of the hole.

Care was taken to ensure the profilometer tracked axially along the hole wall during measurement to provide consistent measurements perpendicular to the roughness profile being measured. Probe measurements with increasing or decreasing centre line were discarded and the workpiece realigned, as this indicated the measurement was either going up the side of the hole (increasing case) or going down the side of the hole (decreasing case). The evaluation length and cut off length for each measurement remained the same for each run at 1.25mm and 0.25mm respectively according to ISO4288 [175]. The calibration of the profilometer and hole surface roughness measurement are shown in Figures 4.42a and 4.42b respectively.

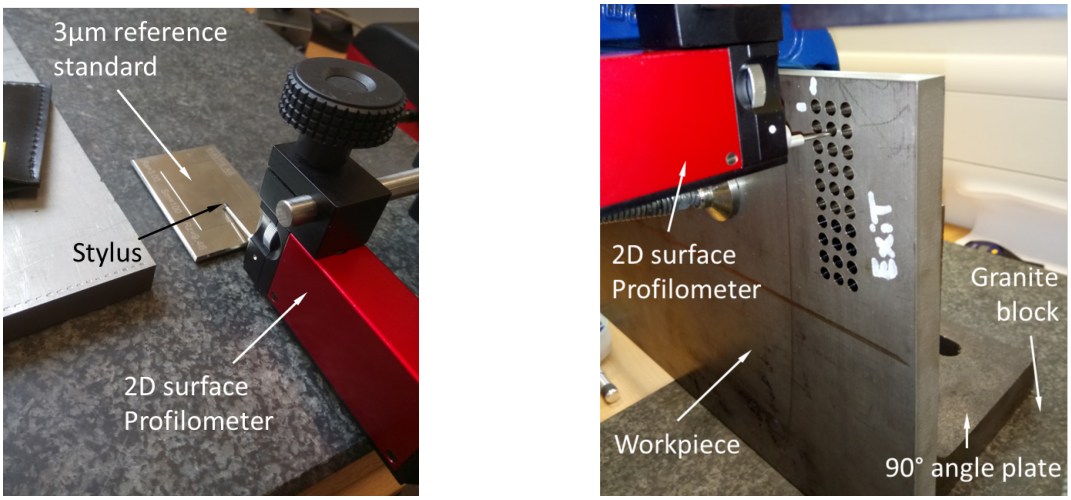

a b

Figure 4.42: a) Calibration of the profilometer using a reference roughness surface of *Ra*= 3µm.b) Making roughness measurements of the drilled holes.

5 Initial trials to assess cryogenic drilling functionality

Cryogenic machining with liquid carbon dioxide (LCO_2) has not been previously conducted with Sandvik Coromant R846 tooling. To ascertain the behaviour of the CoroDrill R846 (as described in Section 4.4) when drilling Ti6Al4V, trials were conducted on typical industrial machinery to represent, as close as possible, an industrial drilling process.

This chapter details the initial trials that were conducted to investigate the tool behaviour and identify a machine operating window for use in further investigative trials. The objectives of the chapter were to:

1. Test the operation of the machine when using the LCO_2 fluid supply mechanism.
2. Measure and quantify the LCO_2 delivery through the machine tool, and qualify with manufacturer stated values with on machine settings.
3. Study the effects of using LCO_2 with conventional cutting data.
4. Identify an operating window for operating with LCO_2.

5.1 Testing the LCO_2 cryogenic mass flow rate through the machine tool

LCO_2 is stored in pressurised cylinders (typically 58 bar at 20°C) adjacent to the machine tool (Starrag LX051). Dip tubes contained within the cylinders extract the liquid from the bottom of the cylinders in to supply pipes, 1mm internal diameter. The supply pipes transfer the LCO_2 through the machine tool, via a mass flow control valve, controlled with a coriolis flow meter. The LCO_2 is supplied in liquid form through the spindle and to the back of the toolholder (Figure 4.4). The LCO_2 travels through the toolholder and in to a small cavity behind the tool and then in to the two coolant holes of the cutting tool, pressure losses from the expansion of the flow in to the two coolant channels is assumed to be negligible.

The LCO_2 mass flow rate supplied is controlled via the machine controller. The Rother AerosolMaster 4000 cryolub contained on this particular machine can be used to control pressurised air flow, MQL, and LCO_2 flow. The manual accompanying the machine states that the mass flow rate of the LCO_2 can be set between 60% and 100% of the maximum mass flow rate of 10kg/hr (e.g. between 6kg/hr and 10kg/hr).

Tests clarifying these mass flow rates were conducted at 60, 80 and 100% on machine settings. Three measurements were conducted for each of the mass flow rate settings. To conduct a measurement, the mass of the cylinders, which sit on weighing scales, was allowed to drop by the smallest unit. The timer was then started. The timer was stopped once a total of 0.5kg of carbon dioxide was consumed. The results from these tests are shown in Figure 5.1. The three settings tested are in agreement with the

setting on the machine, providing 5.9, 8.1 and 10.3 kg/hr mass flow rate measurements for the 60, 80 and 100% settings respectively.

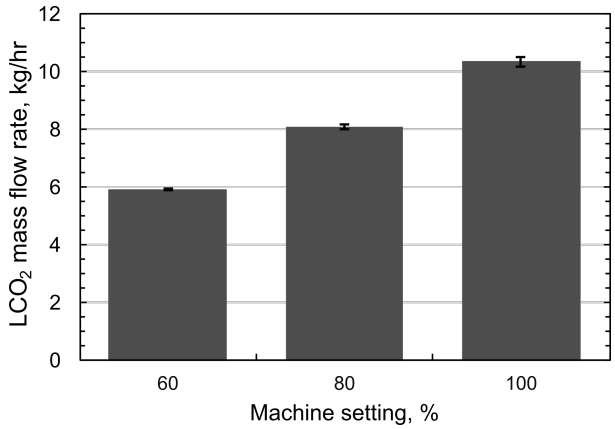

Figure 5.1: Mass flow measurements of the LCO_2 expended out of the tool to clarify the settings of the controller on the machine.

5.2 First drilling trials with the CoroDrill R846 heat resistant super alloy (HRSA) optimised drill

The first exploratory trial using LCO_2 with the R846 drill, optimised for through tool emulsion MWFs, was conducted at nine speed and feed combinations across the full range of the Sandvik Coromant recommended cutting data obtained from the CoroPlus ToolGuide [176], see Table 5.1.

Cutting speed, m/min	Cutting feed, mm/rev
30	0.06
40	0.08
50	0.1

Table 5.1: Cutting Data used in the first exploratory trial with the optimised HRSA drill geometry R846 and liquid carbon dioxide (LCO_2)

Minimisation of experiment bias was done through the randomisation of the speed and feed run order, presented in Table 5.2. A single tool was used for the duration of the experiment as long tool life (in the order of hundreds of holes) was expected of the R846 when drilling Ti6Al4V. The runout of the tool (maximum radial deviation when the tool is rotated) in the toolholder was measured at 10µm. Each run consisted of nine holes. The test set-up as described in Section 4.33 without the thermal camera, was employed. The mass flow rate of the coolant was set to 10kg/hr throughout as this was recommended by the machine tool manufacturer.

Run Order	Speed, m/min	Rotation speed, rpm	Feed, mm/rev	Feed (penetration) rate, mm/min
1	50	2653	0.1	265
2	30	1592	0.06	95
3	40	2122	0.08	170
4	50	2653	0.06	159
5	50	2653	0.08	212
6	30	1592	0.08	127
7	40	2122	0.06	127
8	40	2122	0.1	212
9	30	1592	0.1	159

Table 5.2: The selected randomised run order for the initial trials utilising LCO_2 and R846 tools.

5.2.1 Chip formation

For each run, chips were collected from those that landed in the cardboard collector. A random sample of the chips captured for each of the runs are presented in Figure 5.2. These images provide a qualitative assessment of the chip form and the likelihood of chip jamming, and chips nesting around the tool during machining, leading to drill breakages.

The chip formation, observed across the cutting speed and feed range selected, was long with inadequate shearing and segmentation. The chips shown for these cutting data are likely to nest and get trapped around the drill leading to tool failure, when compared to the ideal chip form (small and segmented).

Improvements in the chip formation are observed with increasing feed, illustrated with an increased frequency of chips that are shorter in length. The chips also appear to be more open when compared to chips in the low feed range with chips displaying more packing and concertina-like characteristics which are prone to tangling dangerously nesting around the tooling.

The improvement in the chips formation through a reduction in the chip size was quantified by measuring the mass of the chip. Longer, less desirable chips would have a larger mass than smaller, more desirable chips. Measurements of the chip mass were made using a high precision scale with resolution of 0.1mg. It was assumed that any contamination or oil contained on the chip would be negligible to the chip mass, therefore cleaning of the chips was not required.

The results from these chip mass measurements are presented in in Figure 5.3a. The data is presented as box-plots to illustrate the distribution of the chip mass within the sample. The box represents the inter-quartile range, with the whiskers representing 95% of the data. The line illustrates the median, while the cross and data labels provide mean values for the sample.

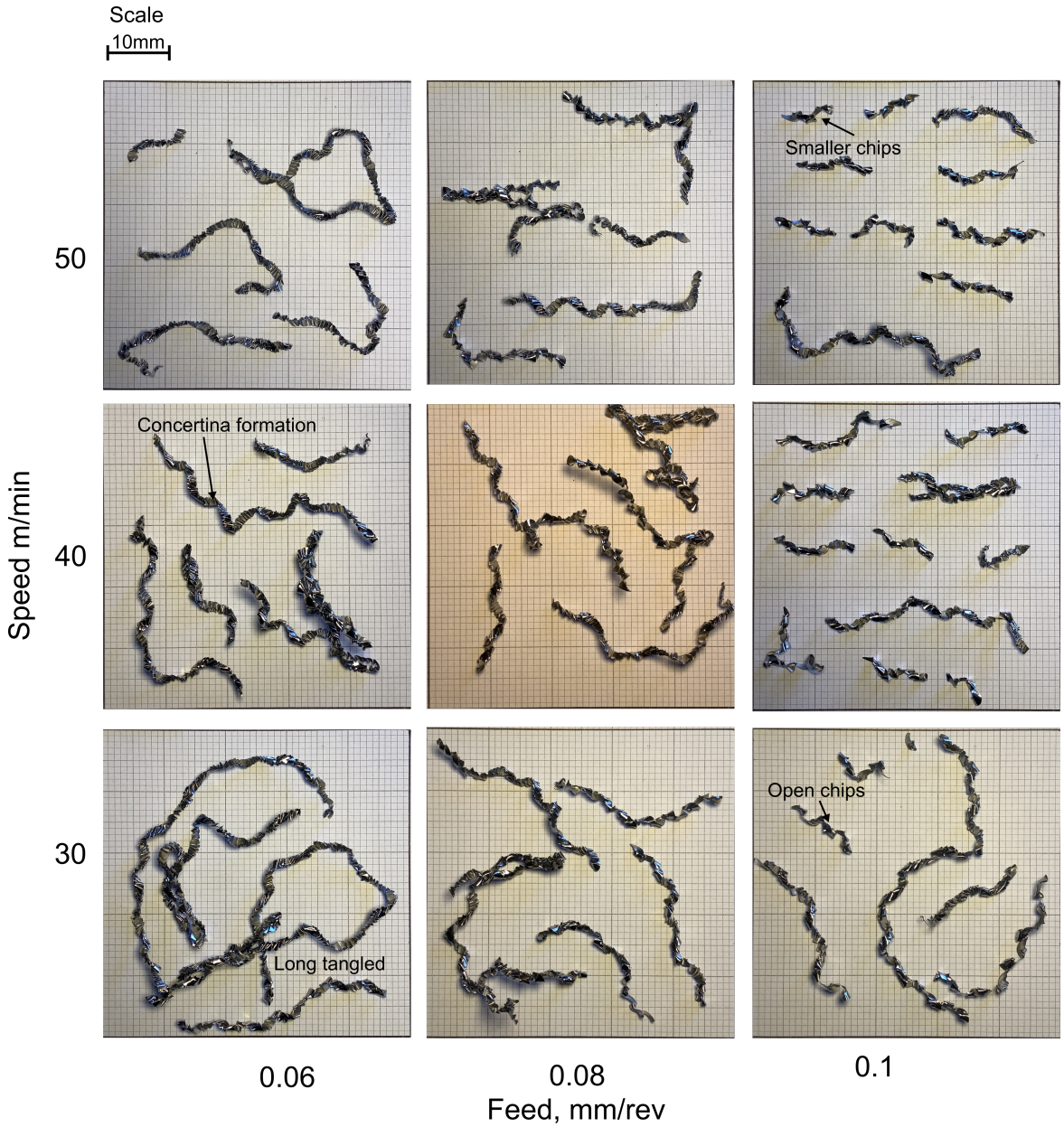

Figure 5.2: Samples of chips from each cutting speed and feed combination, to provide a qualititative understanding of the chip form produced with the R846 drill with LCO_2 cooling. The large subdivisions of the grid are 10mm apart and the smaller divisions are 1mm apart.

Figure 5.3b shows the how the ratio of the chip mass to the uncut chip thickness varies for the different cutting speeds and feeds. A clear correlation between the two graphs depicting chip mass and chip mass uncut thickness ratio. Therefore chip mass is a good indicator of the chip length in this case, as expected.

Results show that at the lower cutting speed of 30m/min, chip mass distribution reduces with increasing cutting feed, with a range of 0.45g for 0.06mm/rev to 0.2g for 0.08mm/rev and 0.15g for 0.1mm/rev. Inline with the increase in feed, the mean mass of the chips drops from 0.140g to 0.083g and then 0.055g from 0.06 to 0.08 and 0.1mm/rev respectively indicating chips of shorter length. It can be noted that where there is a larger chip mass (longer chips) there is a larger upper whisker, inferring that there

are some long chips in that sample. The samples at the higher speed show an initial increase in chip mass followed by a decrease, with increasing feed. The largest chip mass mean values occur at feed rates of 0.08mm/rev for both the 40 and 50m/min speeds, with chip mass values of 0.234g and 0.222g with ranges of 0.65g and 0.7g for 40 and 50m/min respectively. At 40 and 50m/min, both 0.06mm/rev and 0.1mm/rev give chip mass smaller than at 0.08mm/rev. In contrast to 30m/min the lowest chip mass occurs at 0.06mm/rev, with the lowest range. However, when the chip thickness is taken into consideration, shorter chips are again found at the higher feed rate of 0.1mm/rev.

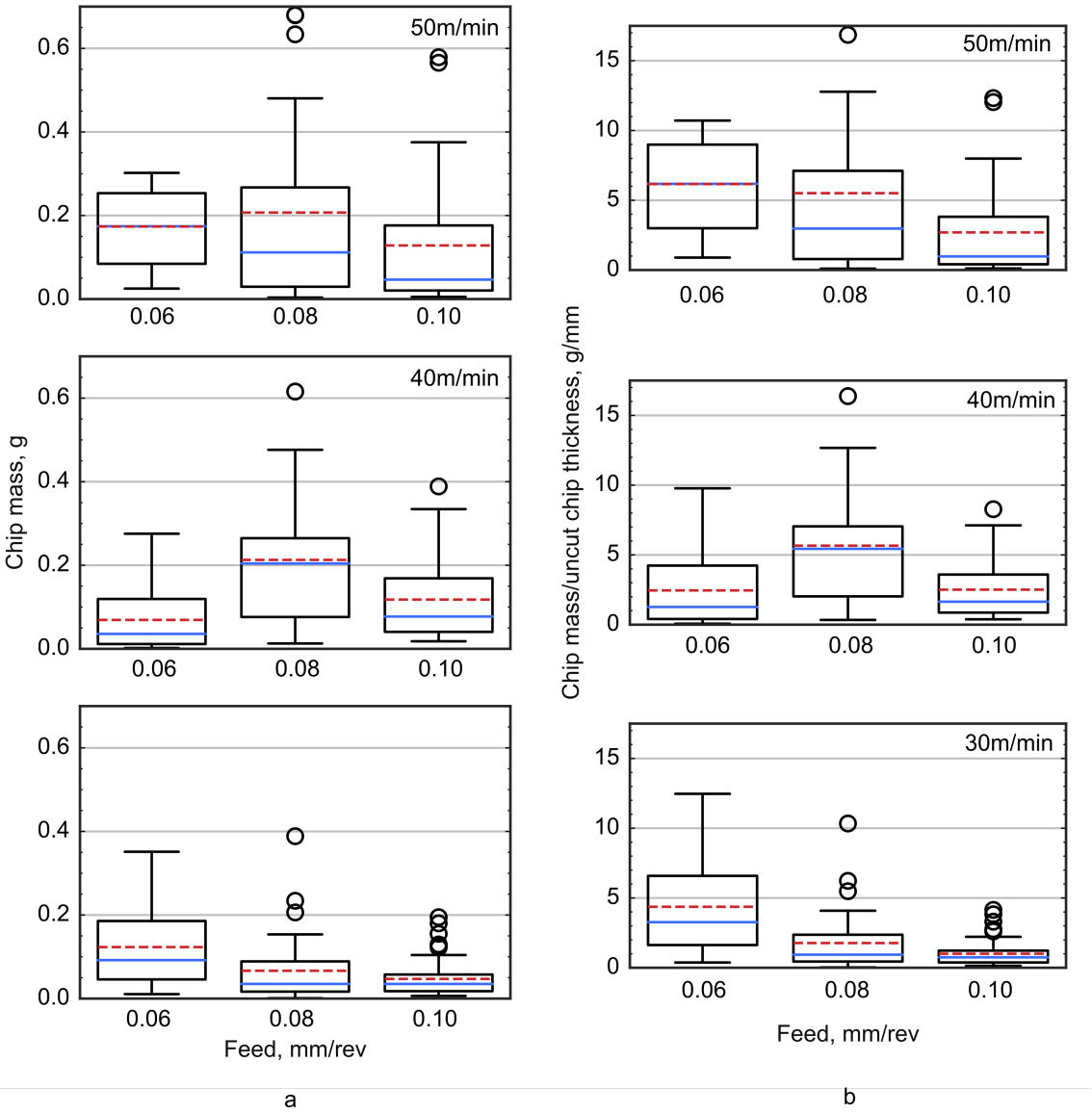

Figure 5.3: a.Box plot showing the chip mass of the sample of chips collected. b. Box plot showing the chip mass of the sample of chips collected. The mean values are labelled and depicted as the cross.

Chip mass, and in turn chip length is smallest at 30m/min cutting speeds, with chip mass increasing linearly with increasing cutting speed, shown in the main effects plot of the data, Figure 5.4a and 5.4b. Increasing the feed also reduces the chip length, which is highlighted in Figure 5.4b, when uncut chip

thickness is taken in to consideration.

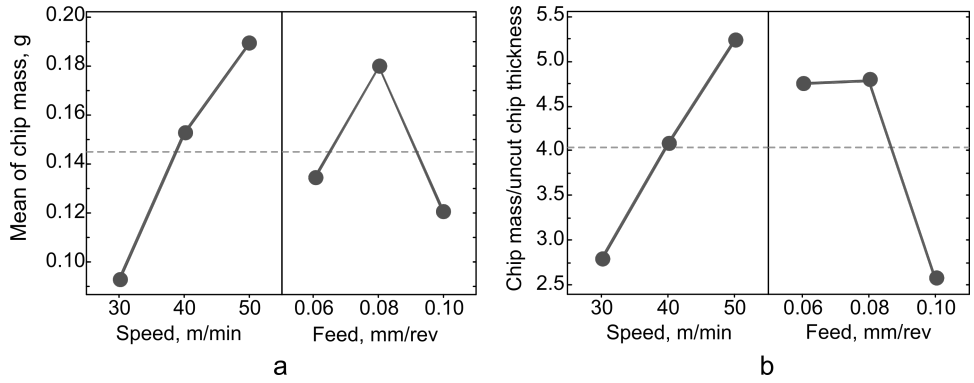

Figure 5.4: a. Main effects plot for the mean of the chip mass with emulsion recommended cutting data. b. Main effects plot for the mean of the chip mass to uncut chip thickness ratio with emulsion recommended cutting data.

5.2.2 Surface roughness

The surface roughness of the internal surface of the nine holes drilled in each run were measured using the method described in Section 4.16.3 and are presented in Figure 5.5. Where the longest chips are formed, at the 40m/min and 0.08mm/rev cutting data the roughness is the largest with a median Ra value of 1.85µm and Rmax=16µm, however at 50m/min and 0.08mm/rev the surface roughness was comparable to the other holes with Ra<1.5µm, Rz<9µm and Rmax<15µm. It was expected that the longer chips would cause the roughest holes due to scratching of the long chip on the internal surface of the hole as it is expelled out of the hole during drilling. With increased cutting speed lower values of surface roughness were recorded due to an increased rate of chip evacuation from the hole at the higher cutting speed, not allowing the chip sufficient time to interact with the hole surface and cause scratches.

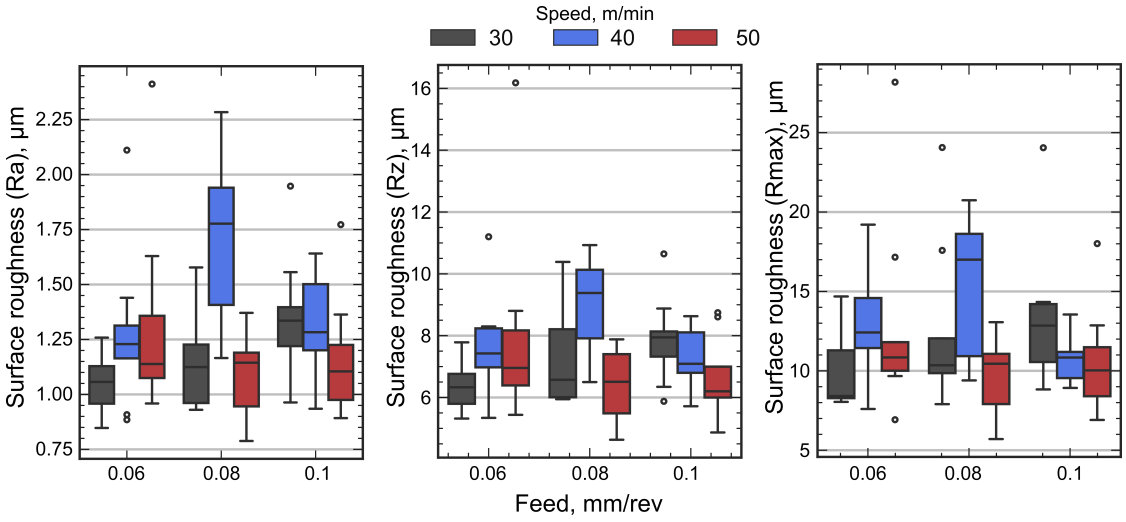

Figure 5.5: The surface roughness of the internal surface of the drilled holes for various speed and feed combinations, displayed as various parameters a. R_a b. R_z c.R_{max}

5.2.3 Burr height

Burr height measurements of the holes were captured, using the method described in Section 4.16.2, and are presented in Figure 5.6. The height of the burr was found to be consistent for each cutting data, with a range between 0.1mm and 0.15mm

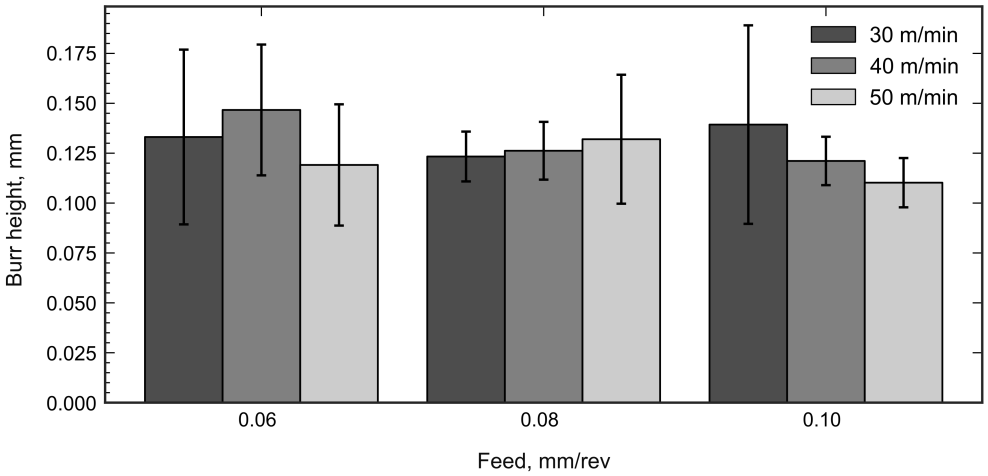

Figure 5.6: Burr height measurements for the initial trials using recommended cutting data for emulsion.

5.2.4 Summary

Ensuring correct chip control is the first step of analysing the cutting process. Without chips that are easily evacuated out of the drilled hole, the process is unstable. This is because of the high risk of tool failure with the increased likelihood of chip nesting, and jamming leading to spikes in torsional forces exceeding the torsional strength of the tool. The initial results have shown that, with cutting data in the recommended range for the R846 drilling titanium with emulsion, the chip formation is inadequate and therefore further cutting data needs to be explored. The results show that by increasing the feed and reducing the speed smaller chips are produced. It was hypothesised that expanding the cutting data in these directions would further improve the chip formation through the production of smaller, easier to evacuate chips. The burr height and surface roughness measurements were within expected values for a drilling process [32].

5.3 Testing the hypothesis of expanded cutting data to improve chip formation.

To determine whether chip formation could be improved with a change in the cutting parameters, the above hypothesis was tested. Using the same test set-up as the previous experiment, decreased cutting speed and increased feed were tested at the parameters in Table 5.3.

Factors	Levels
Cutting speed, m/min	20, 40
Cutting feed, mm/rev	0.12, 0.14, 0.16, 0.18, 0.2

Table 5.3: Expanded cutting data tested with increased values of feed and a lower value of cutting speed.

The run order was again randomised in these trials, as used previously again to remove any effects of systematic bias. A new tool was used for each of the trials, with know measured edge rounding, measured using the method described in Section 4.13. This was to ensure that no adhered material from previous runs would alter the shape of the cutting tool edge rounding. Again these tools were assigned to each run randomly.

Tool Number	Run Order	Speed (m/min)	Rotation (RPM)	Feed (mm/rev)	Penetration Rate (mm/min)
1	1	40	2122	0.16	340
3	2	20	1061	0.14	149
6	3	40	2122	0.14	297
8	4	40	2122	0.12	255
7	5	20	1061	0.2	212
10	6	20	1061	0.16	170
5	7	20	1061	0.18	191
4	8	40	2122	0.18	382
9	9	40	2122	0.2	424
2	10	20	1061	0.12	127

Table 5.4: The run order used when studying the expanded cutting data operating window with higher feed and lower cutting speed. A new tool was used for each run, and randomly assigned, while the run order of the cutting data was also randomised.

5.3.1 Chip formation

Chips were once again captured using the previous method. A sample of the these is presented in Figure 5.8. A qualitative analysis of these chips shows that for the 20m/min cutting speed a mixture of small (ideal chips) with some longer chips. At 40m/min and 0.12mm/rev longer chips were captured, but with an open structure. There is some evidence of smaller chips at this cutting data. With increasing feed, there is increased frequency of the smaller chips.

For the highest feed tested, 0.2mm/rev, at both 20m/min and 40m/min small chips are found with some longer chips showing partial shear, partial shear is presented in Figure 5.7. The partial shear provides evidence of the ductility of the material.

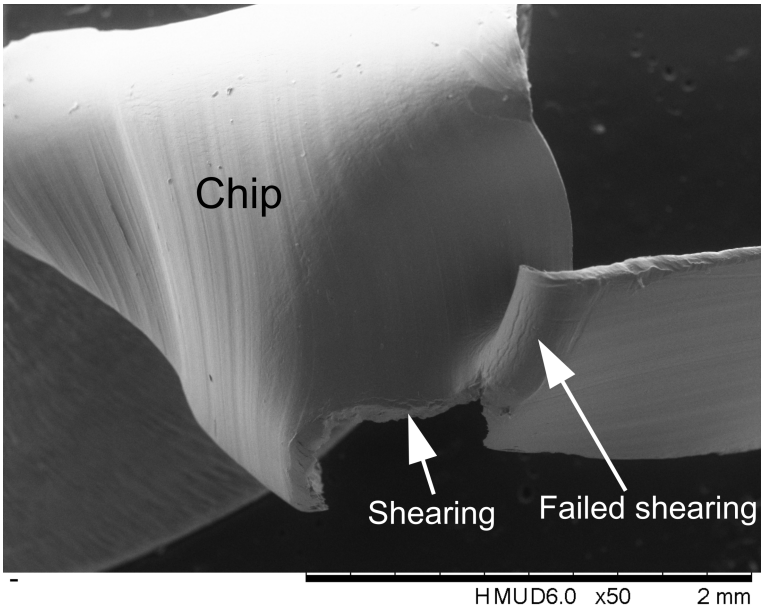

Figure 5.7: SEM image to show the partial shearing of the chips.

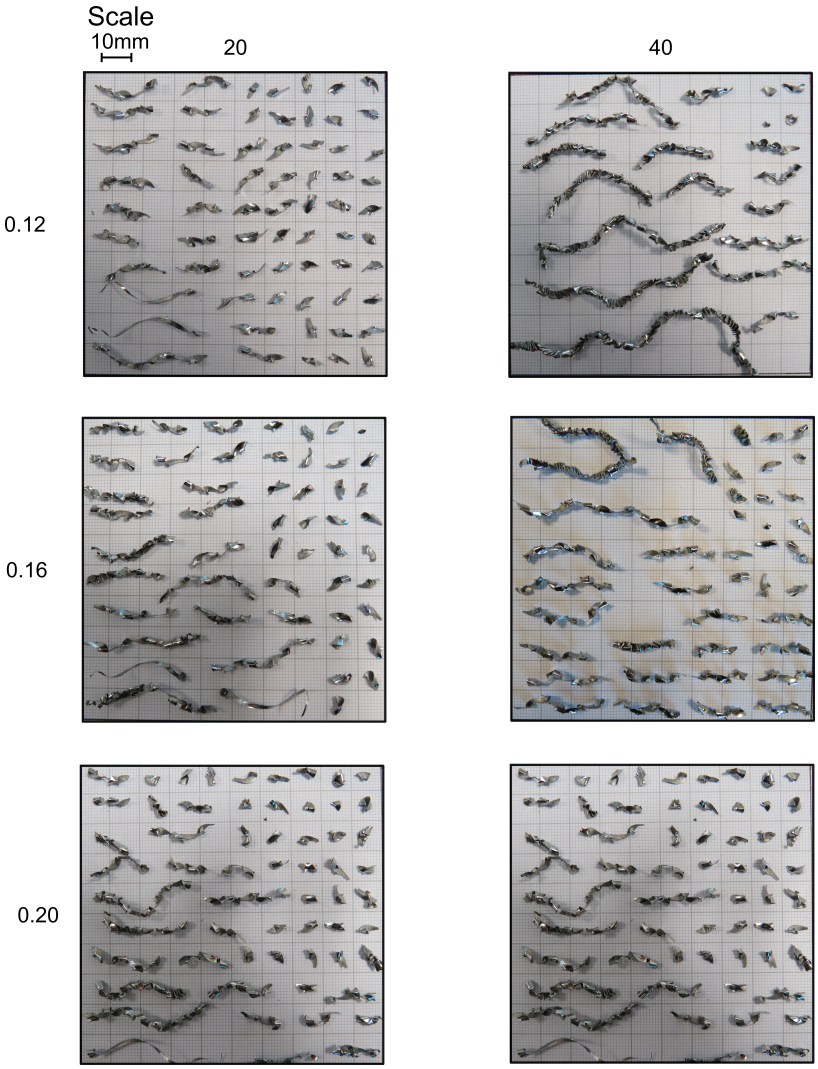

Figure 5.8: Images of the chip formation at the cutting speeds and feeds tested.

The chip mass for these cutting data was captured, using the techniques used in the initial experiment, and is presented in Figure 5.9a. Note the same y-scale as the previous cutting data plot (Figure 5.3), highlights the reduction in the chip size with these cutting data. A clear, marked reduction in the chip size is found for the new cutting data. With chip mass mean measurements between 0.019 and 0.025g for 20m/min and slightly higher chip mass mean measurements of 0.068,0.045 and 0.035g for 40m/min at 0.12, 0.16 and 0.2mm/rev.

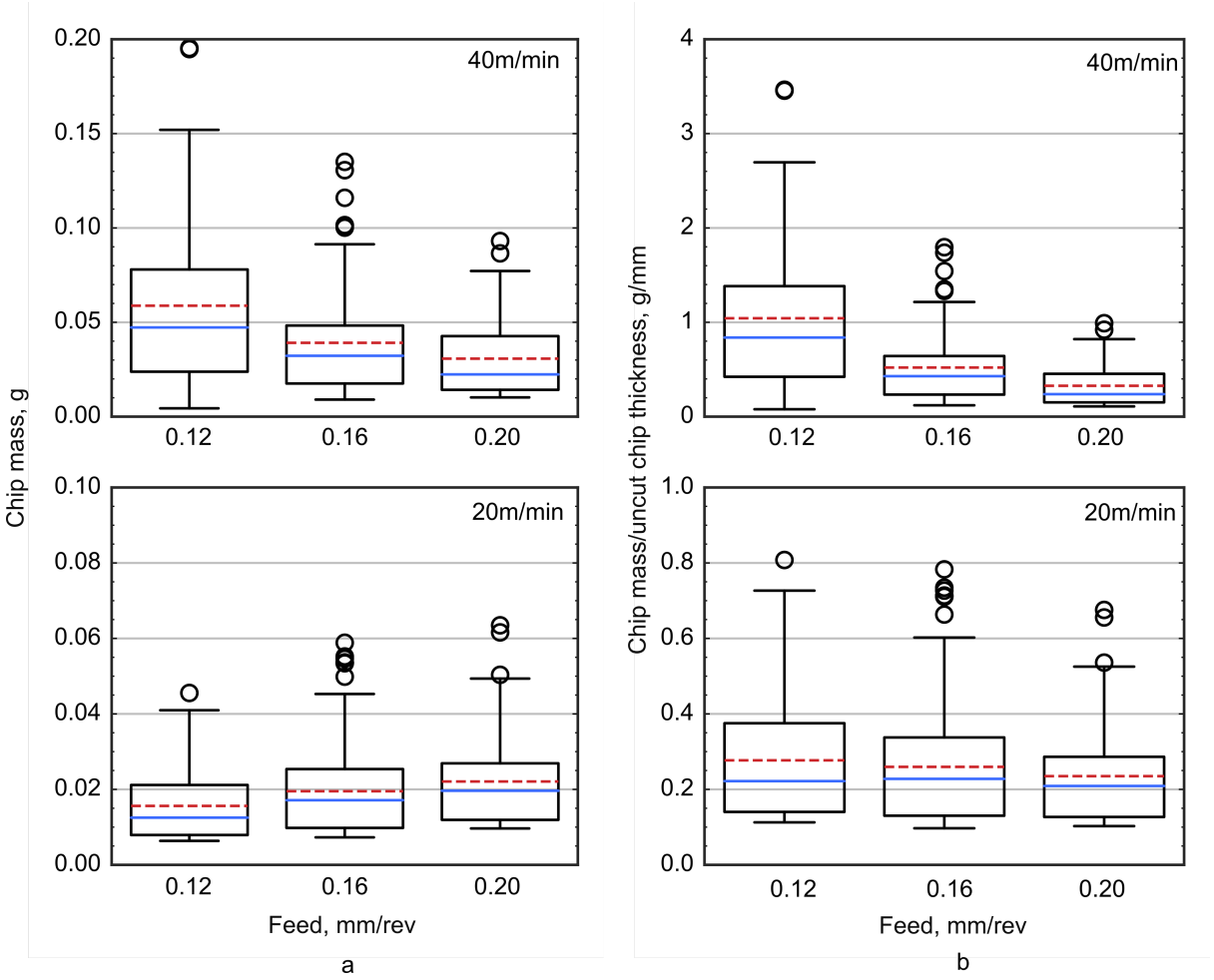

Figure 5.9: a. Box plot of the chip mass for cutting data with increased feed and reduced cutting speed. b. Box-plot of the ratio of chip mass to uncut chip thickness to remove the influence of the chip thickness on the chip mass. (note the difference in the y-scale from that in previous experiment)

Considering the chip length, Figure 5.9b, similar length chips are obtained for 20m/min. For 40m/min the feed rate shows to have an impact on the chip length with increasing feed.

Figures 5.10a and 5.10b show that with increasing speed the chip mass increases. The uncut chip thickness has an effect on the mass of the chip when the chips are short, as little change is observed for the chip mass with varying the feed between 0.12 and 0.2mm/rev. However, incorporating the uncut chip thickness with the chip mass, Figure 5.10b, increasing the feed up to 0.2mm/rev results in the lowest mean chip mass/ t_0 ratio (chip length).

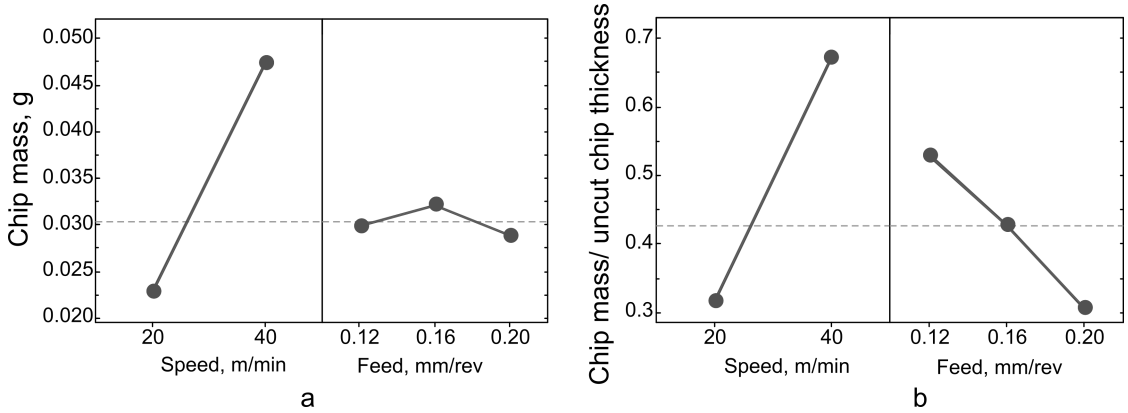

Figure 5.10: a. The main effects plots for the model for chip mass mean for both speed and feed. b. The main effects plots for the mean chip mass, uncut chip thickness ratio model. The dotted line represents the overall mean.

The interaction of the speed and feed, Figure 5.11, illustrates the best speed feed combination to obtain the smallest chip length at 0.2mm/rev for 40/min and all feeds for 20m/min.

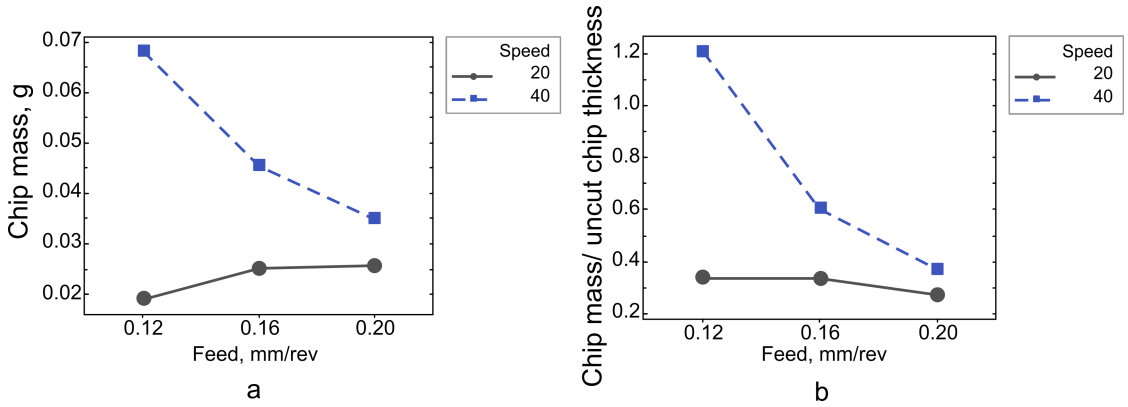

Figure 5.11: Interaction plots showing how the speed and feed influence a. the chip mass b. the chip mass/uncut chip thickness.

The surface roughness was captured using the method described in Section 4.16.3, and summarised in box-plots (Figure 5.12). Displayed on the same y-axis as that of the previous cutting data shows how the surface roughness is improved with the improved chip formation at these cutting data, for all of the surface roughness metrics captured.

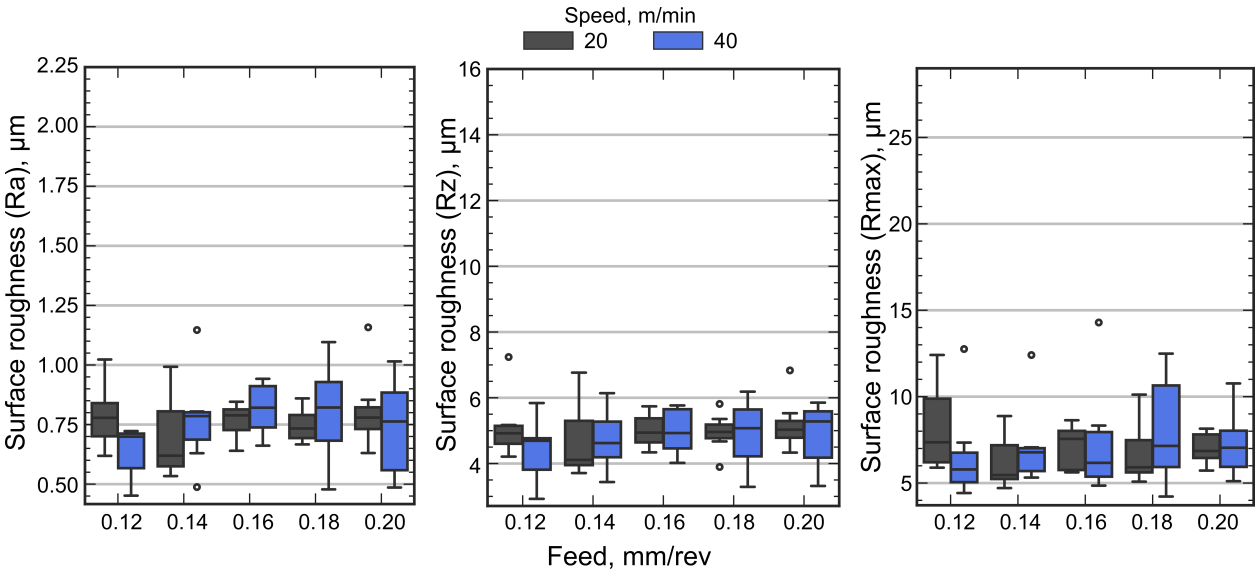

Figure 5.12: The surface roughness captured for the new cutting data at increased feed and reduced cutting speed. The boxes represent the interquartile range, whiskers 95% of the data and the bar is the median of the data.

The exit burr height measurements, shown in Figure 5.13, indicate that the exit burrs of the new cutting data are higher than the previous recommended region of cutting data. Increased exit burr height is expected with increased feed of the drill due to the increased thrust force and subsequent pressure on the material at drill exit, leading to greater plastic deformation of the material around drill exit [177, 178].

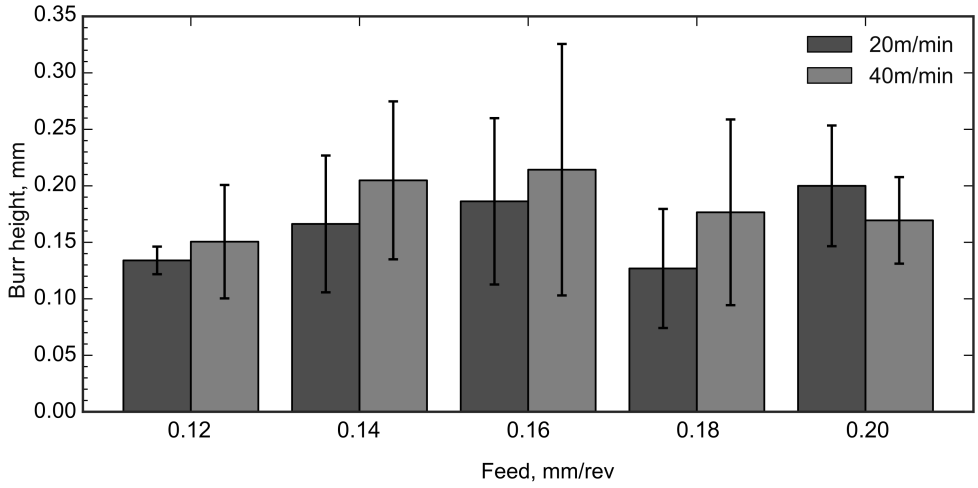

Figure 5.13: Burr height measurements of the new cutting data, displaying the mean value of the captured data, error bars at 1 standard deviation.

5.3.2 Summary of increasing the cutting feed

The hypothesis of improving the chip formation by increasing the feed and reducing the speed has been proved. Improvements in the chip formation are observed with increased feed. The transition to the improved chip formation occurs earlier at the lower cutting speed of 20m/min, while this only occurs at 0.2mm/rev the highest feed tested for 40m/min.

The surface roughness, correlated with the improved chip formation, has reduced for these cutting data, while the burr heights have experienced a small increase, albeit not significant.

The positive implications of this indicates that the process is not limited to a lower cutting speed, and that greater productivity process parameters can be used. In fact the highest penetration rate cutting data has provided adequate chip formation. Perfect singular chips have not been produced for any of the cutting data, with some shear chaining of chips occurring across all cutting data. Therefore further experimentation will focus on the cutting data of 40m/min at 0.2mm/rev to provide both a productive and stable process.

Further increases of the feed were considered to determine whether the chip formation could be improved further. However, it was felt that the tools were close to the buckling limit and further feed increases would lead to a greater frequency of drill breakage and chisel damage negatively affecting the hole geometry.

5.4 Conclusions of chapter

This chapter has presented the preliminary novel work of the first time R846 drills have been used to drill Ti6Al4V with through tool LCO_2 on an industrial type set-up.

- The LCO_2 mass flow rate has been measured at three settings across the working range of the system. The measurements have been found to correspond to within $<5\%$ of those cited by the machine tool manufacturer.
- The function of the cutting tool has been tested with conventional cutting data range recommended in Sandvik Coromant literature. Results have been presented for the chip formation, surface roughness and burr height. It was found that at these cutting data insufficient chip formation was observed, with a unstable cutting process. From the data presented a hypothesis was generated to determine improvements, and identify an operating window for the cutting process.
- Surface roughness showed improvements with chip formation, but no relationship with cutting speed, nor cutting feed were identified.
- Burr height has been shown to increase with the increased feed, as expected, large variance is however noted, which may be a product of the cryogenic process. Therefore comparisons with alternative cutting data would be a useful context to frame this data.
- Increasing the cutting feed resulted in improved chip formation. This improvement was observed at a lower feed for the lower speed tested, whereas a higher feed was required for the higher cutting speed to improve the chip formation.
- Cutting data have been identified which provide the process with adequate chip formation, albeit with some failures of completely singular chips. A cutting speed of 40m/min and 0.2mm/rev have been selected for future experimental trials, as it provides a compromise between productivity and chip formation.

6 Process variables, with forces as primary response.

This chapter focuses on understanding the effect of LCO_2 process parameters (such as LCO_2 mass flow rate and the drill retract distance) on the drilling process. Literature has shown the LCO_2 process parameters to have an impact on the performance of other cutting processes. However, the impact of these in the drilling process have yet to be studied in any depth. The primary focus of this chapter is with the cutting forces as a response.

Therefore the objectives of this chapter were to:

1. Study the LCO_2 process parameters with a D-optimal experimental design approach using the previously ascertained cutting data in Chapter 5 and the experimental set-up, with flat plate dynamometer, described in Section 4.14.
2. Identify the key parameters from the LCO_2 process using forces and hole quality as the primary metrics.
3. Determine empirical relationships between these parameters and the primary metrics.

6.1 Outline and experimental design of the process variables experiment- forces based.

The run order and combinations carried out within the D-optimal experimental design are shown in Table 6.1. Four CoroDrill R846 tools and two stepped workpieces (described in Figure 4.10) were used. The runs were blocked (grouped) according to tool and workpiece, to allow for practical and timely completion of the trial. Within each block the studied factors were randomised. Central positions of each of the factors were completed at the beginning, middle and end of the trial to detect any systematic errors in the results. For each run three holes were drilled.

Run no	BHD, s	FL, kg/hr	FR, mm/rev	RD, mm	WT, mm	Tool	Workpiece
1	3	8	0.16	8.5	10	TOOL 1	1
2	1	6	0.12	2	14	TOOL 1	1
3	5	10	0.2	2	14	TOOL 1	1
4	5	10	0.2	2	14	TOOL 1	1
5	1	10	0.12	15	6	TOOL 1	1
6	3	8	0.16	8.5	10	TOOL 1	1
7	5	6	0.2	15	6	TOOL 1	1
8	1	10	0.12	15	6	TOOL 1	1
9	1	6	0.12	2	14	TOOL 1	1
10	5	6	0.2	15	6	TOOL 1	1
11	3	8	0.16	8.5	10	TOOL 1	1
12	3	8	0.16	8.5	10	TOOL 2	1
13	5	6	0.12	15	14	TOOL 2	1
14	5	10	0.2	2	6	TOOL 2	1
15	1	10	0.2	15	14	TOOL 2	1
16	1	6	0.12	2	6	TOOL 2	1
17	3	8	0.16	8.5	10	TOOL 2	1
18	5	6	0.12	15	14	TOOL 2	1
19	1	6	0.12	2	6	TOOL 2	1
20	5	10	0.2	2	6	TOOL 2	1
21	1	10	0.2	15	14	TOOL 2	1
22	3	8	0.16	8.5	10	TOOL 2	1
23	3	8	0.16	8.5	10	TOOL 3	2
24	5	10	0.12	2	6	TOOL 3	2
25	5	6	0.12	15	14	TOOL 3	2
26	1	10	0.2	15	14	TOOL 3	2
27	1	6	0.2	2	6	TOOL 3	2
28	3	8	0.16	8.5	10	TOOL 3	2
29	5	10	0.12	2	6	TOOL 3	2
30	5	6	0.12	15	14	TOOL 3	2
31	1	6	0.2	2	6	TOOL 3	2
32	1	10	0.2	15	14	TOOL 3	2
33	3	8	0.16	8.5	10	TOOL 3	2
34	3	8	0.16	8.5	10	TOOL 4	2
35	5	6	0.2	2	14	TOOL 4	2
36	1	6	0.2	15	6	TOOL 4	2
37	1	6	0.2	15	6	TOOL 4	2
38	5	6	0.2	2	14	TOOL 4	2
39	3	8	0.16	8.5	10	TOOL 4	2
40	5	10	0.12	15	6	TOOL 4	2
41	5	10	0.12	15	6	TOOL 4	2
42	1	10	0.12	2	14	TOOL 4	2
43	1	10	0.12	2	14	TOOL 4	2
44	3	8	0.16	8.5	10	TOOL 4	2

Table 6.1: Run order for the process variables experiment with forces as main response.

6.1.1 Responses/ dependent variables

The responses measured in this trial are presented in Table 6.2. The responses were grouped according to: hole quality measurements completed on the workpiece after the trial; and in process measurements obtained during the trial. The chip formation was quantified using a scale of 1-10, with 1 being good chip formation and 10 being poor formation of individual chips.

The methods used to capture the hole quality and the cutting forces are described in Section 4.16 and Section 4.14 respectively.

Hole quality	In process
Burr height, mm	Chip formation, (scale of 1=good to 10=poor)
Hole surface roughness (Ra), µm	Normal force, N
Least square diameter, mm	Torque, Nm
Circularity, mm	Area under the torque curve
Max inscribed diameter (mean), mm	Area under torque curve divided by WT

Table 6.2: Explanation of the response variables that are presented from the process variables experiment.

6.2 Data overview of the effects of the process variables captured during the forces rig experimental set-up

The data points captured in this experiment are presented as a pairwise scatter plot in Figure 6.1. The plot is interpreted about the leading diagonal on the plot where the intersection of two smaller plots provides the relationship between those two variables. For example, the smaller plots circled with the orange dotted line show the relationship between the mass flow rate of CO_2 and the normal force. The smaller plot circled on the bottom left show mass flow rate of CO_2 on the x-axis and normal force on the y-axis, and the smaller plot circled on the top right shows the normal force on the x-axis and the mass flow rate on the y-axis. Each datapoint on each smaller plot represents data captured from three holes drilled for each level of the factors, where measurements were taken an arithmetic mean was then calculated. These results are shown for the forces test rig set-up Section 4.14.1.

Figure 6.1 is composed of different sections. The experiment design is shown in the upper left hand corner of the plot illustrating the levels (values of the independent variables) of the factors studied in the experiment. The next section of the plot can be distinguished according to the type of response that is measured, with hole quality responses and in process responses grouped together. The effect of each factor on each response is shown in these sections by following the relevant factor to the desired intersection of the response. The final section shows the interrelationship between each response in the bottom right hand corner of Figure 6.1. This shows the relationship between each response studied. For example increases in normal force acting on the drill coincide with increases in the torsional forces.

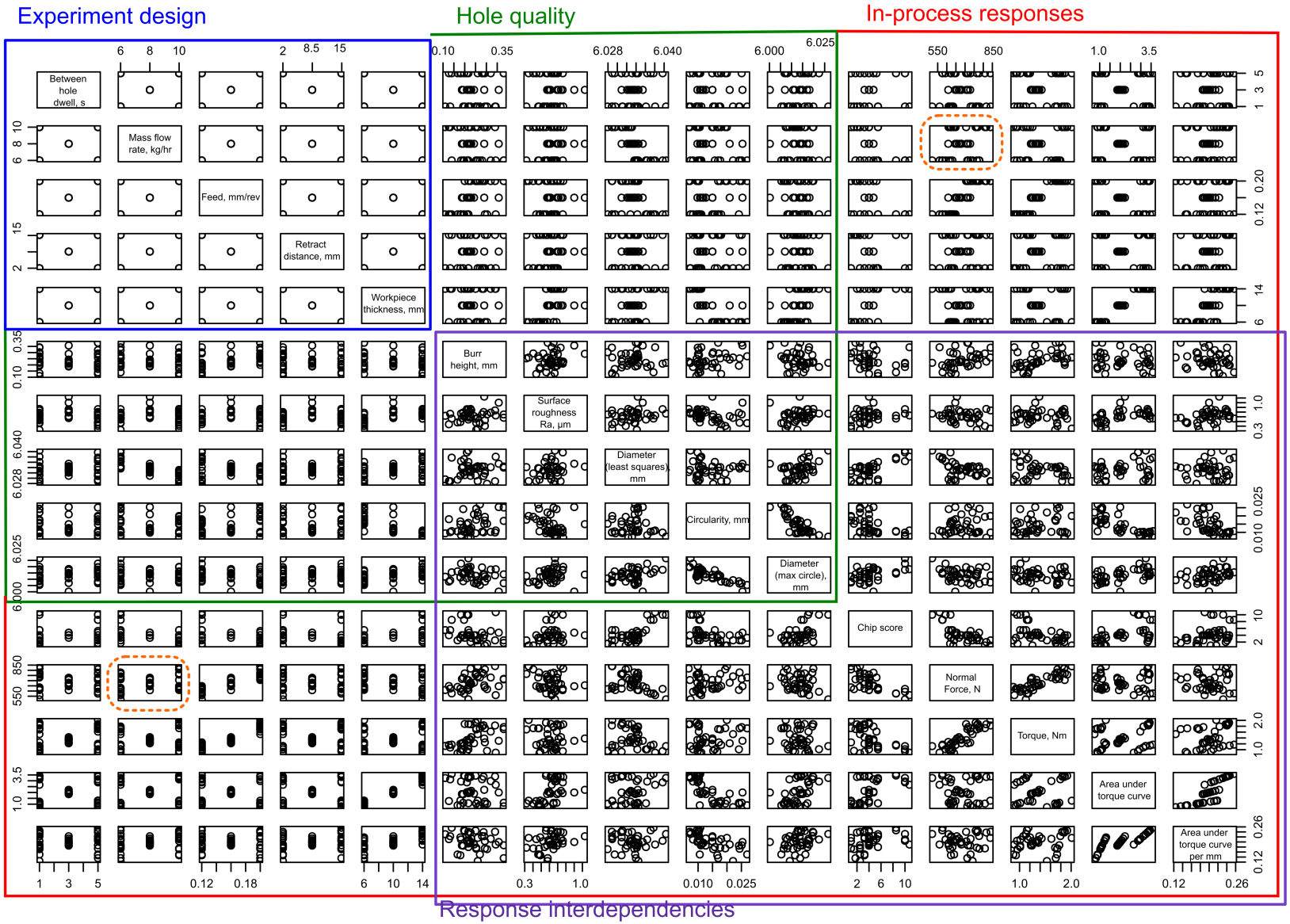

Figure 6.1: Scatter plot of the process variables experiment. Shown is the experimental design, and the levels of these parameters in the design, the hole quality and the in-process responses, and the interdependencies of these responses.

The Pearson correlation, Equation 6.1, shows the extent of a linear correlation within the data. The number of readings in the data set is depicted by n and x_i, y_i are the individual values of the x and y variables.

$$r_{xy} = \frac{n\sum x_i y_i - \sum x_i \sum y_i}{\sqrt{n\sum x_i^2 - (\sum x_i)^2}\sqrt{n\sum y_i^2 - (\sum y_i)^2}} \tag{6.1}$$

The value of the correlation can be between +1 (strong positive correlation) and -1 (strong negative correlation) and zero that there is no linear correlation in the data.

Correlations of the scatter data were calculated using the Pearson correlation coefficient, and are presented in Figure 6.2. Ellipses depict the extent of the correlation, a narrow positive gradient ellipse represents a strong positive correlation, and a narrow negative gradient ellipse shows a negative correlation. Where there are just circles, little to no correlation was found. This tool provides a useful visual representation for determining which parameters are the most influential in the process, and which parameters are least influential. For example, strong positive correlations have been found for feed and forces. With increasing feed the normal force and torsional forces increase, whilst chip form improves (lower value of chip form= improved chip form). Furthermore, the figure also provides information about parameters that have little effect on the process. For example, retract distance and between hole dwell have shown to have little correlation with any other parameter studied. Further quantification of the significance of these factors is further calculated in further sections.

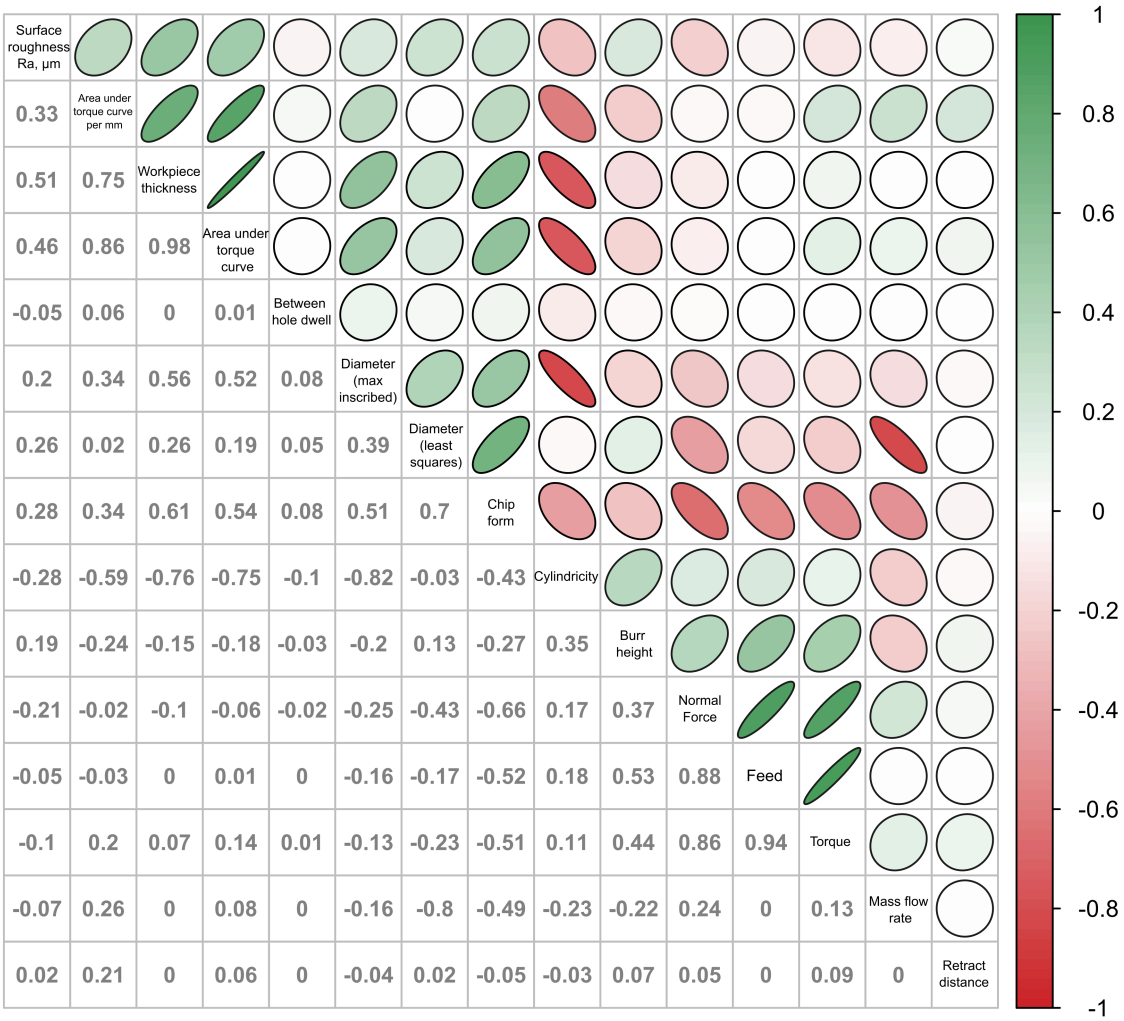

Figure 6.2: The Pearson correlation coefficient values of all factors and responses, with the correlations clustered to improve interpretation.

6.3 Influence of factors in the force experiment

This section expands on the correlations calculated in Figure 6.2 for the force experiment. It provides detailed observations of the influence of the factors in the experiments, and focuses on those factors that have been shown to be influential to the process. Each figure, shown in Figures 6.3, 6.4,6.5 represents the findings from each factor for LCO_2 mass flow rate, feed, and workpiece thickness respectively. Each figure can be interpreted in the same way. The first column of data shows histograms representing the frequency of the data. The top left histogram shows the frequency of the number of experiments carried out at each level for that factor, depicted by the three colours. The smaller, horizontal histograms show the frequency of the data for that particular response measurement.

The top row of the figures shows box plots of the data, with a mean line shown for each of the responses measured. The upper and lower limits of the box plots are the interquartile range. The leading horizontal shows the shape of the distribution of the data, whilst the scatter plots show interrelationships between the responses that have been measured, providing more detail for these interrelationships than from the

previous scatter plots and Pearson correlation plots.

6.3.1 Liquid CO_2 mass flow rate

The mass flow rate of the liquid CO_2 was studied in the range between 6kg/hr and 10kg/hr, with a centre point at 8kg/hr. As has been shown, in Figure 6.2, the mass flow rate is positively correlated with the forces and the area under the torque curve per mm, and negatively correlated with hole diameter and the quality of the chip formation. Therefore, the influence of the LCO_2 mass flow rate on these responses are explored in greater detail in Figure 6.3. The mass flow rate is shown to influence the drilled hole diameter. At a mass flow rate of 6kg/hr, the mean calculated hole diameter was calculated as 6.035mm. With increases in the mass flow rate to 10kg/hr, the mean calculated diameter became smaller at 6.029mm, as shown in Figure 6.3. Good repeatability of the data about the mean for the centre point is also shown for the diameter measurement, indicating a robust data set for all responses observed.

It can be observed from the data that there may be two effects that influence the hole diameter. The first could be that at higher mass flow rate the drill is colder, therefore thermally contracted, resulting in a smaller hole. This is indicated by the changing mean values of the data, in that smaller holes are produced when the LCO_2 mass flow rate is at the highest flow rate setting. The second could be due to poor chip form for certain data points, indicated in the scatter and large tail for the 6kg/hr data. Where poor chip formation occurs, a hole is still formed, however the chips are impeded from extraction due to their long nature. This impedance may cause the chip to rub against the wall of the drilled hole increasing the hole diameter.

The formation of the chips were ranked on a scale of 1- 10 where 1 was good and 10 was poor. The results shown in Figure 6.3 indicate that chip formation was improved with increased LCO_2 mass flow rate. This is shown by tighter spread of data for the higher mass flow rate tested, when compared to the lower mass flow rate tested. It is shown that the worse chips occur when the normal force is the lowest. This may indicate that there is thermal softening of the material occurring at the lower mass flow rates of the LCO_2 causing the poor chip form.

The normal force and the area under the torque curve per mm, indicating the amount of work that is done to produce the hole, show increases for increased LCO_2 mass flow rate. However, the data has a large spread indicating that there may be other factors such as the feed that are also contributing to the change in the forces. Further work is therefore done to try and quantify which parameter has the most influence on these responses, in Section 6.4.

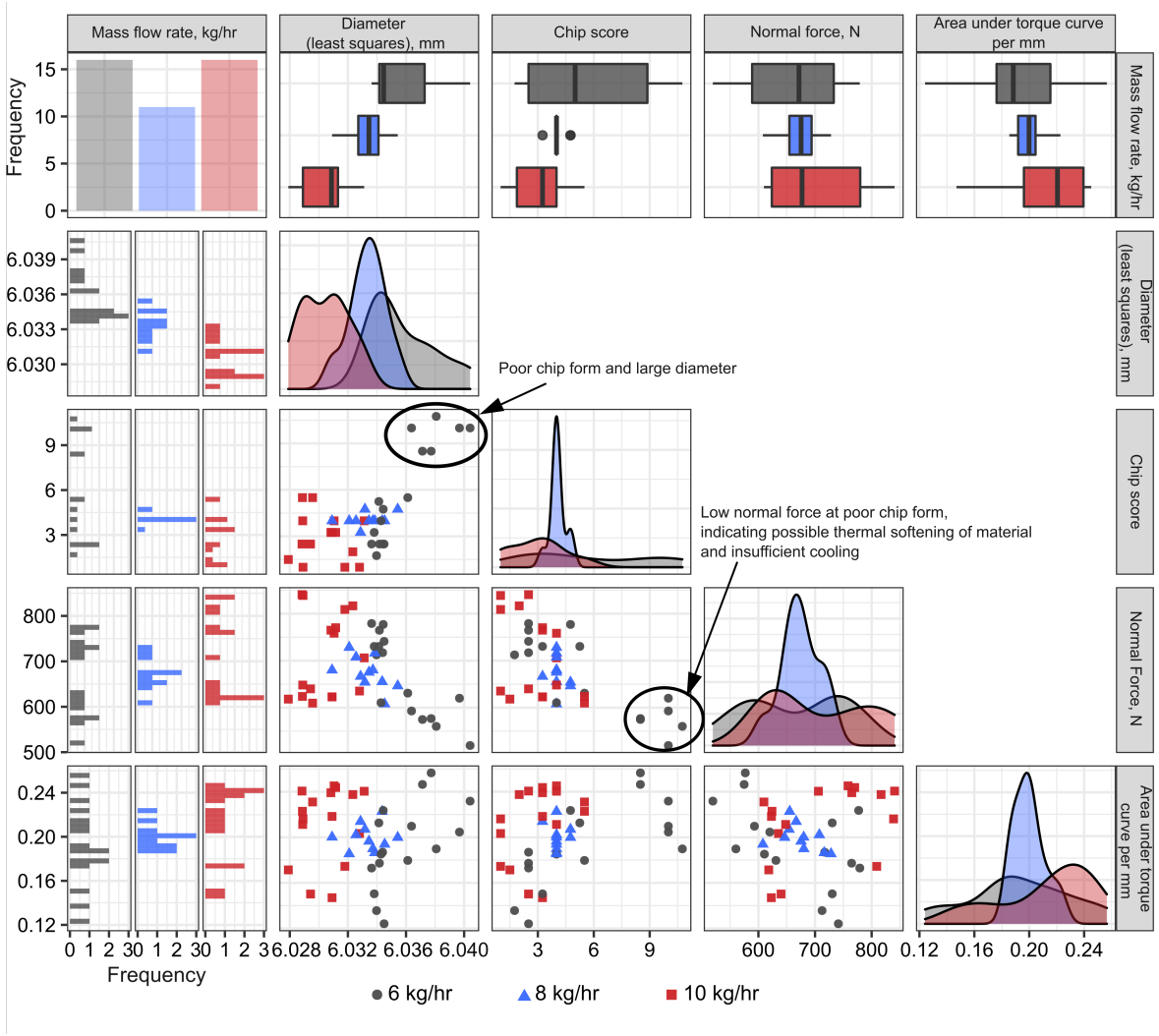

Figure 6.3: Box-plots, scatter and data distributions to show the effect of the mass flow rate factor, and the interrelationships between relevant captured responses.

6.3.2 Feed rate

Both the normal and torsional forces exerted on the drill correlate positively with increased feed with Pearson correlations of 0.94 and 0.88 respectively, Figure 6.2. Normal force and torsional forces are also positively correlated with each other. Figure 6.4, shows that the mean value for the normal force at 0.12mm/rev is 625N which increases to 670N for 0.16mm/rev and then to 750N for feed at 0.2mm/rev. The torsional values observed also increase from 1.05Nm to 1.35Nm and 1.75Nm as the feed increases from 0.12 to 0.16 and 0.2mm/rev. The increase in normal and torsional forces with increasing feed is as expected, and is commonly reported in literature [[179, 180]]. The figure also shows that clearly defined normal distributions of each set of data for each feed were found. This shows a clear relationship between the feed and the measured forces. The increase in normal and torsional forces with increasing feed occurs because of the increased uncut chip thickness and chip load acting on the tool at increased feed [35].

A linear trend of increasing exit burr height with increasing feed is also observed, which is in agreement

with literature [181, 177]. The increase in the burr height is due to the increased uncut chip thickness at increased cutting feed. An increased uncut thickness causes an increase in the volume of material that is plastically deformed on the final rotation of the drill as it exits the drilled hole.

An improvement in chip formation is observed with increased feed (lower chip score indicates improvements in the chip formation). This is shown through the increased distribution of chip score at the lower feed. At the higher feeds, the chip score is consistently lower. This indicates that there are other factors that are also influencing the chip score as well as the feed, i.e. the LCO_2 flow rate and the workpiece thickness.

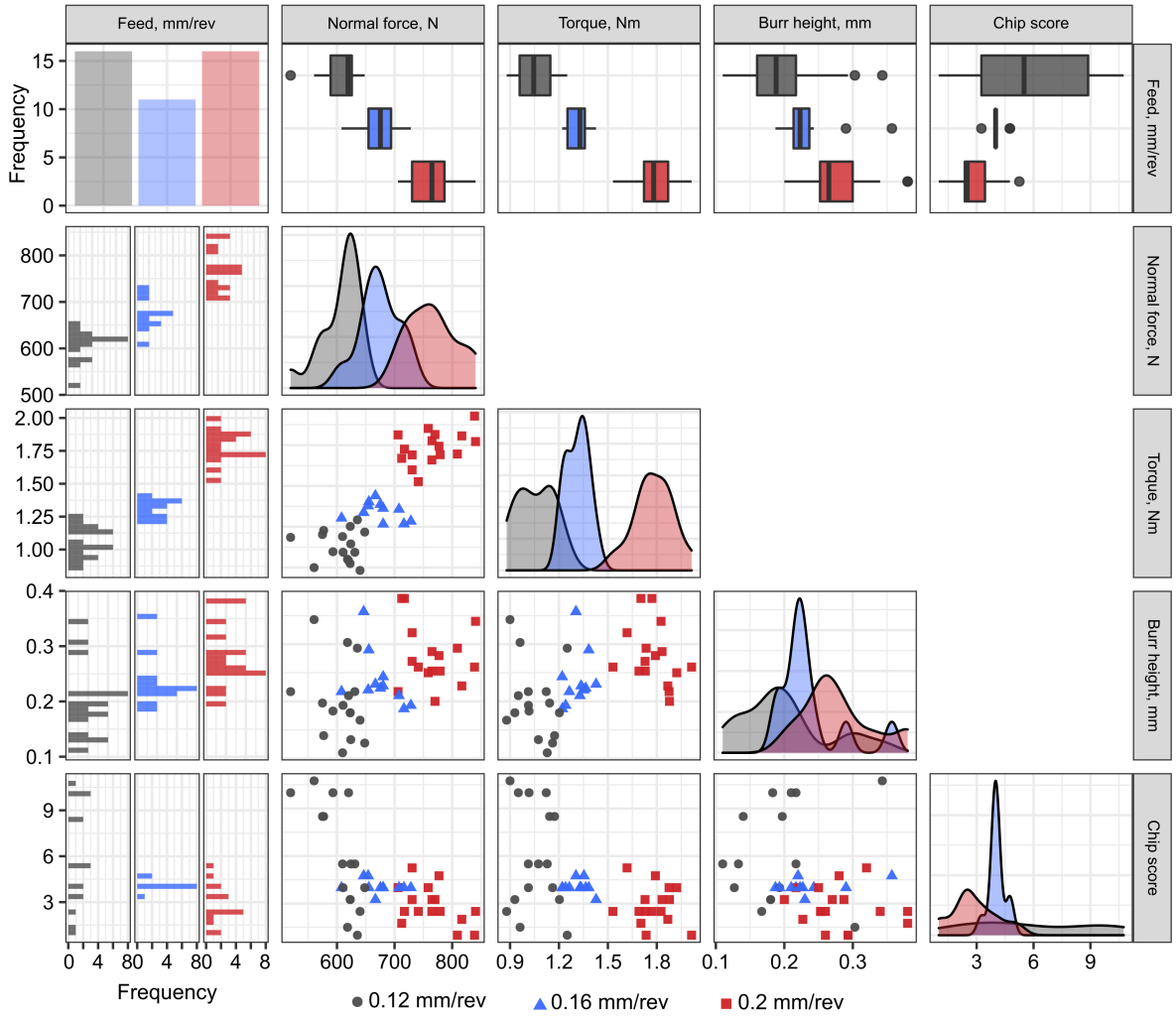

Figure 6.4: The effect of the feed and the interrelationships between the identified significant captured responses.

6.3.3 Workpiece thickness

Figure 6.2 shows that the workpiece thickness is correlated to hole quality (surface roughness, diameter, and shape), the chip formation, and the area under the torque curve (energy used in the process). These correlations are further explored in Figure 6.5. The hole surface roughness increases with larger workpiece thicknesses. At 6mm thickness the mean surface roughness (Ra) was 0.5µm while for the 14mm it was 0.66µm, an increase of 32%. A similar surface roughness was also found for the 10mm

plate as for the 14mm. This improvement in surface roughness coincided with improvement in chip score at the lower workpiece thickness. This indicates that for the workpiece thicknesses of 10mm and 14mm the poor chip formation results in the rubbing of the chips against the internal surface of the drilled holes because of the increased distance the chips have to travel to be extracted from the deeper holes when drilling the thicker workpiece. This is in agreement with work conducted in the study conducted by Batzer et al. [182], where they also found poor chip formation to correlate with increased surface roughness on the drilled wall surface.

The diameter of the holes were found to increase with increased workpiece thickness, Figure 6.5. This is shown as an increase in the diameter max inscribed of 6.010mm to 6.017mm from 6mm workpiece thickness to 14mm. It is anticipated that this is caused by the temperature of the drill increasing and thermally expanding due to increased time in cut and heating of the drill. This is explored further in Chapter 7.

The circularity was shown to be positively correlated with the workpiece thickness with coefficient of 0.56 in Figure 6.2. Figure 6.5 shows this relationship in greater detail. It shows that for the thinner workpiece of 6mm, the circularity was higher, with a mean value of 0.0176mm, 43% higher than for 14mm at 0.01mm. This indicates that at the thinner workpiece thickness the drilled hole deviates further from a perfect circle than for a thicker workpiece. This occurs in drilling where the drill wanders and is less stable. In this instance for the thinner workpiece there is less contact of the drills margin with the drilled hole to act to stabilise the drill.

The area under the torque curve is also presented in Figure 6.5 and represents the total amount of power consumed in the production of the hole. This area increases for increasing workpiece thickness. This makes intuitive sense because deeper holes take longer to drill because more material is removed. When the power consumed per mm is then analysed, upper right in Figure 6.5, it shows that per mm the power consumed increases for workpiece thickness increases. This increase in power per mm for the thicker workpiece could be explained by increased resistance of the drill in extracting longer chips from the hole, and the increase in friction with greater drill area in contact with the drill in machining the deeper hole.

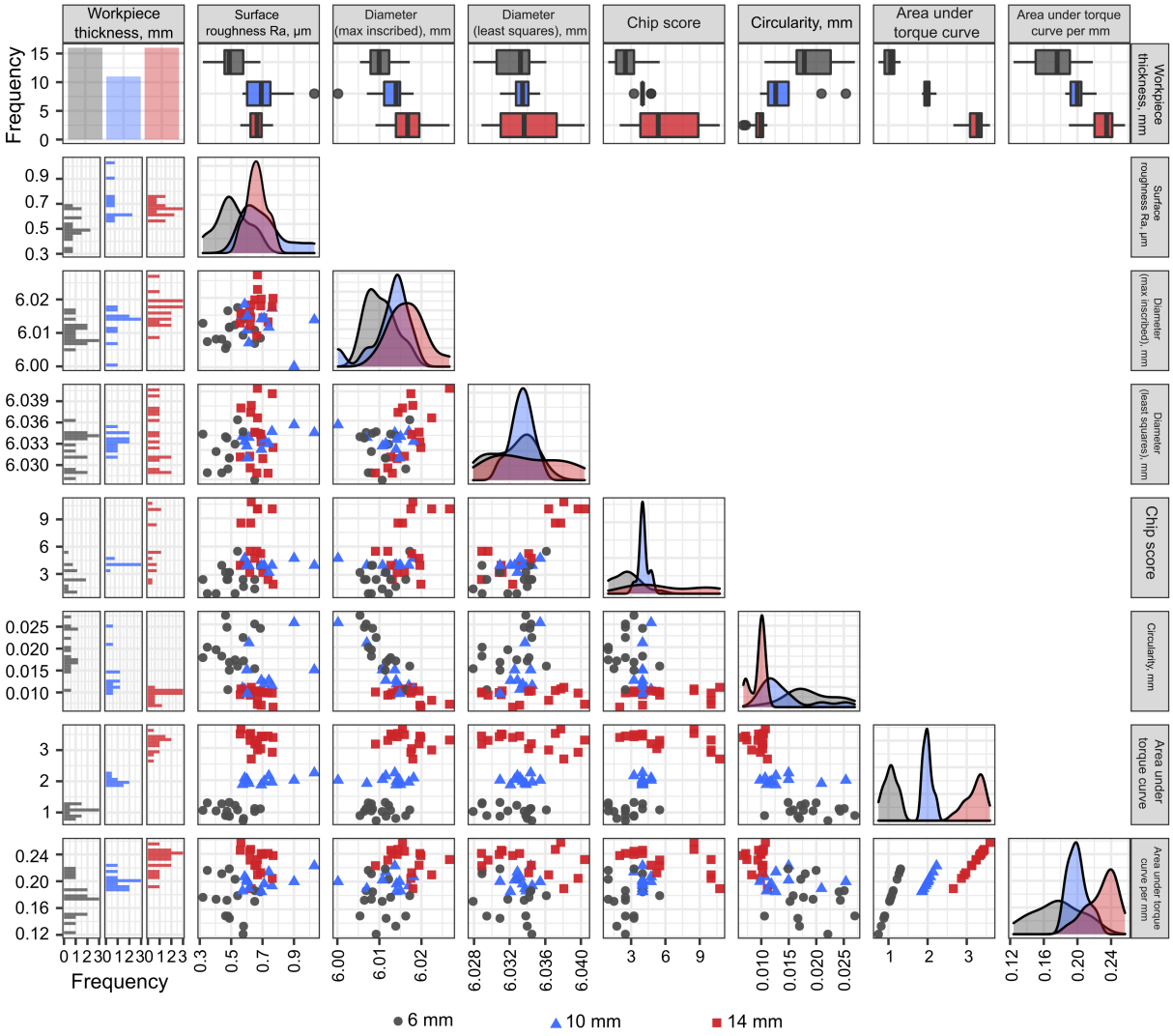

Figure 6.5: The effect of the workpiece thickness and the interrelationships between the identified captured responses.

6.3.4 Summary

Of the five factors studied, only three of those were found to have correlations with the responses; mass flow rate, feed rate and workpiece thickness. The between hole dwell and retract distance factors did not have any correlation with any of the responses measured, nor did they influence any other factors.

The LCO_2 mass flow rate influenced the hole diameter, forces and chip formation. The feed influenced the forces and chip form as expected as well as the burr height. While correlations existed between the workpiece thickness and all the responses measured.

6.4 Significance of the factors on the responses and mathematical modelling of the responses from variables

Correlations and the influence of each of the pertinent factors have been identified in Section 6.3. However, quantification of the importance of each of these factors have been yet to be completed. Therefore, this section aims to quantify the impact of each of the factors on the measured responses. As this study has been conducted using parametric statistics (assuming that the data is normally distributed), validation of these assumptions are carried out in this section also.

These analyses were conducted in MODDE and Minitab statistical software packages using the process outlined in Figure 6.6. For each of the data captured and modelled for each response, an Analysis of Variance was conducted to determine which, if any, of the factors had greater influence on the response than other factors. To determine this a p-value was obtained, and using a threshold of $p<0.05$, determined by Fisher as the limit for statistical significance [183]. The results of these p-values are shown in Table 6.3, and those values fulfilling these limits are highlighted. The normal distribution test for the normal force are presented. For the other responses, refer to Appendix 2.

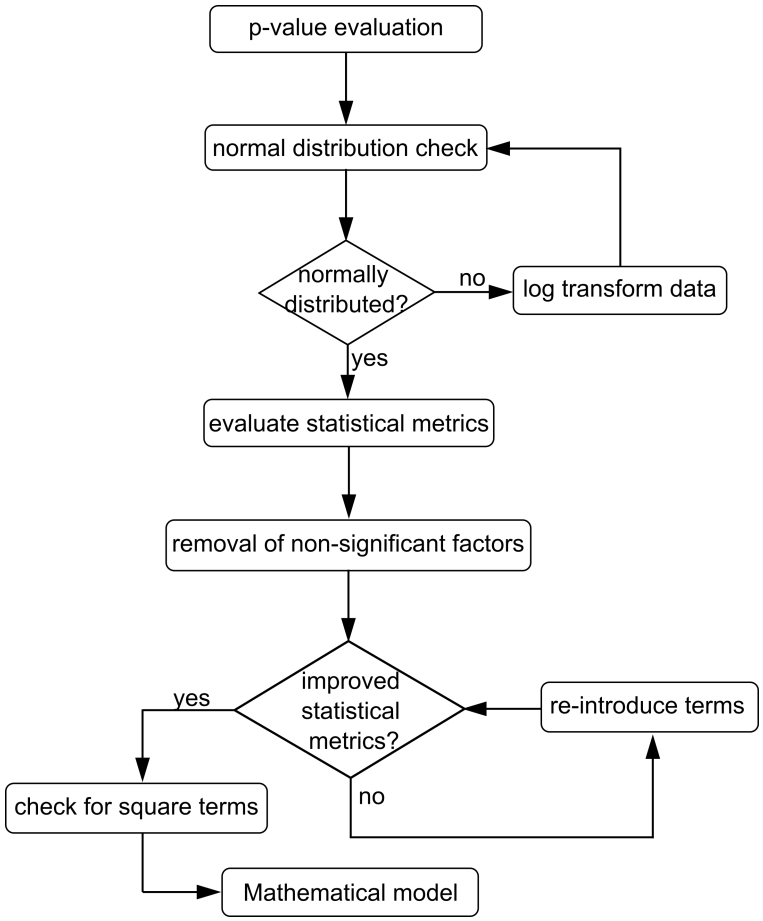

Figure 6.6: Flow chart of the modelling process used to evaluate the statistical metrics of the model for each response term.

p-values	Const.	BHD	FL	Feed	RD	WT	T1	T2	T3	T4
Normal forces	0	0.620	$4.25\text{x}10^{-7}$	$2.23\text{x}10^{-22}$	0.235	0.016	$1.12\text{x}10^{-7}$	$1.97\text{x}10^{-7}$	0.062	0.048
Torque	0	0.800	0.012	$1.81\text{x}10^{-19}$	0.095	0.202	0.883	0.525	0.976	0.656
Energy	0	0.764	0.012	0.649	0.047	$3.69\text{x}10^{-27}$	0.812	0.416	0.474	0.744
Energy/ mm	0	0.552	0.0091	0.730	0.035	$3.37\text{x}10^{-9}$	0.910	0.840	0.477	0.323
Chip form	0	0.153	$1.48\text{x}10^{-10}$	$2.98\text{x}10^{-11}$	0.397	$5.23\text{x}10^{-13}$	0.893	0.740	0.815	0.499
Cylinder (max inscribed)	0	0.553	0.245	0.254	0.796	$2.29\text{x}10^{-4}$	0.565	0.732	0.953	0.406
Diameter (least squares)	0	0.508	$5.54\text{x}10^{-13}$	0.024	0.815	$1.03\text{x}10^{-3}$	$7.23\text{x}10^{-3}$	0.405	0.904	$7.55\text{x}10^{-4}$
Circularity	0	0.488	0.039	0.158	0.889	$4.77\text{x}10^{-10}$	0.736	0.981	0.744	0.973
Burr height	0	0.798	0.032	$5.34\text{x}10^{-6}$	0.480	0.143	$3.63\text{x}10^{-6}$	0.558	0.026	0.016
Surface roughness (R_a)	0	0.669	0.564	0.667	0.846	$2.99\text{x}10^{-4}$	$2.89\text{x}10^{-3}$	0.954	0.257	0.048

Table 6.3: P-value overview table of the factors within each response linear model. Terms with p-values lower than 0.05 correspond to a 5% statistical significance, and are underlined.

Prior to conducting the trials, the tools were inspected and measured using the methodology described in Section 4.13 and the variation from the nominal edge rounding of 36µm are shown in Table 6.4.

Tool number	Edge rounding, µm
Tool 1	24
Tool 2	31
Tool 3	28
Tool 4	36

Table 6.4: Cutting edge rounding radius on the cutting lip of the four tools used in the trials observing the effects on the forces and hole quality.

6.4.1 Normal Forces

The model and the method as outlined in Figure 6.6 is presented for the normal force response. The data sample used in the model is normally distributed, with a normally distributed histogram (despite the two peaks caused by the coarseness of the data) and normal probability plot close to the regression line, Figure 6.7a and 6.7b. This validates the normal distribution assumption of the model, and validates the p-values obtained.

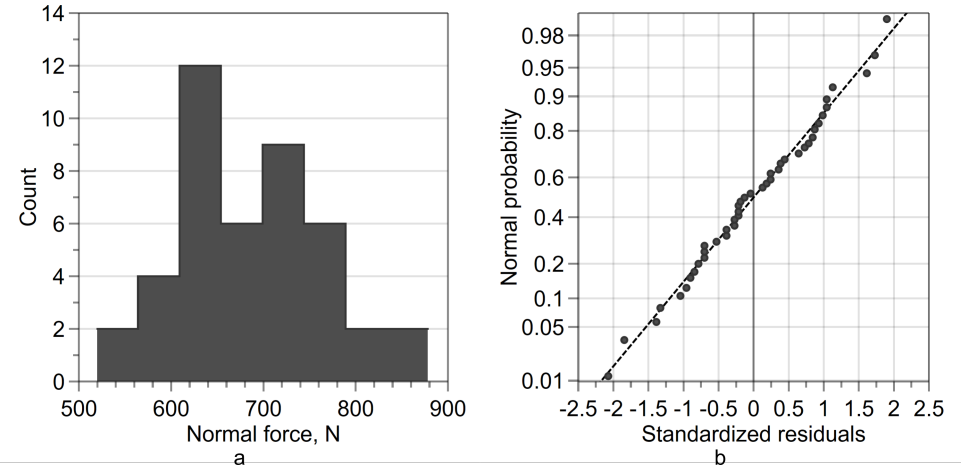

Figure 6.7: Normal distribution of data used in the normal force model shown through a. frequency of data histogram b. normal probability plot.

The contribution of each term in the model is shown in Figure 6.8 as a scaled and centred plot to show the relative impact of each of the factors in the model.

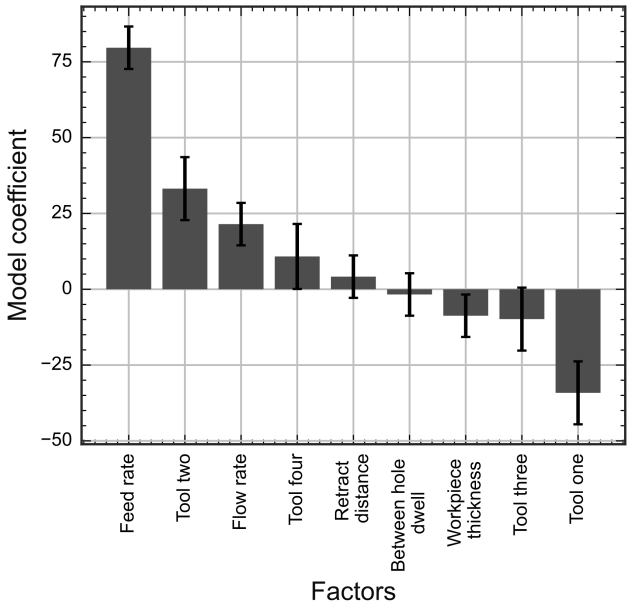

Figure 6.8: Values of the coefficients in the normal force model, scaled and centred to show the relative significant of each of the factors in the model. (fitted with Partial Least squares method)

With all the factors studied included in the model, the statistical metrics are R^2= 0.93, Q^2= 0.88, validity = 0.26 and reproducibility = 0.94. Removing the retract distance and between hole dwell factors from the model, the model is improved with R^2= 0.94, Q^2= 0.91, validity = 0.75. This shows that the model represents the data closely, with good repeatability and reproducibility within the parameter range of the chosen experimental design region.

Using the improved model, the equation for each of the tool is presented in Equations 6.2, with constant term A for each tool and the confidence intervals for the equation shown in Table 6.5.

$$F_z = A + 10.74FL + 1991Feed - 2.184WT \tag{6.2}$$

		95% Confidence interval	
Term	Value	Lower	Upper
Tool 1 (constant)	267	222.1	311.4
Tool 2 (constant)	334	272.7	395.5
Tool 3 (constant)	291	229.6	352.5
Tool 4 (constant)	312	249.9	373.6
Mass flow rate	10.74	7.26	14.22
Feed	1991	1817	2165
Workpiece thickness	2.184	-3.923	-0.444

Table 6.5: The constants and confidence interval for each of the terms within the normal force linear model.

The tools have been shown to influence the normal force, this is expressed as different constant values

in the equations. This variation is explained through the slight differences in tool geometry. An increase in the cutting edge rounding, measured prior to cutting using the method described in Section 4.13, results in an increase in the normal force obtained (Figure 6.9). The cutting edge rounding is within the manufacturing tolerance, indicating the sensitivity of tool manufacturers tolerance on the normal force.

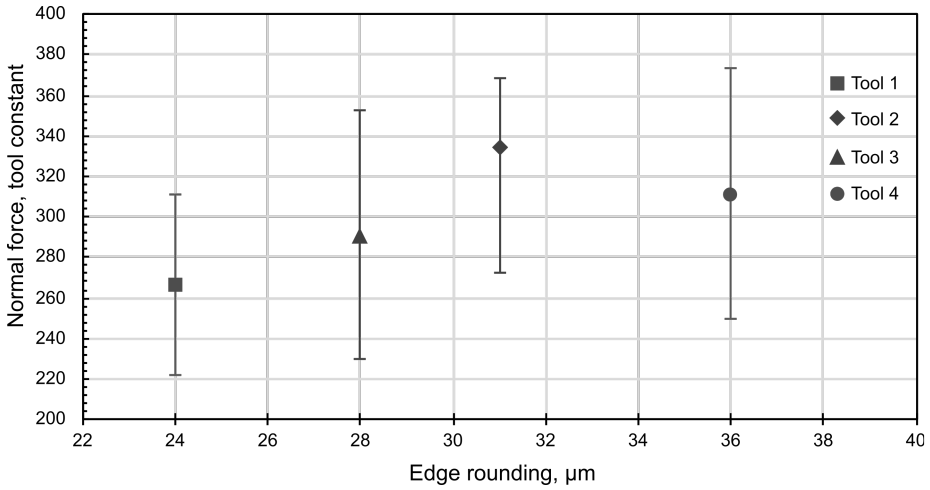

Figure 6.9: Relationship between normal force constant term from the model and the cutting edge rounding.

6.4.2 Torsional forces

The relative contribution of each of the terms within the initial model of the torque is presented in Figure 6.10 as scaled and centred coefficients. The figure shows the feed contributing most to the model, while flow rate and retract distance somewhat, supporting the low p-values (Table 6.3).

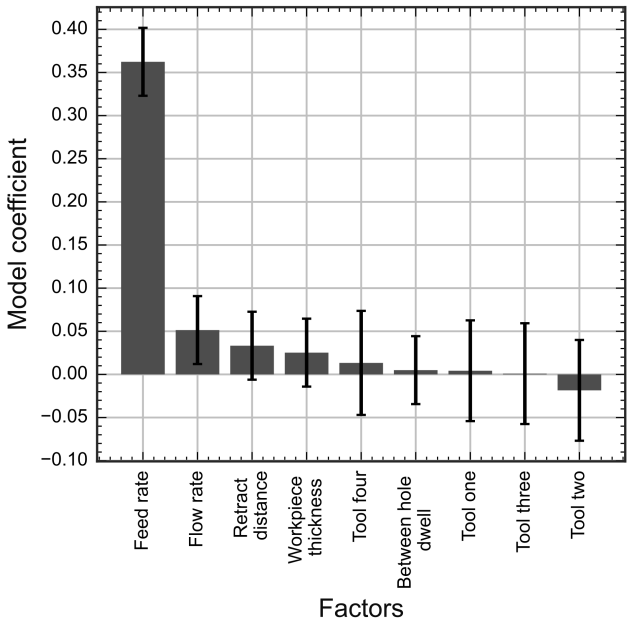

Figure 6.10: Values of the coefficients in the torsional force model, scaled and centred to show the relative significant of each of the factors in the model. (fitted with Partial Least squares method)

The statistical metrics for the initial model, with all terms present, are R^2 = 0.9, Q^2 = 0.86, validity = -0.2 and reproducibility = 0.94. The tools and the between hole dwell appear to have no influence on the torque, with error bars straddling zero. Validity appears low because of the inclusion of terms that have little impact on the model.

Removing the terms associated with each tool and the between hole dwell, and including a squared term, the statistical metrics of the model are improved to R^2 = 0.93, Q^2 = 0.9, validity = 0.4 and reproducibility = 0.94, the empirical model for the torque is described by Equation 6.3.

$$Torque = 1.259 - 0.40FL + 9.06Feed + 0.0063WT + 0.0051RD + 0.027FR^2 \tag{6.3}$$

	95% Confidence interval	
Term	Lower	Upper
Constant	0.229	2.289
Mass flow rate	-0.00157	-0.00110
Feed	-0.0258	-0.0023
Workpiece thickness	0.00010	0.00033

Table 6.6: The confidence interval for each of the terms within the least squares diameter linear model.

6.4.3 Chip form

The model for the chip form, coded where a higher value depicts poorer longer chips, is presented. The values of the scaled and centred coefficients in the model are shown in Figure 6.11. The model shows that with increasing workpiece thickness, chip formation deteriorates. Increased LCO_2 mass flow rate gives improved chip formation, as well as increased feed rate, as previously found.

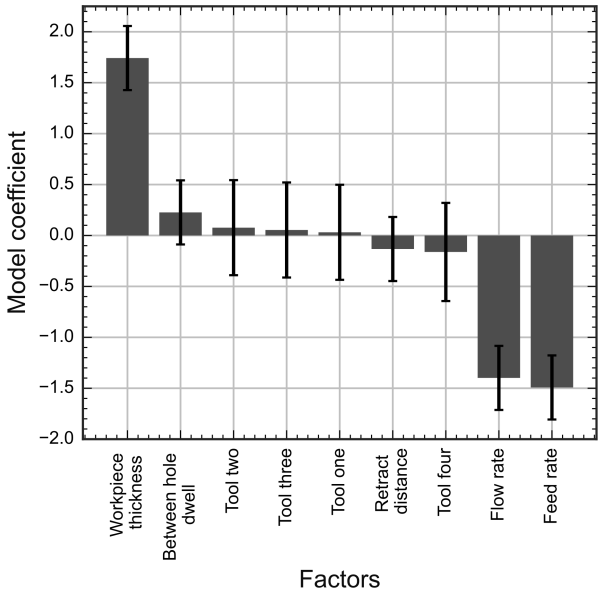

Figure 6.11: Values of the coefficients in the chip form model, scaled and centred to show the relative significant of each of the factors in the model. (fitted with Partial Least squares method)

The initial model that is presented in Figure 6.11 has statistical metrics of R^2 = 0.90, Q^2 = 0.74, validity = -0.2, and reproducibility = 0.97. From this initial model the effect of the tools, and between hole dwell and retract distance have minimal contribution to the model.

Tests of the normality of the data were conducted, and the data was slightly positively skewed due to the greater number of trials with adequate chip formation, and the inability to differentiate between the quality of the chips. Conducting a log transformation on the data, however, did not improve the distribution, Equation 6.4 shows the relationship for the chip form.

$$ChipForm = 11.17 - 0.671FL - 36.62Feed + 0.443WT \tag{6.4}$$

	95% Confidence interval	
Term	Lower	Upper
Constant	9.206	13.142
Mass flow rate	-0.829	-0.514
Feed	-44.55	-28.69
Workpiece thickness	0.363	0.522

Table 6.7: The confidence interval for each of the terms within the chip form linear model.

6.4.4 Hole quality

6.4.4.1 Cylinder (max inscribed)

The cylinder max inscribed measurement indicates the largest cylinder that can be inserted in to the hole. Described be practically as the smallest bolt or screw that can be inserted in to the hole. The model for

this response is presented, and the model coefficients for the scaled and zero model are shown in Figure 6.12. The initial model presented in Figure 6.12 had statistical metrics of R^2 = 0.38, Q^2 = 0.15, validity = 0.79, reproducibility = 0.28.

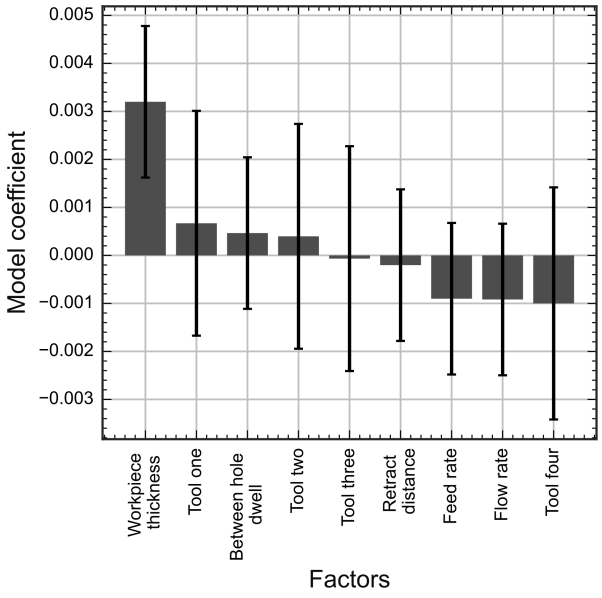

Figure 6.12: Values of the coefficients in the cylinder(max inscribed) model, scaled and centred to show the relative significant of each of the factors in the model. (fitted with Partial Least squares method)

The model shows that the cylinder (max inscribed) is primarily influenced by the workpiece thickness. In that, with increased workpiece thickness the cylinder diameter increases. As shown previously the workpiece thickness influences the circularity of the hole, with a rounder hole seen with thicker workpiece thickness. Thus, the greater stability of the drill in machining thicker workpieces results holes with larger cylinder(max inscribed). Increased circularity implies that the hole is generally more deviant from an idealised perpendicular cylinder geometry, than the size of the ideal cylinder, which you can fit inside that hole. Therefore it becomes smaller.

Other factors studied in the experiment show to have minimal influence on the cylinder(max inscribed) diameter.

After removing the factors that have minimal influence on the cylinder(max inscribed) from the model the statistical metrics improved to R^2 = 0.33, Q^2=0.29 , validity= 0.88, reproducibility=0.28. These metrics remain low due to high replicate variability and noise within the data. Improved model accuracy could be achieved with further study specifically by omitting factors in the study deemed to have no influence, increasing the number of replicates and increase the number of CMM circles taken in each hole to improve the cylinder calculation resolution.

$$Cylinder(MI) = 6.0087 - 0.0225Feed + 0.0008WT \tag{6.5}$$

	95% Confidence interval	
Term	Lower	Upper
Constant	6.0014	6.0161
Feed	-0.0609	0.0158
Workpiece thickness	0.00042	0.0012

Table 6.8: The confidence interval for each of the terms within the cylinder (MIC) linear model.

The model has a high error of 68% (64% due to pure error, or error in experiment), due to the low value of the measurement, and high sensitivity to error, thus greater probability of an outlier being present. This can be alleviated by more measurements within the hole for these characteristics.

6.4.4.2 Diameter (least squares)

The model is formed from the mean values of the diameter least squares measurements at the beginning middle and end of the holes, method described in Section 4.16. The initial model presented in Figure 6.13 had statistical metrics of $R^2 = 0.82$, $Q^2 = 0.67$, validity = 0.80, reproducibility = 0.67.

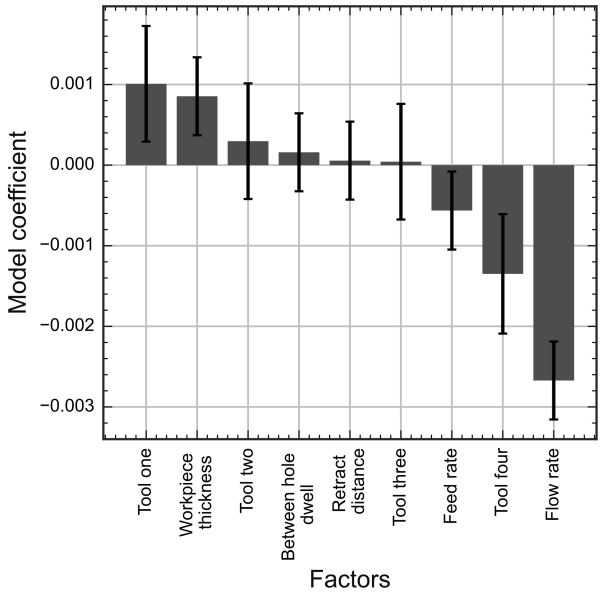

Figure 6.13: Values of the coefficients in the cylinder(max inscribed) model, scaled and centred to show the relative significant of each of the factors in the model. (fitted with Partial Least squares method)

Within the model, the factors LCO_2 mass flow rate, feed, workpiece thickness and tools 1 and 4 are statistically significant, see Table 6.3. The model shows that the increased LCO_2 mass flow rate results in hole diameter closer to the nominal. This influences the hole diameter due to the thermal contraction of the drill, resulting in a smaller tool diameter, and confirms the correlation discussed in Section 6.3.1. Increased workpiece thickness results in larger hole diameter, likely due to increased drill temperature and diameter, drilling through the thicker workpiece. The between hole dwell and retract distance appear to have little thermal impact on the tool, evidenced through no changes in the hole diameter in the model.

The influence of the tools is understandable owing to the difference in the tool diameter across the batches of the tools.

After removing the non-significant factors from the model and refitting the data to form a new model, the statistical metrics of the model were improved to R^2 = 0.82, Q^2= 0.7 , validity = 0.88, reproducibility = 0.68. The mathematical equations describing the model are in Equation 6.6.

$$D_{lsq} = A - 0.00134FL - 0.0141FR + 0.00214WT \tag{6.6}$$

Within the models of each of the least squares diameter for the tools, the confidence intervals at 95% for each of the terms within are presented in Table 6.9.

		95% Confidence interval	
Term	Value	Lower	Upper
Tool 1 (constant)	6.0450	6.0420	6.0480
Tool 2 (constant)	6.0443	6.0401	6.0484
Tool 3 (constant)	6.0440	6.0399	6.0482
Tool 4 (constant)	6.0427	6.0386	6.0469
Mass flow rate	0.00134	-0.00157	-0.00110
Feed	0.0141	-0.0258	-0.00234
Workpiece thickness	0.00214	0.0001	0.0003

Table 6.9: The confidence interval for each of the terms within the least squares diameter linear model.

6.4.4.3 Circularity

The circularity of the holes was captured at three locations for each hole, as described in the method in Section 4.16. The initial model presented in Figure 6.14 had statistical metrics of R^2 = 0.67, Q^2 = 0.53, validity = 0.93, reproducibility = 0.54. From Table 6.3 and Figure 6.14 showing the scaled and centred coefficients of the initial model, indicate that there are only two significant factors in the model, namely the LCO_2 mass flow rate and the workpiece thickness.

With increasing workpiece thickness the circularity of the hole improves, implying that the tool is more stable with the deeper hole. This is possibly due to the greater area of contact of the drill margin in the hole to steady the drill during the cut, and not relying on the chisel for centring the drill to as much of an extent as with the thinner workpiece thicknesses.

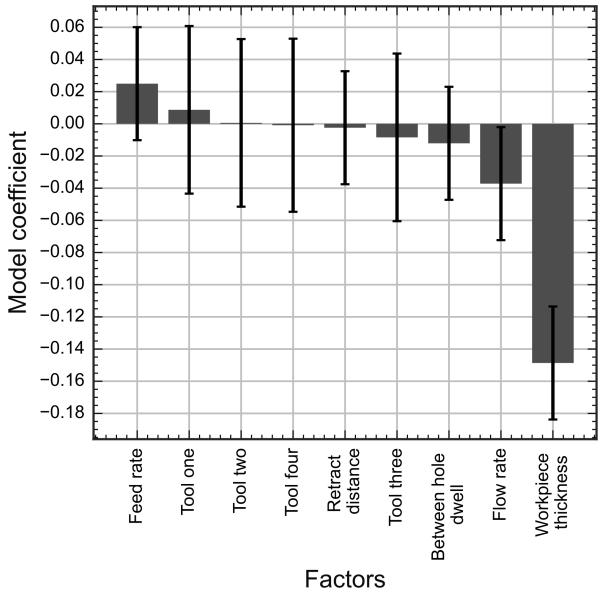

Figure 6.14: Values of the coefficients in the circularity model, scaled and centred to show the relative significant of each of the factors in the model. (fitted with Partial Least squares method)

6.4.4.4 Burr height

Burr height was measured for each of the holes, using the method described in Section 4.16. Presented is the model of the factors fitted to this burr height data. The initial model presented in Figure 6.15 had statistical metrics of R^2 = 0.67, Q^2 = 0.53, validity = 0.93, reproducibility = 0.54. From the p-values in Table 6.3 and Figure 6.15 the feed and tools are the most significant factors within the model in terms of their influence on the hole exit burr height. With increased feed rate, the exit burr height increases, which is similar to what was observed in the initial experiments, Section 5. The relationship between the tool edge rounding and the tool constant model terms for each drill shows no relationship (Figure 6.16) and the contributing influence of tool one is unknown.

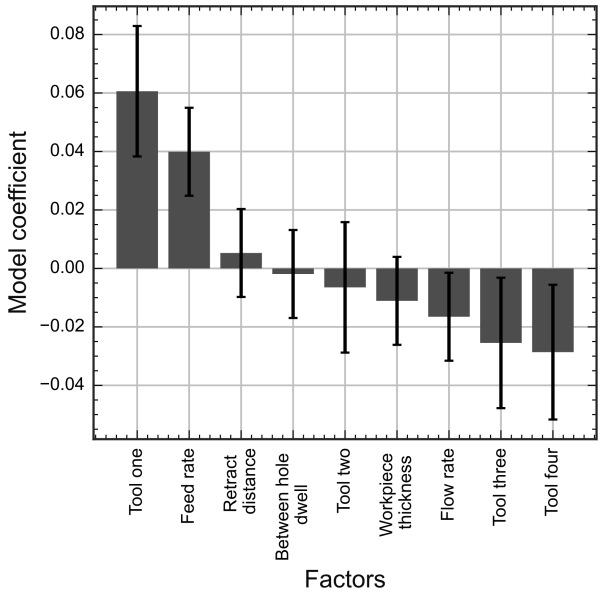

Figure 6.15: Values of the coefficients in the cylinder(max inscribed) model, scaled and centred to show the relative significant of each of the factors in the model. (fitted with Partial Least squares method)

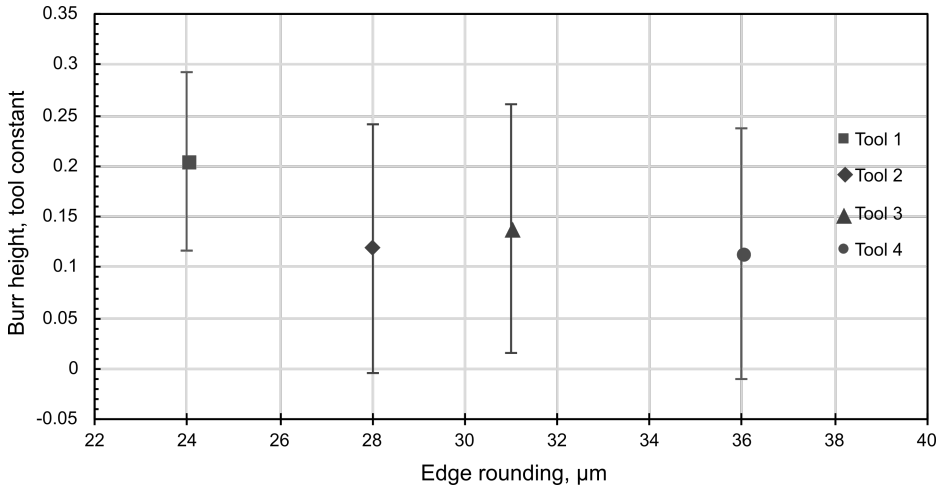

Figure 6.16: Tool burr height model tool constant and edge rounding comparison.

Removing the non-significant factors from the model, the statistical metrics improved to R^2 = 0.64, Q^2= 0.56 , validity = 0.65, reproducibility = 0.64. The equation for the burr height is presented in Equation 6.7. The reason for the low metrics are possibly due to the nature of the burr height that is measured. The maximum burr height is measured because this will be the offset of the plate when it is located on the part. However, in doing so, on occasion there burr height is non-uniform and results in a maximum peak of the burr. .

$$BurrHeight = A + 0.998Feed - 0.00827FL \tag{6.7}$$

		95% Confidence interval	
Term	Value	Lower	Upper
Tool 1 (constant)	0.205	0.1177	0.2924
Tool 2 (constant)	0.138	0.0149	0.2610
Tool 3 (constant)	0.119	-0.0041	0.2420
Tool 4 (constant)	0.114	-0.009	0.2371
Feed	0.998	-0.0258	-0.0023
Mass flow rate	0.00827	0.00010	0.00033

Table 6.10: The confidence interval for each of the terms within the burr height linear model.

6.4.4.5 Surface roughness (R_a)

The initial model for the surface roughness of the holes was fitted using the data from the measurements of the hole, captured using the methods described in . The initial statistical metrics of the model were $R^2 = 0.46$, $Q^2 = 0.27$, validity = -0.2, reproducibility = 0.74. Figure 6.17 shows the unscaled and centred model coefficients, showing that tool one and four as well as the workpiece thickness are the most influential in the model. This is in agreement with the p-values displayed in Table 6.3.

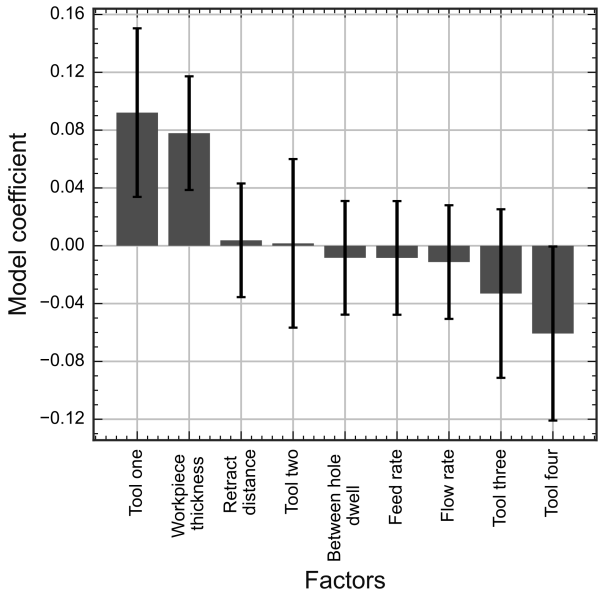

Figure 6.17: Values of the coefficients in the cylinder(max inscribed) model, scaled and centred to show the relative significant of each of the factors in the model (fitted with Partial Least squares method).

After removing these factors from the model the statistical metrics improved to $R^2 = 0.44$, $Q^2 = 0.35$, validity = -0.2, reproducibility = 0.74. The model for the surface roughness is weak and the factors in the model poorly represent the surface roughness, due to having little effect on it. While the model is presented in Equation 6.8 for completeness, it can not be used for predicting the surface roughness.

$$R_a = A + 0.0195WT \tag{6.8}$$

		95% Confidence interval	
Term	Value	Lower	Upper
Tool 1 (constant)	0.5128	0.399	0.626
Tool 2 (constant)	0.4223	0.218	0.626
Tool 3 (constant)	0.3876	0.183	0.592
Tool 4 (constant)	0.3707	0.166	0.574
Workpiece thickness	0.0195	0.010	0.028

Table 6.11: The confidence interval for each of the terms within the least squares diameter linear model.

6.5 Conclusions of chapter

This chapter has presented the first the LCO_2 process parameter study in solid carbide drilling of Ti6Al4V. The experiments were conducted with the force dynamometer set-up and as such the cutting forces in the process were the primary factor studied. The effect of different LCO_2 process parameters on the key responses have been studied.

- The D-optimal experimental design has been conducted successfully and data for each of the responses sucessfully captured.
- Of the process parameters studied within the trial the coolant mass flow rate was deemed to be the most significant. The between hole dwell and the retract distance parameters had little significant impact on the responses measured. One reason for this may be that the levels of these parameters were not sufficiently different to enact a large enough effect on the responses. However, the factor levels were at either end of the predicted range of parameters used in an industrial application. To further expand the parameters to obtain a larger response would have been unrealistic, and not a representative study.
- The thickness of the workpiece and the drill feed were identified as significant factors on the responses studied.
- The relationship of the factors to the responses studied were modelled linearly, and empirical relationships between the key responses and significant terms were created. Of note, the models for the normal and torsional forces were closely modelled with high statistical metrics.

7 The effect of process variables on the temperatures generated

The previous chapter dealt with observing the effect of the LCO_2 process parameters on the cutting forces and the hole quality. The key process parameters were identified, and the number of variables were reduced by removing the insignificant variables. The focus of the work described in this chapter was to further explore the LCO_2 parameters, with fewer variables to understand how they influence the temperature.

Many of the benefits of using LCO_2 and other cryogenic media have been attributed to a decrease in the cutting temperature. Therefore, a study observing a cryogenic drilling process would not be complete without studying temperature. The aims of this chapter are to:

1. Study the previously determined important LCO_2 process parameters (Chapter 6), LCO_2 mass flow rate, feed and workpiece thickness, within a full factorial experimental design using the temperature measurement experimental set-up, Section 4.15.
2. Identify the influence of the LCO_2 mass flow rate, workpiece thickness, and feed on the temperature.
3. Explore the previously determined hypotheses of the relationship of the temperature to the hole diameter and workpiece thickness.
4. Observe the temperature effects when adopting a pecking cycle.
5. Observe the temperature effects over a different number of drilled holes to ascertain the stability of the process.

7.1 Overview of the experiment design

This experiment observes the factors identified as most significant to the performance of the LCO_2 process, namely the LCO_2 mass flow rate, workpiece thickness and the drill feed. The trials observed the temperature at the drill exit using an infrared camera, for details of the experimental set-up refer to Section 4.15. Measurements of the hole quality were also completed.

The experimental design used in the trials, shown in Table 7.1, was a full factorial design at two levels with centre points for each of the factors.

Factor	Levels
Mass flow rate, kg/hr	6, 8, 10
Workpiece thickness, mm	6, 10, 14
Feed, mm/rev	0.12, 0.16, 0.2

Table 7.1: The factors and levels studied in the experiment observing the temperature at the drill hole exit.

The experiment consisted of 8 runs, corresponding to the two levels of the three factors with three centre points. This was repeated, for two replicates, for a total of 22 runs completed. The run order of these runs is presented in Table 7.2. The centre points of the experiment were spaced evenly throughout the experiment, and the other runs were randomised.

For each run the temperature of three holes were gathered according to the methods described in Section 4.33. The arithmetic mean of these values was calculated and is thus presented for each run.

Run number	Workpiece thickness, mm	Mass flow rate, kg/hr	Feed, mm/rev	T, °C
1	10	8	0.16	376
2	14	10	0.2	260
3	14	10	0.12	255
4	6	6	0.12	400
5	10	8	0.16	369
6	14	6	0.2	446
7	14	10	0.12	312
8	6	10	0.12	263
9	10	8	0.16	364
10	6	6	0.2	344
11	14	6	0.2	378
12	6	10	0.2	181
13	6	10	0.2	200
14	10	8	0.16	348
15	6	6	0.12	367
16	14	6	0.12	403
17	6	10	0.12	190
18	10	8	0.16	323
19	14	10	0.2	224
20	6	6	0.2	355
21	14	6	0.12	399
22	10	8	0.16	329

Table 7.2: Run order for the factors in the experiment observing the hole exit temperature.

7.2 Mathematical model for temperature

The temperature data, shown in Table 7.2 was analysed using the process described in Section 6.4, to determine the relevance of each factor, the quality of the data, and determine that the data is normally

distributed for fitting the regression model.

Using the captured mean temperature data, the data was fitted using the partial least squares method. An interaction model was used and thus interaction terms are present. The contribution of each of the factors in the model are presented in Figure 7.1. These data show that the LCO_2 mass flow rate and the workpiece thickness are the most significant factors. With increasing LCO_2 mass flow rate the drill exit temperature is reduced, and with increasing workpiece thickness the drill exit temperature is increased. It appeared that the feed and the interaction terms did not have any influence on the drill exit temperature.

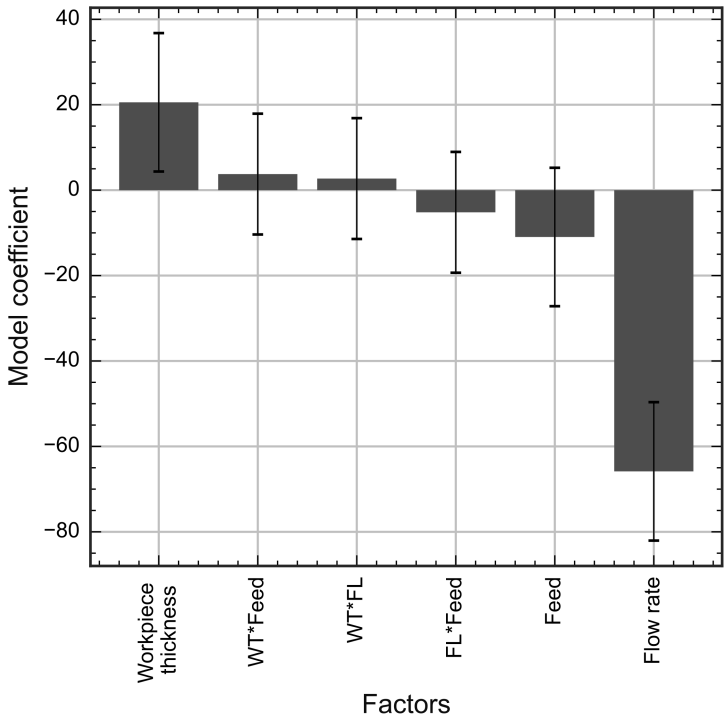

Figure 7.1: The relative importance of each factor on the hole exit temperature during drilling.

An improvement in the mathematical model was achieved through removing the interaction and feed terms from the model, and adding a square term for the LCO_2 mass flow rate. This resulted in improvements to the statistical metrics of the model of $R^2 = 0.88$, $Q^2 = 0.82$, validity = 0.77, reproducibility = 0.86.

Using this model, Equation 7.1, the influence of the the LCO_2 mass flow rate and workpiece thickness are plotted in Figures 7.2a and 7.2b with 95% confidence intervals. They show how, with increasing LCO_2 mass flow rate the drill exit temperature is reduced at an increasing rate, and with increasing workpiece thickness the temperature generated increases. The three-way interaction between the LCO_2 mass flow rate, the workpiece thickness and the drill exit temperature is summarised in Figure 7.2c. The reduction in the temperature with LCO_2 mass flow rate is as expected, due to the increased heat removal capacity of the fluid. This is in line with similar experiments in 42CrMo4 steel observing temperature at the drill exit [140]. The findings on the temperature effect are however valid for the region studied only and cannot be extrapolated for increased mass flow rates. To understand the relationship at these higher flow rates, further trials would be required on a different machine as it is beyond the capacity of

this machine.

$$Temperature(^{\circ}C) = -52 + 5.89WT + 124FL - 10.1FL^2 \tag{7.1}$$

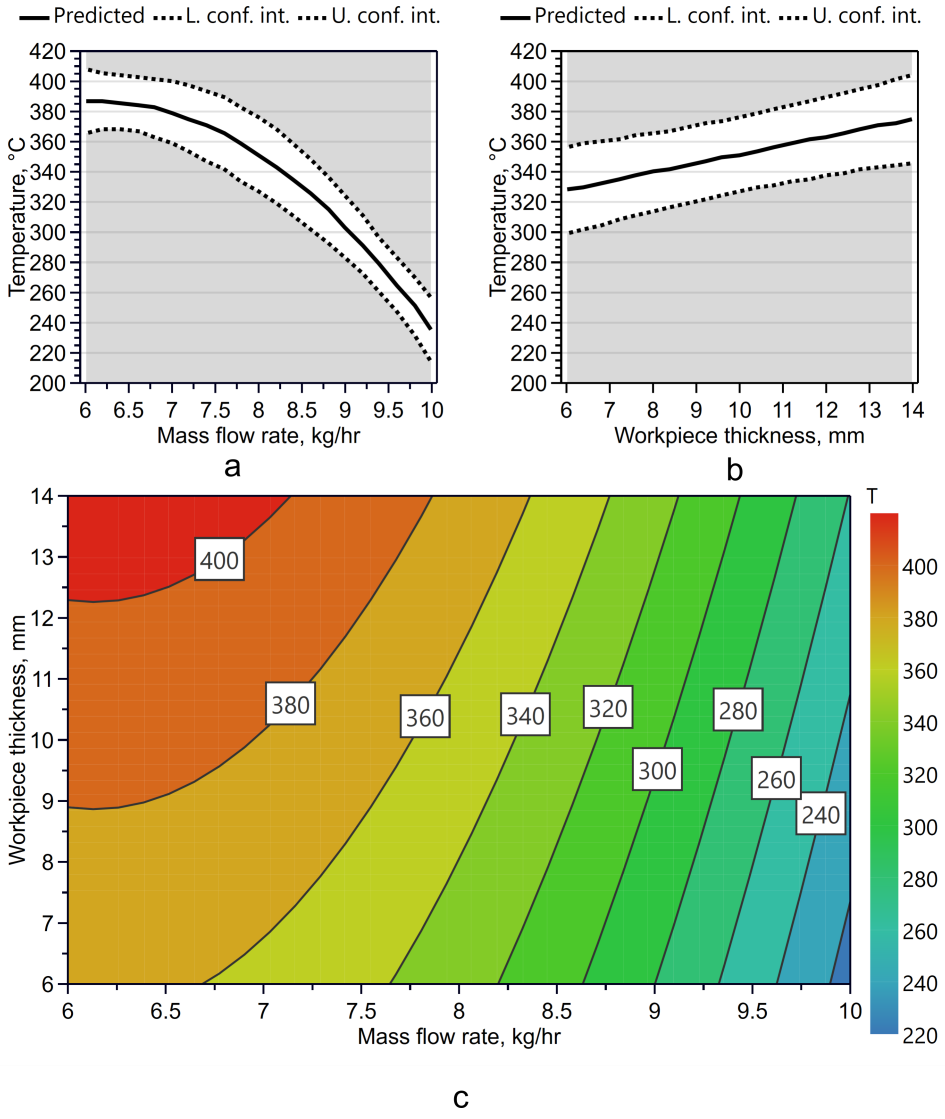

Figure 7.2: The effects of mass flow rate and workpiece thickness on the drill exit temperature. a. Main effect plot of LCO_2 mass flow rate on drill exit temperature. b. Main effect plot of workpiece thickness on the drill exit temperature. c. The contour plot of the expected drill exit temperature across the tested range of the LCO_2 mass flow rate and workpiece thickness. The confidence intervals are set at 95%.

7.2.1 The relationship between drill exit temperature, hole quality and drill parameters

The hypothesis of "the diameter of the drilled will be smaller because of a lower cutting temperature, thus contracting the diameter of the drill" was explored. To do this a new tool was used for each run, which had its own unique geometry.

The geometry of each tool was captured and was inspected for flaws. Specifically the diameter, run-out and edge rounding characteristics were measured using the methods described in Section 4.16. These measurements are presented in Figure 7.3 and 7.4 for each tool and the order in which that tool was used across the 22 runs carried out. The measurements of the tool diameter show that the median diameter of the tools was 6.002mm with an upper limit of 6.015mm and lower limit of 5.992mm. The tools are manufactured to a tolerance of G7 (+0.004/+0.016) therefore some the tools appear undersized. The median run-out measurement of the tools was 0.002mm with a range of 0.006mm, there was one tool with run-out measured 0.015mm.

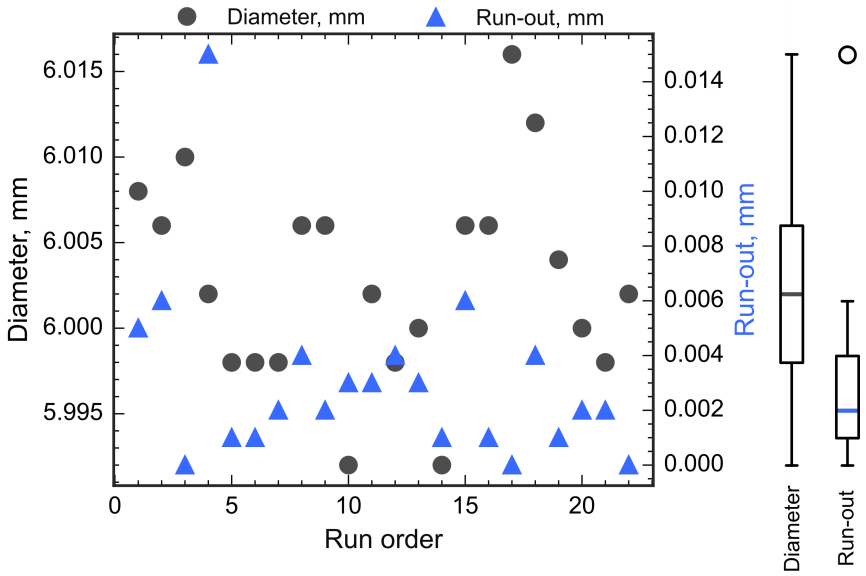

Figure 7.3: Measurements of the drill diameter and run-outs that were used in the temperature experiments.

The tool edge rounding radius on the cutting edge lip of the tools and the radius shape (Kappa) are presented in Figure 7.4. The nominal edge rounding radius for the tools is 30µm, the median value of the measured tools is 33µm. The median Kappa of the tools was 0.95, slightly below the nominal 1.00.

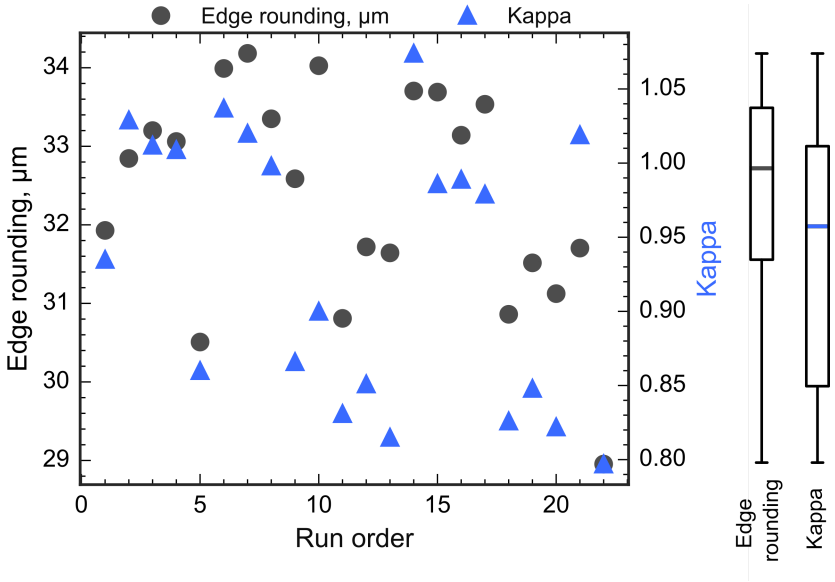

Figure 7.4: Measurements of the drill edge rounding and kappa measurements that were used in the temperature experiments.

Circularity influences the diameter (max inscribed circle), and decreases with increasing workpiece thickness. This is similar to results found in Section 6.4.4.3, where drill stability was deemed as the influencing factor.

7.2.2 Cutting feed

The scatter plots, data distributions and box-plots of the data, grouped according to the feed used in the experiment are presented as a pair plot in the Figure 7.5. The figure shows, for the three cutting feed values used, the relationship between the cutting feed, the maximum temperature, burr height and hole quality metrics. The data for the temperature shows close repeatability around the median of 350°C and a burr height of 0.2mm. Indicating a well controlled experiment for this variable over the time of the experiment. The data shows that there is minimal influence of the feed on the temperature, with a flat distribution of the data for both the upper and lower feed rates used. The flat distribution is indicative of another factor influencing the temperature. As previously observed, the burr height has been found to increase with increasing feed. There is little data to suggest the feed has any influence on the hole geometry in this study, only that it is worth noting that the three smallest diameter measurements occurred at the lower drill feed.

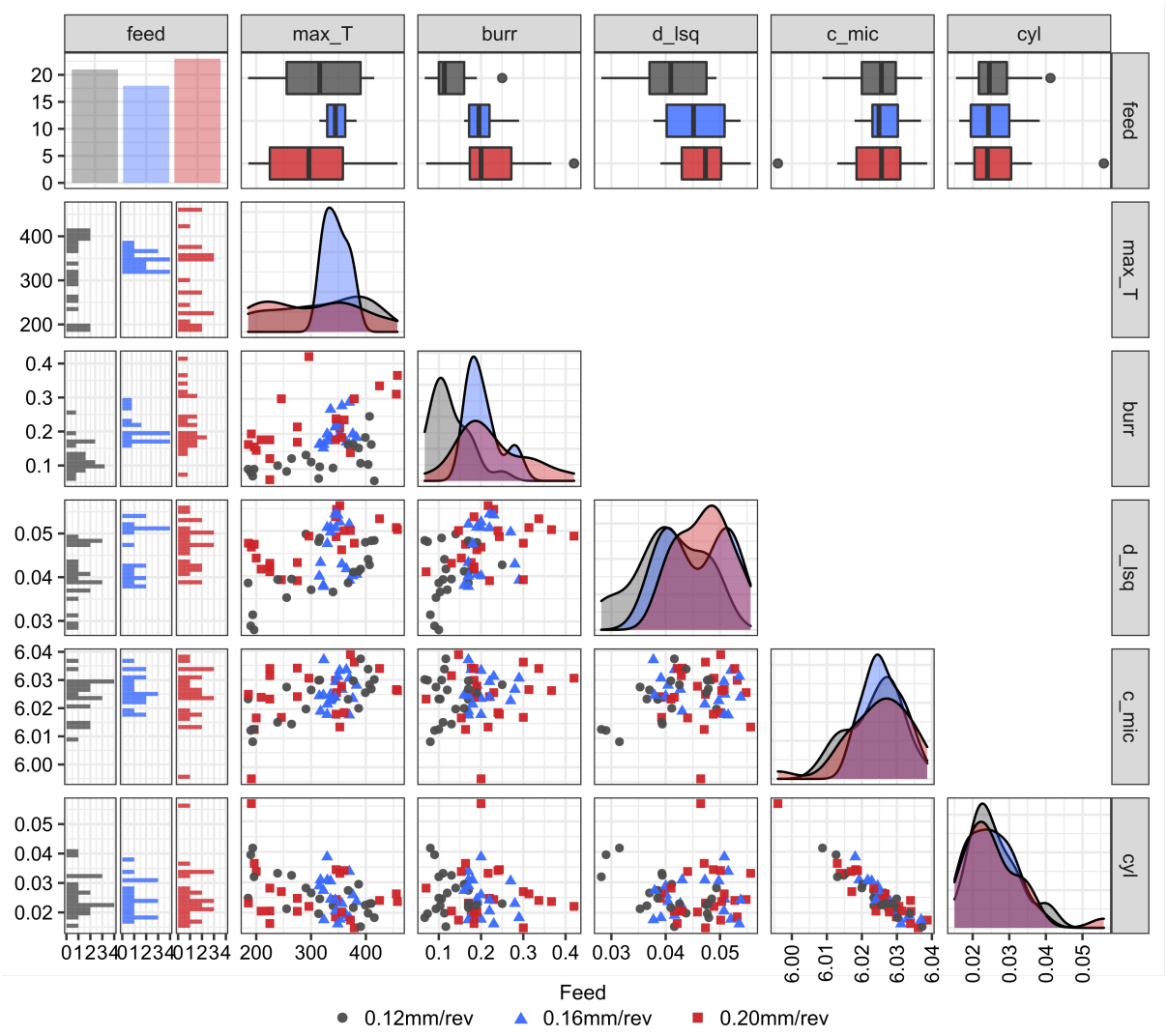

Figure 7.5: The pair plot of the temperature and hole quality, from the experiment capturing drill exit temperature, is presented with the data points coded according to the feed.

7.2.3 LCO_2 mass flow rate

The scatter plots, distribution and boxplots of the data, now organised according to the LCO_2 mass flow rate are presented in the pair plot in Figure 7.6. The data clearly shows the non-linear relationship of the maximum temperature with the mass flow rate, obtained and presented in Section 7.2. The relationship between the max inscribed diameter and the cylindricity of the hole is clearly negatively linear. Improvements in the burr height are observed with the higher mass flow rates, implying that at the higher flow rates and the cooler temperature plastic deformation of the material is minimised leading to smaller burr height. The median burr height is 0.15mm at 10kg/hr as opposed to 0.2mm for 8kg/hr and 6kg/hr. This is inline with the burr height findings found in Chapter 6.

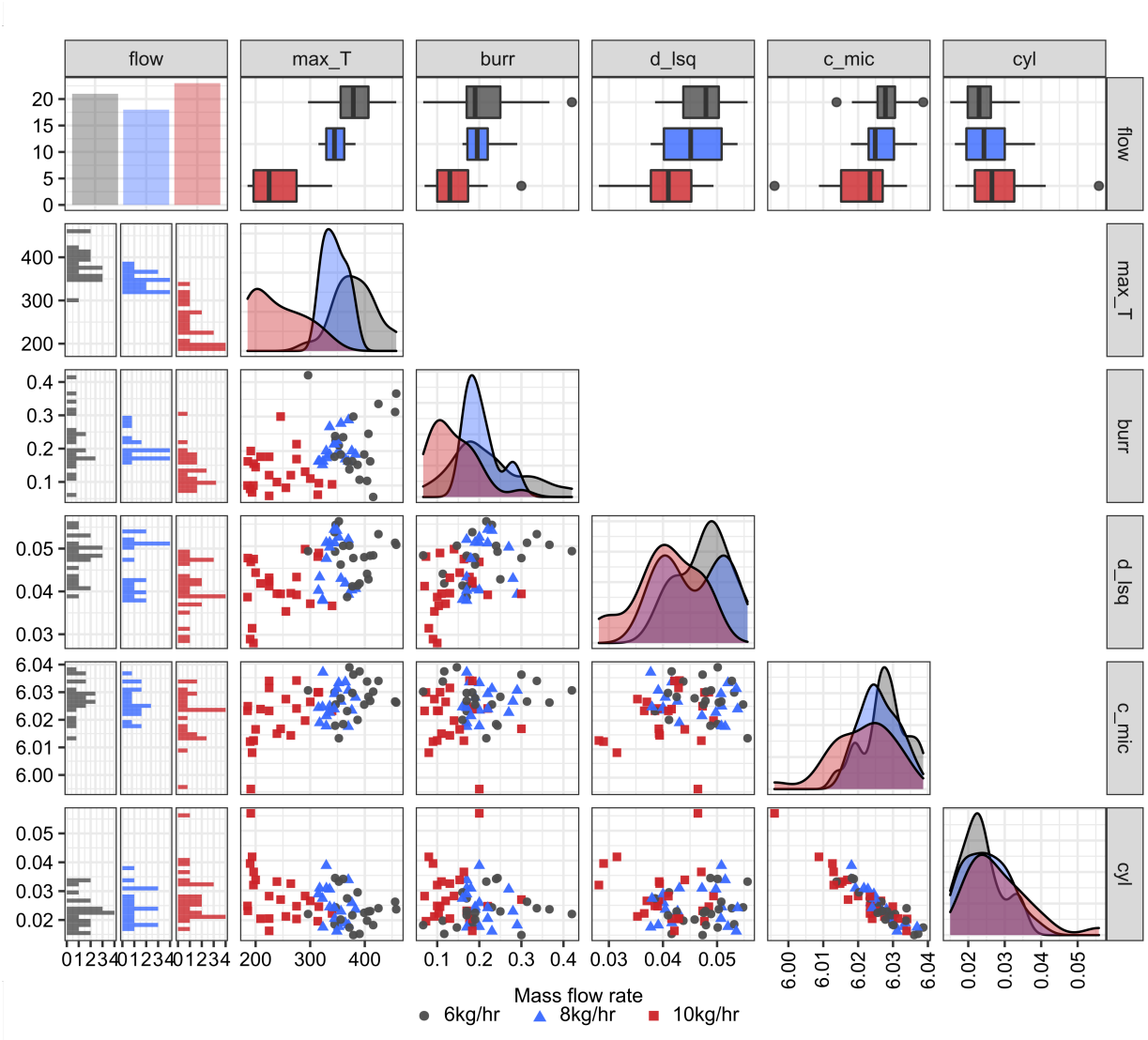

Figure 7.6: The pair plot of the temperature and hole quality, from the experiment capturing drill exit temperature, is presented with the data points coded according to the LCO_2 mass flow rate.

7.2.4 Workpiece thickness

Figure 7.7 shows the pair plot of the pertinent data for the temperature focused experiment, with the data organised according to the thickness of the workpiece. The workpiece thickness, as previously modelled shows decrease in the observed temperature measurement for thinner workpieces. This relationship is also somewhat non-linear. Data presented in this pair plot highlights the difference in the hole circularity at the entrance, middle and exit of the hole, taken as the three measurements conducted, as detailed in Section 4.16. They show the interrelationship of the max inscribed diameter measurement, the cylindricity measurement and the circularity measurements. The results show that, at increased workpiece thickness, the maximum inscribed diameter is highest. This is due to the improved roundness of the hole and not a reduction in the hole diameter, as observed by the little difference in the gauge diameter least squares measurements of the holes and the increased value of the cylindricity and circularity

for the thinner workpiece thickness. This supports the hypothesis from earlier.

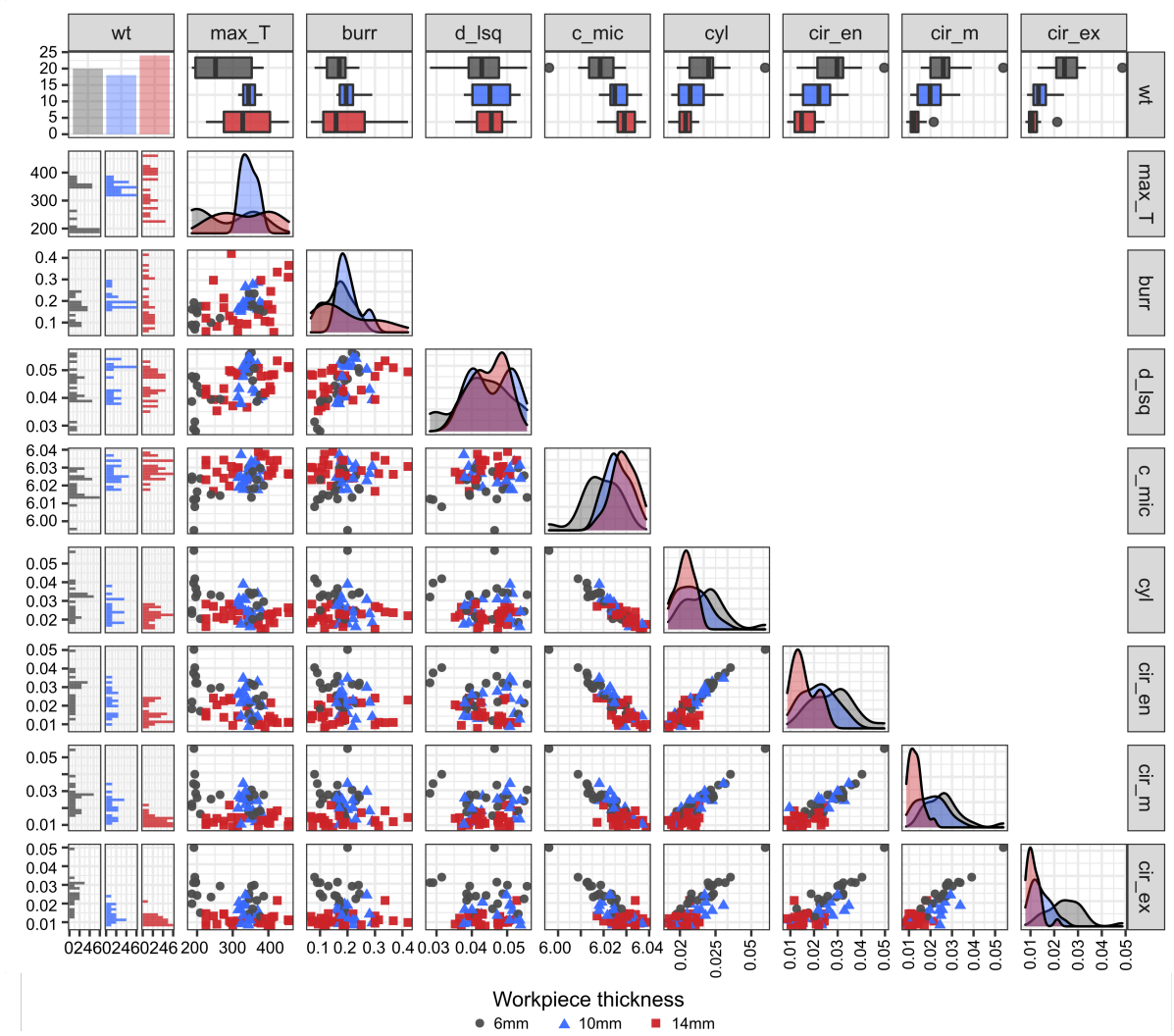

Figure 7.7: The pair plot of the temperature and hole quality, from the experiment capturing drill exit temperature, is presented with the data points coded according to the workpiece thickness.

The findings can be summarised by grouping the feed and the workpiece thickness together in terms of the time in cut. This was calculated by $t_{in-cut(s)} = \frac{workpiece\ thickness(mm) \times 60}{feed\ rate(mm/min)}$.

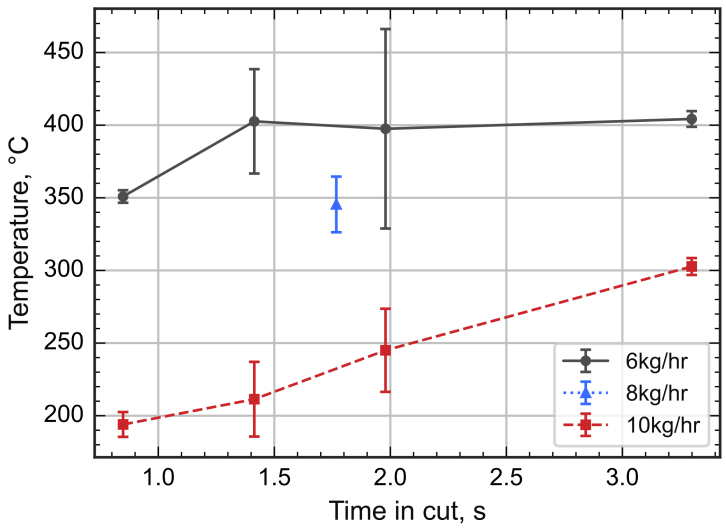

Figure 7.8: Relationship between time in cut and temperature for the different flow rates.

The results have shown the LCO_2 mass flow rate to have the greatest influence on the cutting temperature. The mass flow rate is limited to a maximum of 10kg/hr on the machine, with further increases not achievable with the current machine set-up. Further improvements to the cutting tool performance have been shown with higher mass flow rates upwards of 40kg/hr [115]. As the process is limited in the mass flow rate, alternative ways of improving the cooling capacity and hence performance can be explored. One of these involves exploring the improvements observed by reducing the time in cut through a pecking cycle.

7.3 Drill cycle study (peck drilling)

The influence of the peck on the cutting temperature is explored. A pecking cycle involves drilling through the hole in stages. For example a 10mm hole can be drilled in four cuts by drilling 2.5mm retracting the drill in the opposite direction to the drill feed before then repeating three times to drill through the 10mm plate.

All tests were conducted on plate 10mm thick, with a mass flow rate of 10kg/hr at 40m/min and 0.2mm/rev. The testing of the pecking cycles was done using two pecking cycles. The details for these pecking cycles are shown in Table 7.3, with z=0 the entry surface of the plate, and with the drilling direction in the positive direction.

For the partial peck, the hole was drilled in 0.5mm peck sizes, with a retract distance of 0.05mm between each peck. For the full peck, a 1mm peck size was also used but the drill was retracted to an absolute z coordinate of z=-2mm between each peck. The feed rate of the retract was maintained at the in feed of the drill, 0.2mm/rev.

Drilling cycle	Drill	Retract position
Partial peck	0.5mm	z=-0.05mm (relative)
Full peck	1mm	z= -2mm (absolute)

Table 7.3: Description of each of the peck cycles studied.

For each peck cycle 14 holes were drilled, for three repetitions using a unique drill for each test. Temperature measurements were taken at holes 6 7 and 8. The results of the maximum temperature that was captured for the two peck cycles tested, and presented in Figure 7.9. The results show that there is a clear reduction in the temperature at the hole exit for the full peck, with results around 100°C for the three holes measured compared to the 175°C to 180°C of the partial peck. Converting to Kelvin, the temperature reduction from 448K to 373K corresponds to a reduction of approximately 15%. When compared to drilling with no peck at 40mm/min and 0.2mm/rev where a temperature of 523K (250°C) was achieved, pecking shows a reduction in the temperature of 14% for the partial peck and 28% for the full peck.

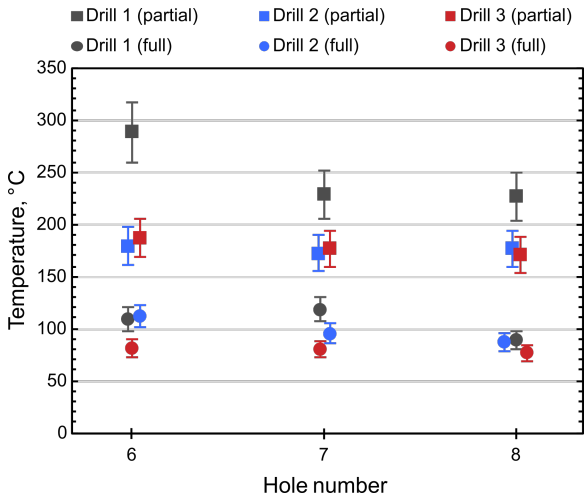

Figure 7.9: Measurements of drill exit temperature for each peck cycles tested.

The full peck drilling strategy resulted in a chipped margin after 7 holes, and is shown in Figure 7.10. Therefore the partial peck was chosen for future study.

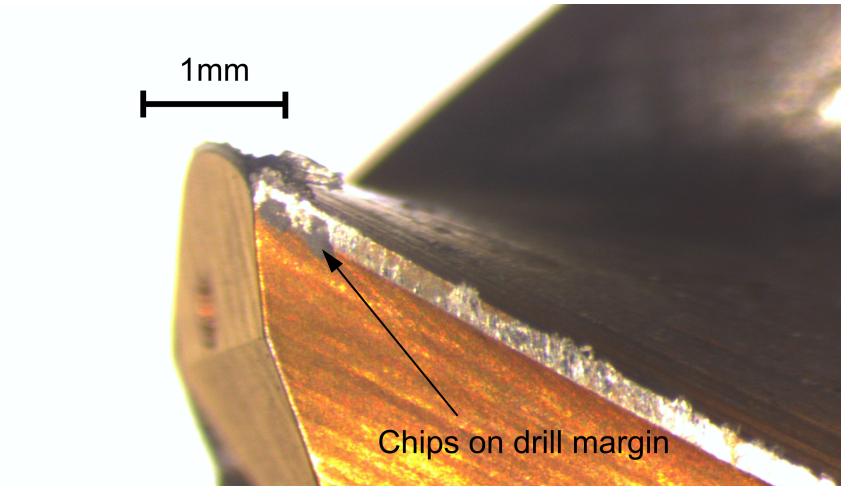

Figure 7.10: Chipping observed in the margin when drilling with the full peck strategy with LCO_2 cooling media.

7.3.1 Burr height and hole quality when peck drilling

The exit burr height was measured for each of the 14 holes in each run for the pecking cycles and extended run holes (no peck). These measurements are presented in Figure 7.11. Data is presented for each tool that was tested. The full peck results show that for tool 3 the burr height is slightly larger that the others, skewing the data towards the higher burr heights.

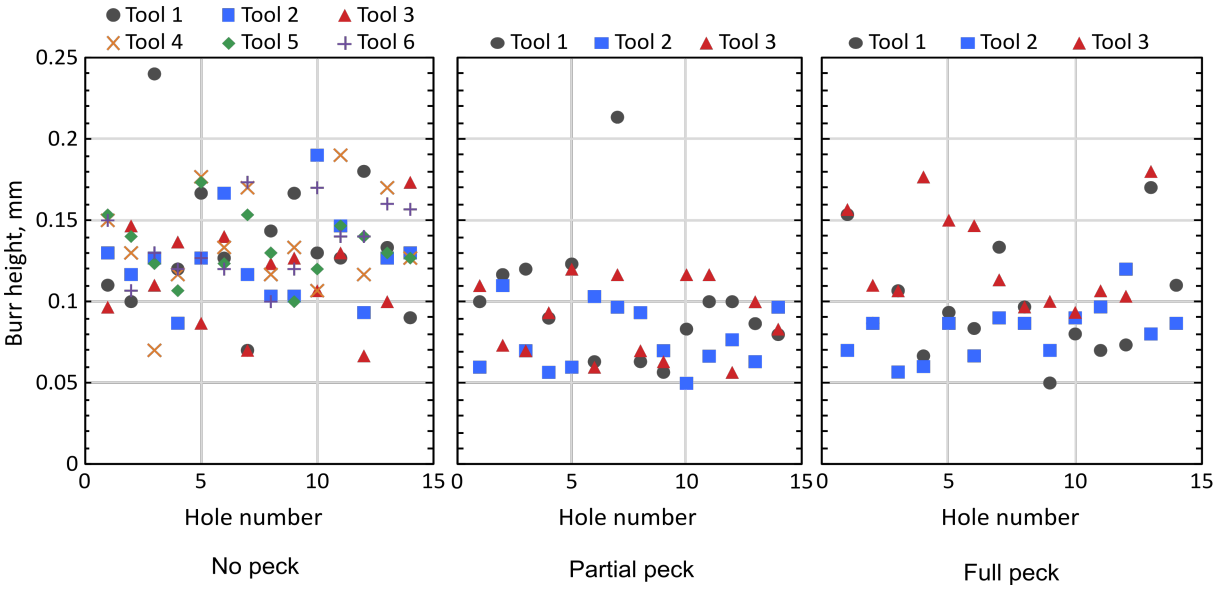

Figure 7.11: Individual measurements indicating the spread and variation in burr height measurements for different tools.

These data are summarised in the box plot in Figure 7.12. They show that the burr height is reduced when using a pecking cycle as opposed to using no peck. It is expected that with an increased number of tools tested that the full peck will result in a similar burr height due to the anomalous tool three skewing the results for the full peck data.

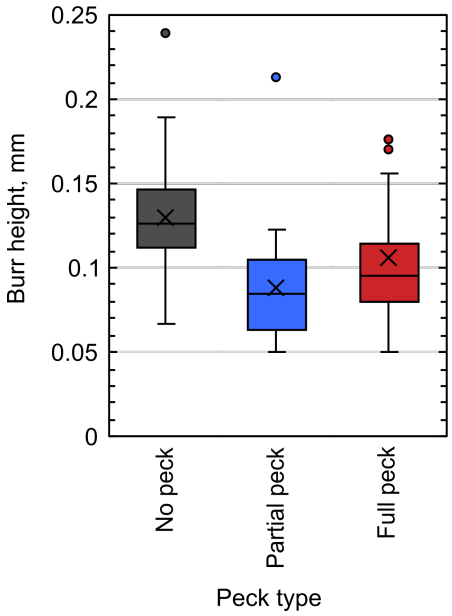

Figure 7.12: Summary of the burr height measurements for each of the peck strategies tested with LCO_2.

7.4 Influence of hole number

For the acquired cutting temperature data, mean measurements were taken of the three holes drilled for each of the runs. To establish whether this temperature is stable for multiple holes, tests of 14 drilled holes were completed. These tests were completed at 40m/min and 0.2mm/rev. Six tests were carried out and mean temperatures were calculated from measurements at holes 6, 7 and 8 and holes 10,11,12, Table 7.4. The order of the tests were randomised, and a separate tool was used to carry out each test.

Run number	Central hole position
1	7
2	11
3	11
4	7
5	11
6	7

Table 7.4: The run order of the tests to establish the influence of drilling a greater number of holes on the hole temperature. A separate tool was used for each of the test runs.

The temperature captured from these tests are shown in Figure 7.13. Each data point represents the mean of the three holes, plotted at the centre hole. The error bars show the standard deviation of the measurements. Each data point represents a different tool, for a total of six tools. An overall mean for each hole measurement position (positions 7 and 11) were calculated as 248°C and 255°C respectively.

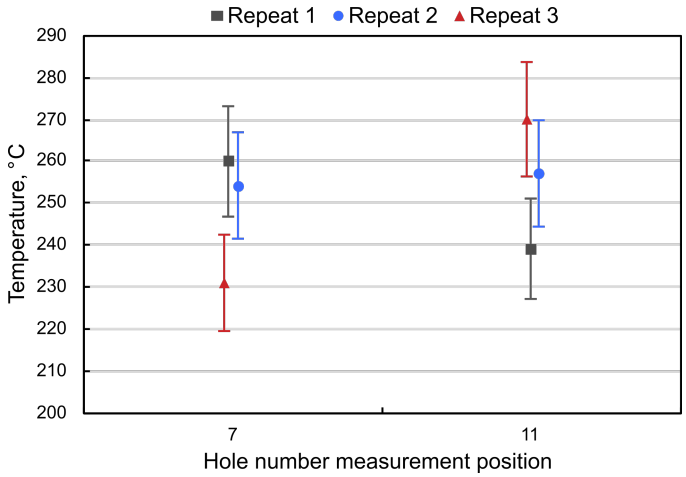

Figure 7.13: The exit temperature of drilling an increased number of holes, taken at 7 and 11 holes.1

The difference between these two values was tested using a t-test which returned a p-value of 0.6, indicating that the differences between the two mean values are non-significant.

7.5 Conclusions of chapter

The drill exit temperature was studied for previously defined important parameters in a full factorial for a range of LCO_2 mass flow rates, feed and workpiece thicknesses. This was completed using an infrared camera directed at the exit surface of a matt black painted surface, and maximum temperature was recorded and modelled using a partial least square regression technique. The following conclusions were found:

- Increasing the LCO_2 mass flow rate results in a reduction in the exit temperature in a non-linear fashion. Increasing the coolant mass flow had an accelerated influence on reducing the drill exit temperature.
- Increases in the workpiece thickness results in a prolonged period in cut, resulting in increases in the cutting temperature.
- The feed of the drill has a non-significant influence on the cutting temperature, therefore phenomena associated with this are likely due to mechanical effects.
- Relative diameters are used to determine the influence on the hole diameter, this shows that with increasing LCO_2 the increased flow does results in smaller diameter holes.
- Peck drilling has shown to reduce the temperature of drilling further and in turn reduce the burr height of the measured holes. Full peck drilling resulted in a large amount of drill margin chipping. Therefore, the partial peck drilling cycle will be adopted going forwards.

8 Observations with alternative tool features, coolant type, and tool geometry

The aim of this chapter is to present the results from the trials changing parameters from the initial operating window identified. This would allow further understanding of the cryogenic drilling process and how it compares to other strategies that are employed. To achieve these comparisons the following objectives were defined:

1. Observe the influence of changing the features on the cutting tool. The specific features that were identified include the coolant hole diameter and position, and the cutting edge rounding. These tool features were numbered prototypes 1 to 8 and are detailed in Section 4.4.1 .
2. Observe how alternative coolant types and strategies (wet, dry and MQL) influence the responses, to enable comparisons to be made against cryogenic machining.
3. Understand the effects of using different tool diameters to determine the adaptability and scalability of the cryogenic process across the tool range.
4. Understand how changing the tool geometry may influence cutting performance by using a different drill type.

8.1 Forces generated with different coolant hole size and position, and cooling strategies

It has been shown in literature [80] that changing the coolant hole position influences cutting performance through improved coolant supply to the cutting zone when using traditional wet coolants. For cryogenic machining, nozzle location and directing the cryogenic media in to the cutting zone has improved cutting performance [30, 94] in turning and milling applications. While it is not possible to alter the direction of the flow in to the cutting zone of the tool, it is possible to move the hole closer to the cutting edge and possibly alter cutting performance. Additionally, coolant hole diameter can influence the coolant velocity, where the pressure gradient between the exit of the coolant holes, essentially reducing the size of the diffuser made between the flank face and bottom of the coolant hole, as the coolant expels to atmospheric pressure.

The prototype tools shown were tested using the test rig and methodology described in Section 4.14 to capture force data. 49 holes were drilled for three repetitions of each prototype, using the drilling peck cycle ascertained from Section 7.3, with constant cutting data previously established. For the prototypes with smaller coolant holes (Prototypes 1,2,3, and 7) the LCO_2 mass flow rate was restricted to 8kg/hr

due to issues with the machine to maintain sufficient back pressure to achieve 10kg/hr with the greater restriction. The results from these tests are presented.

Figure 8.1 shows the normal force measurement results captured for prototypes 1 to 6. The results show, for each drill replicate, close repeatability of the normal force. No trends over time are observed from hole 1 to 49. It is expected to observe small increases in the normal force after the first few holes drilled due to the "bedding-in" (running-in) of the drill where the chisel edge is worn slightly. This was only observed for prototypes 3 and 6. The variation and spikes of low and high normal force were attributed to local variations in the workpiece material hardness and variations in the CO_2 mass flow rate, with the latter likely causing reductions in the normal force due to a drop in the mass flow rate, observed in Chapter 6.

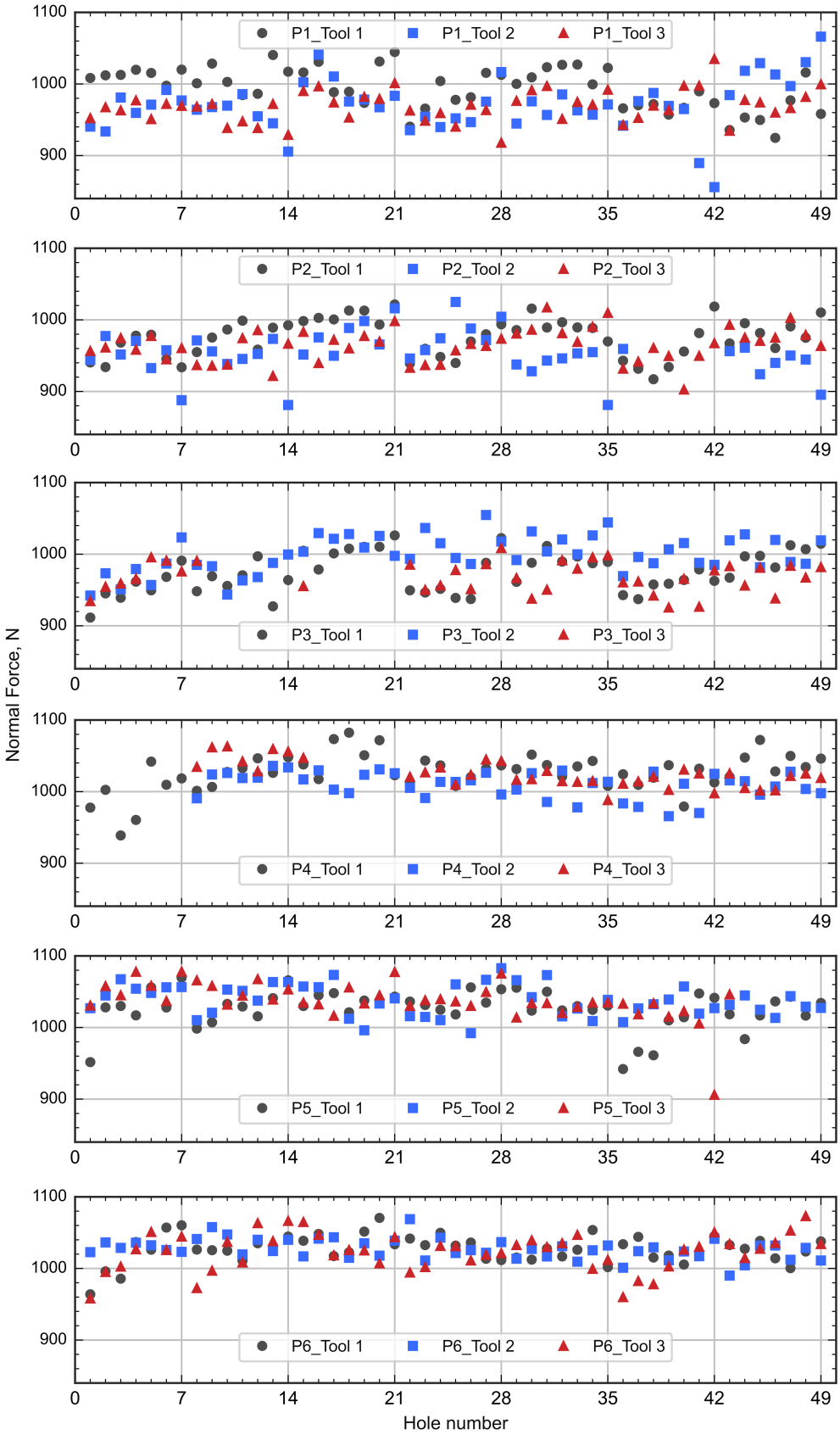

Figure 8.1: The normal force measurements for the individual drills captured for prototypes 1 to 6 with LCO_2 over 49 holes. .

Figure 8.2 shows the normal forces for prototypes 7 and 8 with smaller edge rounding values. Again, good repeatability is observed between each replicate. The increase across the first few holes in prototype 8 is also observed.

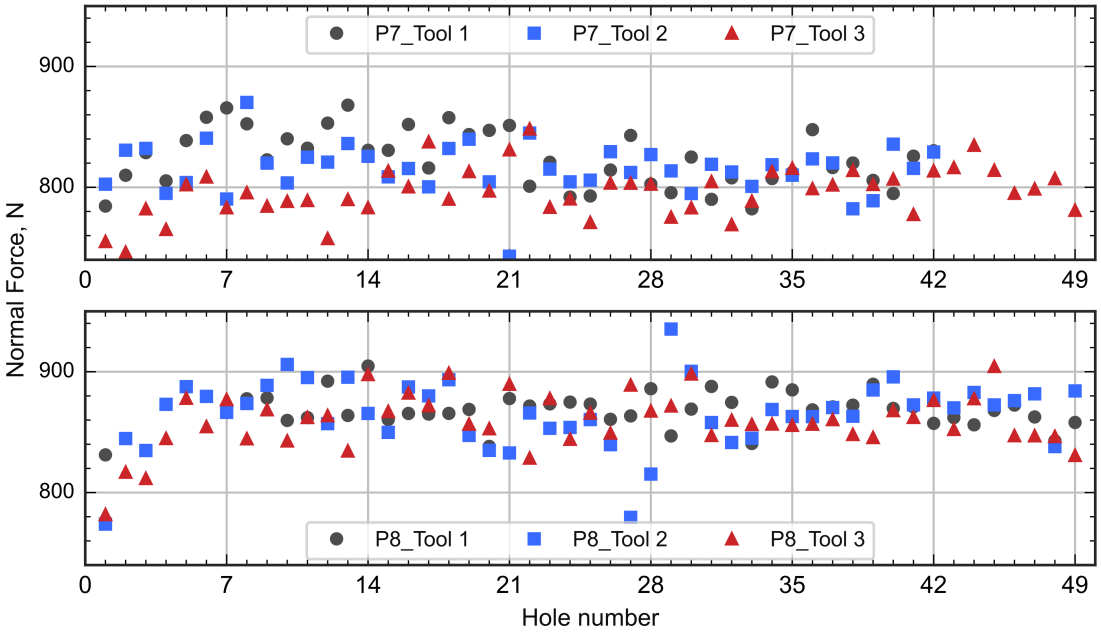

Figure 8.2: The normal force measurements for the individual drills captured for prototypes 7 and 8 with LCO_2 over 49 holes.

In addition to capturing the normal forces, torsional forces were also captured for the prototype drills. Good repeatability is observed for the replicates of each prototype. The range of values captured for all of the prototypes are similar, with no effect observed between each prototype. Of note, however, is the periodicity of these measurements. The measurements were taken in sets of 7 holes, and increases of approximately 0.2Nm are observed in each set from the start to the end of the seven holes. This phenomena is observed across all prototypes. Possible explanations of this could be due to systematic variations in the system set-up whereby slight variations in machine or workpiece alignment occur as the machine moves to drill each hole. This phenomena is often observed by Sandvik Coromant. These variations in the torsional forces are only small, accounting for less than 10% of the overall torque. To further reduce this phenomena, larger holes could be drilled which would increase the measured torque and minimise this effect on the torque measurement.

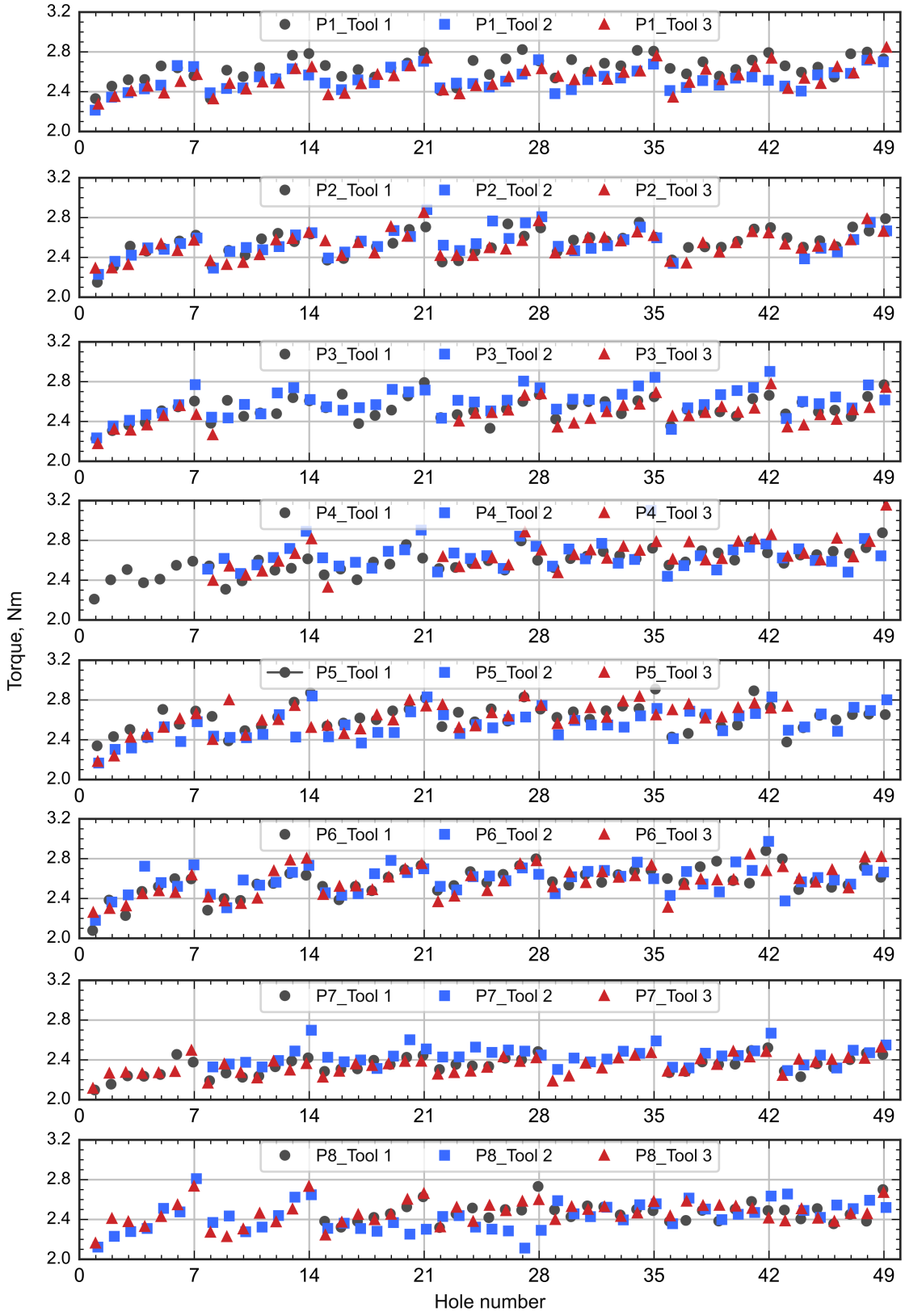

Figure 8.3: Torque measurements for all of the prototype tools tested with LCO_2 for 49 holes.

A comparison of the normal forces for each prototype can be conducted by comparing the data in box plot format, Figure 8.4. The results show that sharper cutting tools prototypes 7 and 8 result in lower normal forces. Larger coolant holes increase the normal force, with prototypes 4, 5 and 6, higher than 1, 2, 3 and 8 higher than 7. Moving the position of the coolant hole has no impact on the normal force.

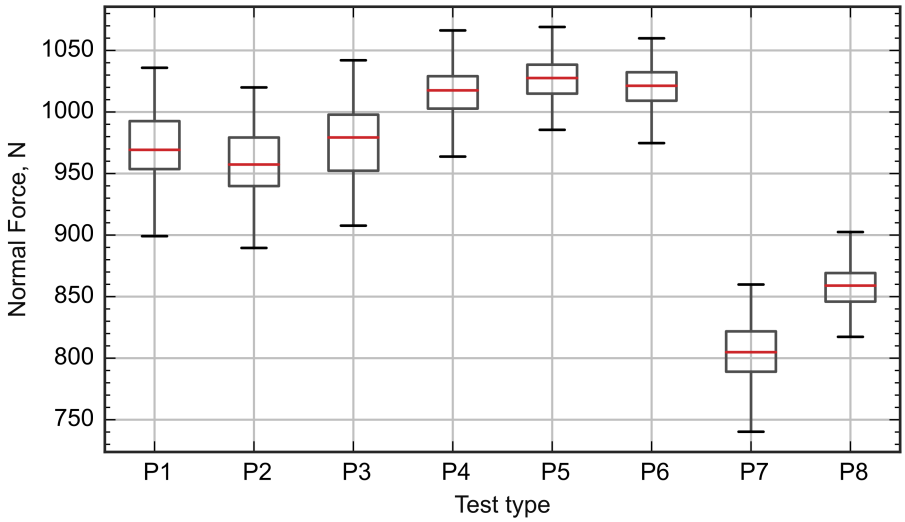

Figure 8.4: Summary graph of normal force measurements for each of the prototype tools tested with LCO_2.

A box-plot summary of the torsional forces is shown in Figure 8.5. They indicate that the sharper tools have reduced torsional forces. The influence of the coolant hole parameters is minimal, however torsional forces are slightly higher for the larger coolant holes.

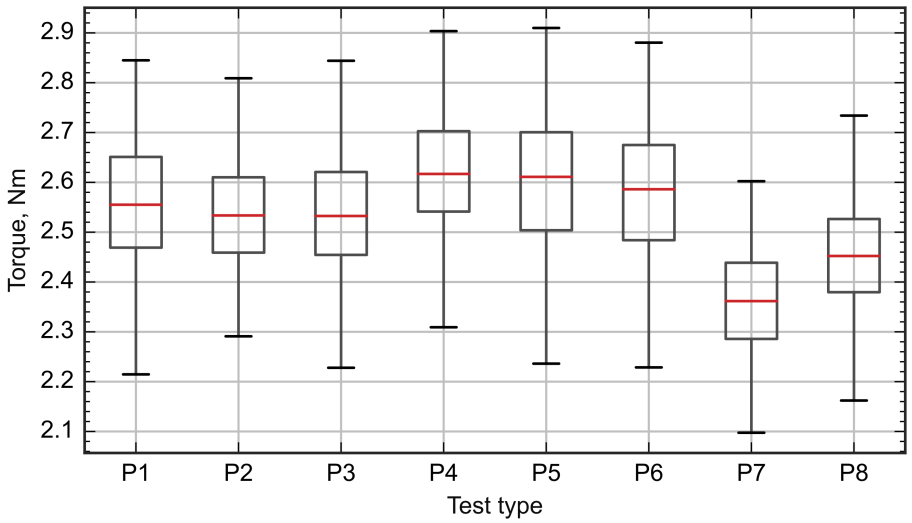

Figure 8.5: Summary graph of prototype torsional force.

Standard CoroDrill R846 drills were tested using the same set-up as for the prototype drills, for three

alternative coolant methods: wet, dry and MQL. The normal force measurements from these experiments are presented in Figure 8.6. Of all the tools tested, the results of the normal force using the wet tools had the closest repeatability to the other repeats.

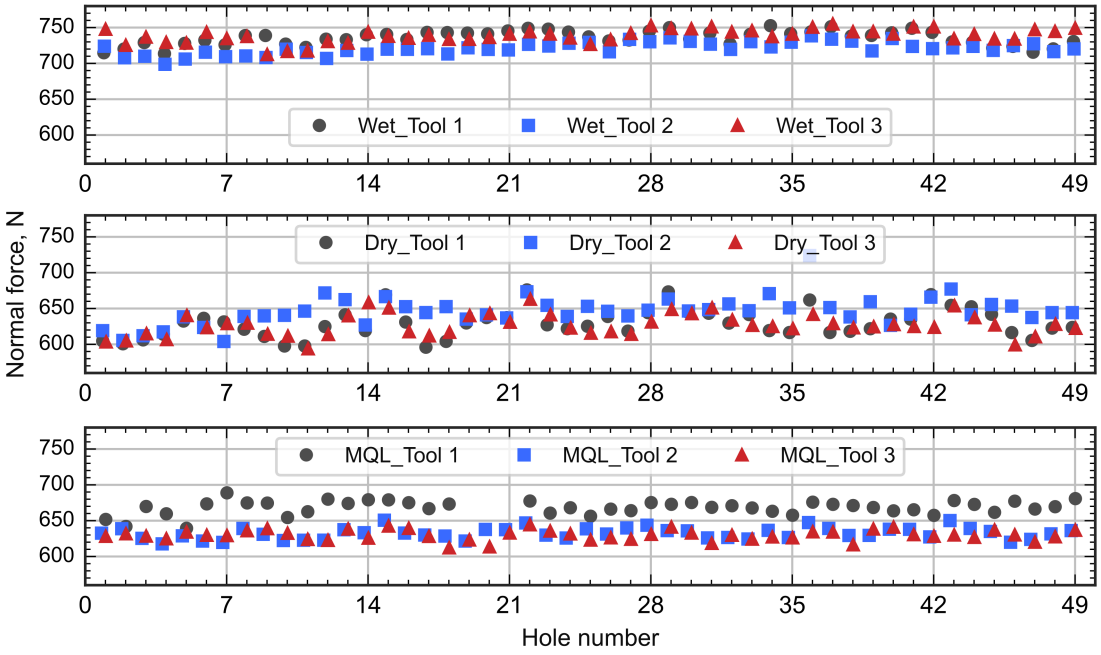

Figure 8.6: Wet, MQL, and dry normal force generated over the 49 holes drilled using R846 drills.

Figure 8.7 shows the scatter diagram for the torsional forces captured for the three alternative coolant strategies. Good repeatability is again shown for all of the replicates. The trials conducted in the wet strategy shows that there is a periodicity in the results obtained as per those results from the LCO_2 trials.

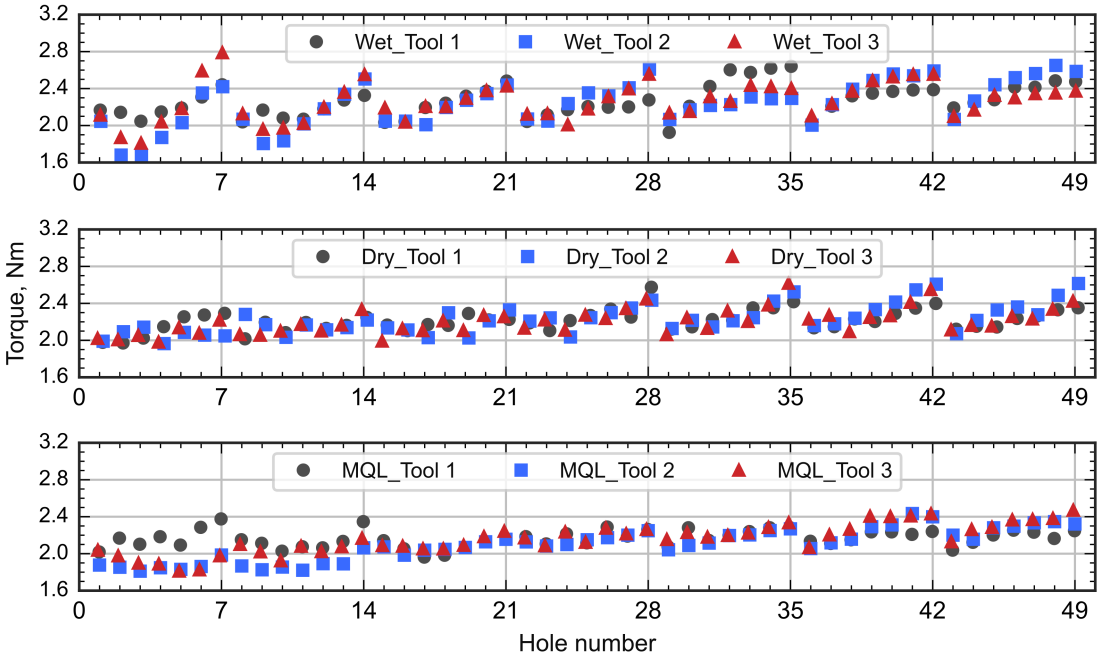

Figure 8.7: Wet, MQL, and dry torsional force generated over the 49 holes drilled using standard tool geometry R846 drill.

A summary of the normal forces for these alternative cooling strategies, is presented as box-plots in Figure 8.8. The results show that the mean value of the normal force for dry cutting is 635N with MQL at similar levels, showing that the addition of lubricant in cutting does not influence the normal force. However, in wet cooling the normal force increases to 730N. These strategies are lower than that of LCO_2 cooling, which produced a normal force of 1025N with the same nominal edge rounding, and 850N with half the edge rounding values.

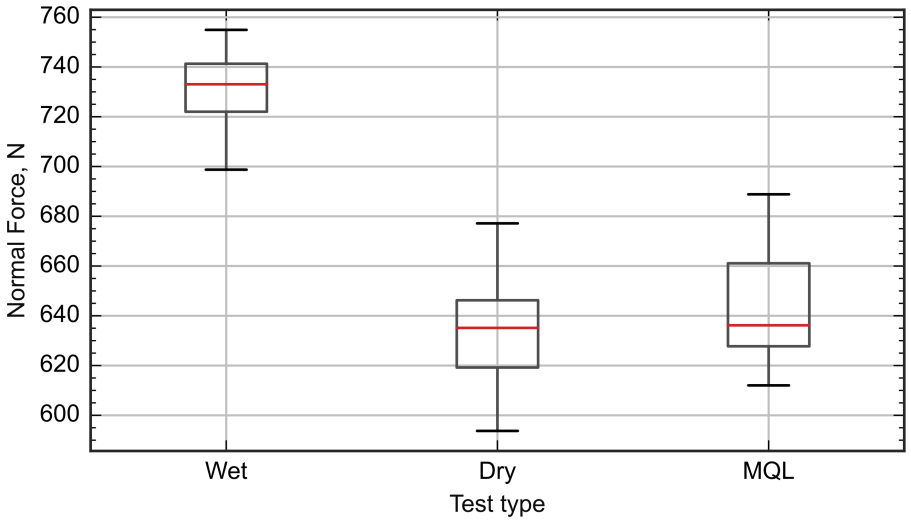

Figure 8.8: Normal force summary for wet, dry and MQL drilling with standard tool geometry of R846.

A summary of the torsional force results for the wet, dry and MQL cutting strategies are presented in Figure 8.9. They show similar mean values for the torque of 2.2Nm. This is in contrast to the higher torsional forces observed with LCO_2 of between 2.35Nm and 2.6Nm. It must be noted however that the spread of the data for these is somewhat large up to 50% of the value measured in the case of the wet coolant for example. This somewhat limits the ability to draw conclusions between the mean values of the torque because of the overlap of the data ranges.

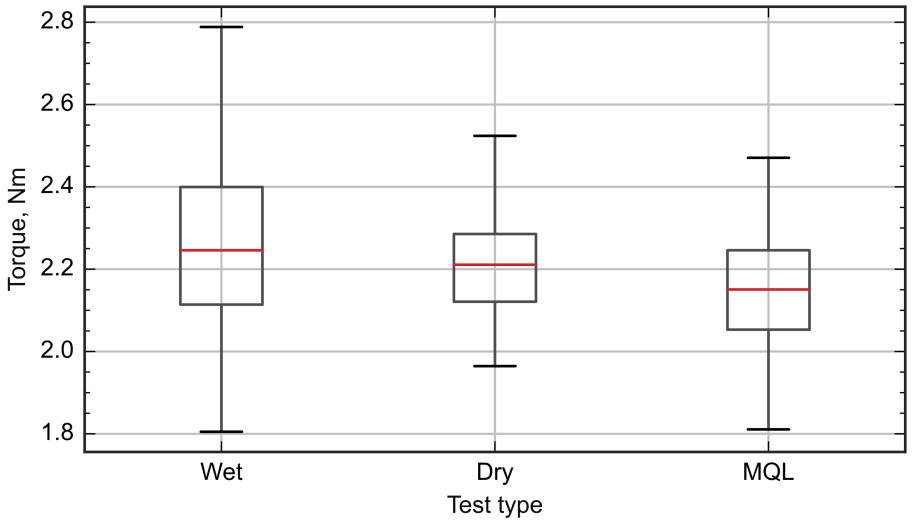

Figure 8.9: Torsional force summary for wet, dry and MQL drilling with standard tool geometry of R846.

Higher normal forces with using LCO_2 have been observed. This is an indication of a lower temperature material being drilled with LCO_2 increasing the material's strength [29] and the thermal softening of the material in dry and MQL strategies reducing those normal forces.

8.1.1 Tool wear with alternative cooling media

The tools used to conduct the trials with the different cooling strategies (wet, dry, MQL) were inspected using scanning electron microscope (SEM) imaging, taken by Sandvik Coromant using their standard operating procedures for capturing SEM images cutting tools.

Figures 8.10 and 8.11 shows images taken of the drill margin, and cutting edge after 49 holes drilled with the wet strategy. The images show little workpiece material adhesion on the drill margin and some on the cutting edge, acting to protect the cutting edge during drilling. Burnt coolant residue is observed for all of the cutting tools tested, and a small amount of flank wear can be observed as the tiny brighter white line closer to the cutting edge.

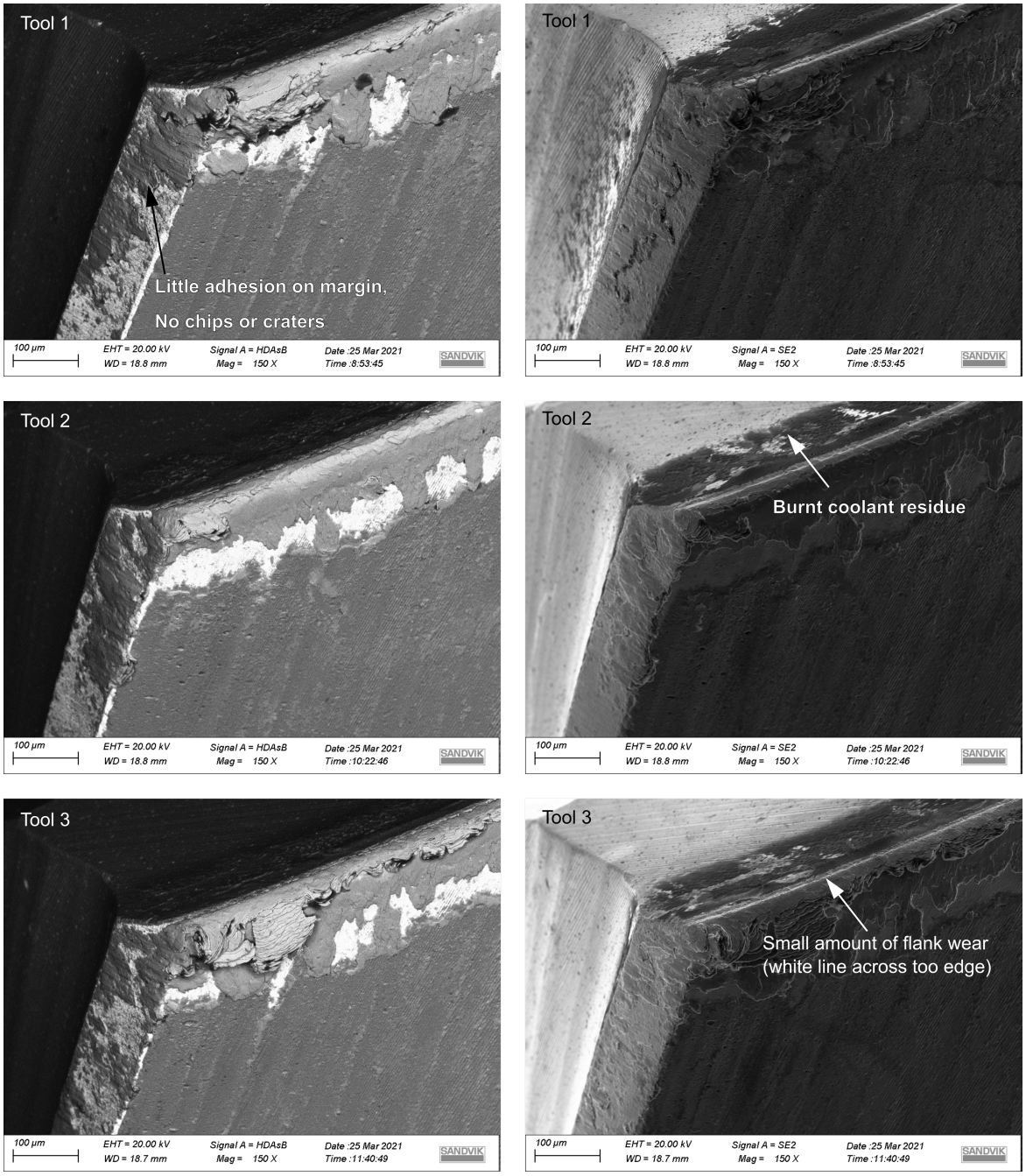

Figure 8.10: SEM image of the tool wear present on the solid carbide drill margin, flank and rake faces, using the wet strategy after 49 holes.

Figures 8.12 and 8.13 shows the three tools used to drill with the dry strategy, they show extensive workpiece material adhesion to all cutting faces. The amount of adhesion on the dry drill is much more pronounced than for the wet strategy. Flank wear is not observed on flank face due to the increase adhered material with this strategy.

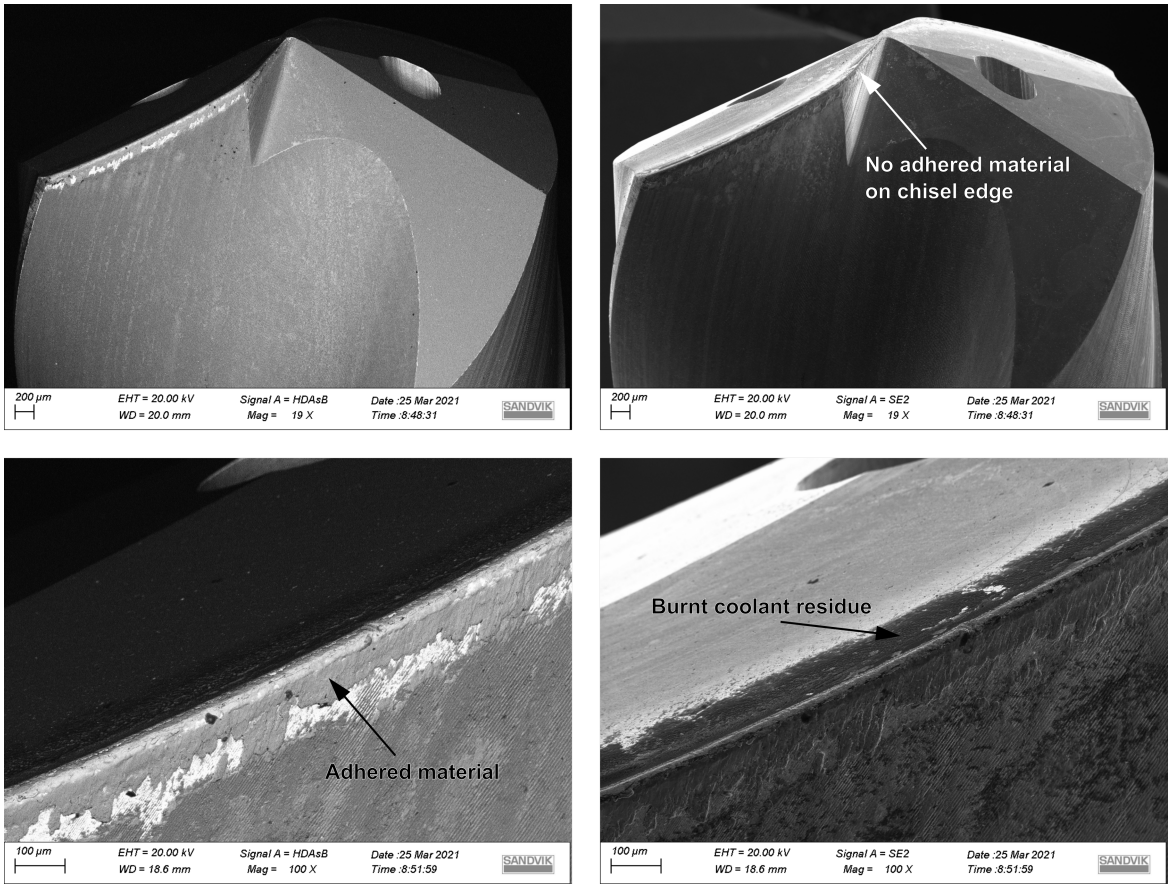

Figure 8.11: Adhered material on the cutting edge of the drill using the wet strategy after 49 holes.

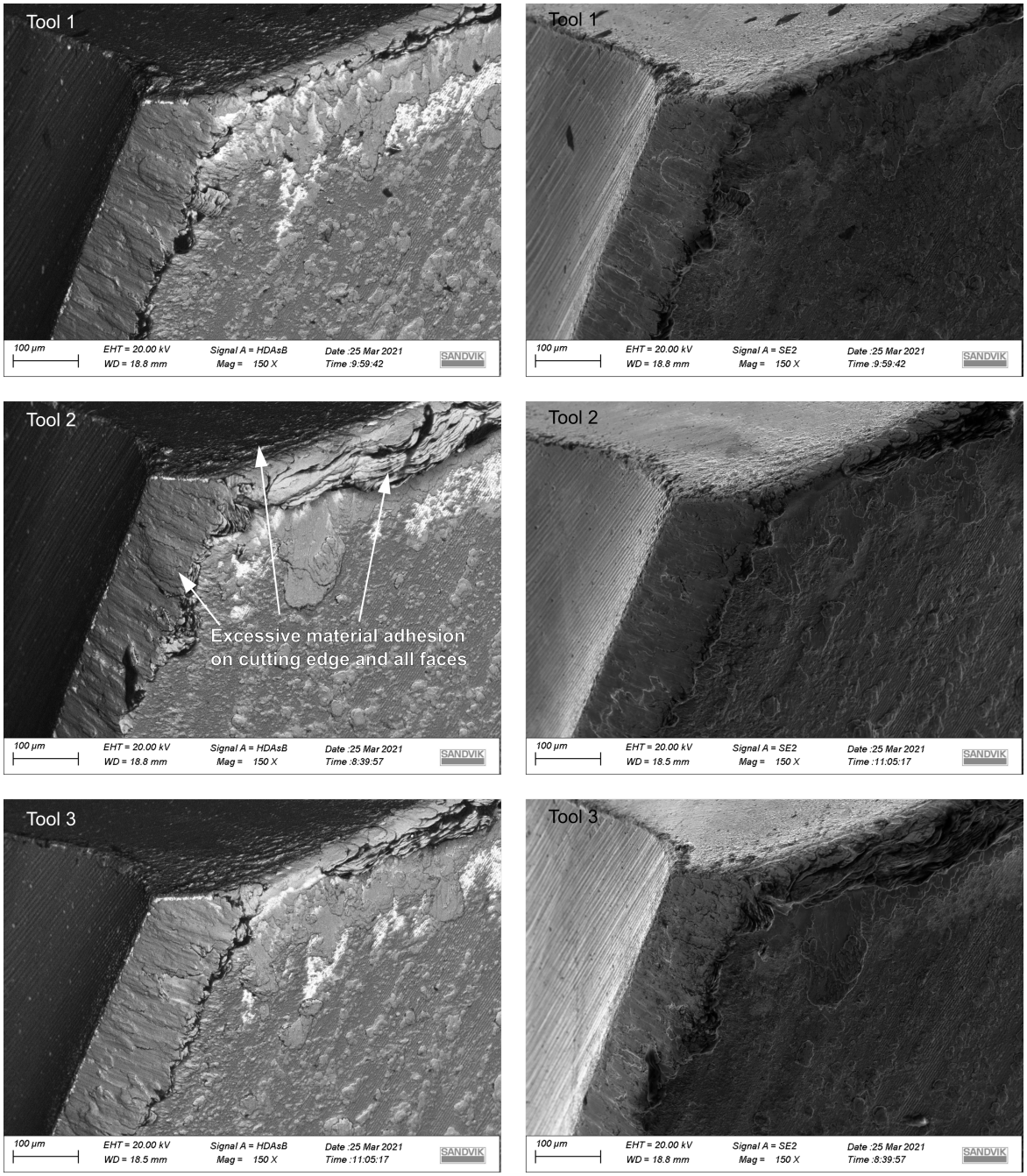

Figure 8.12: SEM image of the tool wear present on the solid carbide drill margin, flank and rake faces, using the dry strategy after 49 holes.

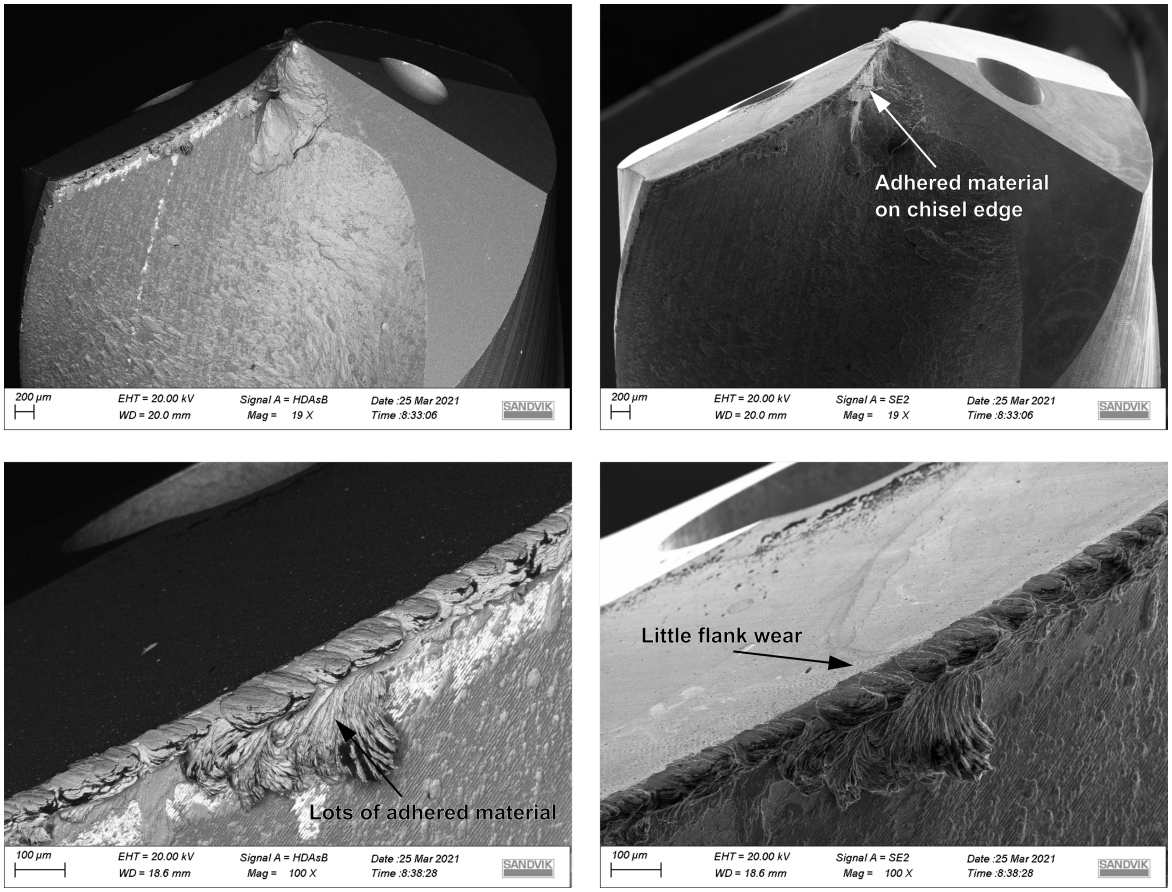

Figure 8.13: Adhered material on the cutting edge of the drill using the dry strategy after 49 holes

Figures 8.14 and 8.15 show SEM images for the margin and the cutting edge. The MQL strategy goes someway to reduce the adhesion of workpiece material on the cutting edges, however, it does not reduce the workpiece material adhesion to as much an extent as the wet strategy due to the not being able to access the margin of the drill. When the cutting edge is observed at the centre of the drill, the lubricating effect of the MQL is apparent, in that it provides the least amount of adhered workpiece material to the drill.

Observations of the adhered material on the tools for LCO_2 drilling is presented in Chapter 9.

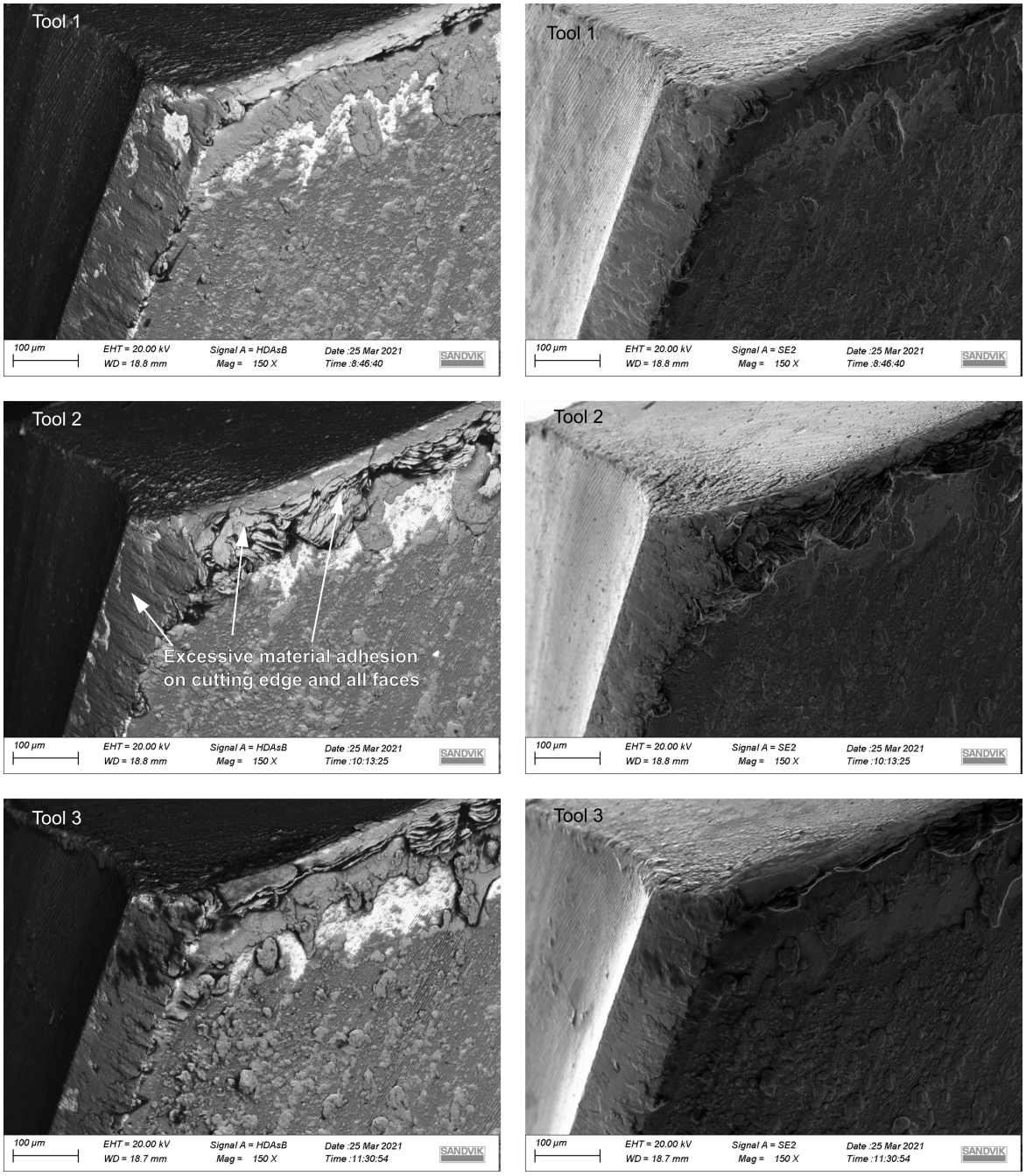

Figure 8.14: SEM image of the tool wear present on the solid carbide drill margin, flank and rake faces, using the MQL strategy after 49 holes.

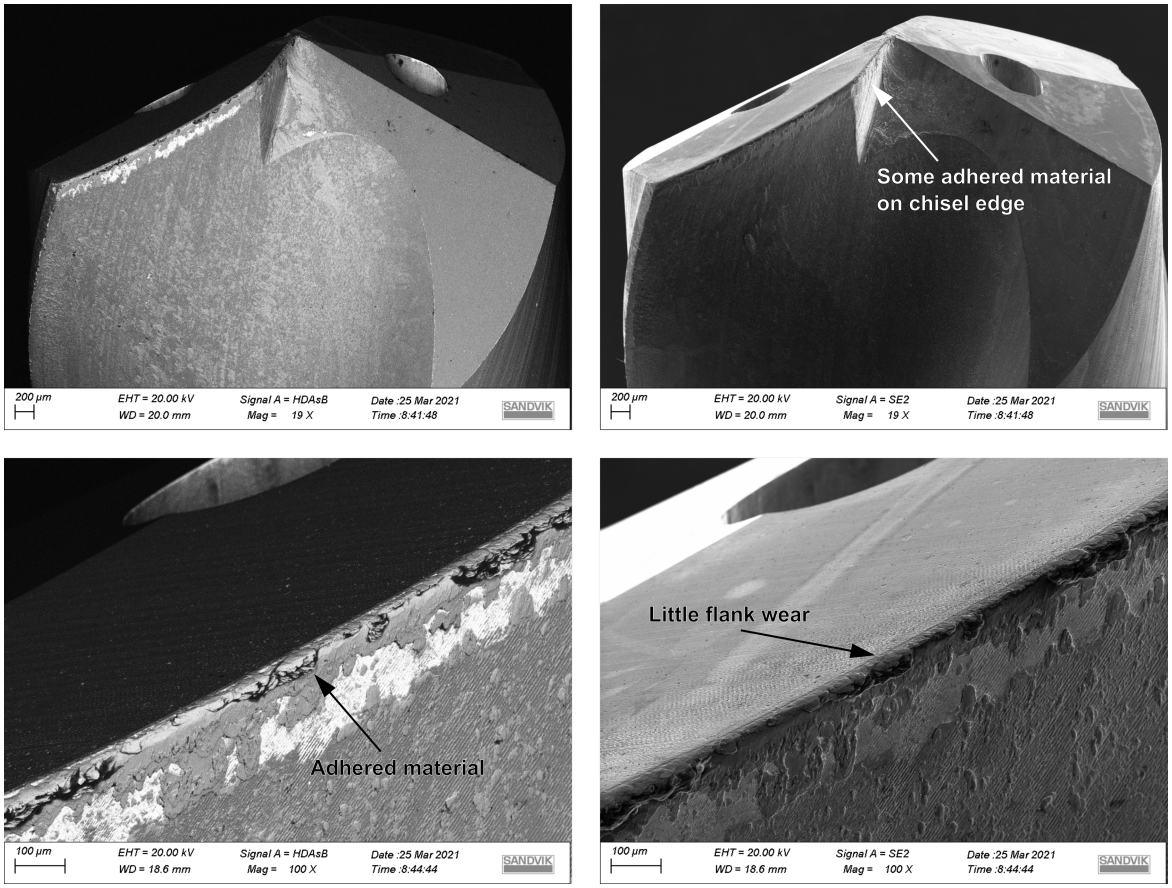

Figure 8.15: Adhered material on the cutting edge of the drill using the MQL strategy after 49 holes.

8.1.2 Hole Quality

The geometry of the holes produced during these trials were measured using the process described in Section 4.16. Two measurements of the diameter were calculated (max inscribed and the least squares), and the absolute values of the diameter are presented in Figure 8.16. The diameter measurements show that there is little difference in the hole diameter between each of the prototypes tested. The absolute diameter results from using the MQL strategy are also comparable to the results from the LCO_2 strategy. In contrast, smaller diameters were observed when using the wet strategy compared to LCO_2 and larger when using the dry strategy.

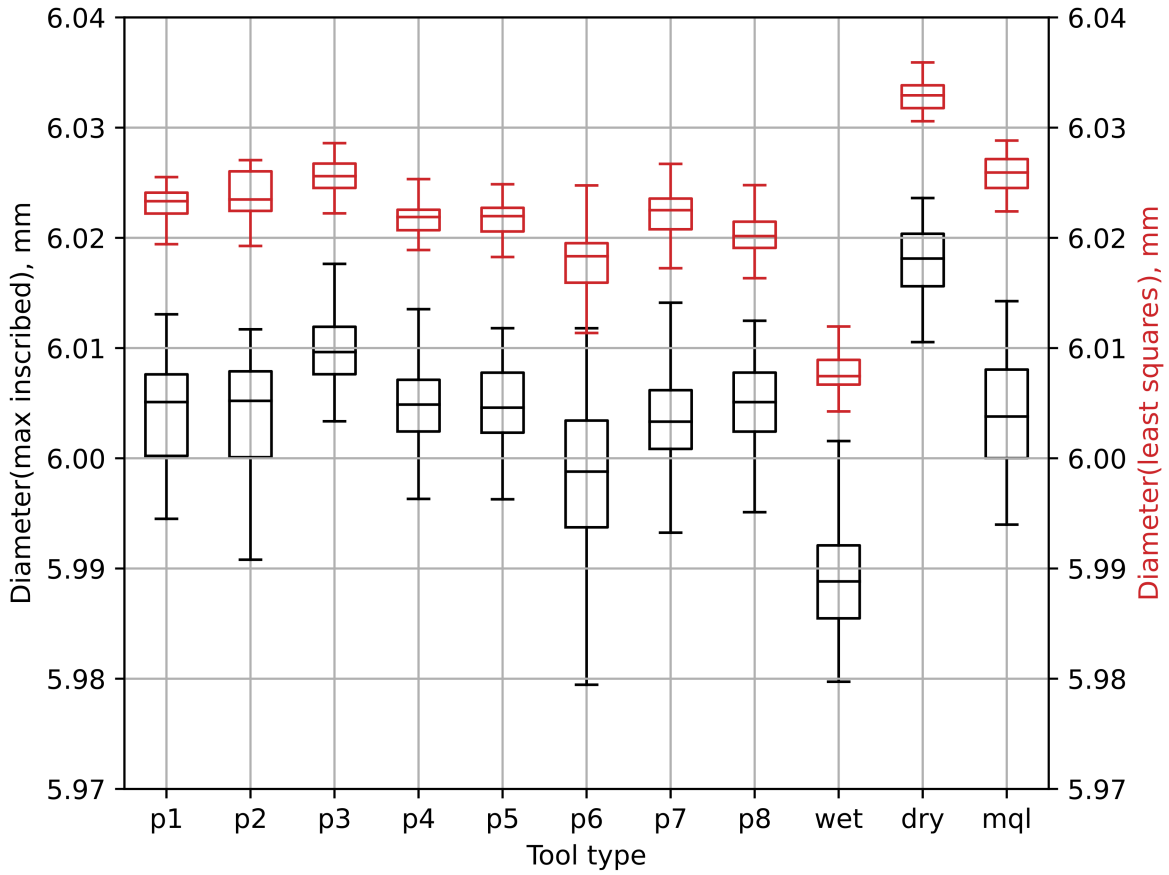

Figure 8.16: Effect of the coolant type on absolute hole diameter, both max inscribed and least squares.

When the gauge hole diameters are observed, and the drill diameter is taken into consideration, increases in the hole diameter from the drill diameter are observed. For wet drilling, drilled hole diameters achieved are similar to those of the drill (diameter least squares), with mean values of 0.002mm observed. When considering the the gauge diameters the behaviour of the different prototypes is highlighted. This behaviour shows that with the smaller coolant hole diameters larger holes are drilled. This is indicative of the lower amount of cooling with the LCO_2 with the smaller coolant holes. One can also infer that wet is cooling better than the LCO_2 strategy.

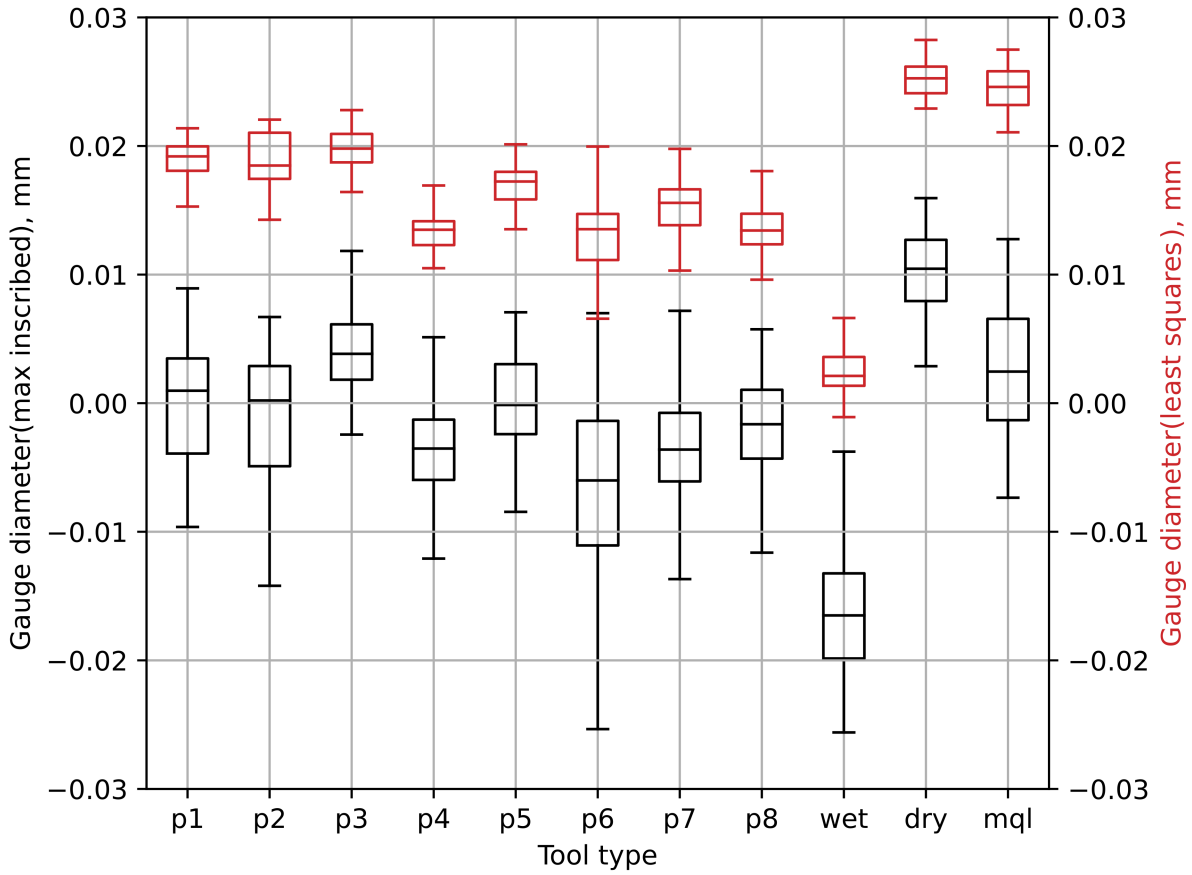

Figure 8.17: Effect of coolant type and the prototype, accounting for the tool diameter, both for the max inscribed and least squares measurements.

Further hole geometrical parameters were also measured, and are presented in Figure 8.18. The results from the diameter translate to the cylinder results, whereby the different prototypes have no influence on the cylinder, while smaller and larger cylinders are observed for wet and dry strategies respectively. Again, MQL shows similar results to the prototypes. These findings are exaggerated when the least squares diameter measurement method is used to measure the diameter.

Circularity and cylindricity measurement results were similar for all cooling strategies.

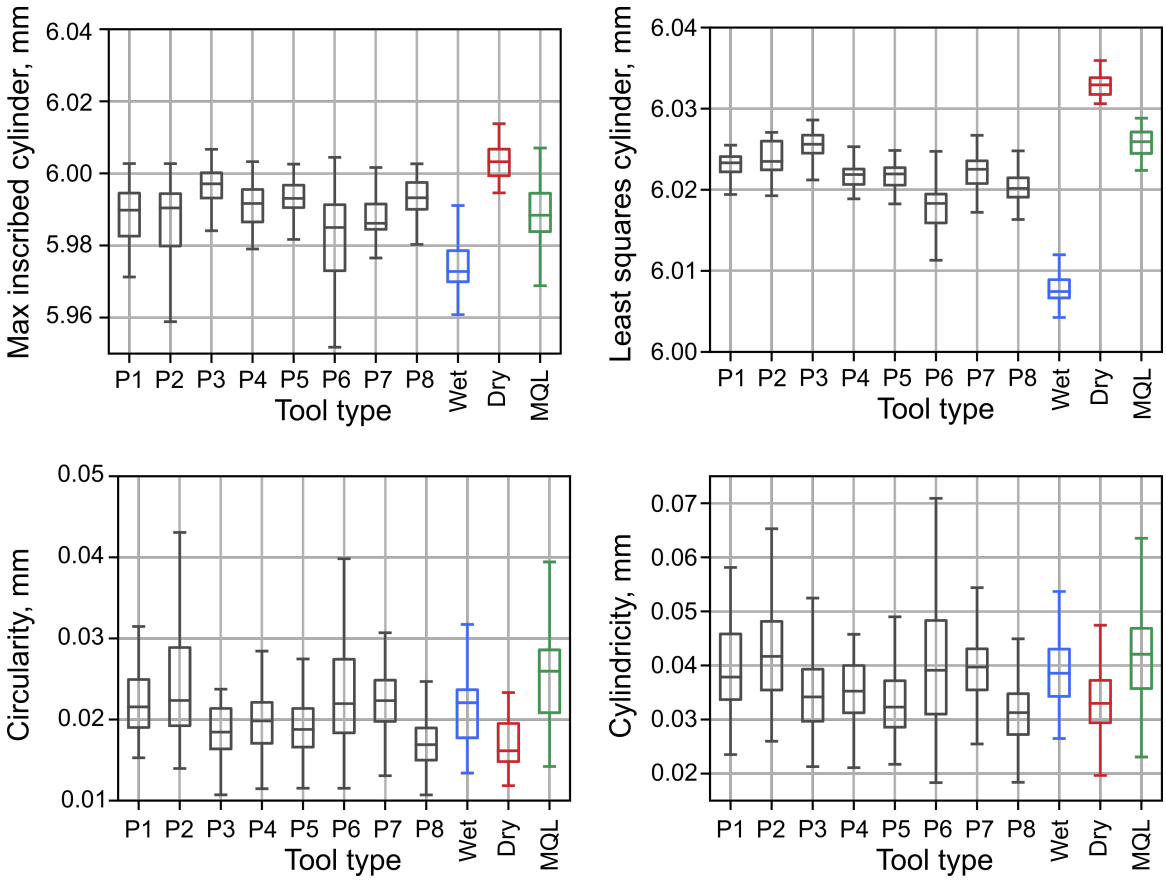

Figure 8.18: Effect of the coolant type and prototype on the cylinder(max inscribed and least squared), circularity and cylindricity of the hole.

The burr height measurements, captured using the method described in Section 4.16.2, for the prototypes and different cooling strategies are shown in Figure 8.19. These measurements were captured for the first five, and last five of the 49 holes drilled. The results show that the burr height increases with a greater number of holes drilled across all of the tests completed. Of the prototypes tested, Prototype 8 provided the lowest burr height, comparable to the burr height measured for wet drilling. These two strategies are the only ones fulfilling the target of less than 0.1mm burr height.

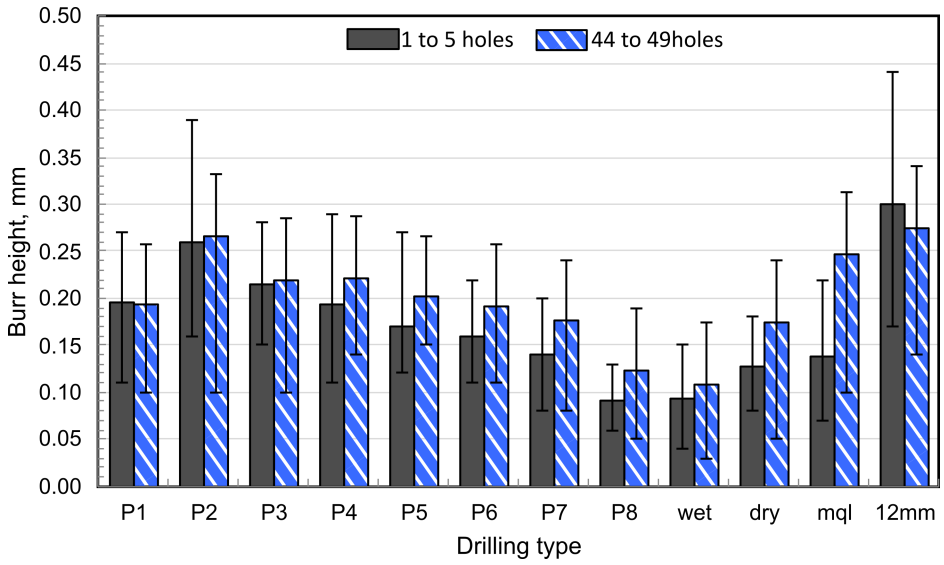

Figure 8.19: Effect of the coolant type and prototype on the burr height. Values shown are the mean calculation between the hole numbers indicated. The error bars are one standard deviation from the mean.

Temperature measurements were also conducted on each prototype, again using the set-up described in Section 4.15. Three holes were drilled for each of the measurements conducted, and mean values of these are presented (Figure 8.20), error bars are the standard deviation of the measurements. The results show that the prototype used has only a slight influence on the hole exit temperature, with tight error bars, representing accurate data.

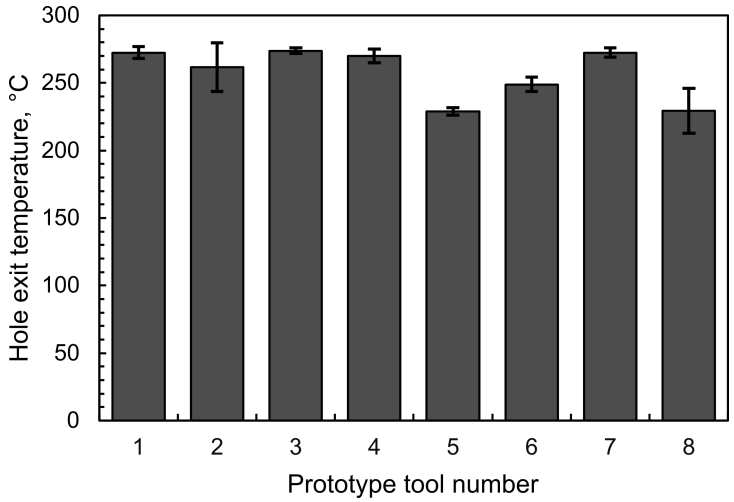

Figure 8.20: Hole exit temperature for each of the prototype tools, error bars represent one standard deviation.

8.2 Alternative tool geometries

As has been shown in Section 4.4, the CoroDrill R846 used throughout this thesis is bow shaped, in contrast to the hook shaped cutting edge offered by competitors tools. Therefore to study the influence of using a different cutting edge shape, trials were conducted in Ti6Al4V with CoroDrill R840 drills with

LCO_2 and flood MWFs using the set-up shown Figure 8.21. This drill has a flat cutting edge without the optimised characteristics of the R846 drill, and it is used as a multi-purpose drill, the flat shape of the cutting edge provides a tighter flute increasing mechanical assistance of the flute to curl the chip.

These experiments were conducted with a drill each for the emulsion and LCO_2 trials, workpiece thickness was set at 10mm thick and no peck cycle was used. Cutting data was provided by Sandvik Coromant and is optimised for use with emulsion coolant. The order in which the parameters were studied were randomised, to remove any experimental bias, Table 8.1.

Run No.	Experiment 1, LCO_2		Experiment 2, Emulsion	
	Speed, m/min	Feed, mm/rev	Speed, m/min	Feed, mm/rev
1	20	0.08	20	0.06
2	20	0.06	50	0.08
3	35	0.06	35	0.06
4	50	0.10	35	0.10
5	35	0.08	20	0.10
6	20	0.10	50	0.06
7	50	0.06	50	0.10
8	35	0.10	35	0.08
9	50	0.08	20	0.08
10	20	0.08	20	0.06

Table 8.1: Randomised run order for the experiments observing a different tool geometry shape.

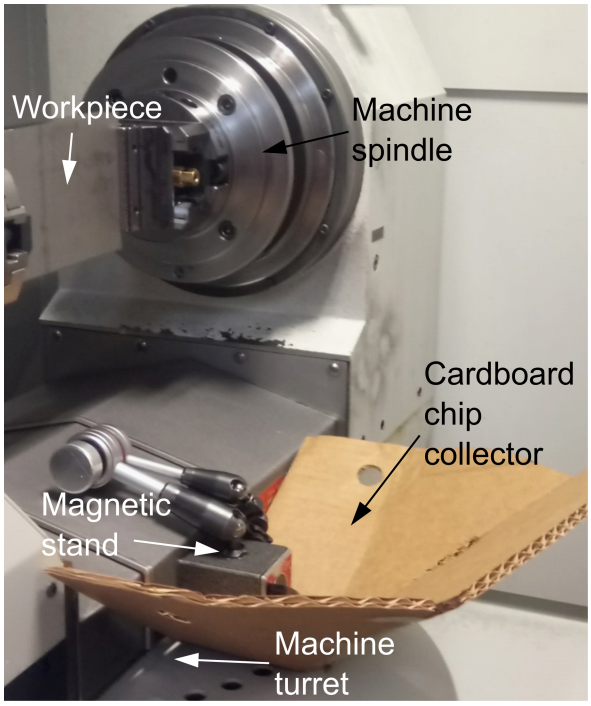

Figure 8.21: Experiment set-up used for alternative geometry trials, with chip collector in place to capture chips. No temperature or force measurement systems were in place.

8.2.1 Chip form

Chips were collected from both experiments, and the qualitative form of the chips is shown in Figures 8.22 and 8.23. The chip form shows comparable trends to those using the CoroDrill R846 drills, with improving chip form with increasing feed. Again the chip form shows how wet coolant is able to produce chips at a smaller size at lower cutting feed, and this phenomena is not unique to the CoroDrill R846 geometry.

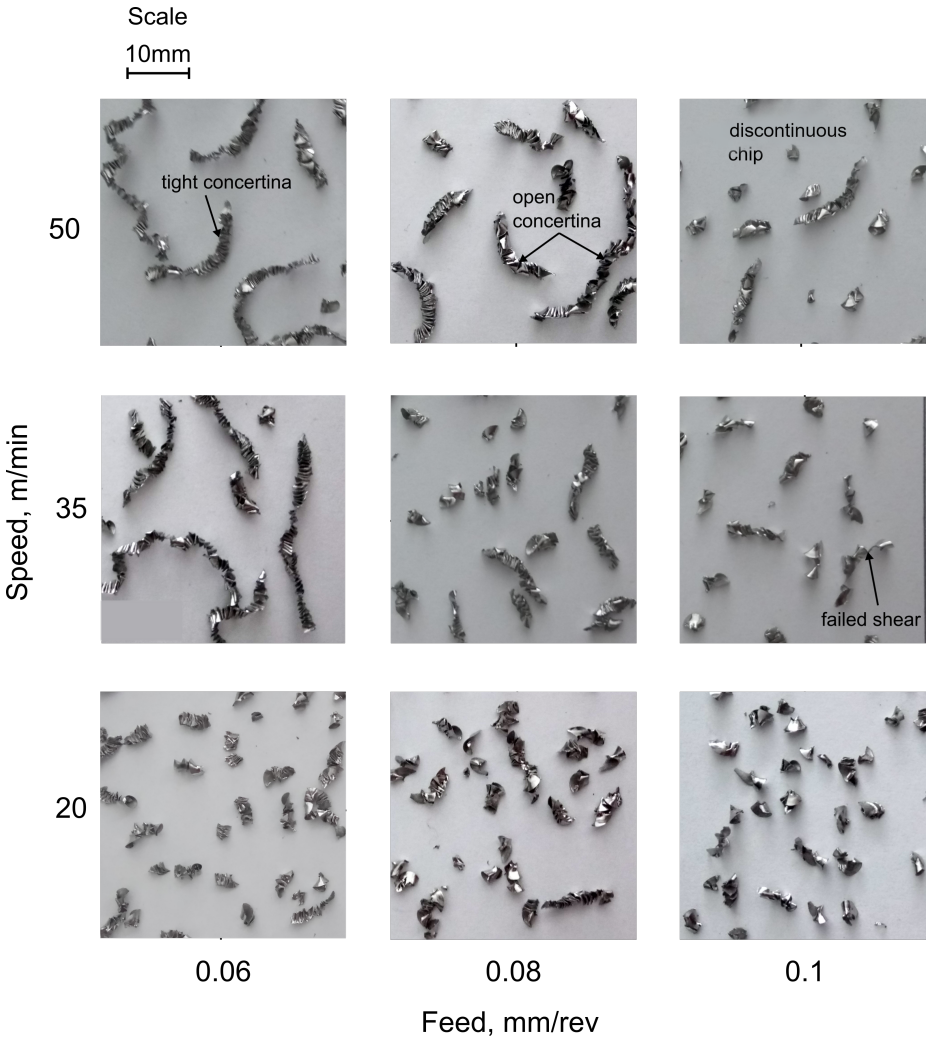

Figure 8.22: Qualitative representation of the chip form for LCO_2 coolant across the range of cutting parameters drilled when drilled using the R840 tool.

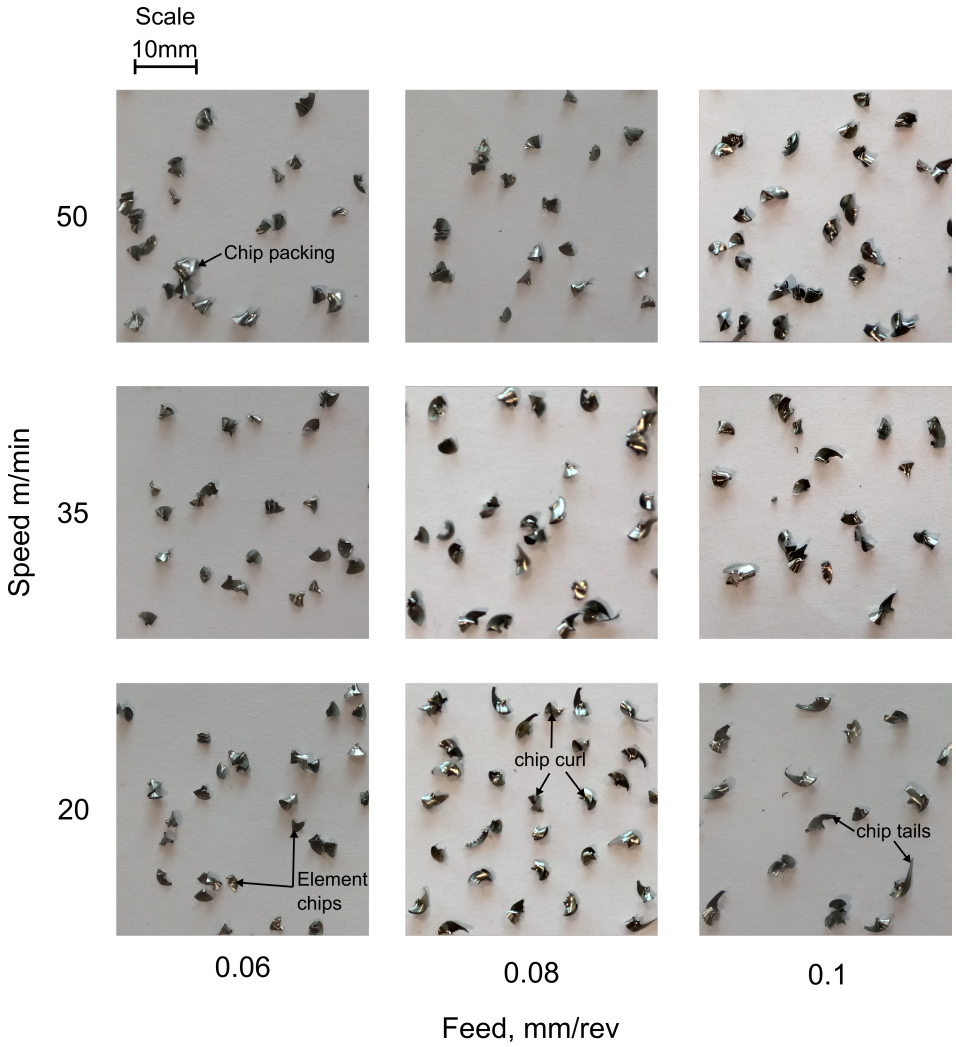

Figure 8.23: Qualitative representation of the chip form for wet coolant across the range of cutting parameters drilled when drilled using the R840 tool.

Surface roughness and burr height measurements were carried out using the techniques described in Section 4.16. They show that for the CoroDrill R840 drill with a straight edge, surface roughness and burr height measurements are more favourable for wet drilling conditions across the range of cutting parameters chosen and more so at the lower cutting speed.

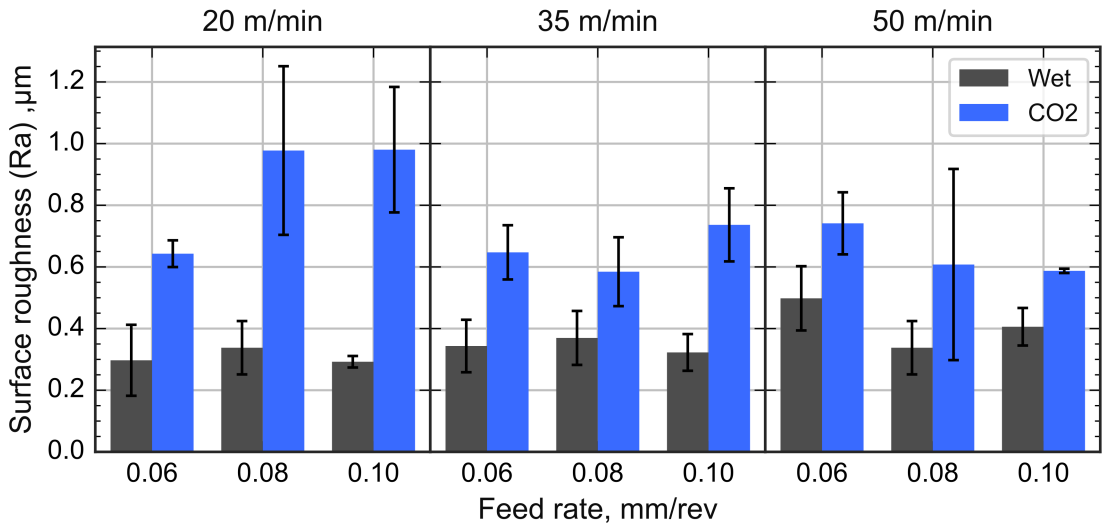

Figure 8.24: surface roughness, Ra results of the holes from initial testing, error bars are represented by 1 s.d.

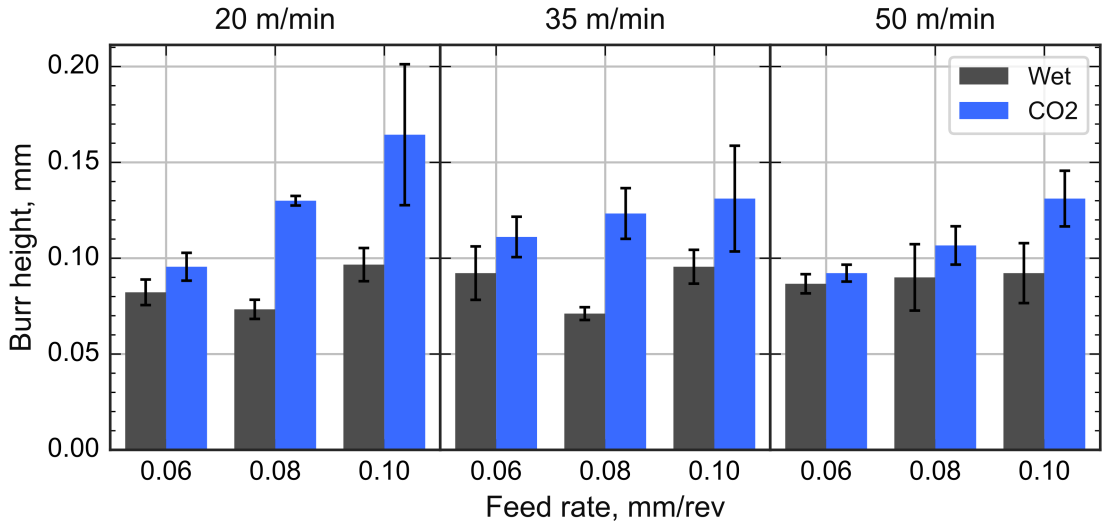

Figure 8.25: Burr height results showing comparison between wet and flood coolant for R840 drill, error bars at one standard deviation from mean.

8.3 Conclusions of chapter

A series of experiments were successfully carried out to observe the effects of changing the parameters from the operating window identified to generate an improved understanding of the cryogenic process. Experiments were completed observing the influence of the coolant hole position and size, using alternative MWFs and using different tooling geometries. The following conclusions were found:

- Over the 49 holes drilled with LCO_2, normal force and torque measurements remained stable, with slight increases over the first several holes as the tool was "bedded-in".
- Sharper cutting tools with lower edge rounding radius resulted in lower force measurements. This impact was more pronounced for the normal force than for the torque.
- Larger coolant hole size resulted in higher forces due to increased LCO_2 mass flow rate and less cooling of the workpiece material prior to cooling.
- Changing the coolant hole position has the least influence on the cutting process.
- LCO_2 was found to produce larger normal forces than other cooling types, while dry and MQL drilling had the lowest normal force due to thermal softening of the workpiece material during drilling. This force can be reduced by using sharper cutting tools.
- Minimal tool wear was observed across all of the tools tested. The quantity of adhered workpiece material on the tools varied for each of alternative cutting media tested. The lubricating properties of both wet and MQL strategies minimised the adherence of workpiece material to the drill. The wet strategy was most successful at preventing adhered material on the drill margin.
- The cooling strategy influenced the hole diameter drilled. Wet drilling produced holes closest to the nominal diameter of the drill. LCO_2 drilled holes larger than the wet strategy but the size was lower than dry and MQL, performing similarly.
- Prototype 8 was shown to produce the best quality holes when considering exit burr height, and hole geometry.
- Alternative cutting edge shaped was tested with the CoroDrill R840, results showed that improved chip formation occurred at lower feed rate than the CoroDrill R846, at the expense of large burr heights.

9 Tool life

9.1 Introduction

The performance of the prototype drills and the previously established pecking drilling cycle (Section 7.3) was further assessed with tool life as the metric. A tool life test provides a productivity assessment of the tool in a production environment, where it is not uncommon for tools to drill hundreds of holes. Up until now the number of holes drilled has been limited to 49. Literature has shown cryogenic drilling to improve tool life with cryogenic media. The work presented in this chapter includes:

1. Tool life tests of the best performing prototype tools (prototype variations 4, 5, 6 and 8), using LCO_2, to determine whether tool life is impacted by coolant hole position or cutting edge rounding.
2. Ascertaining the tool wear mechanism from the tool life tests with LCO_2.
3. Comparing the tool wear and tool wear mechanism to that of wet drilling using the prototype tools and pecking drilling cycle.

9.2 Tool life tests of prototype tools with LCO_2

Four prototype tools were selected for the tool life studies, prototypes 4, 5, 6 and 8. The rationale for selecting these tools was that prototype 8 had been shown to perform the best in the cutting force and burr height tests (Chapter 8), while prototypes 4, 5 and 6 were also chosen because they had the same coolant hole diameter as prototype 8. Three variations of each prototype tool was tested, with LCO_2 coolant at 10kg/hr. The tests involved drilling through 10mm Ti6Al4V ELI plate, and the flank and margin wear were recorded every 20 holes using microscopic imaging. The criteria for maximum tool wear (tool failure) during inspection was determined as 0.4mm for flank wear and for cracks, chips and crater wear on the tool margins.

The number of holes drilled for each of the prototype tools tested is shown in Figure 9.1, where the mean number of holes captured is presented, while the error bars show the maximum and minimum number of holes drilled for the three tested tools for that prototype variant. The prototype tools were deemed to have failed when chips formed and exceeded the 0.4mm limit on the margin. The results show that the tool with the greatest mean tool life was prototype 6 with 240 holes drilled, while the maximum number of holes was drilled by prototype 5. However, prototype 5 also had the lowest number of holes drilled, this is due to the fact that the tool chipping wear type is unstable. The other three prototypes did contrarily have a close spread of results, with mean values ranging between 150 and 240 holes drilled.

The flank wear measurements captured for each tool is within the prescribed tool wear limit of 0.4mm, as shown in Figures 9.2 to 9.6. With increasing hole number an initial acceleration in the flank wear was

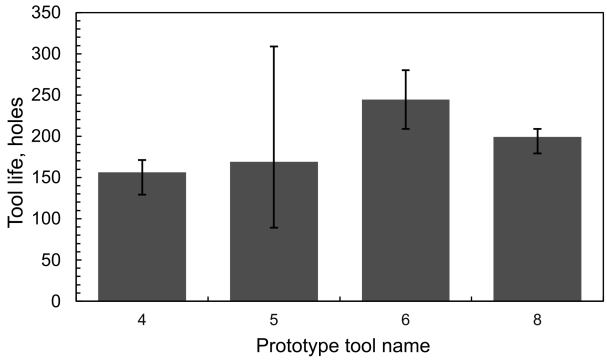

Figure 9.1: The tool life testing results for each of the four prototype tools tested using LCO_2.

observed which then flattened with subsequent holes. None of the flank wear measurements showed a re-acceleration in the wear leading to severe wear, which would likely happen towards the end of the flank wear tolerance of 0.4mm leading to tool failure. The tools are still within the steady wear regime and it is expected that these tools would be able to drill more holes, if flank wear was the limiting wear mechanism.

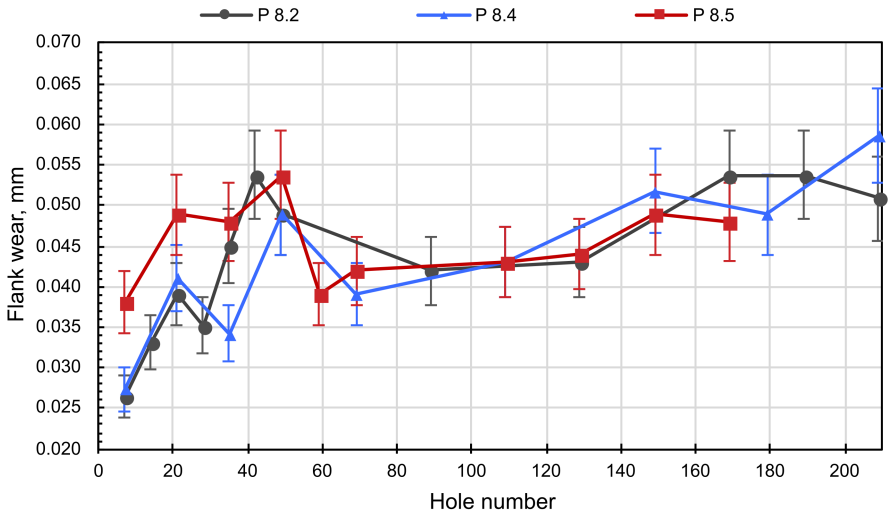

Figure 9.2: Development of flank wear for prototype tool 8 using LCO_2, with cutting edge rounding x0.5 and central large coolant hole, error bars represent plus minus 10% to account for measurement error.

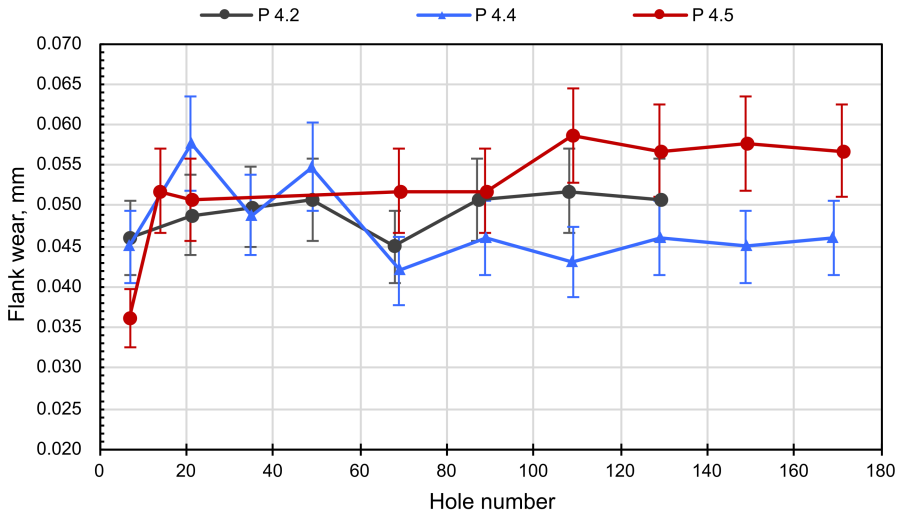

Figure 9.3: Development of flank wear for prototype tool 4 using LCO_2, with cutting edge rounding standard and central large coolant hole, error bars represent plus minus 10% to account for measurement error.

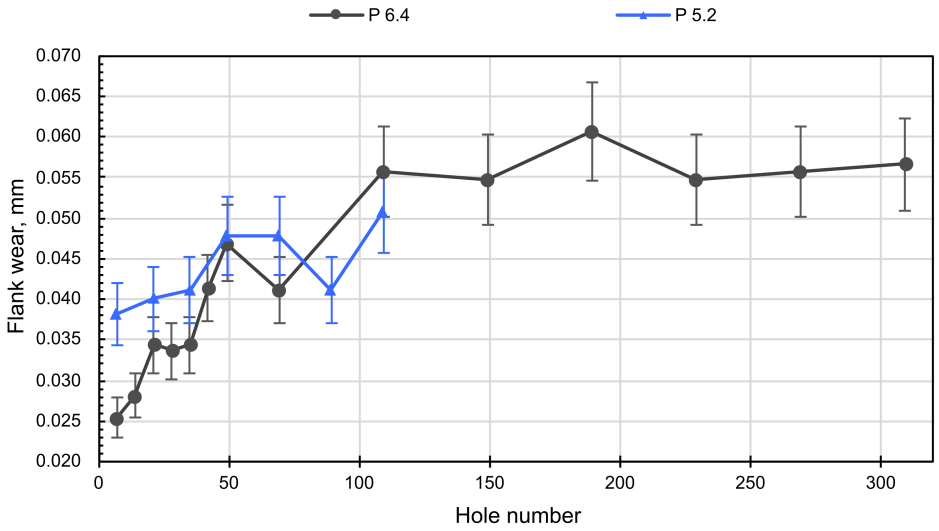

Figure 9.4: Development of flank wear for prototype tool 5 using LCO_2, with cutting edge rounding standard and central large coolant hole, error bars represent plus minus 10% to account for measurement error (note inclusion of prototype 6.4 as it was mislabelled during manufacture).

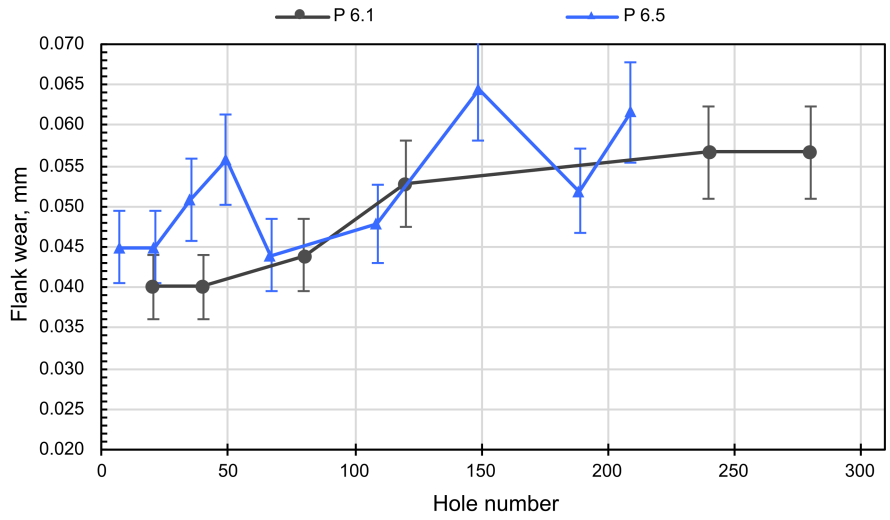

Figure 9.5: Development of flank wear for prototype tool 6 using LCO_2, with cutting edge rounding standard and central large coolant hole, error bars represent plus minus 10% to account for measurement error.

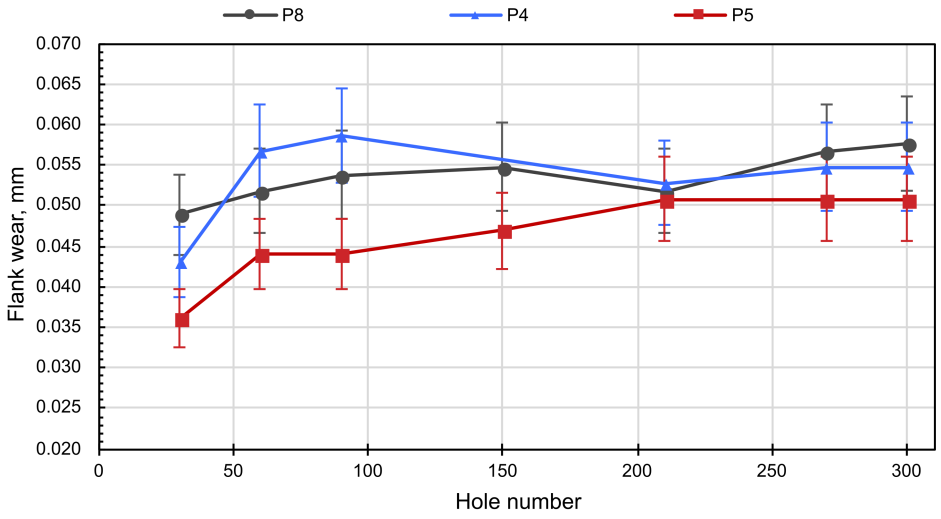

Figure 9.6: Development of flank wear each of the prototypes using flood (wet) coolant, with cutting edge rounding standard and central large coolant hole, error bars represent plus minus 10% to account for measurement error.

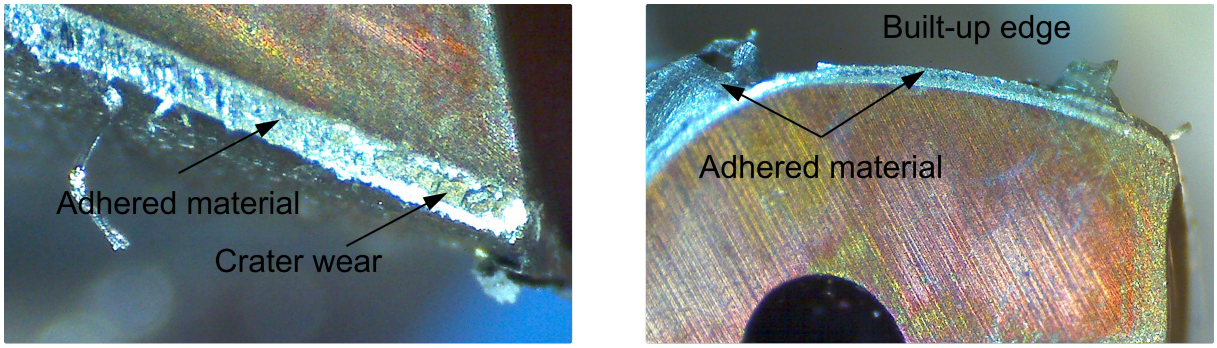

Figure 9.7: a) An example of the chipping and crater wear present on the margin observed for all tools using LCO_2 (shown for prototype 6.4). b) An example of the flank wear observed on the flank face of the tools using LCO_2 (shown for prototype 6.4).

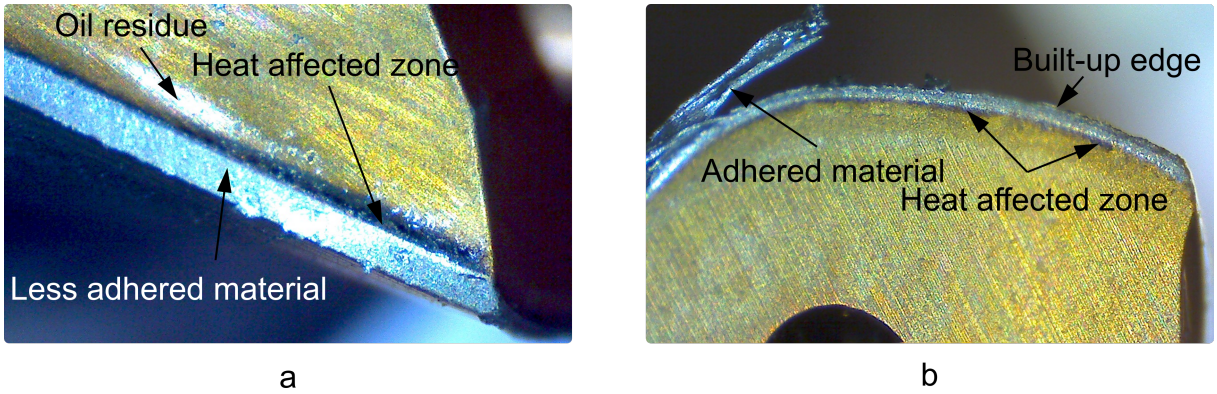

Figure 9.8: a) An example of the heat affected zone (HAZ) behind the margin of the tools (shown for prototype 5.4) observed on all of the tools using flood coolant. b) An example of the flank wear observed on the flank face of the tools (shown for prototype 5.4), showing some HAZ (heat affected zone).

The wear for drilling with LCO_2 has been shown to be crater formation and chipping on the margin exceeding the failure value of 0.4mm in size. While the flank wear is still within below the failure limits. It is hypothesised based on the evidence presented here that there are two causes behind this wear mechanism.

The first is due to the expansion and contraction of the hole intermittently grabbing and releasing the margin of the drill during machining and the pecking cycle employed, causing the fatigue failure of the margin, forming cracks which lead ultimately to chips forming on the margin of the drill.

The second is due to the tool being in contact with the hole wall at the drill margin. This close contact, with lack of lubrication, has resulted in the generation of high temperatures at the margin due to the high friction. This low thermal conductivity of titanium and the high affinity of the titanium to react with the titanium contained within the TiAlN coating of the drill results in large amounts of adhered material on the margin of the LCO_2 drill when compared to the wet drill. This is likely due to the the lack of LCO_2 able to enter this area, similarly observed by Oezkaya et al. [77], and the poor lubricating effects of the LCO_2. The adhesion of material and high temperatures at the margin results in the removal of the tool coating and diffusion of the tool cobalt into the titanium [38]. This removal of material from the

tool results in the formation of the craters on the margin subsequently weakens the margin through the formation of crack initiation sites and the thinning of material on the margin. This leads to chips forming on the rear side of the margin in the opposing direction to the cutting motion. Evidence of this occurring across all of the prototypes testing is observed in the margin SEM images of the tools, with examples shown in Figures 9.14 to 9.15.

9.3 Hole quality with increased number of holes during the tool life tests

The effect of the tool wear on the quality of the drilled hole is presented in this section. Data was captured for the hole geometry and exit burr height (using the measurement techniques described in Section 4.13). The tool wear has been shown to have no influence on the hole diameter or hole circularity for each of the holes drilled in the LCO_2 test (Figures 9.9 and 9.10), with measured hole diameters of 6.02±0.01mm and hole circularity between 0.01 and 0.03mm. Therefore the effect of the crater wear and chips on the drill margin have no impact on hole diameter and circularity.

Exit burr height measurements for the LCO_2 coolant, Figure 9.11, show an increase with hole number, up to 100 and 150 holes drilled, before reaching a plateau of 0.28mm for prototype 4 and 5, and 0.29mm for prototype 6. Whereas, those tools employing the traditional flood coolant approach showed consistent measurements of exit burr height, throughout the tool life trial, of 0.16mm. Prototype 8, the sharper tool had consistently lower burr heights for each cooling strategy. For flood coolant, prototype 8 produced holes with exit burrs heights of 0.12mm and for LCO_2 the exit burrs started at 0.09mm before plateauing at 0.19mm.

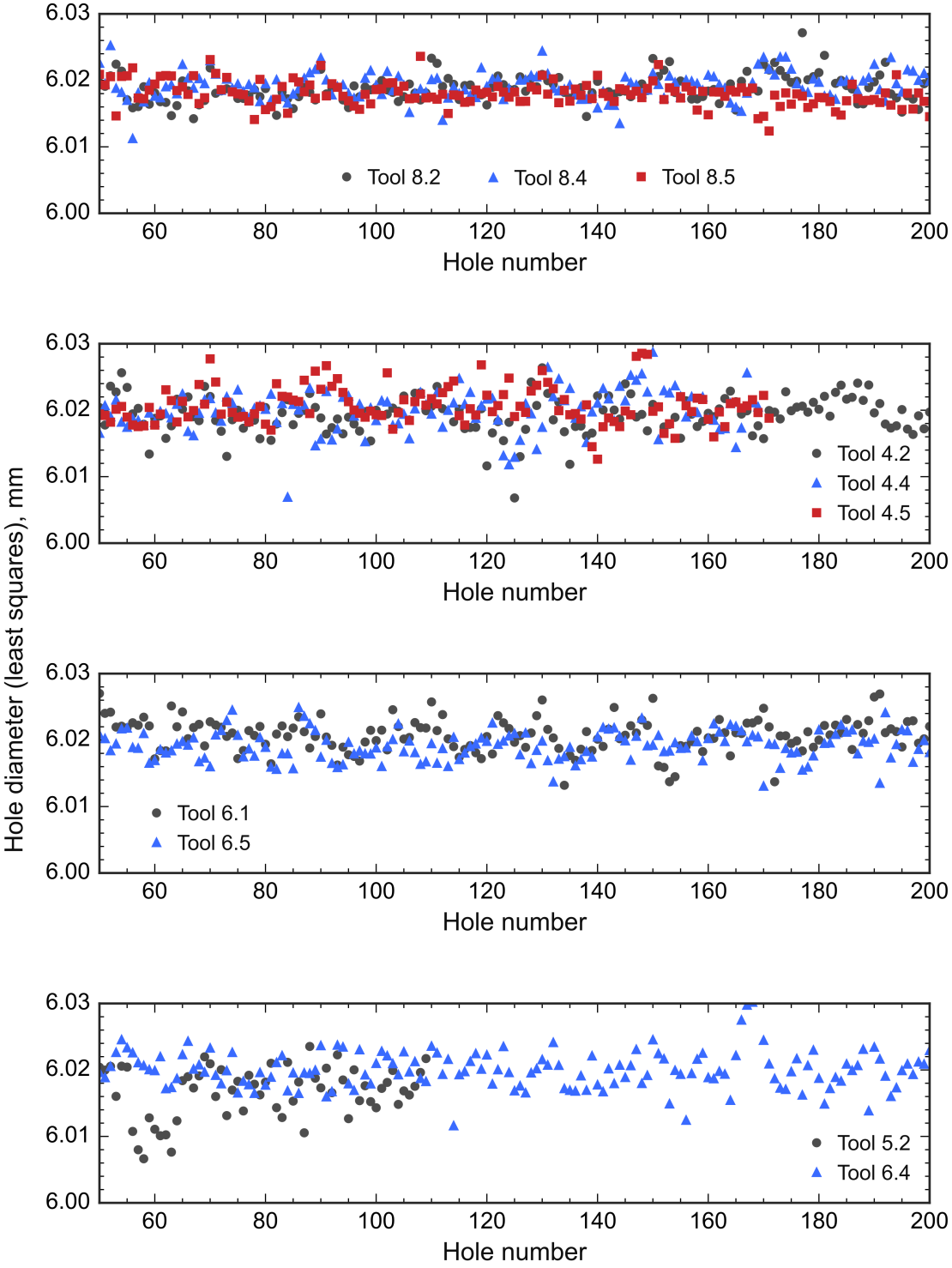

Figure 9.9: Hole diameter (least squares) for each of the holes in the LCO_2tool life tests.

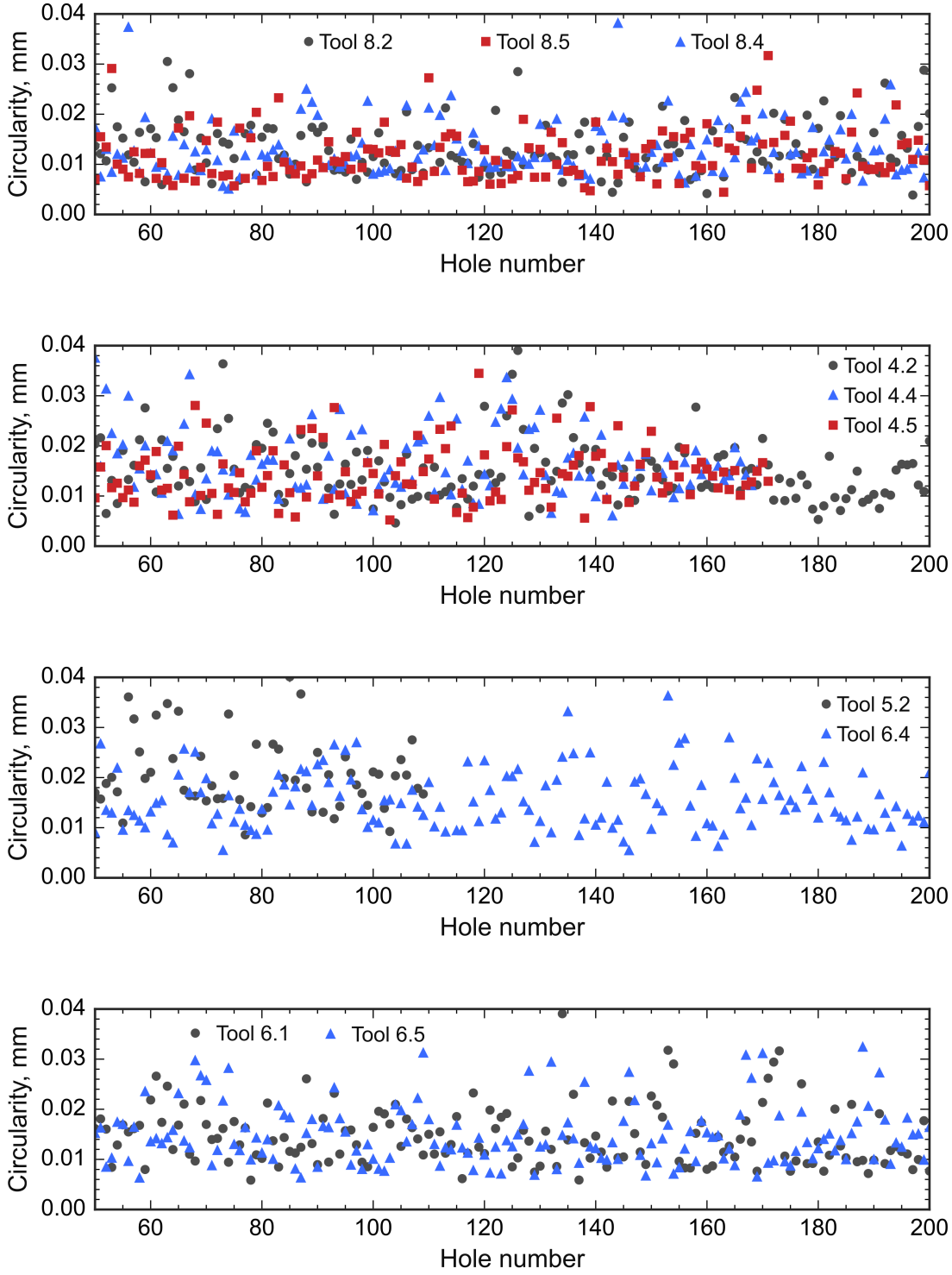

Figure 9.10: Circularity for each of the holes in the LCO_2 tool life tests.

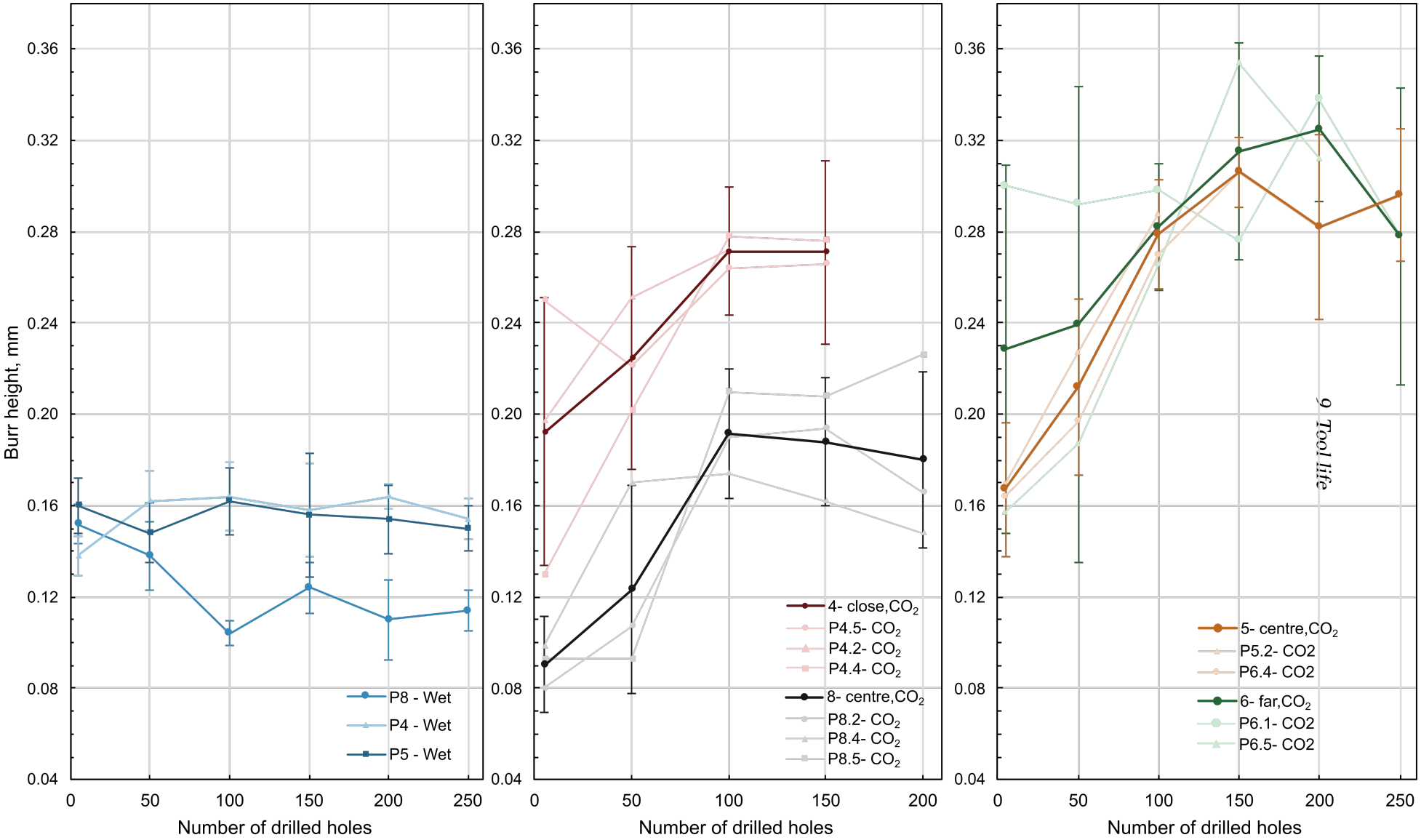

Figure 9.11: Burr height for each individual cutting tool comparing flood to LCO_2. For the LCO_2 tools, the thicker line indicates the mean value of the individual readings, while the error bars denote the standard deviation of the 5 measurements used to capture each reading.

9.4 SEM images of tools

Detailed SEM images of the prototype tools are presented of the cutting edge in Figures 9.12 and 9.13, and of the margin in Figures 9.14 and 9.15. The trends observed across each of the prototypes tested remain true between the comparison of the tools used with LCO_2 and flood coolant. These trends are increased adherence of workpiece material to the primary and secondary cutting edge, and the margin in the case of LCO_2 machined tools. Burnt cooling residue is observed on the flank face of the wet tools that were tested (shown as the darker region on the SEM images), indicating high temperature and no coolant flow [79]. Crater wear and subsequent chipping is observed on the margin of all the prototypes tested with LCO_2. Less adhered material was observed on the tool margin of the prototype with flood coolant. All the tools with flood coolant showed no damage on the margin, with the exception of prototype 5.4 which showed a small chip, 0.1mm in size (Figure 11.10). No crater is observed for this tool, and therefore will have formed due to the high load on the tool, also shown by the HAZ and burnt coolant residue behind the margin and on the cutting edge of the tool, Figure 9.8.

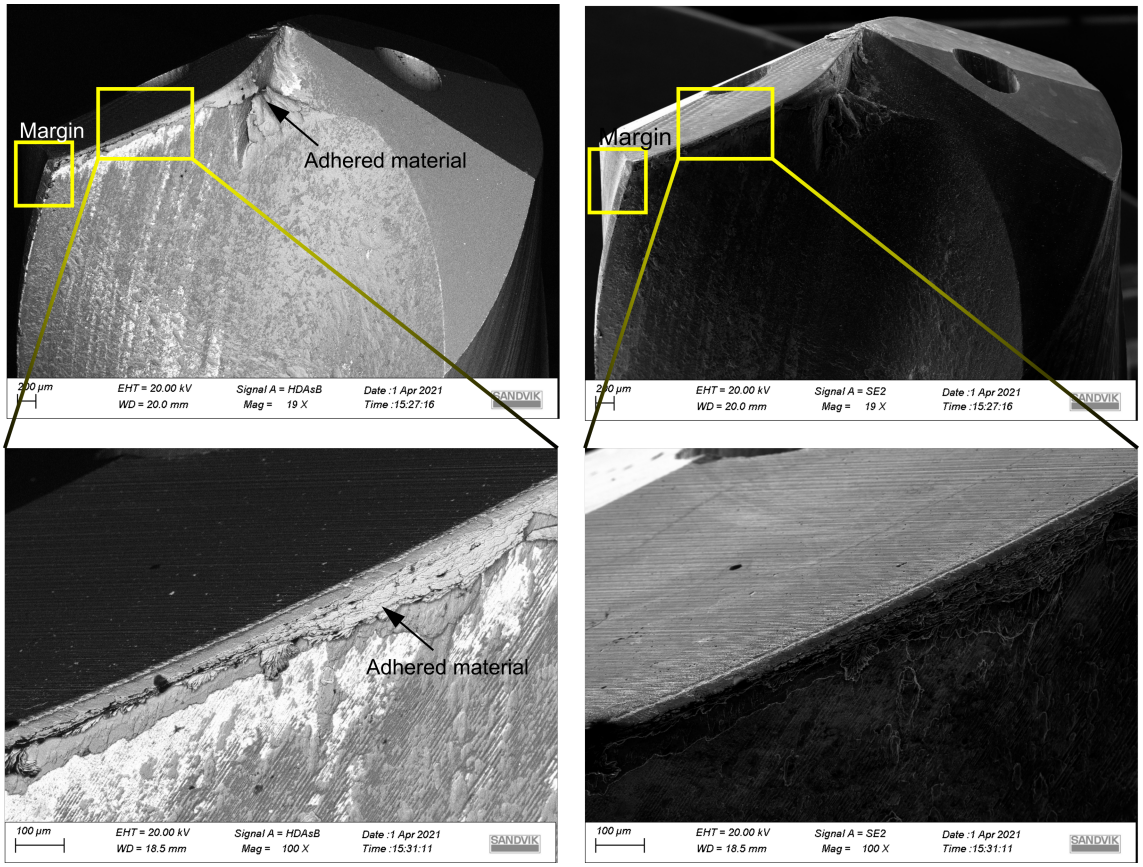

Figure 9.12: Prototype 8.2, SEM image of the tool wear present on the LCO_2 drilled solid carbide drill, after 209 holes.

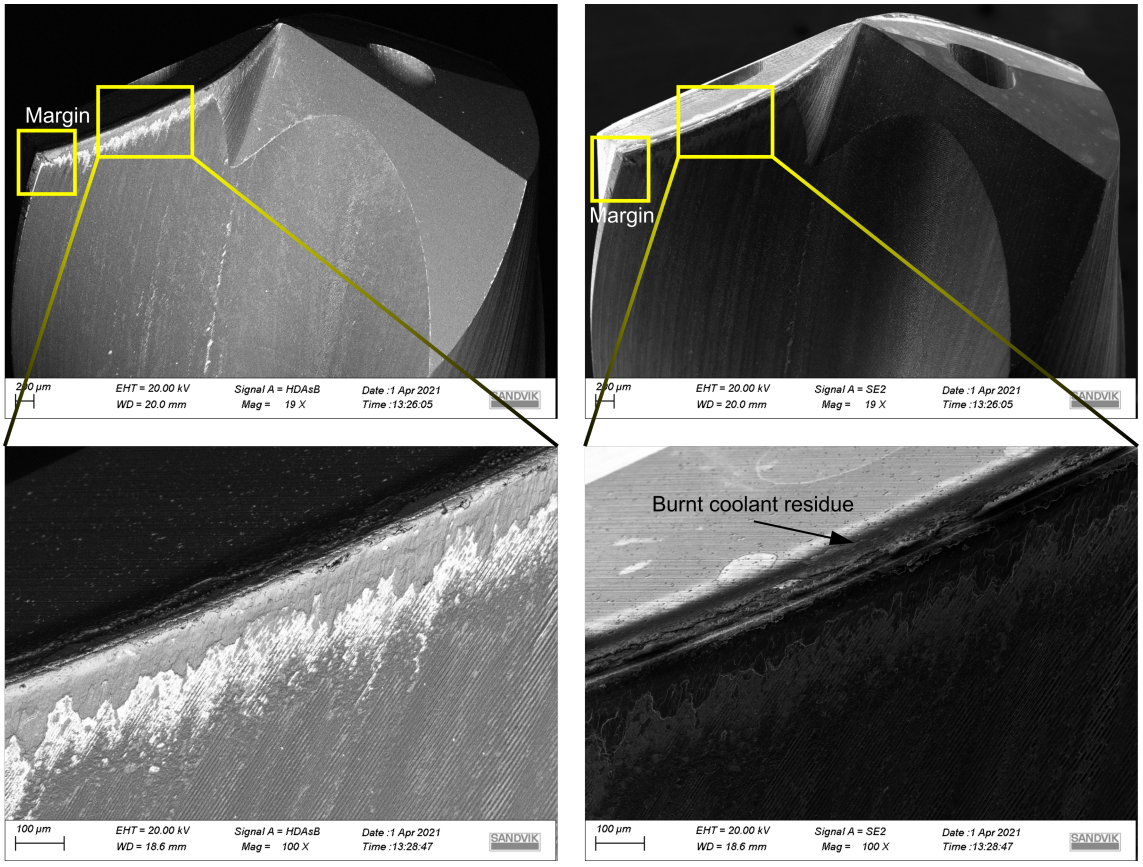

Figure 9.13: Prototype 8.3, SEM image of the tool wear present on the wet drilled solid carbide drill, after 300 holes.

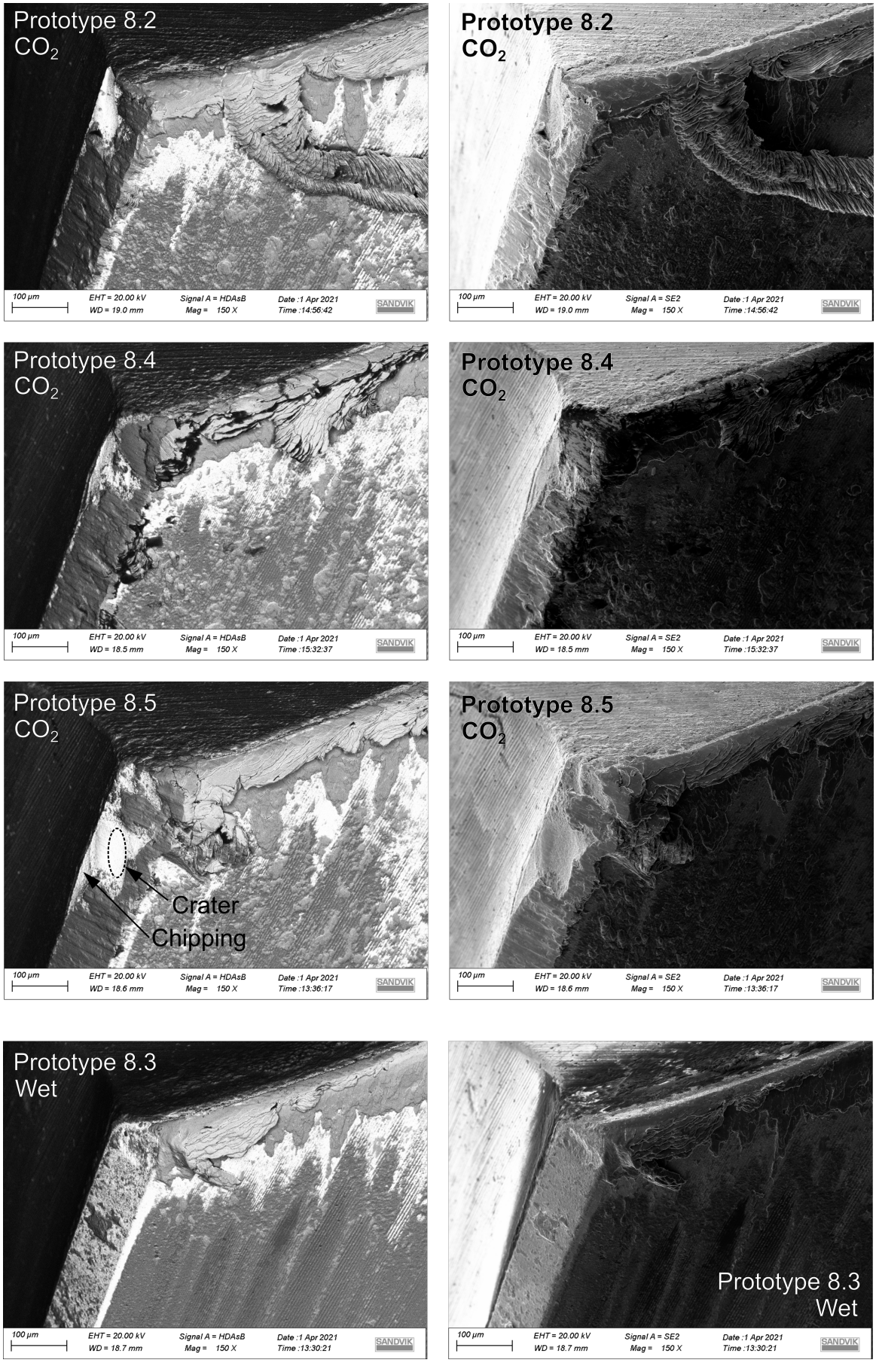

Figure 9.14: Prototype 8 comparison with wet, SEM image of the tool wear present on the LCO_2drilled solid carbide drill.

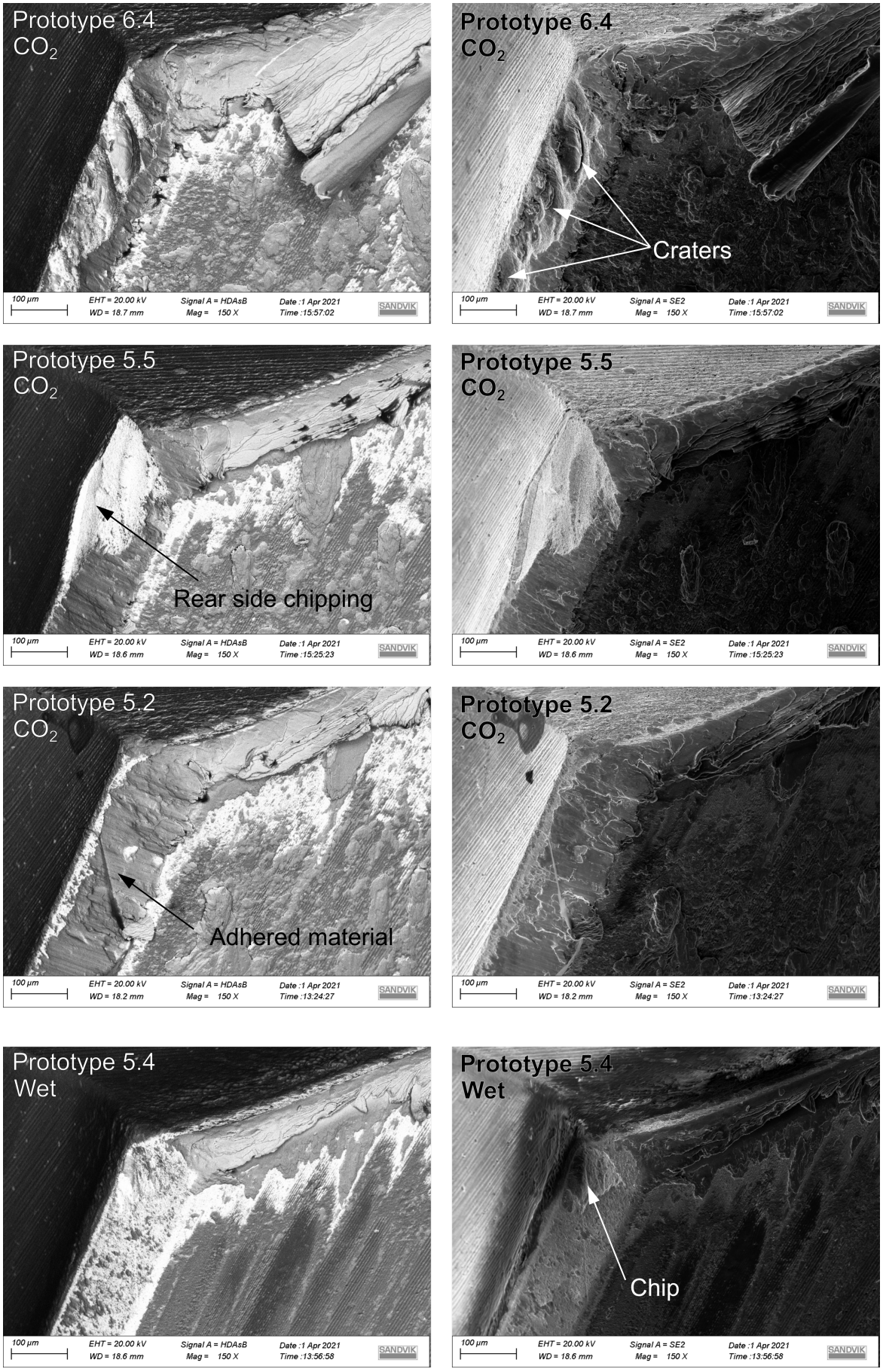

Figure 9.15: Prototype 5 comparison with wet, SEM image of the tool wear present on the LCO_2drilled solid carbide drill.

9.5 Conclusions of chapter

Tool life tests were conducted for prototype tools 8, 4, 5 and 6 to compare the tool wear mechanism for LCO_2 cooling media against traditional flood coolant (prototype 6 was conducted for LCO_2 only, due to a low number of prototype 6 available as one of the tools failed pre-inspection). The tests were conducted successfully and the following conclusions were found:

- The tool wear mechanism for the prototypes using the LCO_2 approach was identified as diffusion wear. Where, due to the lack of lubrication and high temperatures in this region, material from the tool diffused into the workpiece. This resulted in the formation of craters on the margin leading to a weakened margin resulting in material breaking from the drill margin. Additionally Increased material adhesion was found on the cutting edge of the drill and the chisel gash for the LCO_2 approach when compared to the wet (flood) approach.
- The number of holes drilled with the LCO_2 approach varied prior to tool failure. This is due to the characteristics of the wear mechanism, where the location of the crater formation and the local characteristics and grain size of the substrate is different for each tool and thus the onset of the margin break varies. Also, the crater wear can be hidden by the adhesion of the material to the margin in the crater, therefore the size of the formed crater could be hidden during tool inspection.
- The prototypes employing the wet strategy drilled 300 holes with no tool failures. A small chip was observed on one of the prototypes caused by the high load on the tool from the increased feed.
- Heat affected zone (HAZ) was observed behind the the margin and cutting edge of the prototypes using through tool flood coolant.
- All tools during the tests showed no change in the hole geometry over the tool life.
- Sharper tools produced a lower burr height for both the wet and LCO_2 approach.
- Burr height was found to increase for the first 100 holes for the tools using LCO_2 before reaching a plateau, while for the tools using flood coolant, the burr height remained consistent for the full range of tool life. The increased adhesion of material to the tool when using LCO_2 has been suggested as the cause for this burr height increase, due to the increase in edge rounding on the tool.

10 Discussion

10.1 Introduction

This chapter discusses the findings of the thesis and is structured according to each of the responses (dependent variables) that have been studied. Therefore, observations from multiple chapters will be pulled together and included under the various headings.

10.2 Chip formation

Chip formation in drilling is a critical factor in determining a successful process. As discussed previously, this is because with improper chip formation (chips that are long), the rotational motion of the drill is impeded due to chips clogged in the hole. This leads to torsional forces exerted on the drill exceeding the torsional strength of the drill, resulting in drill failure through breakage.

The chip formation when using LCO_2 has been shown to be inadequate when machined at cutting speed and feed typically used for drilling Ti6Al4V under wet conditions (Chapter 5). It was found that increased feed was required to improve chip form. It is suggested that the lower lubricity when using LCO_2 [98] compared to wet, is a possible cause of the different chip formation and the requirement for increased feed. This is because of the increased friction between the tool rake face and the chip being formed, resulting in the flow of the chip over the rake face of the tool being compromised with insufficient curl over the rake face.

This lack of curl prevents the chip from shearing and producing smaller chips. It has been shown by Aramcharoen [184] that by directing LN_2 between the rake face and the flowing chip, the chip curl improves. It is understood that when a cryogenic fluid is directed correctly into the interface between the rake face and forming chip, a lubricating layer of gas is formed (for both LN_2 and LCO_2 [110, 111, 112]). This lowers the friction, resulting in a lower contact area of the chip and tool, with a smaller secondary deformation zone, providing chip curl and improved chip formation through the curl acting mechanically on the chip to shear.

Rake face delivery of the cryogenic fluid in a solid carbide drilling context would require a redesign of the drill manufacture and how the coolant delivery channels are incorporated into the tool. Currently, they are extruded in a helix along with the drill when it is formed resulting in flow towards the bottom of the drilled hole. This method would not allow rake face delivery. One alternative may be to design the channels with an additive manufacture approach which would provide more freedom of choice to coolant hole location. However, whether this is possible and economically viable remains an open question. Alternatively, rake face delivery with indexable insert drills such as the CoroDrill 880 [185] could be easily implemented as the coolant channels are already in place on this drill and would just require repositioning. As the tool is an indexable tool, modifications to the tool would need to be completed

only once and multiple tests could be carried out simply by replacing the inserts.

When increased feed is used, it is hypothesised that this improved the chip form because of the increased uncut chip thickness and thus less impact of the friction on the flow of the chip over the tool, allowing it to flow over the tool correctly and strain soften the chip to a lesser degree [186]. Additionally, the impact of the heat transfer into the chips from the secondary deformation zone may also be causing the change in chip form. Shah et al. [104] attributed their poor chip formation, the chip was found to buckle and concertina, to the thermal softening of the chip material.

For a thinner chip the secondary deformation zone imparts a greater amount of heat per total volume of the produced chip resulting in a greater amount of thermal softening per unit volume. While for thicker chips this heat is dissipated into a greater chip volume, with less thermal softening occurring [187]. With increased temperature, and thinner chips, the behaviour of the chip is therefore more ductile, preventing the shearing of the chip resulting in the concertina-like chips as observed. This work has shown that with the decreasing cutting temperature, as shown when machining thinner workpiece thickness, and using higher LCO_2 mass flow rates (Chapter 7), improved chip form have been found, through reducing the thermal softening of the formed chip, leading to improved chip shearing.

Peck drilling has been shown, for the first time with LCO_2, to successfully provide a way of forming the chip for the deeper drilled hole, where the momentum of the evaporated gaseous CO_2 would not provide a sufficient chip evacuation mechanism (see Chapter 7). The intermittent cutting of the peck motion allowed the breaking of the chips due to the interruption of the chip formation. However, it should be noted that the production rate of the process is impacted. For the final peck that was chosen (0.5mm drill, with 0.05mm retract) an extra 0.1mm of drill travel is required for each 0.5mm, therefore the drill travels 20% further. This is the case as the retract feed was equal to the drill feed. This 20% increased distance means that production would take 20% longer that a hole of equal depth without retracting.

10.3 Cutting forces

Both the normal (thrust) force and torsional forces acting on the drill have been shown to be positively correlated with increased drill feed. These findings are in agreement with literature [188, 189, 137, 148] and are as expected. The increased forces are observed due to the increased workpiece engagement of the tool leading to increased uncut chip thickness. This results in a greater volume of material being sheared to form the chip, requiring a larger force to remove the material.

This work has shown the mass flow rate of LCO_2 to be positively correlated with the normal force (Chapter 6), whereby at higher values of tested mass flow rate, higher normal forces were observed. Similarly, larger coolant holes have also resulted in larger forces (Chapter 8) due to the increased mass flow rate attainable. These increases in mass flow rate correspond to a reduction in temperature (Chapter 7). These findings of increases in force at lower temperatures is in line with results found in milling with cryogenic fluids. The consensus is that when cryogenic fluids are used, a greater amount of heat is removed when compared to other MWFs. This increased heat removal results in a lower degree of thermal softening to occur, thus reducing cutting forces [123, 124, 125]. Again, this is supported by the force measurements captured with dry, MQL and wet, in this work which are lower than for the LCO_2. The normal force for wet was 730N, dry was 640N, and MQL was 640N. In comparison to 850N for

LCO_2 (Prototype 8). Additionally, due to less thermal softening of the material at lower temperatures, the friction coefficient at the contact has also been shown to increase [103, 3], contributing to the increase in the thrust force that has been measured.

These increased forces observed with LCO_2 would mean that drills would need to be designed to withstand the increased thrust forces, with increased web thickness. While the lack of thermal softening to keep the forces low has resulted in increased thrust forces, it also has negative effect on the chip formation (Figure 6.3) where the thermal softening of the chip results in poorly formed chips, which is also aligned with lower normal cutting force. Therefore, as discussed previously lubrication is required to counteract the increased friction that has been observed.

One method that has been attempted in this work has been to move the coolant hole channel to various distances from the cutting edge to try and alter the penetration of the LCO_2 into the cutting zone (Section 8.1), as has shown to improve penetration with a wet strategy [80]. This change in coolant hole position has shown to have little influence on the cutting forces, and therefore has had little influence on the penetration into the cutting zone. Therefore, to lower the forces, lubricant would be required to provide lubrication to the process, lowering the friction between the tool and the workpiece [98]. However, to maintain a fully dry process as with no contaminating oils, as demanded by the medical industry, alternative solutions would be required.

One alternative would be to consider different tool coatings. The TiAlN used in this case is designed for HRSA materials operating at high cutting temperatures. This coating is designed to protect the tool from extreme temperatures and thus acts as a thermal barrier and offers no ability to remove heat through the tool [190]. Alternative coatings, whilst not offering the same hot hardness as TiAlN, can offer improved tribological conditions. Molybdenum disulphide and titanium nitride have been shown to improve tribological conditions and support heat removal into the bulk of the cutting tool [190], beneficially removing heat in a cryogenic process. This is achieved by limiting the adhesion of the workpiece material to the tool, lowering the tool contact area and thickness of shear zones surrounding the tool. Further, it is anticipated that the addition of MQL into the process should allow improved lubrication in the cutting zone [114], and reduce the friction where a lubricating cushion is not able to be set up in these instances .

The edge rounding of the tool has been modified to a smaller edge rounding for prototype 7 and 8 in Section 8.1. A smaller edge rounding has shown to produce a lower normal force. For a sharper tool, with lower edge rounding, there is a smaller ploughing force acting on the tool in the feed direction (Figure 4.17). This is because there is a smaller contact area between the tool and the workpiece, with fewer contacting asperities, lowering the contact friction and thus the measured thrust force.

It is important to note that these findings are for through tool, when externally applieded, Shah et al. [104], a reduction in normal force when machining with LCO_2, over that for wet machining was found because the fluid was unable to reach the interface between the tool and the workpiece as the chip was being formed. The LCO_2 will have sublimated and evaporated before it will have had the opportunity to cool the tool, essentially the drill will behave like a dry tool. Therefore supply of cryogenic coolant is recommended through tool supply in drilling [135]. This however poses challenges due to the necessity of altering current machine spindle and tool holder to deliver the cryogenic fluid to the rear of the tool, adding an upfront cost to the process.

Increasing the LCO_2 mass flow rate had negligible influence on the torque. The improvement of the

chip formation with the increased LCO_2 mass flow rate does not influence the torque indicating that there is no contributing effect on the packing of the chips in the flute at the range cutting data studied. Additionally the different coolant strategies that were also tested (wet, dry and MQL) did not show any change to the torque, whereas Khanna et al. [139] found a decrease in the torque with LN_2 drilling of Inconel 718 when compared to dry, due to less workpiece material adhesion to the drill using LN_2 indicating sufficient penetration of the cryogen to the cutting zone. In their work comparing LN_2 with dry, Merzouki [137] were able to distinguish a small reduction in the torque when using LN_2. This is due to the larger 12mm diameter drills producing higher torque (between 8 and 14Nm) increasing the resolution of the difference (10%). This has not been possible with the smaller drill diameters and lower torque values, approximately 2Nm, and the periodicity between each set of seven holes due to the characteristics of the machine. Increasing the cutting feed did result in higher torque due to the increased uncut chip thickness, as expected due to the increased contribution of the cutting edges to the torque [137].

10.4 Temperature

The relationship between the temperature and LCO_2 mass flow rate was found to reduce with a squared relationship, which accelerated as the LCO_2 mass flow rate increased. This is because the increasing LCO_2 mass flow rate resulted in a greater volume of LCO_2 in the vicinity of the hot cutting edge during machining removing a greater amount of heat. These results are as expected and are in line with others [140]. The model cannot be extrapolated beyond the operating window studied and is valid only between 6 and 10kg/hr, therefore it is unknown whether further increases in the flow rate would result in improved cooling leading to further improvements in performance, as an optimal cutting temperature exists for different tool-workpiece pairs. For example further increases of the LCO_2 mass flow rate upwards of 50kg/hr have been shown to be beneficial to tool performance [115] because of the improved heat removal capacity. However, an optimal LCO_2 mass flow rates of 7kg/hr have also been shown to be optimal when drilling 42CrMo4 steel [140] by using MQL with LCO_2 to lower the friction and achieve an optimal temperature, whilst minimising CO_2 usage. Furthermore, as stressed by Supekar et al. [166] it is important to optimise delivery with correct nozzle placement to meet cooling and lubrication needs of process whilst minimising CO_2 usage as much as possible in order to have low impact on the environment and improve the sustainability of the process.

The thickness of the workpiece to be machined is also a pertinent consideration when deciding on the process LCO_2 mass flow rate, because it has been shown in Section 7.2 that increases in the workpiece thickness, increase drilling temperature due to the build up of heat in the longer drilling cycle as opposed to a shorter drilling cycle for thinner workpieces. It is therefore clear that the LCO_2 assisted drilling temperature increases linearly with increasing workpiece thickness. Thus, to achieve the optimal cutting temperature [101], further tuning of the LCO_2 mass flow rate for different sized workpiece thickness would be required. Herein, material and other process parameters need to be considered when selecting and optimising the LCO_2 mass flow rate for a drilling operation.

Additionally, pecking has shown to influence the cutting temperature, with an increased peck size leading to lower temperature (Section 7.3), as greater cooling is achieved. However, this results in premature margin failure because of the increased friction at the margin of the tool due to the cold

temperatures and increased adhesion on the margin observed during the longer pecks, resulting from a lack of lubricating fluid in this region and low thermal softening of the material.

10.5 Hole geometry

10.5.1 Hole diameter

Increases in the LCO_2 mass flow rate have been shown to produce smaller holes closer to that of the nominal drill diameter. This is in agreement with work conducted by Merzouki et al. [137] where they compared the hole diameter of LN_2 to dry drilling. This shows that a colder drill results in a smaller drilled hole. Further evidence of this relationship has been shown with observations of the gauge hole diameter (difference between measured drill diameter and hole diameter) and temperature measurements with negative correlation, and the peck drilling studies completed in Section 7.3.1, where increased duration between each peck resulted in lower temperature measurements and smaller hole diameters caused due to the thermal contraction of the drill at the cold temperatures.

Drilling with wet coolant has been found to produce holes closest to the nominal diameter than for all other cooling strategies tested. The largest holes relative to the intended diameter were produced for dry drilling and MQL strategies. This further indicates that heat removal plays a part in the produced hole diameter, particularly where the drills with smaller coolant holes, at lower LCO_2 mass flow rate, have drilled larger holes than for the drills with larger coolant hole sizes. As the wet strategy has produced the smaller holes, the overall heat capacity of the fluid (larger with wet coolant [101]) in the removal of the heat during drilling, has an influence. The hole diameter has shown to be stable for a large number of holes drilled, during the tool life studies (Section 9.3), despite the tool wear experienced on the margin of the drills. For Prototype 8 the diameter of the drilled holes remained below the upper limit of 6.03 and a hole tolerance of H9 as the specification for Sandvik Coromant tools, meaning that the process produces holes of the required quality.

10.5.2 Circularity

The influence of the workpiece thickness has been shown to influence the circularity of the drilled hole. When the workpiece thickness is reduced, circularity measurement increases so that the hole shape deviates further from a perfect circle. The reason for this is due to the reduced stability of the drill, there is a smaller area of contact between the margin and drilled hole wall when compared to during drilling deeper holes with increased drill bending. Reductions in hole circularity was expected with the use of LCO_2 as observed by Khanna et al. [139]. However, there was no observable impact of LCO_2 on the circularity of the holes throughout all of the experiments. The results from Khanna et al. were in Inconel 718, which is more difficult to machine than Ti6Al4V, and the drill experienced chipping on the cutting edge during dry drilling tests, explaining the improvement over the dry. The difference in behaviour for different material means that further studies are required to explain the impact of using LCO_2 in different materials on hole circularity.

10.6 Exit burr height

The increased cutting feed, required for adequate chip formation when using the CoroDrill R846 geometry in LCO_2 drilling, resulted in an increase in the exit burr height of the drilled hole. For the initial trials with lower feed, consistent burr heights were observed, however when the operating window was altered with increased values of feed, to improve the chip formation, the burr height was found to increase with increased cutting feed. This relationship agrees with work conducted by Rana et al. [177], where they state that it is due to a greater of volume of material deformed on drill exit with increased cutting feed and the increase in the normal force contributing to a greater volume of plastic deformation forming the exit burr. Additionally, with the higher cutting feed, more of the tool corner is engaged in the cut and as the margin does not cut well as increased ploughing at the margin will occur increasing exit burr.

An increase in burr height over time, due to tool wear, has been shown in Section 9.2, as expected [169, 150]. For LCO_2 assisted drilling, a step increase in the burr height was observed and it is believed this was caused by damage that occurred on the drill margin during drilling, as Franczyk et al. [178] have shown. This possibly explains the different burr height observed by Tool 1 in Section 6.4.4.4, where damage to the drill margin could not be identified due to the adhered material on the margin. Prototype type and cooling media were found to influence the burr height as well. The most favourable prototype was Prototype 8, with larger coolant holes and smaller edge rounding, producing holes with exit burr smaller than dry and MQL strategies. This suggests that the larger coolant hole protects the margin by preventing adhered material on the margin, and cooler cutting (Chapter 7) indicating a reduction in the burr height, which is in agreement with the results found by Chaanthini [191] where smaller exit burr was found with pre-cooled material in drilling aluminium.

To this author's knowledge it is the first time the effect of LCO_2 coolant hole supply and edge rounding on the exit burr have been presented. Prototype 8 has shown similar burr height characteristics to that of wet drilling, and that LCO_2 is capable of producing holes that satisfy industry burr height requirement.

Further work to study the effect of the LCO_2 on the subsurface damage of the workpiece is needed. This use of cryogenic media has shown been by Aceves [192] to have negative impact on the subsurface in milling applications. It may be possible therefore that further boring and reaming operations may be required to remove this damaged layer if present.

10.7 Tool life

Tool life tests of prototype tooling with LCO_2 and wet coolant were conducted to identify the tool wear mechanism of LCO_2 assisted drilling.

The wear mechanism for LCO_2 was identified as diffusion wear at the drill margins. This was caused due to the lack of the lubricating properties of LCO_2 resulting the generation of high temperatures at the margin resulting from the high friction. The low thermal conductivity of titanium and the high affinity of the titanium to react with the titanium contained within the TiAlN coating of the drill resulted in large amounts of adhered material on the margin of the LCO_2 drill when compared to the wet drill. This is likely due to the the lack of LCO_2 able to enter this area, similarly observed by Oezkaya et al. [77], and the poor lubricating effects of the LCO_2 [98]. The adhesion of material and high temperatures at the margin results in the removal of the tool coating and diffusion of the tool cobalt into the titanium [38].

This removal of material from the tool margins resulted in the formation of the craters on the drill margin. This loss of material from the drill margin subsequently weakened the margin through the formation of crack initiation sites and the thinning of material on the margin, which was then observed to crack off the tool.

Therefore this wear on the drill margin resulted in lower tool life for the LCO_2 drilling strategy when compared to the wet strategy, with stable flank wear observed (Chapter 9) . This indicates the need to improve the protection of the drill margin with a LCO_2 cooling strategy through the use of improved lubrication at the margin [71]. This can be achieved through the addition of MQL into the LCO_2, or maybe through the use of textured tools on the margin, whereby adhesion of workpiece material has been found to be reduced [193] when dry machining would be required. However this would increase the production cost of the drill due to increased number of operating steps required to produce the drill.

No work to the author's knowledge, has been published showing the influence of LCO_2 on the tool wear of solid carbide tools when drilling Ti6Al4V. Flank wear measurements were low and in line with those observed with wet. If the adherence of workpiece material to the drill margin, to prevent subsequent diffusion wear, can be lowered by improving lubrication and lowering friction at this interface. Either through the methods suggested above or through alternative cutting tools with modifications to the margin surface [194], or even using a different tool (Figure 10.1). It is possible that drilling may perform similarly to wet based on the flank wear observations, however further study is required. Furthermore, the temperature measurements of the prototypes showed close repeatability and variations in the temperature measured, therefore it is possible that different coolant hole positions will have an influence on the flank wear and is therefore a future consideration for optimal drill design, as the temperature is known to influence largely abrasive flank wear (Figure 2.9).



Figure 10.1: Walter Titex DC170 drill utilising no margin.

11 Conclusions

11.1 Introduction

To conclude the work conducted in this thesis the outcomes and impact will be considered against each objective defined in Section 1.2.

The aim of this work was to understand the behaviour and characteristics influencing the performance of Sandvik Coromant solid carbide tooling when used in LCO_2 assisted drilling of Ti6Al4V.

11.2 Objective 1: Determine a suitable operating window for LCO_2 assisted drilling

Initial trials at cutting parameters that would typically be used for wet drilling of titanium using CoroDrill R846 drills resulted in an unstable process with insufficient chip formation. Observation of the data revealed that the chip formation improved with increased cutting feed. It was clear that to attain improvements to the chip formation, and allow safe study of the process, the operating window would need to be expanded. Further tests were therefore conducted at cutting feeds above the original operating window.

Increasing the cutting feed did provide an operating window of cutting data to be able to further study LCO_2 assisted drilling resulting in improved chip formation and internal hole surface roughness.

11.3 Objective 2: Observe the influence of LCO_2 process parameters on forces, temperature and workpiece quality

It was evident in literature that there was little work around cryogenic drilling, particularly work using LCO_2 and solid carbide drills. However, literature did show coolant mass flow rate and pre-cooling effects of the tool to impact the process. The importance of capturing forces, temperature and workpiece quality metrics was identified both from a scientific and industrial perspective for tool design, process understanding and tool performance.

Variables influencing the cutting process were identified from literature and a methodology utilising design of experiment techniques for studying these pertinent variables was devised. Cutting force and temperature measurement methods were also developed for the horizontal drilling set-up. The importance of the LCO_2 mass flow rate, workpiece thickness and cutting feed was identified while between hole dwell and retract distance did not show any influence on the responses (dependent variables).

Empirical mathematical models for forces, temperature and workpiece quality were successfully generated. The models generated for the forces (normal and torque), and temperature data showed good fit to the data, evident by small confidence intervals and high R^2 values. In terms of the workpiece quality, the

diameter (least squares) was modelled with good fit to data, however with surface roughness was not influenced by changing the process parameters.

Peck drilling with a partial peck of 0.5mm cut with a retract of 0.05mm has shown a reduction in the temperature measured and in turn reduced exit burr height. Peck drilling was adopted for assessing the other objectives.

11.4 Objective 3: Determine the impact of altering key design features on the drill with a view to positively improve the LCO_2 drilling process

Prototype tools were manufactured with changes to the coolant hole size and position away from the drill cutting edge. Experiments using these prototypes were then conducted to determine the influence of these parameters when using LCO_2 cooling media. The tools using the larger coolant supply holes were found to cool the workpiece to a greater extent and increase the normal cutting force. This was attributed to the increased mass flow rate attainable with the larger coolant hole sizes due to the inability of the machine tool to maintain the 10kg/hr mass flow rate. Literature had shown changing the coolant hole position in drilling to impact the cutting process in wet drilling. However, changing the position of the coolant holes had minimal effect on the cutting process and just changing the position was not enough to allow the LCO_2 to access the cutting interface to a greater extent. Slots machined in to margin and flank faces may improve this. Computational fluid dynamics (CFD) modelling could be used to further understand the streamlines of this rapdily sublimating and evaporating fluid at the drill exit, though it remains a non-trivial undertaking.

Sharper cutting tools with a reduced edge radius have been shown to counteract the increase of the normal force with using LCO_2 and produce holes with the smallest burr height and good hole geometry. For changes to the cutting edge shape, improved chip formation was observed due to the improved mechanical action to curl the chip, but this was at the expense of increased exit burr height.

11.5 Objective 4: Compare observations to alternative cooling media

Trials were conducted with standard CoroDrill R846 drills to compare wet, dry and MQL cooling media at process parameters determined to be the most suitable for LCO_2. Lower normal forces were observed for the dry and MQL strategies. This highlighted the increased cooling effect of LCO_2 and thermal softening of the workpiece when drilling dry, and with MQL. While torque forces were unchanged for each strategy.

The effect of the addition of lubricant to the process was highlighted whereby it reduced the amount of adhered material on the drill cutting edge. The wet strategy was shown to access and lubricate the margin to a greater extent than the MQL strategy due to less adhered material on the margin.

The MQL and dry strategies produced holes of diameter furthest from the drill nominal diameter, and the holes were larger in diameter than the LCO_2 strategy.

11.6 Objective 5: Apply the changes to the LCO_2 process and determine tool life and tool wear mechanism in comparison to wet drilling with emulsion

Tool life trials were conducted with four prototype tools (4, 5, 6 and 8). These were conducted for LCO_2 and wet cooling strategies. The tools tested with LCO_2 were tested until tool failure occurred while the wet drills were tested to 300 holes which did not fail. The number of holes drilled by the tools drilling with LCO_2 failed with a varying number of holes.

The tool wear mechanism identified for the LCO_2 drilling strategy was identified as chemical wear due to the high adhesion of titanium workpiece material on the margin of the drill. The manifested itself and crater wear and subsequent chipping of the margin due to weakening. All the tools tested with the LCO_2 drilling strategy failed in this way. In contrast the tool wear on the tools adopting the wet drilling approach experienced flank wear, however a small chip was identified on one of the drills using the wet drilling strategy.

Flank wear measurements between both drills were similar. Therefore if the adhesion of workpiece material on the drill margin can be minimised or prevented and thus remove the crater wear in this region on the then it is believed that the LCO_2 drilling tool can perform similarly to the wet drilling strategy.

11.7 Concluding remarks and recommendations

In light of the findings from this thesis, LCO_2 assisted drilling of Ti6Al4V is possible with changes to the parameters of the current drilling parameters with wet coolants typically used. The thesis has shown the workpiece quality to be similar to that produced during wet drilling in terms of burr height and hole geometry. Therefore this thesis provides a LCO_2 assisted drilling solution for the CoroDrill R846 tool that Sandvik Coromant can offer to customers and facilitate added value in to the manufacturing chain through improved sustainability and worker health.

Work remains to improve the productivity of the tool due to the lower tool life than with wet drilling, however future work has been suggested to improve the wear characteristics of the drill margin. If stable flank wear can become the limiting factor LCO_2 assisted drilling measurements have shown similar wear behaviour to the wet drill.

Recommendations from this work can therefore be summarised as:

- Operate with increased cutting feed (0.2mm/rev for 6mm drill) from that normally adopted to enable adequate chip formation.
- Use the as high a LCO_2 mass flow rate to further improve chip form and reduce exit burr height.
- Utilise as small a cutting edge rounding as possible to counteract the increased material strength and subsequent normal forces, whilst at the same time maintaining the integrity of the cutting edge (no chipping or plastic deformation). A nominal edge rounding of 18µm has shown to provide a decrease in normal force whilst maintaining the integrity of the cutting edge.
- Use a shallow peck cycle to further reduce cutting temperature and exit burr height.

- Investigate suggestions for future work in Chapter 10 to reduce or eliminate the adherence of material at the drill margin to transfer the wear mechanism to flank wear on the cutting tool flank face.

11.8 Future work

The future work that has been identified can be summarised as:

1. Establish the relationship between the normal force and the cutting edge rounding to determine whether the manufacturing tolerances of the edge rounding on the tool need adjusting to achieve consistent normal forces. A change in edge rounding nominal value from 36µm to 18µm in prototypes 7 and 8 has shown a reduction of normal force by 20%.

2. Carry out tests at higher LCO_2 mass flow rates to determine the limiting benefit of increasing the LCO_2 mass flow rate alongside economics costs due to increasing LCO_2 consumption and carbon emissions.

3. Conduct experiments with LCO_2 with different workpiece materials, due to the different material properties of the workpiece material, and their behaviour at colder temperatures will influence hole geometry and cutting forces differently.

4. Explore different tool types:
   a) Investigate the process in drills with no margin.
   b) The tool shape has shown to influence chip formation at lower cutting feed at the expense of burr height. However, it warrants further investigation.
   c) Investigate the influence of machining a slot in to the flank and margins of the drill to facilitate fluid flow to the margin.
   d) Investigate the effect of changing the surface characteristics of the margin the prevent the adherence of material.
   e) Investigate alternative coating materials to reduce the adherence of the Ti6Al4V to the TiAlN coating of the drill.

5. Investigate the effect of the process on the subsurface integrity of the hole to detect any presence of damaging white layer that may need to be removed in subsequent boring or reaming operations.

6. Investigate the use of lubricant dissolved in $scCO_2$ to provide lubrication to the margin and to reduce the adhesion of workpiece material in this region.

11.9 Papers in preparation

Work from this thesis is expected to be presented in journal papers, preliminary titles for these include:

1. The effect of cutting data on chip formation in LCO_2 drilling of Ti6Al4V.
2. A multivariate study of process parameters on the key performance variables in LCO_2 drilling.
3. The effect of coolant type on the performance of solid carbide drilling.
4. Tool wear mechanisms of LCO_2 and wet drilling of Ti6Al4V.

Appendix 1 - Kistler dynamometer specifications (9129AA)

KISTLER
measure. analyze. innovate.

Multicomponent Dynamometer

Type 9129AA

–10 ... 10 kN, Cover Plate 90x105 mm

Multicomponent dynamometer for measuring the three components of the resultant force vector and the three components of the resultant moment vector.

- Small design
- Large measuring range
- Small temperature error
- For cutting force measurements
- For general multicomponent force measurements



Description

The dynamometer consists of four 3-component force sensors which are mounted under high preload between the cover plate and the two lateral base plates.
Because of the special mounting of the sensors, a small temperature error is achieved. The force sensors each contain three crystal crystal disks, one of which is sensitive to pressure in the y direction and the two others to shear force in the x or z directions. The forces are measured with practically no displacement. The outputs of the four built-in force sensors are passed to the 9-pole flange socket. Multicomponent force-moment measurements are possible.
The four sensors are mounted with ground isolation. This largely avoids ground loop problems.
The dynamometer is corrosion-resistant and protected against the ingress of cooling lubricant. Used together with connecting cable Type 1687B... or Type 1677A..., the dynamometer is sealed according to degree of protection IP67.

Quartz multicomponent dynamometers measure easily, directly and very accurately.

Application Examples

- Cutting force measurement in superfinishing
- Multicomponent force measurement
- Force measurement in confined spaces
- Measurement of the three cutting forces F_c, F_f, F_p while turning outside and inside diameters on lathes with turret-type tool heads (see data sheet for Type 9129A...)

Technical Data

Max. permitted measuring range (Force application point at cover plate surface)	F_x, F_y, F_z M_x, M_y, M_z	kN N·m	–10 ... 10 –500 ... 500
Calibrated measuring range 100 %	F_x, F_y, F_z	kN	0 ... 10
Calibrated partial meas. range 10 %	F_x, F_y, F_z	kN	0 ... 1
Calibrated partial meas. range 1 %	F_x, F_y, F_z	kN	0 ... 0,1
Overload	F_x, F_y, F_z	%	20
Threshold		N	<0,01
Sensitivity (rated)	F_x F_y F_z	pc/N pc/N pc/N	≈–8,1 ≈–4,1 ≈–8,1
Linearity, all ranges	F_x, F_y, F_z	±%/FSO	≤±0,3
Hysteresis, all ranges	F_x, F_y, F_z	%/FSO	≤0,3
Crosstalk	$F_z \rightarrow F_x$, F_y $F_x \leftrightarrow F_y$ F_x, $F_y \rightarrow F_z$	% % %	≤±2 ≤±2 ≤±2
Rigidity	c_x, c_z c_y	N/µm N/µm	≈1 000 ≈4 000
Natural frequency (Type 9129AA mounted on rigid base)	$f_n(x)$ $f_n(y)$ $f_n(z)$	kHz kHz kHz	≈3,5 ≈4,5 ≈3,5
Operating temperature range		°C	0 ... 70
Capacitance	F_x, F_y, F_z	pF	≈180
Isolation resistance		Ω	$>10^{13}$
Ground isolation		Ω	$>10^{8}$
Degree of protection EN60529			IP67
Weight Dynamometer		kg	3,2
Cover plate		kg	2,0
Mounting surface		mm	90x105
Connection			Fischer flange 9 pin neg.

This information corresponds to the current state of knowledge. Kistler reserves the right to make technical changes. Liability for consequential damage resulting from the use of Kistler products is excluded.

©2009 ... 2012, Kistler Group, Eulachstrasse 22, 8408 Winterthur, Switzerland
Tel. +41 52 224 11 11, Fax +41 52 224 14 14, info@kistler.com, www.kistler.com
Kistler is a registered trademark of Kistler Holding AG.

9129AA_000-709e-10.12

KISTLER
measure. analyze. innovate.

Dimensions

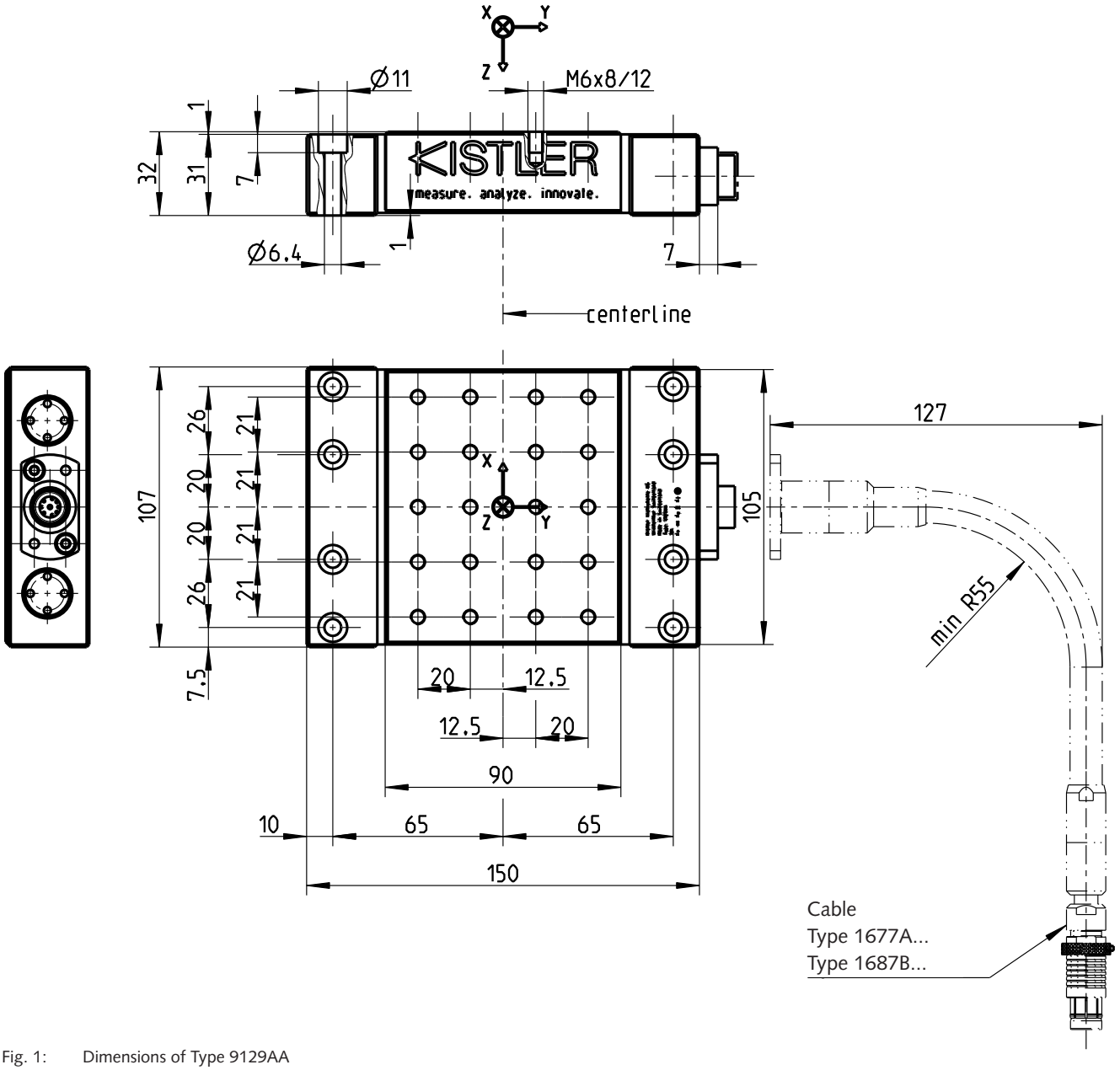

Fig. 1: Dimensions of Type 9129AA

9129AA_000-709e-10.12

This information corresponds to the current state of knowledge. Kistler reserves the right to make technical changes. Liability for consequential damage resulting from the use of Kistler products is excluded.

©2009 ... 2012, Kistler Group, Eulachstrasse 22, 8408 Winterthur, Switzerland
Tel. +41 52 224 11 11, Fax +41 52 224 14 14, info@kistler.com, www.kistler.com
Kistler is a registered trademark of Kistler Holding AG.

KISTLER
measure. analyze. innovate.

3-Component Force Measurement F_x, F_y, F_z with 4-Channel Charge Amplifier

Dynamometer
Type 9129AA

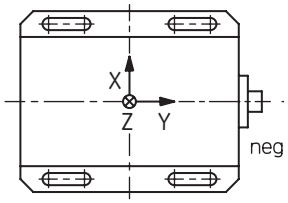

Cable

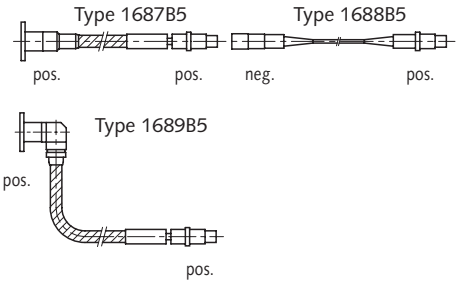

Charge Amplifier
Type 5070Ax01xx

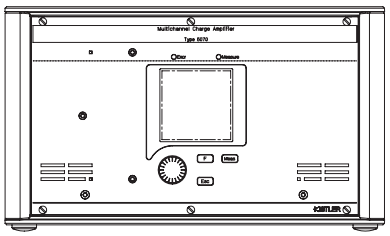

3 output signals
from charge amplifier

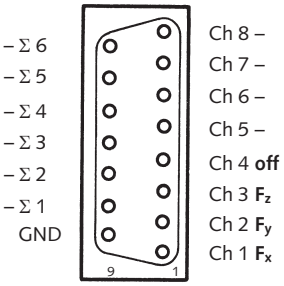

Fig. 2: Example of a measuring system with standard dynamometer

6-Component Force and Moment Measurement F_x, F_y, F_z, M_x, M_y, M_z with 8-Channel Charge Amplifier

Dynamometer
Type 9129AA

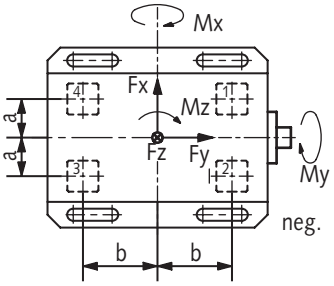

Cable

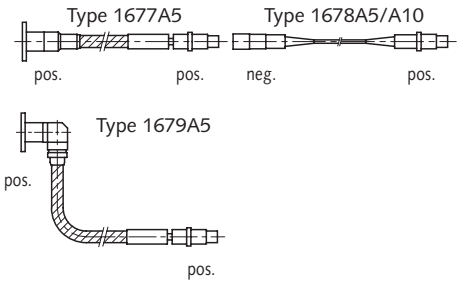

Charge Amplifier
Type 5070Ax11xx

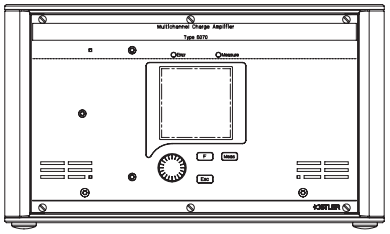

8 output signals
from charge amplifier

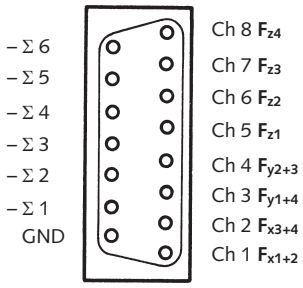

Fig. 3: Example of a measuring system with standard dynamometer

This information corresponds to the current state of knowledge. Kistler reserves the right to make technical changes. Liability for consequential damage resulting from the use of Kistler products is excluded.

©2009 ... 2012, Kistler Group, Eulachstrasse 22, 8408 Winterthur, Switzerland
Tel. +41 52 224 11 11, Fax +41 52 224 14 14, info@kistler.com, www.kistler.com
Kistler is a registered trademark of Kistler Holding AG.

KISTLER
measure. analyze. innovate.

6-Component Force and Moment Measurement F_x, F_y, F_z, M_x, M_y, M_z with 8-Channel Charge Amplifier with 6-Component-Summing Calculator

Dynamometer
Type 9129AA

Cable

Charge Amplifier
Type 5070Ax21xx

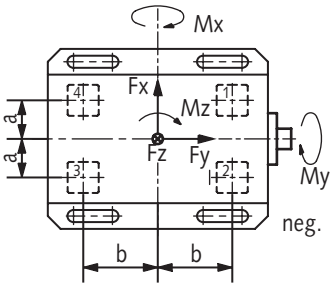

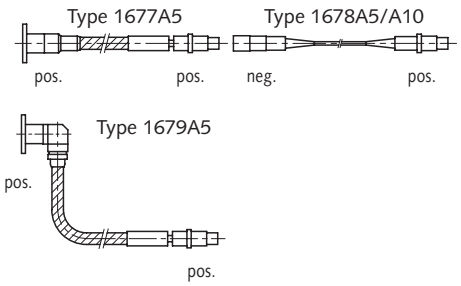

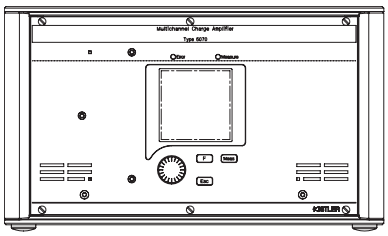

8 output signals from charge amplifier
6 output signals from summing calculator

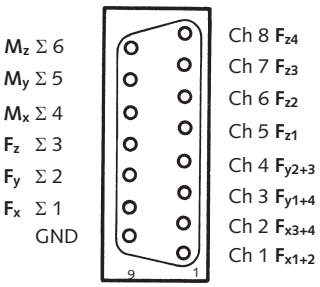

Fig. 4: Example of a measuring system with standard dynamometer

Values a,b for Type 9129AA:

a mm	b mm
33	50,5

Mounting

The dynamometer can be screwed onto any clean, surface-ground mounting surface, such as on a machine tool table. Mounting on a magnet plate is also possible. Please note that uneven mounting surfaces may cause internal distortion, placing additional heavy load on the individual measuring elements and possibly increased crosstalk.

M6 tapped blind bores are available on the cover plate for mounting the force-introducing components such as workpieces or tool holders. The mounting surfaces of the force-introducing components must be face-ground so that good mechanical connection to the cover plate is achieved.

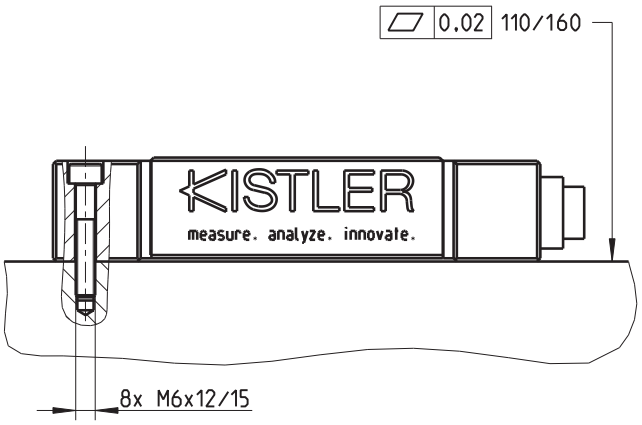

Fig. 5: Mounting the dynamometer

This information corresponds to the current state of knowledge. Kistler reserves the right to make technical changes. Liability for consequential damage resulting from the use of Kistler products is excluded.

©2009 ... 2012, Kistler Group, Eulachstrasse 22, 8408 Winterthur, Switzerland
Tel. +41 52 224 11 11, Fax +41 52 224 14 14, info@kistler.com, www.kistler.com
Kistler is a registered trademark of Kistler Holding AG.

KISTLER
measure. analyze. innovate.

Signal Conditioning

A charge amplifier is also needed to build a complete measuring system. The measurement signal is converted into an electrical voltage in the individual channels. The measured value is exactly proportional to the force acting.

The multichannel charge amplifier Type 5070A... has been specially developed for multicomponent force measurement systems.



Fig. 6: Multichannel charge amplifier Type 5070A...

Data Acquisition and Evaluation

Kistler offers with the DAQ system a universal and easy to operate package, consisting of a hardware for the data acquisition and the DynoWare software. For details see data sheet 5697A_000-745.

Included Accessories	**Art. No.**
• Socket head cap screw M6x35 (8 items)	6.120.110

Optional Accessories

For 3-Component Force Measurements F_x, F_y, F_z	**Type**
• Connecting cable, length l = 5 m (3 leads)	1687B5
	1689B5
• Extension cable, length l = 5 m (3 leads)	1688B5

For 6-Component Force and Moment Measurements F_x, F_y, F_z / M_x, M_y, M_z	**Type**
• Connecting cable, length l = 5 m (8 leads)	1677A5
	1679A5
• Extension cable, length l = 5 m (8 leads)	1678A5

Ordering Code	
• Multicomponent dynamometer –10 ... 10 kN, cover plate 95x105 mm	**Type 9129AA**

9129AA_000-709e-10.12

This information corresponds to the current state of knowledge. Kistler reserves the right to make technical changes. Liability for consequential damage resulting from the use of Kistler products is excluded.

©2009 ... 2012, Kistler Group, Eulachstrasse 22, 8408 Winterthur, Switzerland
Tel. +41 52 224 11 11, Fax +41 52 224 14 14, info@kistler.com, www.kistler.com
Kistler is a registered trademark of Kistler Holding AG.

Appendix 2 - Thermal imaging camera specifications



Model	TIM 160S
Optical resolution	160 x 120 pixels
Temperature ranges	-20 ... 100 °C, 0 ... 250 °C, (20) 150 ... 900 °C [1] additional temperature range: 200 ... 1500 °C (optional)
Spectral range	8 to 14 µm
Frame rate	120 Hz
System accuracy	±2 °C or ±2 %, whichever is greater
Lenses	12° x 9° FOV / f = 13 mm or 30° x 23° FOV / f = 5 mm or 55° x 40° FOV / f = 3 mm or 80° x 54° FOV / f = 2 mm
Thermal sensitivity (NETD) [2]	80 mK with 30° FOV 100 mK with 55° and 80° FOV 300 mK with 12° FOV
Detector	FPA, uncooled (17 µm x 17 µm)
Outputs/digital	USB 2.0 / optional interface USB to GigE (PoE)
Standard process interface (PIF)	0 - 10 V input, digital input (max. 24 V), 0 - 10 V output
Industry process interface (PIF)	2x 0 - 10 V inputs, digital input (max. 24 V), 3x 0/4 - 20 mA outputs, 3x relays (0 - 30 V/ 400 mA), fail-safe relay
Cable length	1 m (standard), 5 m, 10 m, 20 m 5 m and 10 m also available as high temperature USB cable (180 °C or 250 °C)
Power supply	USB powered
Tripod mount	¼-20 UNC
Protection class	IP67
Ambient temperature	0 ... 50 °C
Storage temperature	-40 ... 70 °C
Relative humidity	20 to 80 %, non-condensing
Vibration	IEC 60068-2-6 (sinus-shaped) / IEC 60068-2-64 (broadband noise)
Shock	IEC 60068-2-27 (25 g and 50 g)
Housing (size)	45 mm x 45 mm x 62 - 77 mm (depending on lens and focus position)
Weight	195 g, incl. lens

[1] For the range (20)150 up to 900 °C, the accuracy specification applies from 150 °C
[2] Values apply with 40 Hz and 25 °C room temperature

Scope of supply

TIM 160S

- TIM process camera
  incl. a selectable lens
- Operating instructions
- USB cable 1 m
- Software for real-time processing
  and analyzing thermal images
- Tripod mount
- PIF cable 1 m
- Transport case
- Test certificate

Appendix 3 - Normal distribution data for responses from chapter 6

Torque

The model assumption that the data is from a normally distributed dataset is shown in Figure 11.1, with normally distributed histogram and normal probability plot close to the regression line.

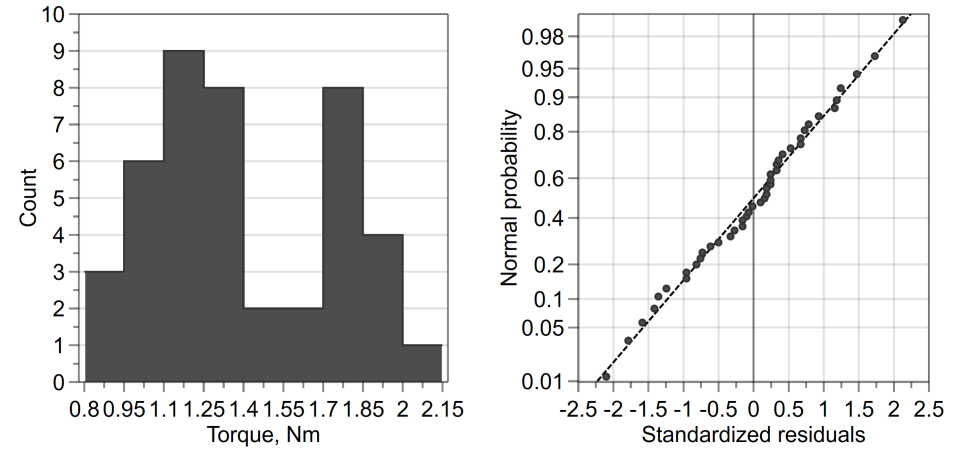

Figure 11.1: Normal distribution of data used in the torque model shown through a. frequency of data histogram b. normal probability plot.

Chip Form

Figure 11.2 shows the distribution of the data used in the chip form model.

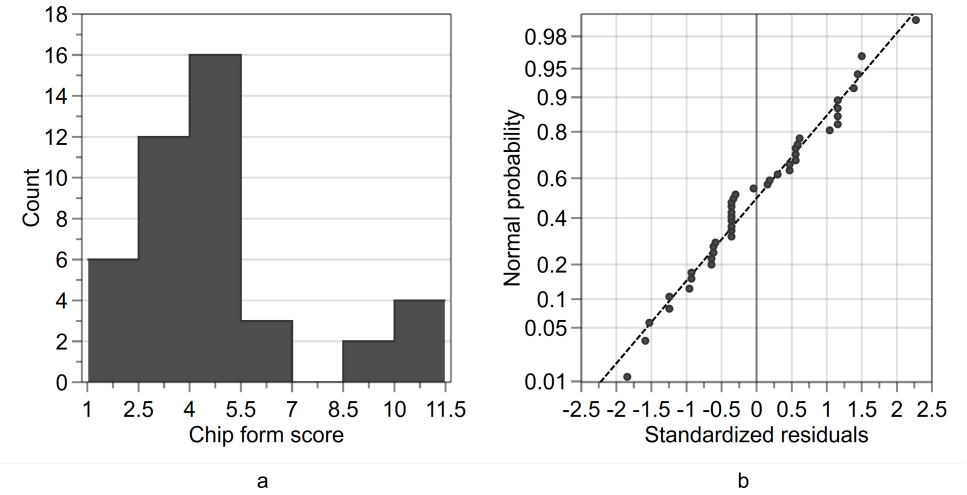

Figure 11.2: Normal distribution of data used in the chip form model shown through a. frequency of data histogram b. normal probability plot.

Cylinder (max inscribed)

The model assumption of normally distributed data is validated, Figure 11.3.

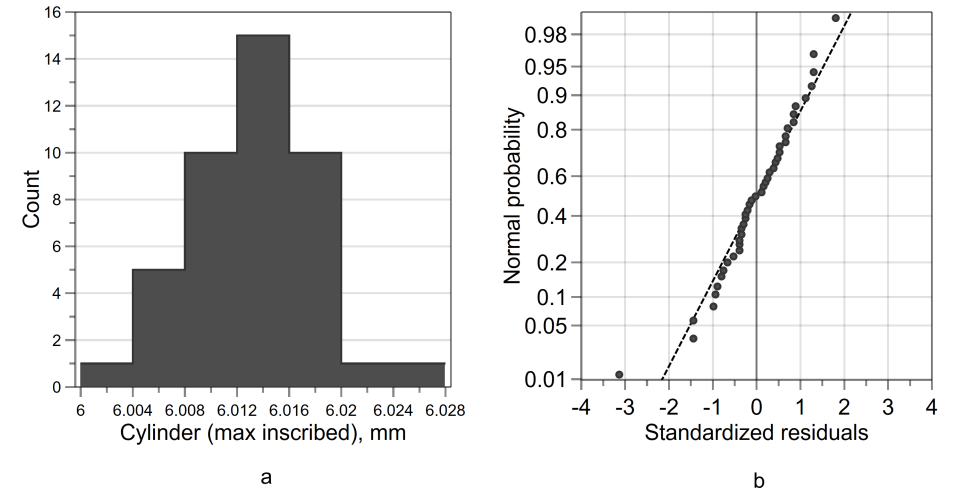

Figure 11.3: Normal distribution of data used in the chip form model shown through a. frequency of data histogram b. normal probability plot.

Diameter (least squares)

and the data comes from a normally distributed sample (Figure 11.4

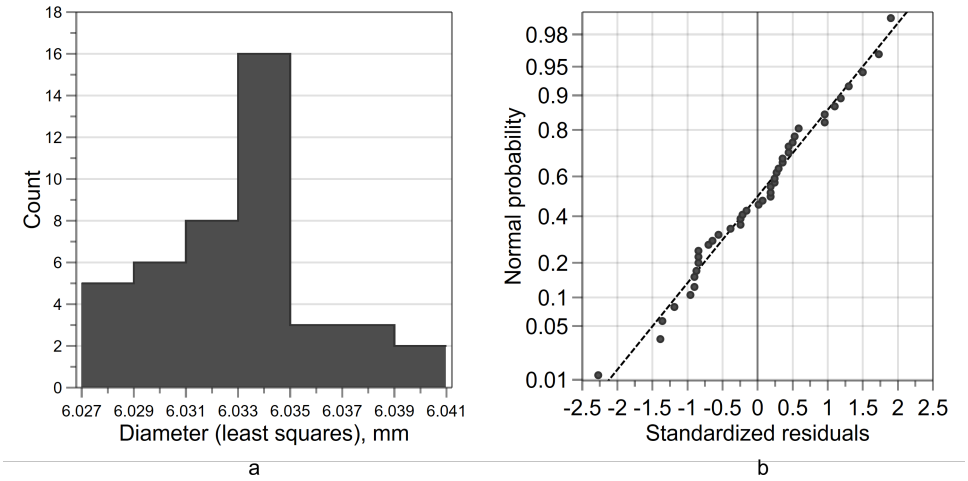

Figure 11.4: Normal distribution of data used in the chip form model shown through a. frequency of data histogram b. normal probability plot.

Circularity

The data within the initial model, as viewed in Figure 11.5, shows that the data is positively skewed, with a greater frequency of data occurring at the lower circularity range.

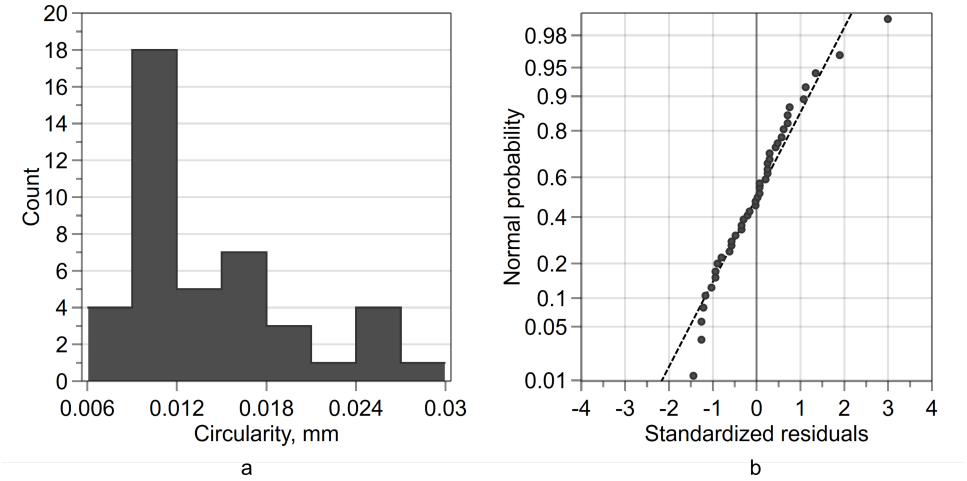

Figure 11.5: Normal distribution of data used in the chip form model shown through a. frequency of data histogram b. normal probability plot.

Burr height

The data used in this model and analysis was captured from a normally distributed set, Figure.

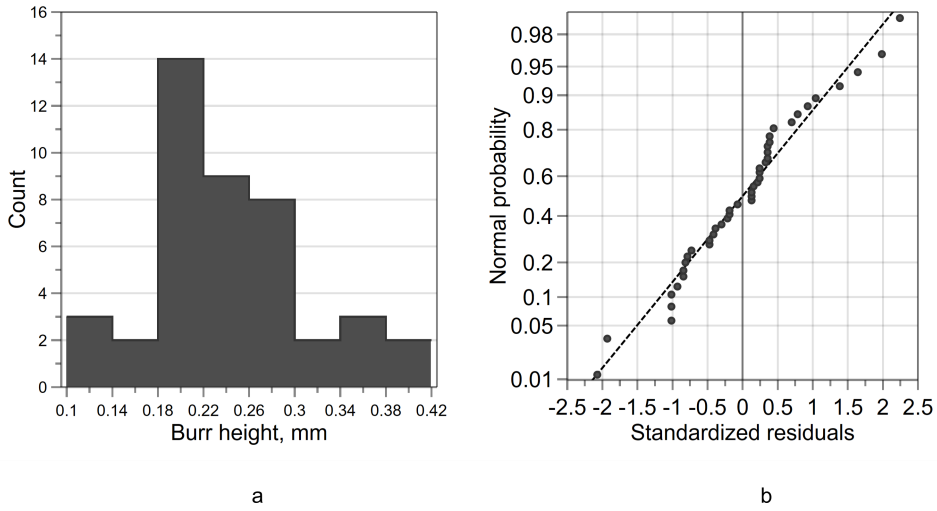

Figure 11.6: Normal distribution of data used in the chip form model shown through a. frequency of data histogram b. normal probability plot.

Surface roughness, Ra

The model is created from normally distributed data, Figure 11.7.

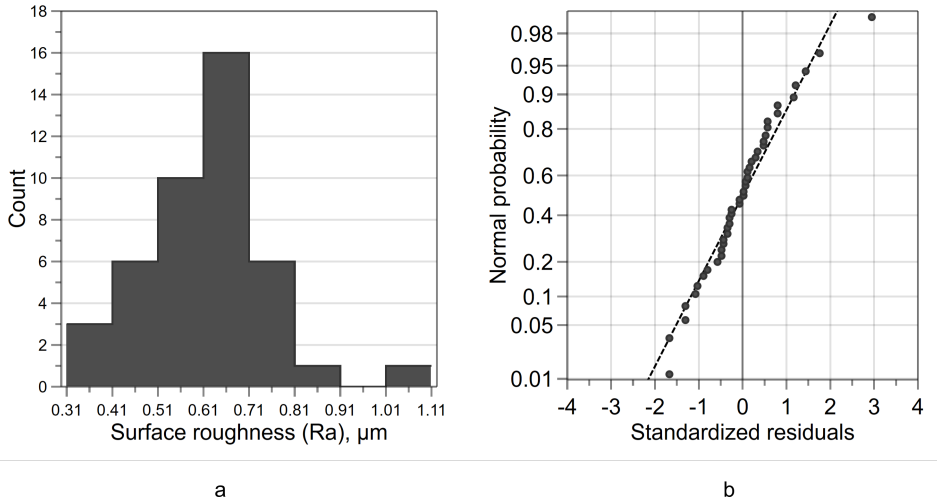

Figure 11.7: Normal distribution of data used in the chip form model shown through a. frequency of data histogram b. normal probability plot.

Appendix 4 - Tool life SEM images

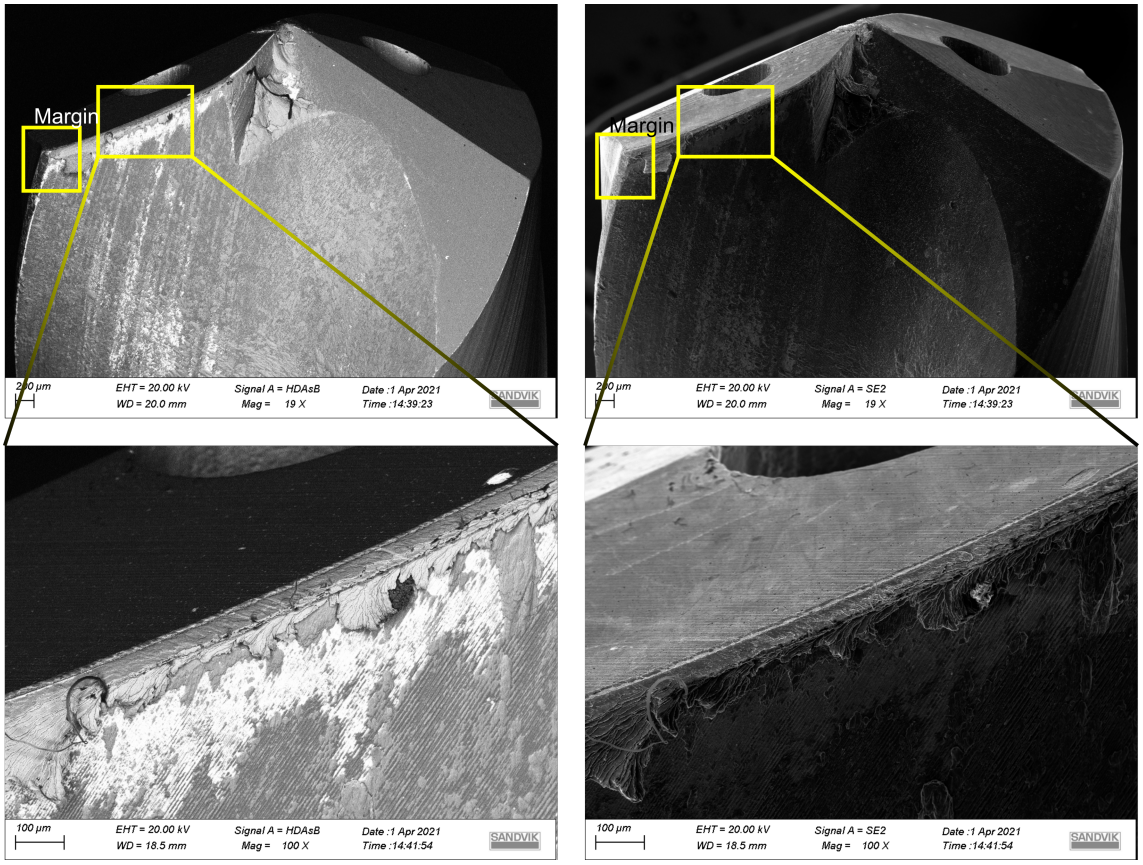

Figure 11.8: Prototype 4.2, SEM image of the tool wear present on the LCO_2 drilled solid carbide drill after 129 holes.

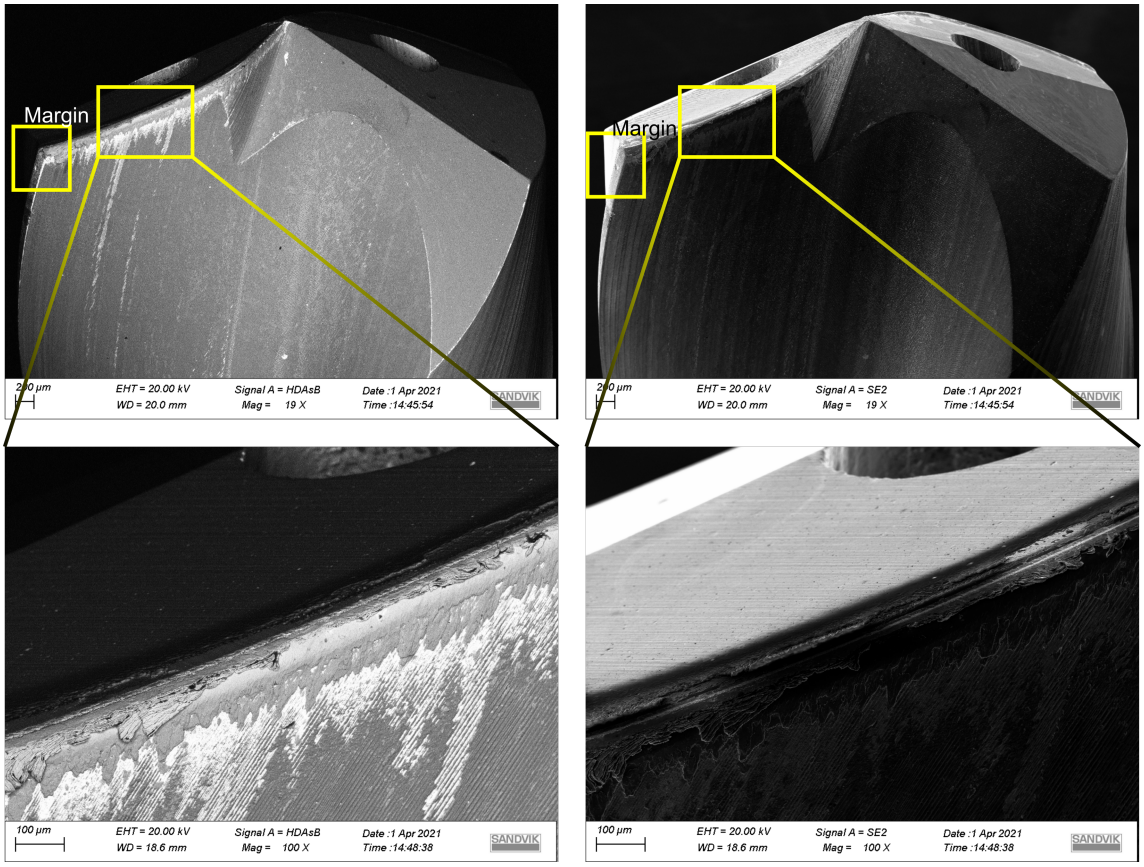

Figure 11.9: Prototype 4.3, SEM image of the tool wear present on the wet drilled solid carbide drill after 300 holes.

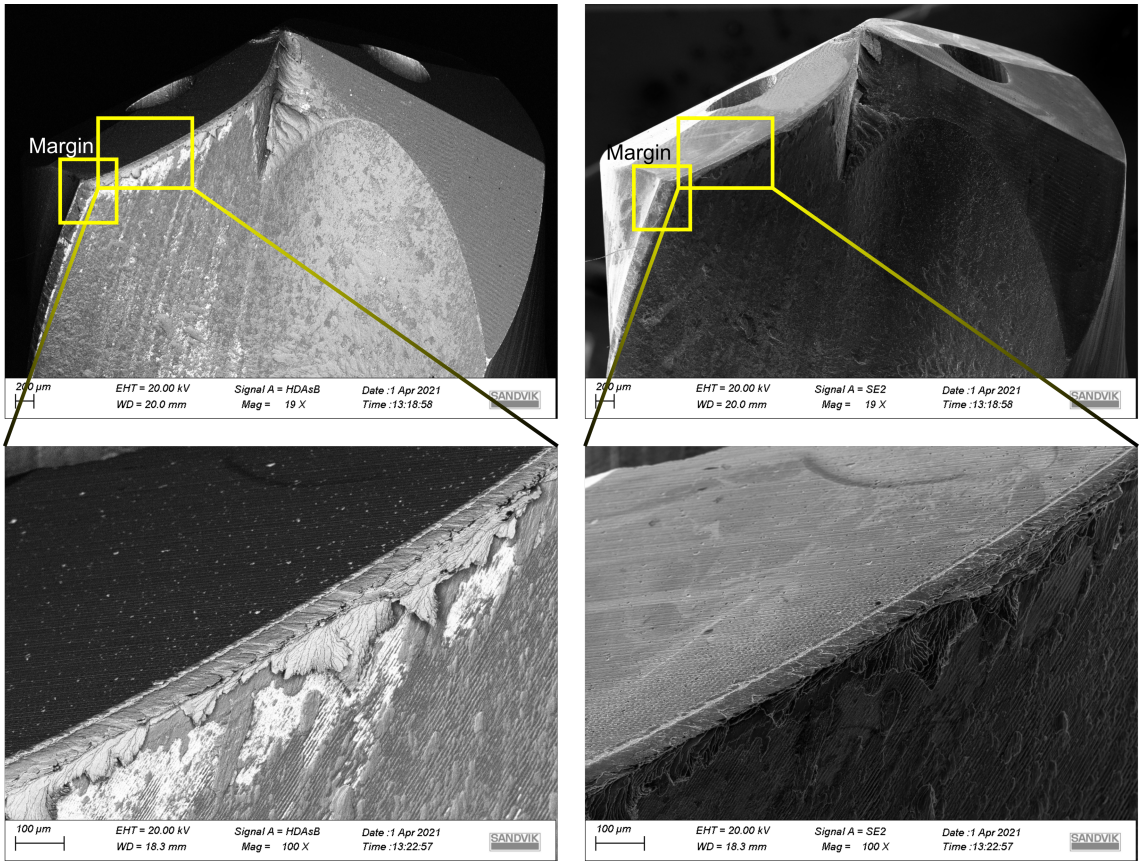

Figure 11.10: Prototype 5.2, SEM image of the tool wear present on the LCO_2 drilled solid carbide drill after 109 holes.

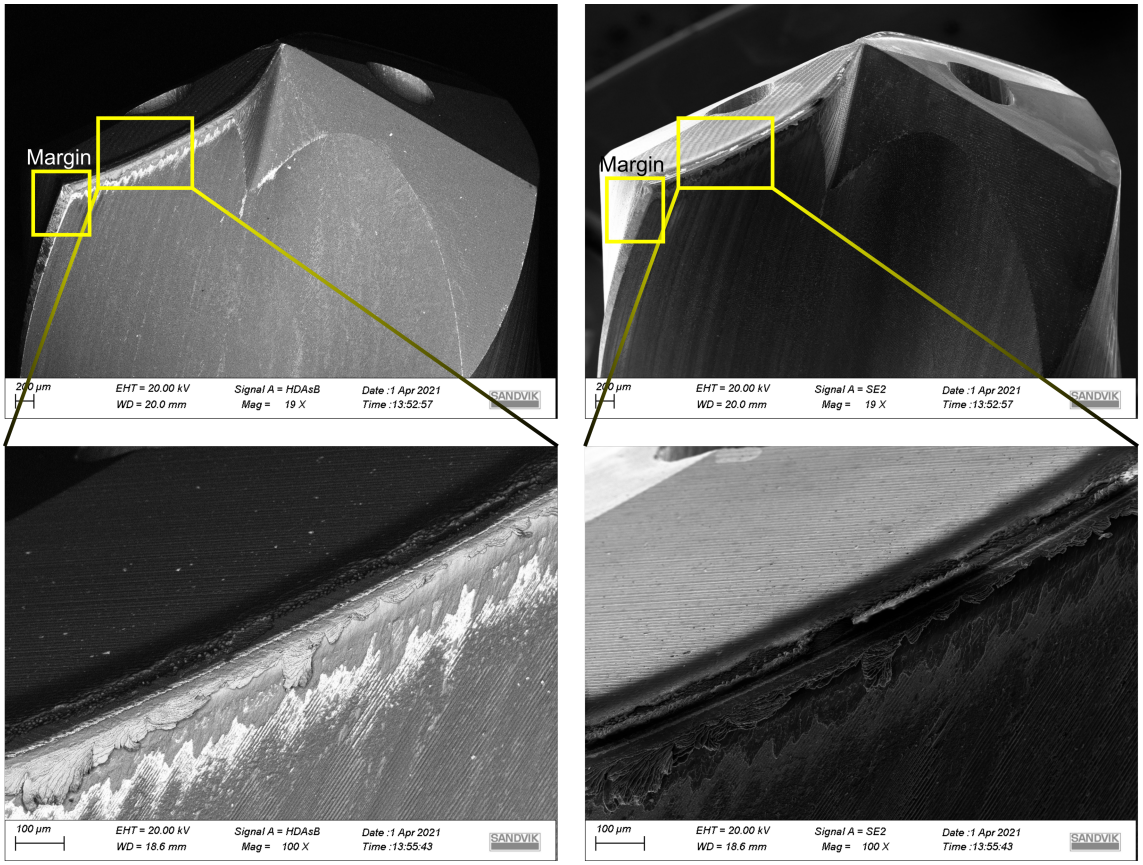

Figure 11.11: Prototype 5.4, SEM image of the tool wear present on the wet drilled solid carbide drill after 300 holes.

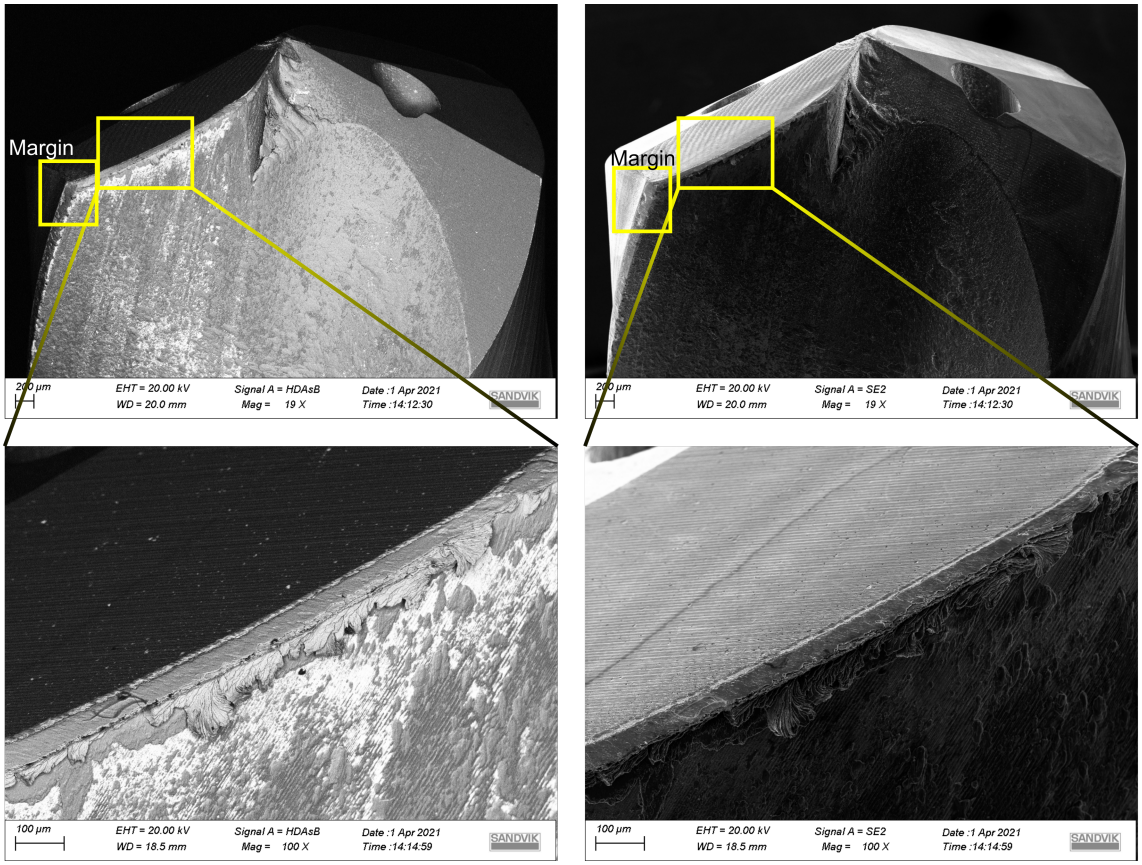

Figure 11.12: Prototype 6.1 SEM image of the tool wear present on the LCO_2 drilled solid carbide drill, after 280 holes.

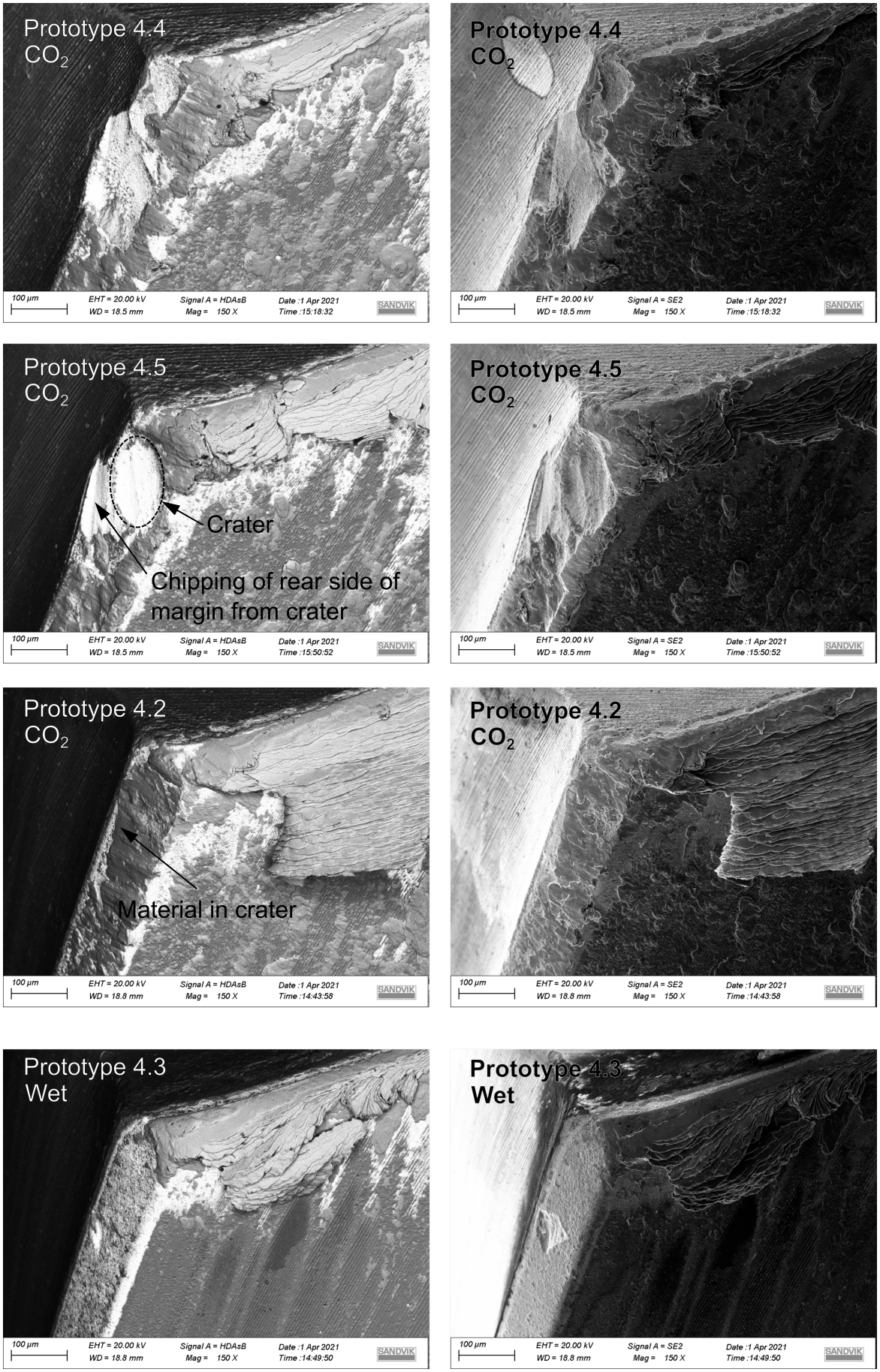

Figure 11.13: Prototype 4 comparison with wet, SEM image of the tool wear present on the LCO_2drilled solid carbide drill.

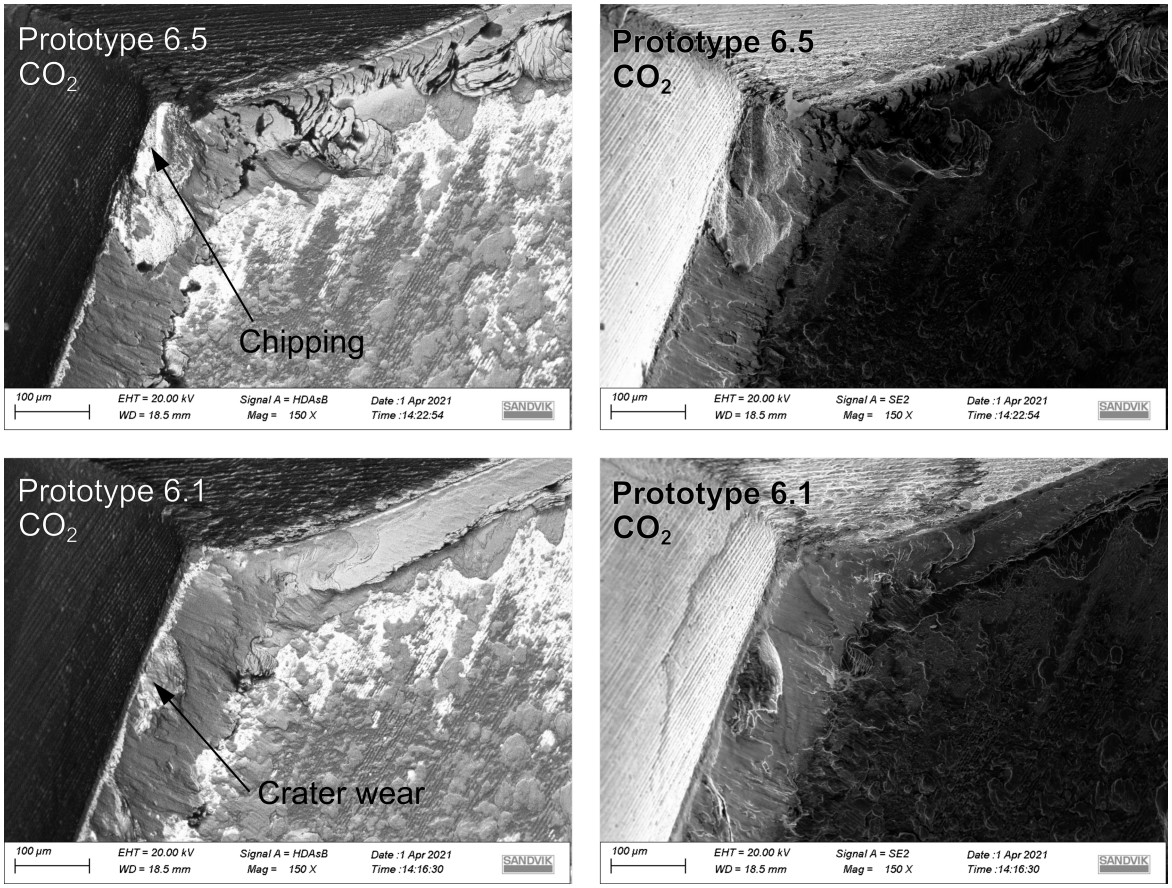

Figure 11.14: Prototype 6 SEM image of the tool wear present on the LCO_2drilled solid carbide drill.

Bibliography

[1] R. Peeters, L. Simone, K. Nelissen, M. Fabbri-Destro, W. Vanduffel, G. Rizzolatti, and G. A. Orban, "The representation of tool use in humans and monkeys: common and uniquely human features," *Journal of Neuroscience*, vol. 29, no. 37, pp. 11 523–11 539, 2009.

[2] "Transforming our world: the 2030 agenda for sustainable development," https://sustainabledevelopment.un.org/post2015/transformingourworld, accessed: 02-12-2020.

[3] I. Jawahir, H. Attia, D. Biermann, J. Duflou, F. Klocke, D. Meyer, S. Newman, F. Pusavec, M. Putz, J. Rech, V. Schulze, and D. Umbrello, "Cryogenic manufacturing processes," *CIRP Annals - Manufacturing Technology*, vol. 65, no. 2, pp. 713–736, 2016. [Online]. Available: http://dx.doi.org/10.1016/j.cirp.2016.06.007

[4] L. Proud, N. Tapoglou, and T. Slatter, "A review of co2 coolants for sustainable machining," *Metals*, vol. 12, no. 2, 2022. [Online]. Available: https://www.mdpi.com/2075-4701/12/2/283

[5] M. Graff, "Disposal of metalworking fluids," in *Metalworking Fluids (MWFs) for Cutting and Grinding*. Woodhead Publishing, 2012, pp. 389–402. [Online]. Available: http://www.sciencedirect.com/science/article/pii/B9780857090614500025

[6] L. Biasetto, R. Bertolini, H. Elsayed, A. Ghiotti, and S. Bruschi, "Use of cryogenic machining to improve the adhesion of sphene bioceramic coatings on titanium substrates for dental and orthopaedic applications," *Ceramics International*, vol. 45, no. 5, pp. 5941–5951, 2019.

[7] Astakov, *Drills: Science and Technology of Advanced Operations*. CRC Press, 2014.

[8] M. Merchant, "Mechanics of the metal cutting process. i. orthogonal cutting and a type 2 chip," *Journal of Applied Physics*, vol. 16, pp. 267 – 275, 06 1945.

[9] T. Hoshi and H. Zhao, "Study of a High Performance Drill Geometry," *CIRP Annals - Manufacturing Technology*, vol. 38, no. 1, pp. 87–90, 1989.

[10] H. Tönshoff, W. Spintig, W. König, and A. Neises, "Machining of holes developments in drilling technology," *CIRP annals*, vol. 43, no. 2, pp. 551–561, 1994.

[11] S. Sharif and E. Rahim, "Performance of coated- and uncoated-carbide tools when drilling titanium alloy Ti6Al4V," *Journal of Materials Processing Technology*, vol. 185, no. 1, pp. 72–76, 2007.

[12] Z. Zhao and S. Y. Hong, "Cryogenic properties of some cutting tool materials," *Journal of Materials Engineering and Performance*, vol. 1, no. 5, pp. 705–714, 1992. [Online]. Available: http://dx.doi.org/10.1007/BF02649252

[13] M. P. Bryan, "Fundamentals of stiff paste extrusion," Ph.D. dissertation, University of Cambridge, 2016.

[14] J. Garcia, V. C. Cipres, A. Blomqvist, and B. Kaplan, "Cemented carbide microstructures: a review," *International Journal of Refractory Metals and Hard Materials*, vol. 80, pp. 40–68, 2019.

[15] O. Erik, "Machinery's Handbook 28th Larger Print Edition," 2008.

[16] M. I. D. Santana and M. L. Polli, "The Influence of Twist Drill Main Cutting Edge Preparation in Drilling Process," *Materials Research*, vol. 18, no. supl.2, pp. 148–153, 2015. [Online]. Available: http://apps.webofknowledge.com/full{_}record.do?product=WOS{&}search{_}mode=GeneralSearch{&}qid=9{&}SID=1Dynn42AcOe89vOg1KG{&}page=1{&}doc=1{%}5Cnhttp://www.scielo.br/scielo.php?script=sci{_}arttext{&}pid=S1516-14392015000800148{&}lng=en{&}nrm=iso{&}tlng=en

[17] A. Paul, S. G. Kapoor, and R. E. DeVor, "Chisel edge and cutting lip shape optimization for improved twist drill point design," *International Journal of Machine Tools and Manufacture*, vol. 45, no. 4-5, pp. 421–431, 2005.

[18] A. Salama and A. ElSawy, "The dynamic geometry of a twist drill point," *Journal of Materials Processing Technology*, vol. 56, no. 1-4, pp. 45–53, 1996. [Online]. Available: http://www.sciencedirect.com/science/article/pii/0924013695018190

[19] V. P. Astakhov, *Geometry of Single-point Turning Tools and Drills: Fundamentals and Practical Applications*, 2010, vol. 53, no. 9.

[20] Y. C. Yen, A. Jain, and T. Altan, "A finite element analysis of orthogonal machining using different tool edge geometries," *Journal of Materials Processing Technology*, vol. 146, no. 1, pp. 72–81, 2004.

[21] R. M'Saoubi, D. Axinte, S. L. Soo, C. Nobel, H. Attia, G. Kappmeyer, S. Engin, and W.-M. Sim, "High performance cutting of advanced aerospace alloys and composite materials," *CIRP Annals - Manufacturing Technology*, vol. 64, no. 2, pp. 557–580, 2015.

[22] B. Denkena, A. Lucas, and E. Bassett, "Effects of the cutting edge microgeometry on tool wear and its thermo-mechanical load," *CIRP Annals - Manufacturing Technology*, vol. 60, no. 1, pp. 73–76, 2011.

[23] C. Rodríguez, *Cutting edge preparation of precision cutting tools by applying micro-abrasive jet machining and brushing*, 2009. [Online]. Available: http://books.google.com/books?hl=en&lr=&id=NfRFEgFRmD4C&oi=fnd&pg=PA1&dq=Cutting+edge+preparation+of+precision+cutting+tools+by+applying+micro-abrasive+jet+machining+and+brushing&ots=Gg-zYmpGzY&sig=q4ztuTawKtjrVKvtbx4ZHTPCho4%5Cnhttp://books.google.com/bo

[24] C. F. Wyen and K. Wegener, "Influence of cutting edge radius on cutting forces in machining titanium," *CIRP Annals - Manufacturing Technology*, vol. 59, no. 1, pp. 93–96, 2010. [Online]. Available: http://dx.doi.org/10.1016/j.cirp.2010.03.056

[25] B. Denkena and D. Biermann, "Cutting edge geometries," *CIRP Annals - Manufacturing Technology*, vol. 63, no. 2, pp. 631–653, 2014. [Online]. Available: http://dx.doi.org/10.1016/j.cirp.2014.05.009

[26] R. Komanduri, "Some clarifications on the mechanics of chip formation when machining titanium alloys," *Wear*, vol. 76, no. 1, pp. 15–34, 1982.

[27] V. P. Astakov, *Tribology of Metal Cutting*, B. Briscoe, Ed. Elsevier, 2006.

[28] F. Ke, J. Ni, and D. A. Stephenson, "Continuous chip formation in drilling," *International Journal of Machine Tools and Manufacture*, vol. 45, no. 15, pp. 1652–1658, 2005.

[29] W. Zhao, W. Su, L. Li, D. Fang, and N. Chen, "Evolution of mechanical properties of ti-6al-4v alloy in the temperature range of 20 to- 196Â° c," *Metals and Materials International*, pp. 1–11, 2020.

[30] M. Bermingham, S. Palanisamy, D. Kent, and M. Dargusch, "A comparison of cryogenic and high pressure emulsion cooling technologies on tool life and chip morphology in ti-6al-4v cutting," *Journal of Materials Processing Technology*, vol. 212, no. 4, pp. 752–765, 2012.

[31] Y. lin KE, H. yue DONG, G. LIU, and M. ZHANG, "Use of nitrogen gas in high-speed milling of Ti-6Al-4V," *Transactions of Nonferrous Metals Society of China (English Edition)*, vol. 19, no. 3, pp. 530–534, 2009. [Online]. Available: http://dx.doi.org/10.1016/S1003-6326(08)60307-6

[32] S. Kalpakjian and S. R. Schmid, *Manufacturing Engineering and Technology*. Prentice Hall, 2009.

[33] B. Mills, *Machinability of engineering materials*. Springer Science & Business Media, 2012.

[34] J. F. Archard and W. Hirst, "The wear of metals under unlubricated conditions," *Proceedings of the Royal Society of London. Series A. Mathematical and Physical Sciences*, vol. 236, no. 1206, pp. 397–410, 1956.

[35] T. Childs, K. Maekawa, T. Obikawa, and Y. Yamane, *Metal Machining Theory and Applications*. Arnold, London (2000), 2000.

[36] T. Nguyen, P. Kwon, D. Kang, and T. R. Bieler, "The origin of flank wear in turning ti-6al-4v," *Journal of Manufacturing Science and Engineering*, vol. 138, no. 12, 2016.

[37] J. Garcia, M. F. Moreno, J. Östby, J. Persson, and H. C. Pinto, "Design of coated cemented carbides with improved comb crack resistance," *Proc. 19th Plansee Semin., Reutte, Austria*, 2017.

[38] O. Hatt, "On the mechanism of tool crater wear in titanium alloy machining," Ph.D. dissertation, University of Sheffield, 2016.

[39] S. Zhang, J. F. Li, J. Deng, and Y. Li, "Investigation on diffusion wear during high-speed machining ti-6al-4v alloy with straight tungsten carbide tools," *The International Journal of Advanced Manufacturing Technology*, vol. 44, no. 1, pp. 17–25, 2009.

[40] J. Nomani, "Built-up edge mechanisms in the machining of duplex stainless steels," Ph.D. dissertation, Deakin University, 2014.

[41] S. Coromant, "Wear guide," 2018.

[42] R. Boyer, "An overview on the use of titanium in the aerospace industry," *Materials Science and Engineering: A*, vol. 213, no. 1, pp. 103 – 114, 1996. [Online]. Available: http://www.sciencedirect.com/science/article/pii/0921509396102331

[43] D. M. J, *Titanium: a technical guide*, 2nd ed. ASM International, 2000.

[44] R. Pederson, O. Babushkin, F. Skystedt, and R. Warren, "Use of high temperature x-ray diffractometry to study phase transitions and thermal expansion properties in ti-6al-4v," *Materials science and technology*, vol. 19, no. 11, pp. 1533–1538, 2003.

[45] P. J. Arrazola, A. Garay, L. M. Iriarte, M. Armendia, S. Marya, and F. Le Maître, "Machinability of titanium alloys (Ti6Al4V and Ti555.3)," *Journal of Materials Processing Technology*, vol. 209, no. 5, pp. 2223–2230, 2009.

[46] E. Ezugwu and Z. Wang, "Titanium alloys and their machinability - a review," *Journal of Materials Processing Technology*, vol. 68, no. 3, pp. 262–274, 1997.

[47] E. O. Ezugwu, J. Bonney, and Y. Yamane, "An overview of the machinability of aeroengine alloys," *Journal of Materials Processing Technology*, vol. 134, no. 2, pp. 233–253, 2003.

[48] E. O. Ezugwu, "Key improvements in the machining of difficult-to-cut aerospace superalloys," *International Journal of Machine Tools and Manufacture*, vol. 45, no. 12-13, pp. 1353–1367, 2005.

[49] A. R. Machado and J. Wallbank, "Machining of titanium and its alloys- a review," *Proceedings'of the Institution of Mechanical Engineers Part B: Journal of Engineernig Manufacture*, vol. 204, no. 1, pp. 53–60, 1990.

[50] S. Sharif, E. A. Rahim, and H. Sasahara, *Titanium Alloys- Towards Achieving Enhanced Properties for Diversified Applications*. InTech, 2012, ch. Machinability of Titanium Alloys in Drilling. [Online]. Available: http://www.intechopen.com/books/titanium-alloys-towards-achieving-enhanced-properties-for-diversified-applications/drilling-of-titanium-alloys

[51] N. A. Abukhshim, P. T. Mativenga, and M. A. Sheikh, "Heat generation and temperature prediction in metal cutting: A review and implications for high speed machining," *International Journal of Machine Tools and Manufacture*, vol. 46, no. 7-8, pp. 782–800, 2006.

[52] E. O. Ezugwu and C. J. Lai, "Failure modes and wear mechanisms of M35 high-speed steel drills when machining inconel 901," *Journal of Materials Processing Tech.*, vol. 49, no. 3-4, pp. 295–312, 1995.

[53] A. Saini, B. Pabla, and S. Dhami, "Developments in cutting tool technology in improving machinability of Ti6Al4V alloy: A review," *Proceedings of the Institution of Mechanical Engineers, Part B: Journal of Engineering Manufacture*, vol. 230, no. 11, pp. 1977–1989, 2016. [Online]. Available: http://pib.sagepub.com/lookup/doi/10.1177/0954405416640176

[54] S. K. Choudhury and G. Raju, "Investigation into crater wear in drilling," *International Journal of Machine Tools and Manufacture*, vol. 40, no. 6, pp. 887–898, 2000.

[55] J. Hua and R. Shivpuri, "A Cobalt Diffusion Based Model for Predicting Crater Wear of Carbide Tools in Machining Titanium Alloys," *Journal of Engineering Materials and Technology*, vol. 127, no. 1, p. 136, 2005. [Online]. Available: http://materialstechnology.asmedigitalcollection.asme.org/article.aspx?articleid=1427376

[56] S. Zhang, J. F. Li, J. X. Deng, and Y. S. Li, "Investigation on diffusion wear during high-speed machining Ti-6Al-4V alloy with straight tungsten carbide tools," *International Journal of Advanced Manufacturing Technology*, vol. 44, no. 1-2, pp. 17–25, 2009.

[57] R. Komanduri and W. R. Reed, "Evaluation of carbide grades and a new cutting geometry for machining titanium alloys," *Wear*, vol. 92, no. 1, pp. 113–123, 1983.

[58] G. E. Box, W. G. Hunter, J. S. Hunter *et al.*, *Statistics for Experimenters*. John Wiley and sons New York, 1978, vol. 664.

[59] P. F. de Aguiar, B. Bourguignon, M. Khots, D. Massart, and R. Phan-Than-Luu, "D-optimal designs," *Chemometrics and intelligent laboratory systems*, vol. 30, no. 2, pp. 199–210, 1995.

[60] P. Harper, J. Wilday, and M. Bilio, "Assessment of the major hazard potential of carbon dioxide (co2)," *Health and Safety Executive*, pp. 1–28, 2011.

[61] S. Wang and A. F. Clarens, "Analytical model of metalworking fluid penetration into the flank contact zone in orthogonal cutting," *Journal of Manufacturing Processes*, vol. 15, no. 1, pp. 136–140, 2013. [Online]. Available: http://dx.doi.org/10.1016/j.jmapro.2012.09.015

[62] S. Sun, M. Brandt, and M. Dargusch, "Thermally enhanced machining of hard-to-machine materials - a review," *International Journal of Machine Tools and Manufacture*, vol. 50, no. 8, pp. 663 – 680, 2010. [Online]. Available: http://www.sciencedirect.com/science/article/pii/S0890695510000738

[63] R. Span and W. Wagner, "A new equation of state for carbon dioxide covering the fluid region from the triple-point temperature to 1100 k at pressures up to 800 mpa," *Journal of physical and chemical reference data*, vol. 25, no. 6, pp. 1509–1596, 1996.

[64] Y. Kawamura, N. Matsumoto, and T. Nakano, "Realization of the triple point of carbon dioxide evaluated by the its–90," *Metrologia*, vol. 57, no. 1, p. 015004, 2020.

[65] I. H. Bell, J. Wronski, S. Quoilin, and V. Lemort, "Pure and pseudo-pure fluid thermophysical property evaluation and the open-source thermophysical property library coolprop," *Industrial*

& Engineering Chemistry Research, vol. 53, no. 6, pp. 2498–2508, 2014. [Online]. Available: http://pubs.acs.org/doi/abs/10.1021/ie4033999

[66] C. N. WebBook, "NIST Standard Reference Database Number 69, Thermo- physical Properties of Fluid Systems."

[67] E. Brinksmeier, D. Meyer, A. Huesmann-Cordes, and C. Herrmann, "Metalworking fluids - Mechanisms and performance," *CIRP Annals - Manufacturing Technology*, vol. 64, no. 2, pp. 605–628, 2015.

[68] "Astm d2881-19 standard classification for metalworking fluids and related materials," ASTM International, West Conshohocken, PA, Tech. Rep., 2019.

[69] R. Evans, "Selection and testing of metalworking fluids," in *Metalworking Fluids (MWFs) for Cutting and Grinding*. Elsevier, 2012, pp. 23–78.

[70] T. Childs, K. Maekawa, and P. Maulik, "Effects of coolant on temperature distribution in metal machining," *Materials Science and Technology*, vol. 4, no. 11, pp. 1006–1019, 1988.

[71] D. Haan, S. Batzer, W. Olson, and J. Sutherland, "An experimental study of cutting fluid effects in drilling," *Journal of materials processing technology*, vol. 71, no. 2, pp. 305–313, 1997.

[72] F. Klocke, L. Settineri, D. Lung, P. C. Priarone, and M. Arft, "High performance cutting of gamma titanium aluminides: Influence of lubricoolant strategy on tool wear and surface integrity," *Wear*, vol. 302, no. 1-2, pp. 1136–1144, 2013.

[73] A. Nandy, M. Gowrishankar, and S. Paul, "Some studies on high-pressure cooling in turning of ti-6al-4v," *International Journal of Machine Tools and Manufacture*, vol. 49, no. 2, pp. 182–198, 2009.

[74] E. Brinksmeier, D. Lucca, and A. Walter, "Chemical aspects of machining processes," *CIRP Annals*, vol. 53, no. 2, pp. 685–699, 2004.

[75] C. Cassin and G. Boothroyd, "Lubricating action of cutting fluids," *Journal of mechanical engineering science*, vol. 7, no. 1, pp. 67–81, 1965.

[76] A. B. Mohd Hadzley, R. Izamshah, A. Siti Sarah, and M. Nurul Fatin, "Finite element model of machining with high pressure coolant for Ti-6Al-4V alloy," *Procedia Engineering*, vol. 53, pp. 624–631, 2013. [Online]. Available: http://dx.doi.org/10.1016/j.proeng.2013.02.080

[77] E. Oezkaya, N. Beer, and D. Biermann, "Experimental studies and CFD simulation of the internal cooling conditions when drilling Inconel 718," *International Journal of Machine Tools and Manufacture*, vol. 108, pp. 52–65, 2016.

[78] A. Johns, R. Hewson, E. Merson, J. Summers, and H. Thompson, "Internal twist drill coolant channel modelling using Computational Fluid Dynamics," *11th World Congress on Computational Mechanics, WCCM 2014, 5th European Conference on Computational Mechanics, ECCM 2014 and 6th European Conference on Computational Fluid Dynamics, ECFD 2014*, 2014.

[79] M. Bücker, E. Oezkaya, U. Hensler, and D. Biermann, "A new flank face design leading to an improved process performance when drilling high-temperature nickel-base alloys," *Available at SSRN 3722782*, 2020.

[80] F. Fallenstein and J. C. Aurich, "CFD based investigation on internal cooling of twist drills," *Procedia CIRP*, vol. 14, pp. 293–298, 2014. [Online]. Available: http://dx.doi.org/10.1016/j.procir.2014.03.112

[81] G. Reitz, "Die Grösse des geistlichen und ritterschaftlichen Grundbesitzes im ehemaligen Kur-Trier," Ph.D. dissertation, 1919.

[82] K. Uehara and S. Kumagai, "Chip formation, surface roughness and cutting force in cryogenic machining," *Ann. CIRP*, vol. 17, no. 1, pp. 409–416, 1968.

[83] D. P. Adler, W. W.-S. Hii, D. J. Michalek, and J. W. Sutherland, "Examining the Role of Cutting Fluids in Machining and Efforts To Address Associated Environmental/Health Concerns," *Machining Science and Technology*, vol. 10, no. 1, pp. 23–58, 2006. [Online]. Available: http://www.tandfonline.com/doi/abs/10.1080/10910340500534282

[84] E. Yasa, S. Pilatin, and O. Çolak, "Overview of Cryogenic Cooling in Machining of Ti Alloys and a case study," *Journal of Production Engineering*, vol. 2, no. July, pp. 1–9, 2012.

[85] S. Cordes, F. Hübner, and T. Schaarschmidt, "Next generation high performance cutting by use of carbon dioxide as cryogenics," *Procedia CIRP*, vol. 14, pp. 401–405, 2014. [Online]. Available: http://dx.doi.org/10.1016/j.procir.2014.03.091

[86] C. MacHai and D. Biermann, "Machining of titanium alloy ti-10v-2fe-3al under cryogenic conditions: Cooling with carbon dioxide snow," *Journal of Materials Processing Technology*, vol. 211, no. 6, pp. 1175–1183, 2011. [Online]. Available: http://dx.doi.org/10.1016/j.jmatprotec.2011.01.022

[87] C. Knowlen, A. Mattick, A. P. Bruckner, and A. Hertzberg, "High efficiency energy conversion systems for liquid nitrogen automobiles," *SAE transactions*, pp. 1837–1842, 1998.

[88] F. Pusavec, P. Krajnik, and J. Kopac, "Transitioning to sustainable production–part i: application on machining technologies," *Journal of Cleaner production*, vol. 18, no. 2, pp. 174–184, 2010.

[89] S. Y. Hong and Z. Zhao, "Thermal aspects, material considerations and cooling strategies in cryogenic machining," *Clean Technologies and Environmental Policy*, vol. 1, no. 2, pp. 107–116, 1999.

[90] A. Stoll, K. Busch, C. Hochmuth, and B. Pause, "Modern Cooling Strategies for Machining of High-Temperature Materials," *Innovations of Sustainable Production for Green Mobility: Energy-Efficient Technologies in Production*, pp. 299–316, 2014.

[91] S. D. Supekar, A. F. Clarens, D. A. Stephenson, and S. J. Skerlos, "Performance of supercritical carbon dioxide sprays as coolants and lubricants in representative metalworking operations,"

Journal of Materials Processing Technology, vol. 212, no. 12, pp. 2652–2658, 2012. [Online]. Available: http://dx.doi.org/10.1016/j.jmatprotec.2012.07.020

[92] Z. Zhao and S. Y. Hong, "Cooling strategies for cryogenic machining from a materials viewpoint," *Journal of Materials Engineering and Performance*, vol. 1, no. 5, pp. 669–678, 1992. [Online]. Available: http://dx.doi.org/10.1007/BF02649248

[93] S. Y. Hong, Y. Ding, and W.-c. Jeong, "Friction and cutting forces in cryogenic machining of Ti-6Al-4V," *International Journal of Machine Tools and Manufacture*, vol. 41, no. 15, pp. 2271–2285, 2001.

[94] A. Shokrani, V. Dhokia, P. Muñoz-Escalona, and S. Newman, "State-of-the-art cryogenic machining and processing," *International Journal of Computer Integrated Manufacturing*, vol. 26, no. November, 2013.

[95] S. Y. Hong, "Lubrication Mechanisms of LN2 in Ecological Cryogenic Machining," *Machining Science and Technology*, vol. 10, no. 1, 2006.

[96] N. S. M. El-Tayeb, T. C. Yap, V. C. Venkatesh, and P. V. Brevern, "Modeling of cryogenic frictional behaviour of titanium alloys using Response Surface Methodology approach," *Materials and Design*, vol. 30, no. 10, pp. 4023–4034, 2009. [Online]. Available: http://dx.doi.org/10.1016/j.matdes.2009.05.020

[97] C. Courbon, L. Sterle, M. Cici, and F. Pusavec, "Tribological effect of lubricated liquid carbon dioxide on ti6al4v and aisi1045 under extreme contact conditions," *Procedia Manufacturing*, vol. 47, pp. 511–516, 2020.

[98] A. F. Clarens, K. F. Hayes, and S. J. Skerlos, "Feasibility of metalworking fluids delivered in supercritical carbon dioxide," *Journal of Manufacturing Processes*, vol. 8, no. 1, pp. 47–53, 2006.

[99] N. R. Dhar, S. Paul, and a. B. Chattopadhyay, "Role of Cryogenic Cooling on Cutting Temperature in Turning Steel," *Journal of Manufacturing Science and Engineering*, vol. 124, no. 1, p. 146, 2002.

[100] S. Sun, M. Brandt, and M. Dargusch, "Machining Ti-6Al-4V alloy with cryogenic compressed air cooling," *International Journal of Machine Tools and Manufacture*, vol. 50, no. 11, pp. 933–942, 2010.

[101] F. Pušavec, D. Grguraš, M. Koch, and P. Krajnik, "Cooling capability of liquid nitrogen and carbon dioxide in cryogenic milling," *CIRP Annals*, vol. 68, no. 1, pp. 73–76, 2019.

[102] M. Dix, R. Wertheim, G. Schmidt, and C. Hochmuth, "Modeling of drilling assisted by cryogenic cooling for higher efficiency," *CIRP Annals - Manufacturing Technology*, vol. 63, no. 1, pp. 73–76, 2014. [Online]. Available: http://dx.doi.org/10.1016/j.cirp.2014.03.080

[103] M. Bermingham, J. Kirsch, S. Sun, S. Palanisamy, and M. Dargusch, "New observations on tool life, cutting forces and chip morphology in cryogenic machining Ti-6Al-4V," *International Journal of Machine Tools and Manufacture*, vol. 51, no. 6, pp. 500–511, 2011.

[104] P. Shah, N. Khanna, A. K. Singla, and A. Bansal, "Tool wear, hole quality, power consumption and chip morphology analysis for drilling ti-6al-4v using ln2 and lco2," *Tribology International*, p. 107190, 2021.

[105] K. Venugopal, S. Paul, and A. Chattopadhyay, "Tool wear in cryogenic turning of ti-6al-4v alloy," *Cryogenics*, vol. 47, no. 1, pp. 12–18, 2007.

[106] ——, "Growth of tool wear in turning of Ti-6Al-4V alloy under cryogenic cooling," *Wear*, vol. 262, no. 9, pp. 1071–1078, 2007.

[107] P. Lequien, G. Poulachon, J. Outeiro, and J. Rech, "Hybrid experimental/modelling methodology for identifying the convective heat transfer coefficient in cryogenic assisted machining," *Applied Thermal Engineering*, vol. 128, pp. 500–507, 2018.

[108] A. Bordin, S. Bruschi, A. Ghiotti, and P. F. Bariani, "Analysis of tool wear in cryogenic machining of additive manufactured Ti6Al4V alloy," *Wear*, vol. 328-329, 2015.

[109] S. Kumar *et al.*, "Multi-response optimization of ti-6al-4v milling using alcrn/tialn coated tool under cryogenic cooling," *Journal of Production Systems and Manufacturing Science*, vol. 1, no. 1, pp. 29–41, 2020.

[110] M. Dhananchezian and M. P. Kumar, "Cryogenic turning of the ti–6al–4v alloy with modified cutting tool inserts," *Cryogenics*, vol. 51, no. 1, pp. 34–40, 2011.

[111] B. D. Jerold and M. P. Kumar, "Experimental comparison of carbon-dioxide and liquid nitrogen cryogenic coolants in turning of aisi 1045 steel," *Cryogenics*, vol. 52, no. 10, pp. 569–574, 2012.

[112] ——, "The Influence of Cryogenic Coolants in Machining of Ti-6Al-4V," *Journal of Manufacturing Science and Engineering*, vol. 135, no. June 2013, 2013.

[113] A. Bagherzadeh and E. Budak, "Investigation of machinability in turning of difficult-to-cut materials using a new cryogenic cooling approach," *Tribology International*, vol. 119, pp. 510–520, 2018.

[114] N. Khanna, C. Agrawal, M. K. Gupta, Q. Song, and A. K. Singla, "Sustainability and machinability improvement of nimonic-90 using indigenously developed green hybrid machining technology," *Journal of Cleaner Production*, p. 121402, 2020.

[115] M. I. Sadik, S. Isakson, A. Malakizadi, and L. Nyborg, "Influence of Coolant Flow Rate on Tool Life and Wear Development in Cryogenic and Wet Milling of Ti-6Al-4V," *Procedia CIRP*, vol. 46, pp. 91–94, 2016.

[116] A. Shokrani, I. Al-Samarrai, and S. T. Newman, "Hybrid cryogenic mql for improving tool life in machining of ti-6al-4v titanium alloy," *Journal of Manufacturing Processes*, vol. 43, pp. 229–243, 2019.

[117] F. Pusavec, T. Lu, C. Courbon, J. Rech, U. Aljancic, J. Kopac, and I. Jawahir, "Analysis of the influence of nitrogen phase and surface heat transfer coefficient on cryogenic machining performance," *Journal of materials processing technology*, vol. 233, pp. 19–28, 2016.

[118] N. Tapoglou, C. Taylor, and C. Makris, "Milling of aerospace alloys using supercritical co2 assisted machining," *Procedia CIRP*, vol. 101, pp. 370–373, 2021.

[119] Q. An, C. Cai, F. Zou, X. Liang, and M. Chen, "Tool wear and machined surface characteristics in side milling ti6al4v under dry and supercritical co2 with mql conditions," *Tribology International*, vol. 151, p. 106511, 2020.

[120] A. Shokrani and S. T. Newman, "A new cutting tool design for cryogenic machining of ti–6al–4v titanium alloy," *Materials*, vol. 12, no. 3, p. 477, 2019.

[121] D. Gross, M. Appis, and N. Hanenkamp, "Investigation on the productivity of milling ti6al4v with cryogenic minimum quantity lubrication," *Modern Machinery science journal*, 2019.

[122] M. Nalbant and Y. Yildiz, "Effect of cryogenic cooling in milling process of AISI 304 stainless steel," *Transactions of Nonferrous Metals Society of China (English Edition)*, vol. 21, no. 1, pp. 72–79, 2011. [Online]. Available: http://dx.doi.org/10.1016/S1003-6326(11)60680-8

[123] A. Aramcharoen and S. K. Chuan, "An experimental investigation on cryogenic milling of inconel 718 and its sustainability assessment," *Procedia Cirp*, vol. 14, pp. 529–534, 2014.

[124] F. Pusavec, H. Hamdi, J. Kopac, and I. Jawahir, "Surface integrity in cryogenic machining of nickel based alloy Inconel 718," *Journal of Materials Processing Technology*, vol. 211, no. 4, 2011.

[125] Y. Kaynak, T. Lu, and I. S. Jawahir, "Cryogenic Machining-Induced Surface Integrity: A Review and Comparison with Dry, MQL, and Flood-Cooled Machining," *Machining Science and Technology*, vol. 18, no. 2, 2014.

[126] W. Zhao, F. Ren, A. Iqbal, L. Gong, N. He, and Q. Xu, "Effect of liquid nitrogen cooling on surface integrity in cryogenic milling of ti-6al-4 v titanium alloy," *The International Journal of Advanced Manufacturing Technology*, vol. 106, no. 3, pp. 1497–1508, 2020.

[127] A. Kummamkandath, A. Duchosal, A. Morandeau, R. Serra, and R. Leroy, "Influence of both rake and flank faces metal working fluid (mwf) strategies on machinability of ti-6al-4v alloy," *MM Science Journal*, vol. 2019, no. 04, pp. 3114–3121, 2019.

[128] G. M. Pittalà, "A study of the effect of co2 cryogenic coolant in end milling of ti-6al-4v," *Procedia Cirp*, vol. 77, pp. 445–448, 2018.

[129] F. Wang, Y. Wang, and H. Liu, "Tool wear behavior of thermal-mechanical effect for milling ti-6al-4v alloy in cryogenic," *The International Journal of Advanced Manufacturing Technology*, vol. 94, no. 5, pp. 2077–2088, 2018.

[130] D. Bhattacharyya and D. P. W. Horrigan, "A study of hole drilling in Kevlar composites," *Composites Science and Technology*, vol. 58, no. 2, pp. 267–283, 1998.

[131] V. Dhokia, A. S. Chaharsooghi, and S. Newman, "Cryogenic Machining of Carbon Fibre," in *12th International Conference of the European Society for Precision Engineering & Nanotechnology*, 2012.

[132] N. Govindaraju, L. S. Ahmed, and M. Pradeep Kumar, "Experimental Investigations on Cryogenic Cooling in the Drilling of AISI 1045 steel," *Materials and Manufacturing Processes*, vol. 29, pp. 1417–1421, 2014.

[133] L. S. Ahmed and M. P. Kumar, "Cryogenic Drilling of Ti-6Al-4V Alloy Under Liquid Nitrogen Cooling," *Materials and Manufacturing Processes*, vol. 31, no. 7, pp. 951–959, 2015. [Online]. Available: http://www.tandfonline.com/doi/full/10.1080/10426914.2015.1048475

[134] L. S. Ahmed, N. Govindaraju, and M. Pradeep Kumar, "Experimental Investigations on Cryogenic Cooling in the Drilling of Titanium Alloy," *Materials and Manufacturing Processes*, vol. 31, no. 5, pp. 603–607, 2016. [Online]. Available: http://www.tandfonline.com/doi/full/10.1080/10426914.2015.1019127

[135] M. I. Sadik, "Application of Different Cooling Strategies in Drilling of Metal Matrix Composite (MMC)," *Materials Science Forum*, vol. 836-837, pp. 3–12, 2016.

[136] T. Kanagaraju, S. R. Boopathy, and B. Gowthaman, "Effect of cryogenic and wet coolant performance on drilling of super duplex stainless steel (2507)," *Materials Express*, vol. 10, no. 1, pp. 81–93, 2020.

[137] J. Merzouki, G. Poulachon, F. Rossi, Y. Ayed, and G. Abrivard, "Effect of cryogenic assistance on hole shrinkage during ti6al4v drilling," *The International Journal of Advanced Manufacturing Technology*, vol. 108, no. 9, pp. 2675–2686, 2020.

[138] N. Khanna, F. Pusavec, C. Agrawal, and G. M. Krolczyk, "Measurement and evaluation of hole attributes for drilling cfrp composites using an indigenously developed cryogenic machining facility," *Measurement*, vol. 154, p. 107504, 2020.

[139] N. Khanna, C. Agrawal, M. K. Gupta, and Q. Song, "Tool wear and hole quality evaluation in cryogenic drilling of inconel 718 superalloy," *Tribology International*, vol. 143, p. 106084, 2020.

[140] L. Sterle, P. Krajnik, and F. Pušavec, "The effects of liquid-co2 cooling, mql and cutting parameters on drilling performance," *CIRP Annals*, 2021.

[141] R. P. Zeilmann and W. L. Weingaertner, "Analysis of temperature during drilling of Ti6Al4V with minimal quantity of lubricant," *Journal of Materials Processing Technology*, vol. 179, no. 1-3, pp. 124–127, 2006.

[142] Q.-P. Tran, M.-C. Tsai, T.-C. Hsiao, and S.-C. Huang, "Experimental influence of twist angle and cryogenic gas on quality of drilled hole in carbon fiber reinforced plastic composites," *Measurement and Control*, vol. 53, no. 5-6, pp. 943–953, 2020.

[143] E. Bagci and B. Ozcelik, "Investigation of the effect of drilling conditions on the twist drill temperature during step-by-step and continuous dry drilling," *Materials and Design*, vol. 27, no. 6, pp. 446–454, 2006.

[144] D. Biermann and H. Hartmann, "Reduction of burr formation in drilling using cryogenic process cooling," *Procedia CIRP*, vol. 3, no. 1, pp. 85–90, 2012.

[145] A. A. Khan and M. I. Ahmed, "Improving tool life using cryogenic cooling," *Journal of Materials Processing Technology*, vol. 196, no. 1, pp. 149–154, 2008.

[146] D. Biermann, H. Abrahams, and M. Metzger, "Experimental investigation of tool wear and chip formation in cryogenic machining of titanium alloys," *Advances in Manufacturing*, vol. 3, no. 4, pp. 292–299, 2015.

[147] L. Shakeel Ahmed and M. Pradeep Kumar, "Multiresponse optimization of cryogenic drilling on Ti-6Al-4V alloy using topsis method," *Journal of Mechanical Science and Technology*, vol. 30, no. 4, pp. 1835–1841, 2016. [Online]. Available: http://dx.doi.org/10.1007/s12206-016-0340-1

[148] U. Koklu and H. Çoban, "Effect of dipped cryogenic approach on thrust force, temperature, tool wear and chip formation in drilling of az31 magnesium alloy," *Journal of Materials Research and Technology*, vol. 9, no. 3, pp. 2870–2880, 2020.

[149] N. Khanna, C. Agrawal, M. Dogra, and C. I. Pruncu, "Evaluation of tool wear, energy consumption, and surface roughness during turning of inconel 718 using sustainable machining technique," *Journal of Materials Research and Technology*, 2020.

[150] J. L. Cantero, M. M. Tardí, J. A. Canteli, M. Marcos, and M. H. Miguélez, "Dry drilling of alloy Ti-6Al-4V," *International Journal of Machine Tools and Manufacture*, vol. 45, pp. 1246–1255, 2005.

[151] M. I. Sadik and S. Isakson, "The role of PVD coating and coolant nature in wear development and tool performance in cryogenic and wet milling of Ti-6Al-4V," pp. 4–10, 2017.

[152] A. M. Abdelhafeez, S. L. Soo, D. K. Aspinwall, A. Dowson, and D. Arnold, "Burr formation and hole quality when drilling titanium and aluminium alloys," *Procedia CIRP*, vol. 37, pp. 230–235, 2015. [Online]. Available: http://dx.doi.org/10.1016/j.procir.2015.08.019

[153] R. Patil, S. Shinde, D. Marla, and S. Joshi, "Experimental analysis of burr formation in drilling of ti-6al-4v alloy," *International Journal of Mechatronics and Manufacturing Systems*, vol. 9, no. 3, pp. 237–253, 2016.

[154] N. Joy, S. Prakash, A. Krishnamoorthy, and A. Antony, "Experimental investigation and analysis of drilling in grade 5 titanium alloy (ti-6al-4v)," *Materials Today: Proceedings*, vol. 21, pp. 335–339, 2020.

[155] X. Rimpault, J.-F. Chatelain, J. E. Klemberg-Sapieha, and M. Balazinski, "Burr height monitoring while drilling cfrp/titanium/aluminium stacks," *Mechanics & Industry*, vol. 18, no. 1, p. 114, 2017.

[156] N. T. Mathew and L. Vijayaraghavan, "Drilling of titanium aluminide at different aspect ratio under dry and wet conditions," *Journal of Manufacturing Processes*, vol. 24, pp. 256–269, 2016.

[157] S. G. Harris, E. D. Doyle, A. C. Vlasveld, J. Audy, and D. Quick, "A study of the wear mechanisms of Ti1-xAlxN and Ti1-x-yAlxCryN coated high-speed steel twist drills under dry machining conditions," *Wear*, vol. 254, no. 7-8, pp. 723–734, 2003.

[158] S. Dolinšek, B. Šuštaršič, and J. Kopač, "Wear mechanisms of cutting tools in high-speed cutting processes," *Wear*, vol. 250-251, no. PART 1, pp. 349–356, 2001.

[159] E. Bennett and D. Bennett, "Minimizing human exposure to chemicals in metalworking fluids," *Lubrication Engineering*, vol. 43, no. 3, pp. 167–175, 1987.

[160] P. Kumar, S. Jafri, P. Bharti, and M. Siddiqui, "Study of hazards related to cutting fluids and their remedies," *International Journal of Engineering Research & Technology (IJERT)*, vol. 3, no. 7, pp. 1225–1229, 2014.

[161] N. Khanna, C. Agrawal, D. Y. Pimenov, A. K. Singla, A. R. Machado, L. R. R. da Silva, M. K. Gupta, M. Sarikaya, and G. M. Krolczyk, "Review on design and development of cryogenic machining setups for heat resistant alloys and composites," *Journal of Manufacturing Processes*, vol. 68, pp. 398–422, 2021.

[162] R. U. Ayres, "Life cycle analysis: A critique," *Resources, conservation and recycling*, vol. 14, no. 3-4, pp. 199–223, 1995.

[163] IEA. (2022) Renewable share of global electricity generation 2019. [Online]. Available: https://www.iea.org/fuels-and-technologies/renewables

[164] C. Agrawal, J. Wadhwa, A. Pitroda, C. I. Pruncu, M. Sarikaya, and N. Khanna, "Comprehensive analysis of tool wear, tool life, surface roughness, costing and carbon emissions in turning ti–6al–4v titanium alloy: Cryogenic versus wet machining," *Tribology International*, vol. 153, p. 106597, 2021.

[165] A. F. Clarens, J. B. Zimmerman, G. A. Keoleian, K. F. Hayes, and S. J. Skerlos, "Comparison of life cycle emissions and energy consumption for environmentally adapted metalworking fluid systems," *Environmental science & technology*, vol. 42, no. 22, pp. 8534–8540, 2008.

[166] S. D. Supekar, D. J. Graziano, S. J. Skerlos, and J. Cresko, "Comparing energy and water use of aqueous and gas-based metalworking fluids," *Journal of Industrial Ecology*, vol. 24, no. 5, pp. 1158–1170, 2020.

[167] A. Al-Mamoori, A. Krishnamurthy, A. A. Rownaghi, and F. Rezaei, "Carbon capture and utilization update," *Energy Technology*, vol. 5, no. 6, pp. 834–849, 2017.

[168] F. Impero, M. Dix, A. Squillace, U. Prisco, B. Palumbo, and F. Tagliaferri, "A comparison between wet and cryogenic drilling of cfrp/ti stacks," *Materials and Manufacturing Processes*, vol. 33, no. 12, pp. 1354–1360, 2018.

[169] U. Prisco, F. Impero, and F. Rubino, "Peck drilling of cfrp/titanium stacks: effect of tool wear on hole dimensional and geometrical accuracy," *Production Engineering*, vol. 13, no. 5, pp. 529–538, 2019.

[170] J. Foltz and M. Gram, "Introduction to Titanium and Its Alloys," in *Heat Treating of Nonferrous Alloys*. ASM International, 06 2016. [Online]. Available: https://doi.org/10.31399/asm.hb.v04e.a0006253

[171] *E527-16 Standard Practice for Numbering Metals and Alloys in the Unified Numbering System (UNS)*, ASTM International Std., 2016. [Online]. Available: https://doi.org/10.1520/E0527-16

[172] J.-M. Oh, B.-G. Lee, S.-W. Cho, S.-W. Lee, G.-S. Choi, and J.-W. Lim, "Oxygen effects on the mechanical properties and lattice strain of ti and ti-6al-4v," *Metals and Materials International*, vol. 17, no. 5, pp. 733–736, 2011.

[173] P. Regtien and E. Dertien, "8 - piezoelectric sensors," in *Sensors for Mechatronics (Second Edition)*, second edition ed., P. Regtien and E. Dertien, Eds. Elsevier, 2018, pp. 245 – 265. [Online]. Available: http://www.sciencedirect.com/science/article/pii/B9780128138106000082

[174] *Kistler force dynamometer Type 9129AA datasheet*.

[175] ISO4288-98, "Geometric product specification (gps). surface texture. profile method- rules and procedures for the assessment of surface texture," ISO, Tech. Rep., 1998.

[176] S. Coromant. (2017) Coroplus toolguide. [Online]. Available: www.sandvik.coromant.com/en-gb/products/pages/toolguide.aspx

[177] A. Rana, G. Dongre, and S. S. Joshi, "Analytical modeling of exit Burr in drilling of Ti6Al4V alloy," *Sadhana - Academy Proceedings in Engineering Sciences*, vol. 44, no. 6, pp. 1–19, 2019. [Online]. Available: https://doi.org/10.1007/s12046-019-1114-0

[178] E. Franczyk, L. Slusarczyk, and W. Zebala, "Drilling burr minimization by changing drill geometry," *Materials*, vol. 13, no. 14, p. 3207, 2020.

[179] R. F. Hamade, C. Y. Seif, and F. Ismail, "Extracting cutting force coefficients from drilling experiments," *International Journal of Machine Tools and Manufacture*, vol. 46, no. 3-4, pp. 387–396, 2006.

[180] P. Zhang, N. Churi, Z. J. Pei, and C. Treadwell, "Mechanical drilling processes for titanium alloys: a literature review," *Machining Science and Technology*, vol. 12, no. 4, pp. 417–444, 2008.

[181] J. Kim and D. A. Dornfeld, "Development of an analytical model for drilling burr formation in ductile materials," *J. Eng. Mater. Technol.*, vol. 124, no. 2, pp. 192–198, 2002.

[182] S. Batzer, D. Haan, P. Rao, W. Olson, and J. Sutherland, "Chip morphology and hole surface texture in the drilling of cast aluminum alloys," *Journal of Materials Processing Technology*, vol. 79, no. 1-3, pp. 72–78, 1998.

[183] R. A. Fisher, "Statistical methods for research workers," in *Breakthroughs in statistics*. Springer, 1992, pp. 66–70.

[184] A. Aramcharoen, "Influence of cryogenic cooling on tool wear and chip formation in turning of titanium alloy," *Procedia CIRP*, vol. 46, pp. 83–86, 2016.

[185] S. Coromant. (2022) Corodrill 880. [Online]. Available: www.sandvik.coromant.com/en-gb/products/corodrill_880/pages/default.aspx

[186] M. Calamaz, D. Coupard, and F. Girot, "Numerical simulation of titanium alloy dry machining with a strain softening constitutive law," *Machining Science and Technology*, vol. 14, no. 2, pp. 244–257, 2010.

[187] Y. Gao, G. Wang, and B. Liu, "Chip formation characteristics in the machining of titanium alloys: a review," *International Journal of Machining and Machinability of Materials*, vol. 18, no. 1-2, pp. 155–184, 2016.

[188] E. Kuram, B. Ozcelik, E. Demirbas, and E. Sik, "Effects of the cutting fluid types and cutting parameters on surface roughness and thrust force," in *Proceedings of the world congress on engineering*, vol. 2, 2010, pp. 978–988.

[189] Y. Wei, Q. An, W. Ming, and M. Chen, "Effect of drilling parameters and tool geometry on drilling performance in drilling carbon fiber–reinforced plastic/titanium alloy stacks," *Advances in Mechanical Engineering*, vol. 8, no. 9, p. 1687814016670281, 2016.

[190] J. Rech, "Influence of cutting tool coatings on the tribological phenomena at the tool–chip interface in orthogonal dry turning," *Surface and Coatings Technology*, vol. 200, no. 16-17, pp. 5132–5139, 2006.

[191] M. K. Chaanthini, S. Murugappan, and S. Arul, "Study on hole quality in drilling aa 6063 plate under cryogenic pre-cooling environment," *Materials Today: Proceedings*, vol. 4, pp. 7476–7483, 2017.

[192] M. Aceves, "Subsurface deformation micromechanisms induced during machining of titanium alloys at low temperatures, and a novel testing methodology to examine their machining behaviour," February 2019. [Online]. Available: https://etheses.whiterose.ac.uk/23100/

[193] T. D. Ling, P. Liu, S. Xiong, D. Grzina, J. Cao, Q. J. Wang, Z. C. Xia, and R. Talwar, "Surface texturing of drill bits for adhesion reduction and tool life enhancement," *Tribology Letters*, vol. 52, no. 1, pp. 113–122, 2013.

[194] S. Niketh and G. Samuel, "Drilling performance of micro textured tools under dry, wet and mql condition," *Journal of Manufacturing Processes*, vol. 32, pp. 254–268, 2018.